



UNIVERSITÀ  
degli STUDI  
di CATANIA

Dipartimento  
di Fisica  
e Astronomia  
*"Ettore Majorana"*



PHD PROGRAMME IN PHYSICS  
CICLO XXXVI

---

FABRIZIO MURGANA

FUNCTIONAL RENORMALIZATION GROUP STUDY OF EFFECTIVE MODELS FOR QUANTUM  
CHROMODYNAMICS

---

PHD THESIS

---

SUPERVISORS:  
CHIAR.MO PROF. V. GRECO  
CHIAR.MO PROF. D. RISCHKE

---

ACADEMIC YEAR 2022/2023



# Contents

<b>Deutsche Zusammenfassung</b>	<b>7</b>
<b>1 Introduction</b>	<b>13</b>
<b>2 Quantum Chromodynamics and its symmetries</b>	<b>17</b>
2.1 Introduction to Quantum Chromodynamics	17
2.2 QCD symmetries and chiral symmetry	19
2.2.1 Chiral limit	20
2.2.2 Finite quark masses	21
2.2.3 Spontaneous breaking of chiral symmetry	24
<b>3 The Functional Renormalization Group</b>	<b>27</b>
3.1 Motivation	27
3.2 Wetterich formulation of the Functional Renormalization Group	28
3.3 Approximation schemes	32
3.3.1 Vertex expansion	32
3.3.2 Operator and Derivative Expansion	33
<b>4 The <math>O(N)</math> model</b>	<b>35</b>
4.1 Introduction and motivation	35
4.2 The flow equation in the LPA	37
4.2.1 Formulation in terms of the field $\sigma$ and boundary conditions	38
4.2.2 Conservative formulation	40
4.3 Critical behavior	43
4.3.1 Dimensional reduction	43
4.3.2 Order parameter	45
4.3.3 Critical scaling	47
4.3.4 Critical exponents	49
4.4 Testing the method: numerical precision and error estimates	52
4.4.1 General fit error	54
4.4.2 Error on $m^2$	56
4.4.3 Error on $\sigma_0^{\text{IR}}$	58
4.5 Final remarks	61
<b>5 The two-flavor Quark-Meson model</b>	<b>63</b>
5.1 Introduction and motivation	63
5.2 Approximate axial-vector symmetry and its consequences	65
5.2.1 PCAC	65
5.2.2 Goldberger-Treiman relation	66

5.3	From QCD symmetries to the QM-model Lagrangian . . . . .	67
5.4	Extensions of the model . . . . .	69
5.4.1	Explicit breaking of chiral symmetry . . . . .	70
5.4.2	Finite temperature . . . . .	70
5.4.3	Finite quark-number density . . . . .	71
5.5	Landau Mean-Field study . . . . .	72
5.5.1	Chiral limit . . . . .	72
5.5.2	Finite quark mass . . . . .	75
5.6	Beyond mean field: FRG approach . . . . .	77
5.6.1	Flow equation . . . . .	77
5.6.2	Bosonic contribution to the flow equation . . . . .	78
5.6.3	Fermionic contribution to the flow equation . . . . .	79
5.6.4	Full flow equation and hydrodynamic formulation . . . . .	79
5.6.5	Large- $N_c$ limit: MF reduction . . . . .	81
5.7	Comparison of the results in MF and in FRG . . . . .	82
5.7.1	Litim FRG setup . . . . .	82
5.7.2	Initial condition and model parameters . . . . .	83
5.7.3	MF vs FRG phase diagram . . . . .	83
5.7.4	Critical exponents . . . . .	87
<b>6</b>	<b>Quark Meson model: thermodynamic geometry</b>	<b>95</b>
6.1	Introduction and motivation . . . . .	95
6.2	The thermodynamic geometry . . . . .	96
6.3	FRG setup . . . . .	97
6.3.1	Flow equation in the LPA for the Litim regulator . . . . .	98
6.3.2	UV initial condition . . . . .	99
6.4	QM model thermodynamics . . . . .	100
6.5	Thermodynamic geometry results . . . . .	102
6.5.1	Finite pion mass . . . . .	102
6.5.2	Towards the chiral limit . . . . .	106
6.6	Conclusions and outlook . . . . .	111
<b>7</b>	<b>Quark-Meson model: regulator-dependence study</b>	<b>113</b>
7.1	Introduction and motivation . . . . .	113
7.2	Model and setup . . . . .	114
7.2.1	Quark-Meson model . . . . .	114
7.2.2	RG consistency and parameter dependence . . . . .	115
7.2.3	Preparation and regulators-shape functions . . . . .	117
7.3	Effective potential at leading order in large- $N_c$ expansion . . . . .	118
7.4	Beyond the large- $N_c$ approximation: LPA . . . . .	124
7.4.1	Parameter space and UV independence of the IR observables . . . . .	125
7.4.2	Cutoff Dependence Of Phase Diagram: Quartic Initial Condition . . . . .	128
7.4.3	Cutoff And Regulator Dependence Of Phase Diagram: regulator comparison . . . . .	131
7.5	Conclusions and outlook . . . . .	133
<b>8</b>	<b>Conclusions</b>	<b>135</b>
	<b>Bibliography</b>	<b>137</b>

<b>A</b>	<b>Notations and conventions</b>	<b>151</b>
A.1	Natural units . . . . .	151
A.2	Euclidean and Minkowski metric . . . . .	151
A.3	Pauli matrices . . . . .	151
A.4	Dirac matrices . . . . .	152
A.5	Fourier transform . . . . .	152
<b>B</b>	<b>Introductory elements to functional approaches</b>	<b>153</b>
<b>C</b>	<b>Derivation of the Wetterich equation</b>	<b>157</b>
<b>D</b>	<b>Derivation of the flow equations for different models</b>	<b>159</b>
D.1	O(N) model . . . . .	159
D.2	Quark-Meson model . . . . .	161
D.2.1	Bosonic contribution . . . . .	161
D.2.2	Fermionic contribution . . . . .	162
D.2.3	Fermi-surface regulator . . . . .	164
<b>E</b>	<b>Finite-Volume schemes and conservation laws</b>	<b>171</b>
E.1	Conservation laws and advection-diffusion equations . . . . .	171
E.2	Finite-Volume (FV) schemes . . . . .	173
E.3	LxF and NT central schemes . . . . .	174
E.4	Kurganov and Tadmor fully discrete scheme . . . . .	176
E.5	Semi-discrete formulation . . . . .	179
E.5.1	One-dimensional hyperbolic conservation laws . . . . .	179
E.5.2	One-dimensional advection–diffusion equations . . . . .	180



# Deutsche Zusammenfassung

Einer der faszinierendsten Aspekte der Physik ist die Suche nach einer Beschreibung der uns umgebenden Phänomene und die Erforschung der Prinzipien, die Materie, Energie, Raum und Zeit zugrunde liegen, mit dem Ziel, die Gesetze herauszuarbeiten, die die Phänomene des Universums von den kleinsten, subatomaren Teilchen bis hin zu den größten, kosmischen Strukturen diktieren.

In diesem Zusammenhang besteht eine der größten Herausforderungen der gegenwärtigen Physik darin, das Verhalten stark wechselwirkender Materie zu untersuchen. Die Theorie, die als primäres Werkzeug zur Aufklärung ihrer Eigenschaften und Wechselwirkungen dient, ist die sogenannte Quantenchromodynamik (QCD). QCD ist ein grundlegendes Element der modernen Teilchenphysik und bietet tiefgreifende Einblicke in die Struktur der Materie und die Kraft, die sie zusammenhält. Im Wesentlichen beschreibt die QCD die Dynamik von Quarks und Gluonen, den Grundbausteinen von Teilchen wie Protonen, Neutronen und anderen Hadronen.

Seit dem 20. Jahrhundert erforschen Wissenschaftler die grundlegende Struktur von Materie, was in der Einführung des Standardmodells der Teilchenphysik mündet, eines theoretischen Rahmenwerkes, das auf elegante Weise erklärt, wie subatomare Teilchen interagieren und welche Kräfte ihre Handlungen bestimmen. Innerhalb dieses Modells erweist sich die QCD als die Theorie der stark wechselwirkenden Kraft; neben der Schwerkraft, dem Elektromagnetismus und der schwach wechselwirkenden Kraft eine der vier Grundkräfte.

Die starke Kraft, die durch Teilchen vermittelt wird, die als Gluonen bekannt sind, ist dafür verantwortlich, Quarks zu binden und zusammengesetzte Teilchen, sogenannte Hadronen, zu bilden. Neben dem Flavourfreiheitsgrad, der jeweils durch eine andere Masse und elektrische Ladung gekennzeichnet ist, besitzen Quarks eine grundlegende Eigenschaft, die „Farbladung“, die der standardmäßigen elektrischen Ladung entspricht, jedoch eine andere Bedeutung besitzt. Tatsächlich bezieht sich „Chromodynamik“ im Namen QCD auf die Tatsache, dass die Wechselwirkung zwischen Quarks und Gluonen durch den Austausch von Farbladungen erfolgt, was an die mit dem Charakter der Farbwahrnehmung verbundene Dynamik erinnert.

Ogleich die QCD beträchtliche Fortschritte zum Verständnis der Natur stark wechselwirkender Materie gemacht hat, einschließlich der Erklärung der Hadronenmassen und des Verhaltens bei hohen Energien, nämlich die asymptotische Freiheit, sind mehrere Aspekte noch unklar. Beispielsweise ist der den Farbeinschluss bestimmende Mechanismus, d.h. die Tatsache, dass kein farbgeladenes Objekt beobachtet werden kann, nicht vollständig geklärt.

Diesem Forschungsgebiet wurden sowohl theoretische als auch experimentelle Anstrengungen gewidmet, da die Weiterentwicklung unseres Verständnisses stark wechselwirkender Materie Auswirkungen auf verschiedene Bereiche der Physik hat, vom Verständnis des Zustands des frühen Universums bis hin zur Dynamik dichter und kompakter

Sterne.

Die Merkmale stark wechselwirkender Materie werden häufig im QCD-Phasendiagramm dargestellt, das die erwarteten Phasen als Funktion der Temperatur und des baryochemischen Potentials veranschaulicht. Diese beiden Größen werden häufig gewählt, wenngleich aufgrund der noch vorliegenden erheblichen Verständnislücken es u.U. ratsam ist, andere in Betracht zu ziehen.

Bei einem baryochemischen Potential von Null durchläuft die QCD-Materie einen sanften Übergang von der farbeingeschlossenen hadronischen Materie hin zur Quark-Gluon-Plasmaphase bei hohen Temperaturen, wo Farbfreiheitsgrade freigesetzt werden. Das Phasendiagramm umfasst jedoch zusätzliche Komplikationen.

Wenn das chemische Potential der Baryonen zunimmt, werden Vorhersagen über das Verhalten stark wechselwirkender Materie weniger sicher und stützen sich oft auf effektive Modelle und Näherungen. Die Wiederherstellung der chiralen Symmetrie bei hohem chemischen Potential und niedriger Temperatur, möglicherweise über einen Phasenübergang erster Ordnung, bleibt Gegenstand von Überlegungen, die auf die Existenz eines kritischen Punktes schließen lassen.

Experimentelle Untersuchungen, insbesondere durch Schwerionenkollisionen an Einrichtungen wie dem Large Hadron Collider (LHC) und dem Relativistic Heavy Ion Collider (RHIC) zielen darauf ab, die Eigenschaften stark wechselwirkender Materie zu erforschen und kritische Endpunkte im QCD-Phasendiagramm zu lokalisieren. Theoretische Hilfsmittel wie Gittersimulationen und funktionale Methoden wie die funktionale Renormierungsgruppe (FRG), tragen zum Verständnis der Feinheiten des Phasendiagramms bei.

In diesem Zusammenhang spielen effektive Modelle eine entscheidende Rolle bei der Erfassung wesentlicher Merkmale der QCD, wenngleich diese Vereinfachungen vornehmen. Das Studium effektiver Feldtheorien und -modelle ist für unser Verständnis der Physik von entscheidender Bedeutung, insbesondere wenn wir uns mit grundlegenden Wechselwirkungstheorien wie der QCD befassen. Da diese effektiven Modelle insbesondere so aufgebaut sind, dass sie wesentliche Merkmale der zugrunde liegenden Theorie unter Verwendung einer vereinfachten Teilmenge von Symmetrien und Freiheitsgraden erfassen können, besteht das wesentliche Ziel darin, die kritischen Eigenschaften dieser Modelle zu verstehen und somit eine Möglichkeit zu schaffen, einen Einblick in die tatsächlichen kritischen Phänomene der QCD zu erhalten.

Doch selbst mit effektiven Modellen ist das Verständnis des Verhaltens von Systemen, in denen mikroskopische Elemente stark interagieren, oft sehr schwierig und erfordert den Einsatz geeigneter und leistungsfähiger Werkzeuge. Diese Herausforderung verschärft sich, wenn das System beispielsweise einen Phasenübergang durchläuft, mit der Einführung neuer Freiheitsgrade oder einer Änderung ihrer relativen Relevanz. Folglich muss der theoretische Rahmen diese Regime konsequent überbrücken und den Übergang zwischen verschiedenen physikalischen Skalen und den damit verbundenen Sätzen relevanter Freiheitsgrade detailliert beschreiben.

Eine weit verbreitete Methode zur Bewältigung solcher Szenarien ist die von Wilson entwickelte Renormierungsgruppe (RG). In Kombination mit der Störungstheorie erleichtert diese Methode die Beschreibung von Systemen mit zahlreichen interagierenden Freiheitsgraden, wobei Infrarot-Freiheitsgrade über eine kleine effektive Kopplung interagieren. Allerdings stößt dieser Ansatz bei Systemen ohne geringe Kopplung oder Systemen, bei denen sich die Identifizierung eines Störungsparameters als schwierig erweist, an seine Grenzen.

Eine der uns zur Verfügung stehenden Möglichkeiten, die Herausforderungen der perturbativen RG zu überwinden, ist die sogenannte funktionale Renormierungsgruppe (FRG), auch bekannt als exakte RG oder nicht-perturbative RG (NPRG). Die funktionale



Renormierungsgruppe gehört, wie der Name schon sagt, zur Klasse der funktionalen Methoden, deren Ziel es ist, erzeugende Funktionale von Korrelationsfunktionen zu berechnen, in denen alle physikalischen Informationen enthalten sind. Die FRG verbindet diesen funktionalen Ansatz mit dem RG-Konzept und geht schrittweise mit Schwankungen von Maßstab zu Maßstab um. Durch die Umwandlung von Standardformulierungen der Feldtheorie in eine funktionale Differentialstruktur verwendet die FRG eine Strömungsgleichung, die sogenannte Wetterich-Gleichung als zentrales Werkzeug und bietet so eine genaue Verbindung zwischen Korrelationsfunktionen auf der anfänglichen UV-Skala und der Korrelationsfunktion auf der endgültigen Skala, der IR-Skala, bei der alle Schwankungen herausintegriert wurden. Somit entspricht die Lösung dieser Strömungsgleichungen der Lösung der gesamten Theorie. Angesichts ihrer nicht-störungstheoretischen Natur und ihrer Fähigkeit, Freiheitsgrade über Skalen hinweg zu verbinden, scheint die FRG gut aufgestellt zu sein, um die Herausforderung der Beschreibung von Systemen nahe der Kritikalität und von Phasenübergängen zu beschreiben und stellt ein zuverlässiges Werkzeug für die Untersuchung komplexer Phänomene wie der erwarteten QCD-Phasenübergänge und das damit verbundene Phasendiagramm dar.

Dies ist der Grund, warum wir uns in dieser Arbeit unter der Verwendung der Vorteile effektiver Niedrigenergietheorien dafür entscheiden, uns auf die Verwendung der FRG-Methode zur Untersuchung effektiver Niedrigenergiemodelle für die QCD zu konzentrieren, wobei ein besonderer Fokus auf dem chiralen Phasenübergang liegt.

Jedoch hat die funktionale Natur des FRG-Ansatzes und der Wetterich-Gleichung zur Folge, dass ihre genaue Lösung kaum möglich ist und im Allgemeinen ein Ansatz für die effektive Wirkung erforderlich ist. In dieser Arbeit entscheiden wir uns für die Anwendung der lokalen Potentialnäherung (LPA), die vorschreibt, die Entwicklung nach Gradienten der quanteneffektiven Wirkung bei der nullten Ordnung abzubrechen und nur das quanteneffektive Potential einzubeziehen.

Eine der Hauptideen, die wir in dieser Arbeit verwenden, ist die Schlüsselbeobachtung, dass die FRG-Strömungsgleichung für bestimmte Modelle und Trunkierungsschemata in die Form einer Advektions-Diffusionsgleichung, gegebenenfalls mitsamt eines Quelltermes, umgewandelt werden kann. Diese Art von Gleichungen gehört zu der Klasse von Problemen, mit denen man im Zusammenhang der viskosen Hydrodynamik konfrontiert ist. Daher besteht ein innovativer Ansatz zur Lösung der FRG-Strömungsgleichung in der Wahl einer Methode, die speziell für die Lösung dieser Klasse hydrodynamischer Gleichungen entwickelt wurde. Insbesondere wird das Kurganov-Tadmor-Finite-Volumen-Schema übernommen. In dieser Arbeit wenden wir dieses Schema für die Untersuchung verschiedener physikalischer Systeme an und zeigen die Zuverlässigkeit und Flexibilität dieses Ansatzes. Im ersten Teil der Arbeit diskutieren wir das bekannte  $O(N)$ -Modell als effektives Modell, das lediglich eine Anzahl  $N$  bosonischer Freiheitsgrade umfasst. Bei der Wahl einer geeigneten Anfangsbedingung für das UV-effektive Potential kommt es zu einem spontanen Symmetriebruch der  $O(N)$ -Symmetrie zur  $O(N-1)$ -Untergruppe, was zu  $N-1$  Goldstone-Bosonen, den Pionen und einer radialen Sigma Mode führt. Die  $O(N)$ -Symmetrie wird dann bei ausreichend hoher Temperatur oder bei ausreichend niedrigen Werten des UV-Minimums des Potentials wiederhergestellt, wenn der Dimensionsreduktionssatz verwendet wird. Dieser Phasenübergang ist Gegenstand unserer Studie, die wir unter Verwendung der hydrodynamischen Formulierung durchführen, um die FRG-Strömungsgleichung in der LPA-Trunkierung zu lösen. Wir konzentrieren uns auf die Untersuchung des kritischen Verhaltens des Systems und berechnen die entsprechenden kritischen Exponenten. Besonderes Augenmerk wird auf die Fehlerabschätzung bei der Extraktion der kritischen Exponenten gelegt, was ein notwendiger und noch nicht umfassend erforschter Bereich ist. Die Ergebnisse sind gut kompatibel mit Resultaten aus der Literatur, die mit unterschiedlichen störungsthe-

oretischen und nicht-störungstheoretischen Methoden erzielt wurden, was hilft, dieses Verfahren in seiner Güte zu beurteilen.

Im zweiten Teil der Arbeit stellen wir das Quark-Meson-Modell als niederenergetisches effektives Modell in der QCD vor und richten ein besonderes Augenmerk auf sein chirales Symmetriebrechungsmuster und die anschließende dynamische Quarkmassenerzeugung. Die LPA-Strömungsgleichung ist vom Advektions-Diffusions-Typ mit einem zusätzlichen Quellbeitrag, der auf die Einbeziehung fermionischer Freiheitsgrade zurückzuführen ist. Wir übernehmen daher die entwickelten numerischen Techniken, um das Phasendiagramm des Modells abzuleiten, welches mit dem übereinstimmt, das mit anderen Techniken in der Literatur bereits erhalten wurde.

Wir verfolgen auch einen anderen möglichen Weg zur Untersuchung der kritischen Eigenschaften des Quark-Meson-Modells: die sogenannte thermodynamische Geometrie. Dieser Ansatz basiert auf der Interpretation des Parameterraums des Systems als Differentialmannigfaltigkeit. Aus dem Ricci-Skalar kann man dann relevante Informationen über Phasenübergänge gewinnen.

Mithilfe dieser geometrischen Technik ist es möglich, den chiralen Phasenübergang der QCD aus einer anderen Sicht zu betrachten. Dieser Ansatz beruht auf der Berechnung von Größen, die von Momenten höherer Ordnung des thermodynamischen Potentials beeinflusst werden, ermöglicht so eine umfassendere Analyse des Phasenübergangs.

Insbesondere untersuchten wir den chiralen Crossover, indem wir das Verhalten des Ricci-Skalars  $R$  bis zum kritischen Punkt hin untersuchten, wobei er ein Maximum am Crossover aufweist. Wir haben diese Analyse dann im chiralen Limes wiederholt, wo erwartet wird, dass der Phasenübergang zweiter Ordnung ist und der Peak in eine scharfe Divergenz übergehen sollte. Darüberhinaus bleibt der Ricci-Skalar bei niedrigen Werten des chemischen Potentials negativ, was darauf hindeutet, dass bosonische Fluktuationen die Fähigkeit des Systems verringern, die fermionische statistische Abstoßung von Quarks vollständig zu überwinden. Andererseits haben wir in Übereinstimmung mit molekularfeldtheoretischen (MF) Studien festgestellt, dass  $R$  zunimmt und das Vorzeichen wechselt, wenn das chemische Potenzial zunimmt und sich dem kritischen Punkt nähert.

Schließlich nutzen wir die numerischen Fortschritte, um das Problem der Wahl des Regulators in den FRG-Berechnungen anzugehen. Dies stellt sich als besondere Herausforderung heraus, wenn bestimmte Näherungen zur Lösung der FRG-Strömungsgleichung verwendet werden, und verdient eine umfassende Untersuchung. Insbesondere haben wir eine Vakuumparameterstudie durchgeführt und die RG-Konsistenzforderung verwendet, um die Auswirkung der Wahl des Regulators auf die physikalischen Observablen und auf das Phasendiagramm des Modells zu bestimmen. Mit dieser Studie entwickeln wir eine systematische Methode zum Vergleich der Ergebnisse für verschiedene Regulatoren. Wir zeigen, wie wichtig die Wahl eines geeigneten UV-Grenzwerts bei der Bestimmung UV-unabhängiger IR-Observablen ist und welche Auswirkungen die Trunkierung der effektiven Durchschnittswirkung und die Wahl des Regulators auf letztere haben.

Wir haben diese sowohl in der Mean-Field/Large- $N_c$ -Näherung als auch im vollständigen LPA-Fall untersucht. In der MF-Näherung fanden wir eine perfekte Übereinstimmung der Ergebnisse innerhalb verschiedener Regulatorklassen und Regulatorformfunktionen, wie es von der Ein-Schleifen-Universalitätseigenschaft erwartet wird. Dies bestätigt das Verfahren, mit dem wir einen RG-konsistenten UV-Ausgangszustand gefunden haben. Im LPA-Fall haben wir den UV-Parameterraum untersucht. Letzterer ist nicht vollständig zugänglich und weist einige Grenzen auf, die sich in den Grenzbereichen der zugänglichen IR-Krümmungsmasse und in den Phasendiagrammen

widerspiegeln, die für verschiedene Regulatorformfunktionen erhalten werden. Wir haben auch beobachtet, dass diese Banden dazu neigen, an einem einzigen Punkt in der Grenze des divergierenden UV-Grenzwerts zu konvergieren, was darauf hindeutet, dass man einen ausreichend großen UV-Grenzwert wählen sollte, um einen parameterunabhängigen Anfangszustand und damit ein regulatorunabhängiges IR-Potential zu erhalten. Wir fanden weiter heraus, dass die Phasendiagramme, die unter Verwendung der gleichen Regulatorformfunktionen für Bosonen und Fermionen erhalten wurden, eine deutliche Übereinstimmung aufweisen, was wiederum darauf hindeutet, dass unser Vergleichsverfahren tatsächlich erfolgreich war.

Mögliche zukünftige Forschungsrichtungen, die sich aus dieser Arbeit ergeben, könnten sich mit der Untersuchung der Stabilität der erzielten Ergebnisse befassen, wenn die in der funktionalen Renormierungsgruppentechnik verwendete Trunkierungsmethode verfeinert wird. Eine Möglichkeit besteht beispielsweise darin, skalenabhängige, aber nicht feldabhängige Wellenfunktions-Renormierungsfaktoren sowohl für Boson- als auch für Quarkfelder einzubeziehen, was zur sogenannten LPA'-Trunkation führt. Dies wäre äußerst interessant, insbesondere angesichts der möglichen Entstehung inhomogener Phasen bei hohem chemischem Potential.

Darüber hinaus besteht ein alternativer Weg zur Weiterentwicklung und tieferen Erforschung darin, zusätzliche Kondensationskanäle wie die Diquark-Kondensate einzubauen, die zur Untersuchung des Phänomens der Farbsupraleitung bei hohen Dichten verwendet werden könnten. Diese Erweiterung erfordert die Modifizierung des Modells, um verschiedene Freiheitsgrade abzudecken und so die Analyse verschiedener Phänomene und Übergänge über die chirale Natur hinaus zu ermöglichen. Eine solche Erweiterung würde zu einer umfassenderen Kartierung des QCD-Phasendiagramms beitragen, im Einklang mit dem übergeordneten Ziel dieser Arbeit und den laufenden Bemühungen im Bereich der Forschung in der Hochenergiephysik.



## Introduction

One of the main challenges in modern physics is represented by the understanding of the behavior of strongly interacting matter, with a particular focus both on elementary particles, such as quarks and gluons, and on their link with the corresponding composite objects, the hadrons. The theory we currently use to describe this kind of particles and their mutual interactions is the so-called *Quantum Chromodynamics* (QCD). This theory has achieved great results in unraveling the features of strongly interacting matter, such as the explanation of the origin of hadrons' mass and the understanding of the perturbative behavior at high energies, with the related asymptotic freedom [1, 2]. However, QCD presents several aspects which are still not fully understood today, like the rigorous mechanism behind the confinement of color degrees of freedom. In general, a huge effort, both theoretically and experimentally, has been put on this research field. Being able to deepen our current knowledge on the behavior of strongly interacting matter would have a significant impact on several areas of physics, ranging from our understanding of the very hot and relatively dilute early stages of our universe, to the comprehension of the mechanisms that regulate dense and relatively cold compact stars.

The features of strongly interacting matter are usually summarized in the so-called *QCD phase diagram*, in which the expected different stable phases of QCD matter are represented as a function of temperature and baryon chemical potential. Occasionally, also other chemical potential axes, associated to the respective conserved quantities, are included in the phase diagram, like for example the isospin chemical potential (see, e.g., [3, 4] and references therein), but the most common literature studies have focused on the two axes of temperature and baryon chemical potential. This is the case since already the majority of the standard  $T$ - $\mu_B$  phase diagram is uncharted. As an example, a sketch of the conjectured QCD phase diagram is shown in Fig. 1.1.

It is well known that (see, e.g., [5, 6] and references therein) at vanishing baryon chemical potential QCD matter experiences a smooth crossover from a low-temperature, confined hadronic matter, in which chiral symmetry is spontaneously broken, to the so-called *quark-gluon plasma* (QGP), a high-temperature phase, in which color degrees of freedom are deconfined, quark and gluons are weakly interacting and chiral symmetry is approximately restored. Nevertheless, the aforementioned crossover transition represents just the tip of the iceberg, and the QCD phase diagram incorporates many other interesting features. As an example, around  $\mu_B \sim 1$  GeV and at low temperatures, a first-order transition should take place between a hadron gas and a nuclear liquid phase, which leads to ordinary nuclear matter. The first-order line should then end in correspondence of the scale of nuclear binding energies around  $T \sim 15$  MeV, with a second-order critical point. These statements are widely confirmed, both from a theoretical and experimental point of view ( see, e.g., [7, 8, 9, 10]).

Increasing the chemical potential, the precise structure of the QCD phase diagram is

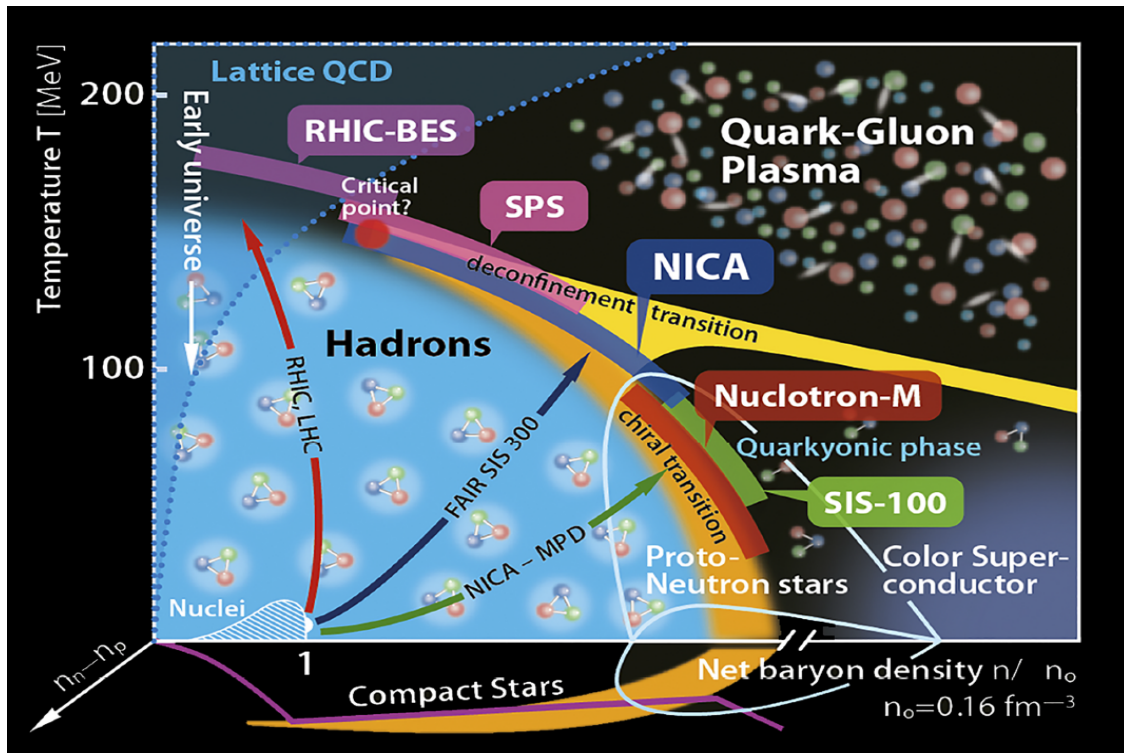


Figure 1.1: Sketch of the conjectured phase diagram of QCD. Figure is taken from Compact Stars in the QCD Phase Diagram (CSQCD) 2017 conference poster.

not certain, and the expected behavior of strongly interacting matter is deduced mostly on the basis of effective models and approximations.

In particular, it is believed that chiral symmetry should be restored in the regime of high chemical potential and low temperature, and that this phase transition should be of first order (see, e.g., [11, 12, 13] and references therein). This would imply the existence of a critical point connecting the conjectured first-order line with the known crossover at low chemical potential. At of this point, the phase transition should become of second order.

It has also been speculated [14] that the confinement/deconfinement-transition line and the chiral symmetry breaking/restoration-transition line do not match for large values of the baryon chemical potential, possibly leading to regions of the phase diagram where chiral symmetric matter is still confined, but the question is not settled yet.

A possible phase that may exist in this regime at high chemical potential is the so-called *quarkyonic phase*, where hadrons, which are still present in this phase, have such a large overlap due to the high densities that quarks may be considered as the relevant degrees of freedom and as almost free [15, 16].

Upon further increasing the baryon chemical potential and keeping the temperature low, it is conjectured that quark-quark pairing may be energetically favored over quark-anti-quark pairing, leading to diquark condensation and the so-called *color-superconducting phase* [17, 18, 19, 20].

From an experimental point of view, the study of the properties of strongly interacting matter and the investigation of the QCD phase diagram, and specifically the location of the critical endpoint, are some of the main goals of modern experiments. Part of these experiments is performed via heavy-ion collisions, like, for example, the ones that take place at the LHC (Large Hadron Collider) and at RHIC (Relativistic Heavy Ion Collider), which belong to the European Council for Nuclear Research (CERN, from the French acronym), in Geneva, and to the Brookhaven National Laboratory (BNL), in Upton, New York, respectively. In the near future, more experiments are expected to be added to

the previous ones, namely the ones performed at FAIR (Facility for Antiproton and Ion Research), in Darmstadt, like for example the Compressed Baryonic Matter (CBM) one, and at NICA (Nuclotron-based Ion Collider fAcility), at the Joint Institute for Nuclear Research (JINR), in Dubna.

From a theoretical viewpoint, a great advancement in the direction of the understanding of the QCD phase diagram has been made with the introduction of lattice simulations, which, as the name suggests, are able to perform non-perturbative calculations by discretizing the theory on a lattice. In particular, lattice studies obtained stunning results in the low chemical-potential regime, like confirming the hypothesis that the phase transition between hadronic matter and QGP is a smooth crossover in the aforementioned regime. However, the reliability of lattice-QCD results is limited to the case of vanishing or small chemical potential, due to the presence of the so-called *sign problem*: a finite chemical potential leads to a complex weight in the probability distribution of field configurations, which do not allow for the correct statistical interpretation of the action (see, e.g., [21, 22, 23, 24]).

Thus, on one hand, the understanding of the behavior of strongly interacting matter, especially in the low-temperature and high-density regime, strictly calls for a non-perturbative approach, like the one provided by lattice QCD. On the other hand, the sign problem limits the availability of the latter in the desired regime. One of the possibilities that are available to tackle this issue is the use of functional methods, which retain the advantage of being non-perturbative and are not affected by any a-priori limitation in the high-density regime. Recently, functional methods have indeed been used to investigate the QCD phase diagram, see, e.g., [25, 26, 27].

In particular, in this work we will use the Functional Renormalization Group (FRG) method, which is a functional non-perturbative method, and has also the advantage of linking physics at different energy scales. These features make FRG perfectly compatible with the task of studying non-perturbative phenomena and in particular phase transitions, like the ones expected for strongly interacting matter.

Nevertheless, also the FRG approach has its own limitations and drawbacks, like, for example, the need for the use of truncations and approximations in the solution of the flow equation and the related convergence of these approximations. Furthermore, especially in the full QCD case, calculations are very demanding and need for further approximations, which often effectively limit the reliability of the results to the  $\mu/T \lesssim 3$  region of the phase diagram (see, e.g., [25] and references therein).

From the previous discussion, we can understand why effective models shine in this contest. They have the ability to capture some of the desired features of the full underlying theory, with a significant simplification, which reduces the need for further approximations. In this thesis we will focus on two models, namely the  $O(N)$  model and the quark-meson (QM) model, which find applicability as QCD effective theories since they are expected to capture the essential features of the chiral phase transition. Nevertheless, no information can be extracted from these models on the extremely high chemical-potential regime of QCD, where, for example, an extension which includes diquarks as degrees of freedom could be considered, leading to the so-called quark-meson-diquark (QMD) model (see, e.g., [17, 18, 28]). Furthermore, these models do not capture the confinement/deconfinement phase transition of QCD, which could be assessed by the inclusion of the Polyakov loop to the model, leading to the so-called Polyakov-loop-quark-meson model (PQM) (see, e.g., [29, 30, 31]).

Due to these limitations, in this work we focus primarily on the chiral phase transition of QCD, and in particular we adopt the FRG as a tool to investigate it. Furthermore, we make use of a recently developed method [32], which is based on casting the FRG flow equation into a hydrodynamic advection-diffusion equation, allowing for a more



appropriate numerical treatment and error analysis.

This thesis is organized as follows: in Chapter 2 we provide a brief overview of QCD and its symmetries, with a special focus on chiral symmetry; in Chapter 3 we introduce the concept of the Functional Renormalization Group in the formulation given by Wetterich; in Chapter 4 we discuss the  $O(N)$  model using the FRG approach in the local-potential approximation (LPA), studying the critical behavior and computing the critical exponents of the model; in Chapter 5 we focus on the QM model and its phase diagram, presenting a comparison between mean-field (MF) results and FRG calculations; in Chapter 6 we introduce the concept of the thermodynamic geometry and apply it to the study of the phase transitions exhibited by the QM model, comparing both MF and FRG results; in Chapter 7 we present a study of the dependence, of the choice of the FRG regulator, of physical observables and of the phase diagram of the QM model; conclusions can be found in Chapter 8. In addition to this, in App. A we establish the notations and the conventions used throughout this work; in App. B we give an overview of the functional approach to QFT; in App. C we present a brief derivation of the Wetterich equation; in App. D we derive the flow equation for the  $O(N)$  model and for the QM model; finally, in App. E we present a brief overview of conservation laws, advection-diffusion equations and the numerical schemes which have been developed in order to solve them.



# Quantum Chromodynamics and its symmetries

## 2.1 Introduction to Quantum Chromodynamics

The theory that we currently use to describe strongly interacting matter is called Quantum Chromodynamics (QCD). It is a quantum field theory and the fields used to represent the fundamental degrees of freedom of the theory are quarks, which are spin-1/2 fermions, and gluons, which are bosons with spin 1. From a more formal point of view QCD is a gauge theory, meaning that, in the Lagrangian, the interaction term between quarks and gluons is obtained by imposing an invariance under local transformations which belong to a gauge group. In particular, the gauge group of QCD is  $SU(3)$ , which is a non-abelian group, i.e., a non-commutative group. This represents a fundamental feature of QCD since, as we will see soon in detail, this implies the possibility for classical 3 and 4 gluon interactions. This feature is absent in abelian gauge theories, like for example Quantum electrodynamics, whose gauge group is the abelian  $U(1)$ . Quarks can interact via the electromagnetic force since they carry an electric charge, which appears in fractions of either  $\pm 1/3$  or  $\pm 2/3$  of the electron elementary charge. However, the most important aspect to us is that they carry another type of charge, the so-called *color charge*, which is the reason why quarks interact via the strong interaction through the exchange of gluons, which mediate the strong force. Formally, quarks belong to the fundamental (vectorial) 3-dimensional representation of the  $SU(3)$ , usually referred to as "triplet", meaning that they can have 3 different colors, usually indicated as "red", "blue" and "green", and the corresponding anti-colors for anti-quarks. These names originate from the fact that the combination of the three different (anti-)colors leads to color singlets, or color neutrality, which is usually referred to as "white". Naturally, the combination of color and its corresponding anti-color results in white as well. Also gluons carry color charge, and they belong to the adjoint representation of  $SU(3)$ , which is a  $3^2 - 1 = 8$ -dimensional representation, meaning that there are 8 possible colors for gluons. That's why the adjoint representation is usually referred to as the "octet". Since the adjoint representation can be formally obtained superposing a triplet and an anti-triplet,  $3 \otimes \bar{3} = 8 \oplus 1$ , gluons are usually indicated as combinations of color and anti-colors. However, QCD shows an interesting feature, the so-called *confinement property*, which implies that only white particles can be observed directly, while quarks and gluons cannot. The white particles that we observe are the so-called *hadrons*. As we pointed out, the combination quark-antiquark is one of the possibility to obtain a white object. Thus hadrons that contain pair of a valence quark and an anti-quark are called *mesons*, like pions, kaons etc.. As previously stated, another possibility for an object to have zero

color charge is to result as the combination of three valence quarks with different colors. Such hadrons made up of three quarks are the so-called *baryons*, like protons and neutrons. As it seems natural, there are more possibilities for color-neutral objects, like for example tetraquarks, formed by two quark-anti-quark pairs, or pentaquarks, composed by quark, anti-quark and three other quarks, and so on. However, these states will not be further explored in this work, and one can refer to [33, 34, 35, 36, 37] and references therein. Quarks also come in six different types, named flavors, which have different masses. These flavors are usually labelled as up (u), down (d), strange (s), charm (c), bottom (b) and top (t). The up and down quarks have a mass of approximately 3-5 MeV, while the strange quark already has a mass of around 100 MeV. Those three flavors are usually referred to as light flavors (mostly u and d but with a bit of stretch also s) and will play, as we will soon see, a fundamental role when dealing with chiral symmetry.

The Lagrangian of QCD then reads:

$$\mathcal{L}_{QCD} = \bar{\Psi}(x) (i\mathcal{D} - M) \Psi(x) - \frac{1}{4} G_{\mu\nu}^a G^{a\mu\nu}. \quad (2.1)$$

We now discuss the various terms that appear in the Lagrangian.

$\Psi(x)$  is a Dirac spinor which collects all the various possible flavors and colors for the quarks. As we discussed, quarks are in the fundamental representation of the SU(3) group, meaning that they have 3 color d.o.f.. This implies that, since they come in six possible flavors and have a 4-component Dirac spinor structure,  $\Psi(x)$  is a  $4 \otimes 6 \otimes 3$  spinor.  $\bar{\Psi}(x) = \Psi^\dagger(x)\gamma^0$  is the Dirac adjoint of  $\Psi(x)$ , where  $\Psi^\dagger(x)$  denotes the hermitian adjoint of the spinor  $\Psi(x)$ , and  $\gamma^0$  is the time-like gamma matrix which acts only on the four-dimensional Dirac structure of  $\Psi(x)$ .  $M$  is a  $(4 \otimes 6 \otimes 3) \times (4 \otimes 6 \otimes 3)$  matrix that contains the masses of quarks, which have electroweak origin, for various flavors and colors, and it is diagonal both in Dirac and in flavor and in color space. The term  $\mathcal{D} = \gamma^\mu D_\mu$  contains the standard gamma-matrices and the covariant derivative  $D$  that originates imposing the local SU(3) invariance of the theory. It is diagonal in flavor space so we can separate this contribution

$$D_\mu^{ff'ij} = \delta^{ff'} D_\mu^{ij}, \quad (2.2)$$

where  $f, f' = 1 \dots 6$  are flavor indices,  $i, j = 1, \dots 3$  are color indices and the structure in color space reads

$$D_\mu^{ij} = \delta^{ij} \partial_\mu - i g_s A_\mu^a(x) T_a^{ij}. \quad (2.3)$$

Here  $A^a(x)$  indicates the gluon fields, with  $a = 1, \dots N_c^2 - 1 = 8$  (a summation over the index  $a$  is implied), meaning that there are eight kinds of gluon. This statement follows from what we already pointed out, since gluons transform under the 8-dimensional adjoint representation of the SU(3) color group.  $T_a$  are eight  $3 \times 3$  matrices and are the generators of the SU(3) group in the fundamental representation. The quantity  $g_s$  is the QCD coupling constant and determines the strength of both quark-gluon and gluon-gluon interactions. We thus can see that the fermionic part has the form

$$\mathcal{L}_{Dirac} = \bar{\Psi}(x) (i\mathcal{D} - M) \Psi(x) = \mathcal{L}_{Free} + \mathcal{L}_{Current}. \quad (2.4)$$

Here we separated the two contributions

$$\mathcal{L}_{Free} = \bar{\Psi}(x) (i\mathcal{D} - M) \Psi(x), \quad (2.5)$$

which is nothing but the simple Lagrangian for free Dirac fields with mass term  $M$ , while

$$\mathcal{L}_{Current} = g_s \bar{\Psi}(x) \gamma^\mu A_\mu^a(x) T_a \Psi(x) \quad (2.6)$$

represents the interaction current mediated by the gluons. From the Feynman-rules perspective, this last term corresponds to a quark-anti-quark-gluon vertex proportional to  $g_s$ . The presence of the SU(3) generators suggests the fact that a gluon's interaction with a quark corresponds to a rotation of the quark in SU(3) color space.

Finally,

$$\mathcal{L}_{Gauge} = -\frac{1}{4}G_{\mu\nu}^a G^{a\mu\nu} \quad (2.7)$$

represents the pure gluonic contribution to the Lagrangian and  $G_{\mu\nu}$  corresponds to the gluon field-strength tensor

$$G_{\mu\nu}^a = \partial_\mu A_\nu^a - \partial_\nu A_\mu^a + g_s f^{abc} A_\mu^a A_\nu^b, \quad (2.8)$$

where the  $f^{abc}$  are the antisymmetric structure constants of the SU(3) group appearing in the corresponding group algebra

$$[T^a, T^b] = i f^{abc} T^c. \quad (2.9)$$

The presence of a quadratic term in the gluon fields in Eq.(2.8) is a direct consequence of the theory being non-abelian, since for abelian theories the structure constants trivially vanish. From this follows that the insertion of Eq.(2.8) into Eq.(2.7) leads to terms which are cubic and quartic in the gluon fields. This implies that the theory allows, already at tree level, 3-gluon and 4-gluon self interactions, which are proportional, respectively, to  $g_s$  and  $g_s^2$ . Once again, this feature is not present in abelian gauge theories, like QED, where photons do not interact with themselves (at tree level, because higher-order diagrams lead to small photon-photon interactions).

As a final remark, as we have seen, the coupling constant  $g_s$  plays a crucial role in the theory. One of the most important features of QCD is that  $g_s$ , or equivalently  $\alpha_s = g_s^2/4\pi$ , becomes weak for processes involving large momentum transfers ("hard processes"). This phenomenon is usually referred to as *asymptotic freedom* and was shown by Gross, Wilczek, Politzer [1, 2] in the context of perturbation theory. This behavior of the coupling constant solidly justifies the use of perturbative QCD (pQCD) at high energy scales and the reliability of the obtained results. On the other hand, when approaching lower momentum transfers ("soft processes"), pQCD would predict the existence of the so-called *Landau pole*, meaning a point where  $\alpha_s$  would diverge. The divergent behavior of  $\alpha_s$  starts from the scale  $\Lambda_{QCD} \sim 200$  MeV, suggesting that, below this scale, perturbative approaches are bound to fail and non-perturbative methods are required. In this work, for example, we will rely on the use of the Functional Renormalization Group (see Chapter 3).

## 2.2 QCD symmetries and chiral symmetry

Besides Poincaré and CP invariance, as we already stated, QCD is a gauge theory, and thus it is endowed with the local SU( $N_c$ ) color symmetry, where  $N_c$  represents a general number of colors, which for real QCD corresponds to  $N_c = 3$ . A special subset of the gauge transformation is the so-called *center* of the SU(3) gauge group, i.e.,  $\mathbb{Z}_3$ , which corresponds to the transformations that commute with every other group element. To this special subset is related the so-called *center symmetry* of QCD, whose breaking and restoration pattern is associated to the transition between confined and deconfined QCD matter, and whose order parameter is the Polyakov loop. In any case, this will not be the focus of this section and of this work, so one can refer to, e.g., [38, 39, 40, 41] and references therein for a discussion on the subject. The type of symmetry we are more

interested in regards the flavor space, and in particular global flavor symmetries. It is clearly sufficient to consider just the Dirac component of the full QCD Lagrangian, since the pure gauge sector is trivially invariant under transformations in the flavor space, meaning that different flavors have the same strong interaction.

### 2.2.1 Chiral limit

As a first step, let us consider the so-called *chiral limit*, which means that we assume that the bare quark masses vanish. Let us also decompose each flavor Dirac spinor into its left-handed and right-handed Weyl spinors, using the projection

$$\Psi_{L/R} = P_{L/R} \Psi, \quad (2.10)$$

where the operator that projects onto the chiral eigenstates is given by:

$$P_{L/R} = \frac{1 \mp \gamma_5}{2}, \quad (2.11)$$

with  $\gamma_5 = i\gamma_0\gamma_1\gamma_2\gamma_3$ . In this way we can rewrite the Dirac Lagrangian separating the two chiral projections

$$\mathcal{L}_{Dirac}^{chiral} = i\bar{\Psi}_L(x)\not{D}\Psi_L(x) + i\bar{\Psi}_R(x)\not{D}\Psi_R(x). \quad (2.12)$$

First of all, from Eq.(2.12) it is clear that  $\mathcal{L}_{Dirac}$  is invariant under the two independent unitary flavor-space transformations  $U_L(1) \otimes U_R(1)$ , which act on the spinors giving them a global phase

$$\Psi'_{L/R}(x) = U_{L/R}(1) \Psi_{L/R}(x) = e^{-i\theta_{L/R}} \Psi_{L/R}(x). \quad (2.13)$$

In terms of the whole Dirac spinor in the chiral representation

$$\Psi(x) = \begin{pmatrix} \Psi_L(x) \\ \Psi_R(x) \end{pmatrix}, \quad (2.14)$$

these two symmetries translate into two corresponding symmetries, the so-called  $U_V(1)$  vectorial symmetry and  $U_A(1)$  axial symmetry. Let us first look at the vectorial transformation

$$\Psi'(x) = U_V(1)\Psi(x) = e^{-i\theta_V}\Psi(x), \quad (2.15)$$

which is obtained when transforming the Weyl spinors using the same angle  $\theta_R = \theta_L = \theta_V$ . The axial symmetry is instead realized when transforming the Dirac spinor in the following way

$$\Psi'(x) = U_A(1)\Psi(x) = e^{-i\gamma_5\theta_A}\Psi(x), \quad (2.16)$$

where the  $\gamma_5$  matrix is a block-diagonal  $4 \times 4$  matrix whose  $2 \times 2$  blocks act on the Weyl spinors, which in the chiral representation for Dirac spinors reads (see App. A)

$$\gamma_5 = \begin{pmatrix} -\mathbb{I}_{2 \times 2} & 0_{2 \times 2} \\ 0_{2 \times 2} & \mathbb{I}_{2 \times 2} \end{pmatrix}. \quad (2.17)$$

The transformation Eq.(2.16) thus relates the two angles of the corresponding Weyl-spinor transformations such that  $\theta_R = -\theta_L = \theta_A$ .

If we now turn our attention back to the chiral Dirac Lagrangian Eq.(2.12), we can notice that it is invariant under other transformations belonging to a larger symmetry

group. In particular, in the Weyl-spinor formulation, it possesses an  $SU_L(N_f) \otimes SU_R(N_f)$  symmetry, under which the Weyl spinors transform as follows

$$\Psi'_{L/R}(x) = SU_{L/R}(N_f) \Psi_{L/R}(x) = e^{-i\vec{T} \cdot \vec{\theta}_{L/R}} \Psi_{L/R}(x), \quad (2.18)$$

where  $\vec{T}$  corresponds to the  $(N_f^2 - 1)$ -dimensional vector of the  $SU(N_f)$  group generators in the fundamental representation and  $\vec{\theta}_{L/R}$  contains the  $(N_f^2 - 1)$  parameters of the transformation. Analogously to the previous case, one can reformulate the transformations Eq. (2.18) in terms of reparametrizations acting on the full Dirac spinors, obtaining an  $SU_V(N_f) \otimes SU_A(N_f)$  transformation defined as follows

$$\Psi'(x) = SU_V(N_f) \Psi(x) = e^{-i\vec{T} \cdot \vec{\theta}_V} \Psi(x) \quad (2.19)$$

and

$$\Psi'(x) = SU_A(N_f) \Psi(x) = e^{-i\gamma_5 \vec{T} \cdot \vec{\theta}_A} \Psi(x), \quad (2.20)$$

where the new parameters can be defined as previously

$$\vec{\theta}_V = \vec{\theta}_L = \vec{\theta}_R \quad (2.21)$$

and

$$\vec{\theta}_A = -\vec{\theta}_L = \vec{\theta}_R. \quad (2.22)$$

In particular the  $SU_V(N_f) \otimes SU_A(N_f)$  symmetry is usually referred to as *chiral symmetry*. So the total symmetry group of the chiral QCD Lagrangian, referred also as the chiral group, is given by

$$U_L(1) \otimes U_R(1) \otimes SU_L(N_f) \otimes SU_R(N_f), \quad (2.23)$$

expressed in terms of Weyl spinors, or equivalently in terms of the chiral Dirac spinors

$$U_A(1) \otimes U_V(1) \otimes SU_A(N_f) \otimes SU_V(N_f). \quad (2.24)$$

In particular we will focus on the latter, since it is easier to recognize which symmetries are fulfilled and which ones are broken.

### 2.2.2 Finite quark masses

We now relax the hypothesis of vanishing quark masses and insert back the mass term in the Dirac Lagrangian to see the effect on the various symmetries. Since we already stated that  $\mathcal{L}_{Dirac}^{chiral}$  is invariant under the chiral-group transformations, we will focus only on the mass term

$$\mathcal{L}_{Dirac}^{mass} = -\bar{\Psi}(x) M \Psi(x). \quad (2.25)$$

We now rewrite it in terms of the right- and left-handed Weyl spinors:

$$\mathcal{L}_{Dirac}^{mass} = -\bar{\Psi}_L(x) M \Psi_R(x) - \bar{\Psi}_R(x) M \Psi_L(x). \quad (2.26)$$

From this expression it is clear that the mass couples left-handed and right-handed spinors, and thus the left and right symmetry groups cannot act independently as it was the case in the chiral limit. This means that part of the flavor symmetry of the initial QCD Lagrangian is said to be *explicitly broken* by the mass term. Thus, let us consider more in detail how the various symmetries are modified due to the presence of the finite mass term.

### $U_V(1)$ symmetry

The  $U_V(1)$  symmetry is still realized by the QCD Lagrangian. In particular, according to *Noether's theorem*, there is a conserved current associated to this symmetry

$$\partial_\mu J^\mu = 0, \quad (2.27)$$

with

$$J_\mu(x) = \bar{\Psi}(x) \gamma_\mu \Psi(x) \quad (2.28)$$

and thus a conserved charge

$$\frac{d}{dt} B(t) = 0, \quad (2.29)$$

with

$$B = \frac{1}{3} \int_{\mathbb{R}^3} d^3x J_0(x) = \frac{1}{3} \int_{\mathbb{R}^3} d^3x \bar{\Psi}(x) \gamma_0 \Psi(x). \quad (2.30)$$

This conserved charge is called *baryon number*, since it basically represents the difference between the number (operator) of quarks and anti-quarks, thus representing the net number of baryons (recalling that quarks have baryon number of  $1/3$ ). The fact that the baryon number is a conserved charge implies that it will be conserved in every process that is governed by the strong interaction, and that every process that violates it is not allowed. For example this is the reason why the proton is stable and does not decay. In fact the proton has baryon number 1 and it is the lightest baryon, implying that it would have to decay into lighter non-baryonic particles with baryon number 0, thus violating baryon-number conservation.

### $SU_V(N_f)$ symmetry

The  $SU_V(N_f)$  symmetry can still be a symmetry of the QCD Lagrangian also in the finite quark-mass case, but it is realized only if the quark masses are equal for all flavors, i.e., if

$$M = m \mathbb{I}_{N_f \times N_f}. \quad (2.31)$$

This symmetry is sometimes referred to as *generalized isospin* symmetry, while the standard *isospin* symmetry corresponds to the case  $N_f = 2$ . The associated conserved Noether current is usually referred to as the *vector current* and is given by

$$V_\mu^k(x) = \bar{\Psi}(x) \gamma_\mu T^k \Psi(x), \quad (2.32)$$

where  $T^k$  corresponds to the  $k$ -th  $SU(N_f)$  generator. If the Lagrangian exactly possesses a given symmetry, then particles belonging to the spectrum of the theory should arrange in multiplets of the symmetry group, which correspond to the invariant subspaces associated with the irreducible representations of  $SU(N_f)$ . Furthermore, every particle belonging to a given multiplet should be degenerate, i.e., have the same mass. This statement can still hold with good approximation even if the masses of the different flavors are not exactly the same, as far as the mass difference is small compared to the typical hadronic scale. For instance, in the case of the two flavors  $N_f = 2$  up and down, the mass difference between up and down quark is very small compared to the hadronic scale  $M_h \sim 1\text{GeV}$ :

$$m_u \simeq 2.2\text{MeV}, \quad m_d \simeq 4.7\text{MeV} \quad (2.33)$$

and thus

$$m_d - m_u \simeq 2.5\text{MeV} \ll M_h. \quad (2.34)$$

From this we conclude that the  $SU_V(2)$  can be considered, with very good approximation, as a symmetry of the theory. This can be seen for example if we consider the isospin doublet given by the proton and the neutron. Indeed their mass difference is very small compared to their mass scale,

$$m_p \simeq 938.3 \text{ MeV} , \quad m_n \simeq 939.6 \text{ MeV} \quad (2.35)$$

and

$$m_n - m_p \simeq 1.3 \text{ MeV} \ll m_p, m_n . \quad (2.36)$$

This clearly testifies that the  $SU_V(2)$  isospin symmetry is realized with very good approximation.

One can also include the strange quark, thus look at the isospin symmetry  $SU_V(N_f = 3)$ . Once again, the mass difference between strange and up or down quark is, on a hadronic mass scale, comparatively small

$$m_s \simeq 93 \text{ MeV} \quad (2.37)$$

and

$$m_s - m_u \simeq 90 \text{ MeV} \ll M_h \simeq 1 \text{ GeV} , \quad (2.38)$$

so that one can assume, to a good approximation, also an approximate  $SU_V(3)$  flavor symmetry of the strong interaction. The  $SU_V(3)$  flavor symmetry is, for example, the one that was behind the renowned classification scheme for hadrons known as the *eightfold way*, introduced by Murray Gell-Mann and Yuval Ne'eman [42, 43] and also based on the independent work of Zweig [44, 45]. The name comes from the fact that the isospin multiplets of the  $SU_V(3)$  along which hadrons are ordered are octets (together with singlets and decuplets). Even if the  $SU_V(3)$  flavor symmetry is fairly fulfilled in QCD, one can see from the hadron multiplets how this is more broken w.r.t. the  $SU_V(2)$  flavor symmetry. This can be clearly verified if one takes into account the  $SU_V(3)$  flavor octet in which proton and neutrons are located, and considers also other particles in the multiplet, like for example  $\Xi^-$ :

$$m_{\Xi^-} \simeq 1322 \text{ MeV} , \quad (2.39)$$

$$m_{\Xi^-} - m_p \simeq 382 \text{ MeV} \gg m_p - m_n \simeq 1.3 \text{ MeV} , \quad (2.40)$$

thus verifying that the mass difference is significantly larger in  $SU_V(3)$  multiplets compared to  $SU_V(2)$  ones. If one keeps on increasing the number of considered flavors, for example including also the charm quark and the  $SU_V(N_f = 4)$  flavor group, the symmetry gets increasingly more explicitly broken. Nevertheless, this symmetry can still be taken into account for the sake of classifying hadrons with the charm quantum number.

### $U_A(1)$ symmetry

The  $U_A(1)$  symmetry is explicitly broken by the finite quark mass. Nevertheless, although being a symmetry of the classical QCD Lagrangian, it is broken, once the theory is quantized, also in the chiral limit. This phenomenon is usually referred to in QFT as an *anomaly*, and in particular the so-called *axial anomaly* is the one related to the specific case of the  $U_A(1)$  symmetry of QCD. More in detail, the axial Noether current

$$J_{5,\mu}(x) = \bar{\Psi}(x) \gamma_\mu \gamma_5 \Psi(x) \quad (2.41)$$

will not be conserved due to quantum corrections

$$\partial_\mu J_{5,\mu}(x) = \frac{\alpha_s}{4\pi} G_{\mu\nu}^a \tilde{G}^{\mu\nu a} , \quad (2.42)$$



where  $\tilde{G}^{\mu\nu a} = \frac{1}{2}\epsilon^{\mu\nu\alpha\beta}G_{\alpha\beta}^a$  is the dual field-strength tensor. The axial anomaly, for example, is the reason why the ninth pseudoscalar meson, the  $\eta'$  is not a pseudo-Goldstone boson and has a large mass compared to pions [46, 47, 48, 49].

### $SU_A(N_f)$ symmetry

The  $SU_A(N_f)$  chiral symmetry is once again explicitly broken by the mass term. This can be seen from the fact that the axial  $SU_A(N_f)$  current

$$A_\mu^k(x) = \bar{\Psi}(x)\gamma_\mu\gamma_5 T^k \Psi(x) \quad (2.43)$$

is not conserved anymore

$$\partial_\mu A_\mu^k(x) = 2i\bar{\Psi}(x) M \gamma_5 T^k \Psi(x) . \quad (2.44)$$

One can notice that, if one can assume a small-mass limit, then the axial current could be considered as approximately conserved. This is indeed is the reasoning behind the so-called *partial conservation of the axial current* (PCAC) and the *Goldberger-Treiman* relations, as we will discuss more in detail in Chapter 5.

### 2.2.3 Spontaneous breaking of chiral symmetry

Summarizing the statements of the previous subsection, the presence of a finite mass term for the quarks explicitly breaks the axial symmetries of the Lagrangian, such that the remaining symmetry group in this case is

$$U_V(1) \otimes SU_V(N_f). \quad (2.45)$$

Since in this work we are interested in describing the non-perturbative low-energy QCD behavior via low-energy effective models, we now specialize the discussion considering only the light flavors. In particular we will not consider the strange flavor, even if extensions of this work are possible with its inclusion, and focus on the case  $N_f = 2$ , including the up and down quark flavors and considering  $m_u = m_d = m$ . In this case, one can argue that the masses of up and down quarks are significantly smaller than  $\Lambda_{QCD}$ , meaning that one can assume to be in the chiral limit to sufficiently good approximation. As we pointed out via Eq. (2.44), since we are considering a small mass term, we can assume the chiral  $SU_A(2)$  symmetry to be an actual symmetry of the QCD Lagrangian. If this would be true, then one should find a trace of it in the hadronic mass spectrum. Namely, one would expect hadrons of the same  $SU_A(2)$  multiplet, or parity partners, to have the same mass, or at least to have small mass differences due to the finite but small current quark mass. Nevertheless, this is far from reality. If, for example, one considers the masses of the vector meson  $\rho$  and the corresponding chiral partner, the axial-vector meson  $a_1$ , one finds

$$m_\rho = 770MeV \quad m_{a_1} = 1260MeV , \quad (2.46)$$

which are significantly different. The explanation to this occurrence is that the  $SU_A(2)$  chiral symmetry is not just (moderately) explicitly broken by the current quark mass, but it is also said to be *spontaneously broken*. This occurs since the vacuum of QCD is not trivial, and thus not invariant under the chiral  $SU_A(2)$  transformation, even in the chiral limit. In particular, in vacuum, the expectation value of the operator  $\bar{\Psi}\Psi$  is not vanishing

$$\langle 0 | \bar{\Psi}\Psi | 0 \rangle = \langle 0 | \bar{\Psi}_u \Psi_u + \bar{\Psi}_d \Psi_d + | 0 \rangle \neq 0 . \quad (2.47)$$



This is the so-called *chiral condensate* and plays a fundamental role in the study of chiral symmetry. In particular, quarks strongly couple to the condensate, obtaining an effective constituent mass  $\sim 300\text{MeV}$ , which is much larger than the current quark mass. This occurrence breaks chiral symmetry dynamically and the phenomenon is referred to as *spontaneous symmetry breaking* (SSB) of chiral symmetry. In this case then, the chiral symmetry  $SU_V(2) \otimes SU_A(2)$  is spontaneously broken down to the residual symmetry of the vacuum,  $SU_V(2)$ . Following then the Goldstone theorem [50, 51], the system should contain a certain number of massless spin-0 excitations, the so-called *Goldstone bosons*. The number of Goldstone bosons is given by the number of generator which generate the transformations under which the vacuum is not invariant. In the analyzed case this group corresponds to

$$(SU_V(2) \otimes SU_A(2)) - SU_V(2) , \quad (2.48)$$

which contains 3 generators. Thus, we expect 3 Goldstone bosons, which correspond to the pions. Increasing temperature and/or density, one expects the quark condensate to melt, restoring chiral symmetry. In this case, the pions become massive and are not Goldstone bosons anymore. In particular they become degenerate with their chiral partner, the  $\sigma$  (which is massive also in the chiral-symmetry broken phase), and the same happens for the  $\rho$  and  $a_1$  mesons. This phase is usually referred to, in a pretty self-explanatory way, as *chirally symmetric* or *chirally restored phase*. Nevertheless, the pattern of spontaneous symmetry breaking/restoration of the chiral symmetry is not exact in real QCD because of the finite quark mass which explicitly breaks the symmetry. In this case, the pions are not exactly massless Goldstone bosons, since they acquire a small but finite mass. Since, also in this case, the biggest contribution to the breaking of chiral symmetry is still provided by the chiral condensate, it still make sense to use the spontaneous symmetry breaking/restoration pattern as a valid guideline. In this case, the pions are thus indicated as *pseudo-Goldstone bosons*. Since the largest component of the hadron masses arises from the SSB of chiral symmetry, it is clear that it is fundamental to incorporate it into the low-energy models used to study QCD. The description of the mechanism of chiral symmetry breaking and restoration and the properties of the system close to this transition will be the main focus of this work. This will be done by means of the introduction of suitable low-energy effective models for QCD. These models have to be constructed in order to be able to reproduce the symmetry breaking/restoration pattern via the introduction of different and suitable degrees of freedom, thus possibly giving us a hint on the physics underlying this phenomenon.



# The Functional Renormalization Group

## 3.1 Motivation

The understanding of the behavior of systems where microscopic degrees of freedom are strongly interacting is the main goal of many areas of physics, ranging from condensed matter [52, 53] to elementary-particle theories [54, 55], to quantum gravity [56, 57]. However, a strictly theoretical approach to these systems is often very difficult, involving the use of suitable and powerful tools. This difficulty becomes even more challenging if the system is facing a phase transition, since new degrees of freedom may arise or become relevant. In this case, the underlying theory must relate consistently the two regimes and thus describe the transition from one set of degrees of freedom to the other.

A widely exploited theoretical method suitable to this situation is the renormalization group (RG) introduced by Wilson [58]. This technique can be combined with perturbation theory in order to describe systems where many interacting degrees of freedom are present and the infrared degrees of freedom interact via a small effective coupling [59]. Unfortunately, this approach cannot be used in systems where such a small coupling, or in general a small perturbative parameter simply does not exist or it is hard to identify. Furthermore the perturbative series does not converge in general and one has to exploit some resummation techniques, often relying on the fine-tuning of some external parameter.

On the other hand, another possible approach to critical systems are computer simulations and Monte Carlo methods, which have been successfully used to obtain high-precision estimates of the critical exponents [60, 61]. However, one of the major issues with these methods is the extremely large amount of computer time needed.

We also mention the existence of other methods which can be used to face critical phenomena. Among these, the conformal-field theory approach [62] led, for example, to a high precision on critical exponents for the Ising model, originally in  $2D$  and later in  $3D$  thanks to the Conformal Bootstrap (CB) technique.

In order to overcome the difficulties of the perturbative RG method and the numerical simulations, a different and powerful kind of approach can be used: the so-called *Functional Renormalization Group* (FRG), also referred as Exact RG or Nonperturbative RG (NPRG). Functional methods aim at the computation of generating functionals of correlation functions, such as the effective action that governs the dynamics of the macroscopic expectation values of the fields. These generating functionals contain all relevant physical information about a theory, once the microscopic fluctuations have been integrated out. The functional RG combines this functional approach with the RG idea of treating the fluctuations not all at once but successively from scale to scale. Instead of studying correlation functions after having averaged over all fluctuations, only the

change of the correlation functions as induced by an infinitesimal momentum shell of fluctuations is considered. From a structural viewpoint, this allows to transform the functional-integral structure of standard field-theory formulations into a functional differential structure. The central tool of the functional RG is given by a flow equation, which describes the evolution of correlation functions and of their generating functional under the influence of fluctuations. It connects, in an exact manner, a well-defined initial quantity, e.g., the microscopic correlation functions in a perturbative domain, with the desired full correlation functions after having integrated out the fluctuations. Hence, solving the flow equation corresponds to solve the full theory. Thanks to the fact that it is non-perturbative and to its underlying logic of connecting degrees of freedom at different scales, it seems clear that the FRG approach is well suited to face the issue of describing systems approaching criticality and phase transitions, and thus a reliable tool to investigate the QCD phase diagram.

### 3.2 Wetterich formulation of the Functional Renormalization Group

The goal of this chapter is to give an overview of the Functional Renormalization Group (FRG) approach in the formulation given by Wetterich et al. [63, 64, 65, 66, 67]. For further references one can also see [68, 69, 70, 71, 72]. The original idea which is at the basis of the FRG approach can be dated back to the concept of spin coarse-graining introduced by Kadanoff [73] and the continuous generalization implemented via momentum-shell integration by Wilson [58, 74, 75, 76, 77] and others, see, e.g., Refs. [78, 79].

The central object of the FRG approach is the effective action  $\Gamma[\phi]$ , which is the generating functional of 1PI vertex functions (see App. B). In principle one could just solve the path integral Eq. (B.1) and from that derive the effective action using its definition via Eq. (B.11). Thus, this approach would correspond to integrate all quantum (or thermal) fluctuations at once. Nevertheless, as one can imagine, this can almost never be achieved due to the complexity of solving the path integral, except for very special cases, e.g. 0-dimensional theories, where the path integral simply reduces to a standard integral [80, 81, 82]. Thus, instead of integrating fluctuations all at once, one can use the FRG approach and follow the idea by Wilson of integrating fluctuations in momentum shells. Then, in order to compute  $\Gamma[\phi]$  within the FRG framework, one introduces another functional, the so-called *effective average action*  $\Gamma_k[\phi]$ . This quantity depends on the parameter  $k$ , which is a coarse-graining scale with physical dimension of a momentum, indicating the momentum shell beyond which fluctuations have been integrated out. From a practical perspective one can think of  $\Gamma_k$  as an effective action depending on coarse-grained fields, averaged in momentum space over a volume in momentum space  $\sim k^d$  [83]. In this way, the momentum components of the averaged fields which are larger than the shell-scale  $k$  can be considered as effectively integrated out. In particular,  $k \rightarrow \infty$  corresponds to the case where no fluctuations have been integrated out while  $k = 0$  signals the full quantum theory, where all the fluctuations have been integrated out. For this reason, it seems natural that the previously mentioned RG-scale dependent effective action  $\Gamma_k[\phi]$  has to coincide with the bare action  $S_{\text{bare}}[\phi]$  in the limit  $k \rightarrow \infty$ , which we will also refer to as the ultraviolet (UV) limit, while it has to coincide with the full quantum effective action  $\Gamma[\phi]$  when  $k \rightarrow 0$ , which we will indicate as the infrared (IR) limit. So we have:

$$\Gamma_{k \rightarrow \infty}[\phi] = S_{\text{bare}}[\phi], \quad \Gamma_{k \rightarrow 0}[\phi] = \Gamma[\phi]. \quad (3.1)$$

In practice, one may not always be able to send  $k \rightarrow \infty$  either from a purely mathematical point of view or for a physical reason, meaning that the theory is valid up to a certain energy scale. Therefore, one usually introduces a UV cutoff scale  $\Lambda$ , which is chosen to be sufficiently large, i.e., much larger than any other physical scale of the theory, and assumes that the bare classical action describes the underlying theory at this scale. However, using a finite cutoff is an approximation and one has to ensure that the results are independent of the choice of  $\Lambda$ , e.g., by respecting Renormalization Group (RG) consistency [84], which we will investigate in Chapter 7.

We now explain how the effective average action is constructed starting from the standard functionals used in QFT, defined in App. B, via the introduction of a dependence on the RG-scale  $k$ .

The first step in order to construct the effective average action is to define an IR-regulated generating functional

$$\mathcal{Z}_k[J] \equiv \int_{\Lambda} \mathcal{D}\varphi e^{-S[\varphi] - \Delta S_k[\varphi] + \int J\varphi}, \quad (3.2)$$

where we have introduced the regulator term

$$\Delta S_k[\varphi] = \frac{1}{2} \int \frac{d^D q}{(2\pi)^D} \varphi(-q) R_k(q) \varphi(q), \quad (3.3)$$

which is quadratic in  $\varphi$  and plays the role of an FRG-scale dependent mass term.

The function  $R_k(q)$  is called *regulator function* and should be chosen in order for  $\Gamma_k$  to satisfy the requirements in Eq. (3.1), i.e., smoothly interpolate between the microscopic action  $S_{\text{bare}}$ , for  $k = \Lambda$ , and the effective action of the original model  $\Gamma$ , for  $k = 0$ . Therefore it has to satisfy the following conditions:

1.

$$\lim_{k^2 \rightarrow \Lambda^2 \rightarrow \infty} R_k(q) \rightarrow \infty \quad (3.4)$$

This condition is necessary to recover the classical limit in the UV, i.e., when fluctuations are not integrated. In particular, condition Eq. (3.4) ensures that the functional integral is saturated for the classical equation of motion. Therefore, all fluctuations are then frozen for  $k = \Lambda$ , as in Landau's mean-field theory, and this justifies the use of a saddle-point approximation, which just singles out the classical field configuration and the bare action, which allows us to conclude  $\Gamma_{k \rightarrow \Lambda} \rightarrow S + \text{const.}$

2.

$$\lim_{k^2/q^2 \rightarrow 0} R_k(q) = 0 \quad (3.5)$$

This ensures the recovery of the physical limit in the  $k \rightarrow 0$  case. In fact, for  $k \rightarrow 0$ , all fluctuations are taken into account and the effective average action has to coincide with the full effective action of the original model,  $\Gamma_{k \rightarrow 0} = \Gamma$ .

3.

$$\lim_{q^2/k^2 \rightarrow 0} R_k > 0 \quad (3.6)$$

This requirement provides the IR regulation to the theory. In this way, we ensure that the regulator suppress the soft modes with momenta  $q^2 \lesssim k^2$ . In fact,  $R_k$  acts like a scale-dependent mass contribution for low momenta, such that low-momentum modes effectively decouple. This can be clearly seen from the fact that one can assume  $R_k \sim k^2$  for  $q^2 \ll k^2$ , meaning that the regulator behaves like a mass term  $m^2 \sim k^2$  and screens the IR modes.

Usually, the regulator is written in a more convenient form in terms of a dimensionless regulator function  $r(y)$  which depends on a dimensionless variable  $y = q^2/k^2$ :

$$R_k(q^2) = q^2 r(y). \quad (3.7)$$

This shape function is most useful due to the role of  $R_k$  as a mass-like term, since in this way it is easier to recover the dispersion relations of the particles involved. We will see this aspect in more detail after we introduced the FRG flow equation. Obviously, the constraints (3.4)-(3.6) translate into the corresponding requirements for  $r(y)$ :

$$r(y \rightarrow 0) \sim \frac{1}{y}, \quad r(y \rightarrow \infty) \rightarrow 0. \quad (3.8)$$

There exist several types of regulator, depending on the choice of the regulator shape function  $r(y)$  and also on the structure of the regulator itself, as we will investigate later in this work. This implies that the choice of the specific shape of the regulator is a delicate issue and can be optimized depending on the problem, see, e.g., Refs. [85, 86, 87, 88] for details.

We now continue with the task of constructing the effective average action. Proceeding as one does for Eq. (B.6), let us consider the connected generating functional

$$W_k[J] = \ln Z_k[J]. \quad (3.9)$$

Following the same line of reasoning which leads to Eq. (B.11), we can define the interpolating effective action  $\Gamma_k$  by a modified Legendre transform which includes the regulator term [83, 89]:

$$\Gamma_k[\phi] = \sup_J \left( \int J\phi - W_k[J] \right) - \Delta S_k[\phi]. \quad (3.10)$$

It is worth noticing that, in this case, the source value  $J = J_{\text{sup}} = J_k[\phi]$  for which the supremum is approached is  $k$ -dependent. In a parallelism with statistical field theory, here  $\phi = \phi_k$  plays the role of an "order-parameter" field while we have to consider  $J_k[\phi]$  as an external current functional of  $\phi$  which is singled out by the sup condition. In order to find the meaning of  $\phi$  (compare to Eq. (B.13)), we choose  $J = J_{\text{sup}}$  thus obtaining:

$$\frac{\delta}{\delta J} \left[ \left( \int J\phi - W_k[J] \right) - \Delta S_k[\phi] \right]_{J=J_{\text{sup}}} = 0, \quad (3.11)$$

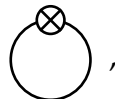
which leads to

$$\phi(x) = \langle \varphi(x) \rangle_J = \frac{\delta W_k[J]}{\delta J(x)}. \quad (3.12)$$

This implies that  $\phi$  corresponds to the scale-dependent expectation value of the field  $\varphi$  in the presence of the source  $J$ . That is why  $\phi$  is usually referred to as the *scale-dependent classical field*. As a final remark, we note that, in general, the addition of the regulator term in the definition Eq. (3.10) spoils the property of convexity of the Legendre transform, which is recovered in the limit  $k \rightarrow 0$ , when the regulator has to vanish. However, the addition of the regulator term helps removing trivial terms that would develop in the flow equation, as one can see for example in studying the Polchinski equation for the Schwinger functional [78]. This is the reason why, sometimes in the literature, a distinction is made between the scale-dependent effective action, which contains only the Legendre transform term of Eq. (3.10), and the proper scale-dependent effective average action, which corresponds to the definition Eq. (3.10) where we have the additional regulator term. We are now ready to introduce the equation that describes the evolution of



the effective average action as one integrates out fluctuations with increasingly smaller momenta, i.e., the equation that describes the evolution of  $\Gamma_k[\phi]$  as  $k$  runs from the UV,  $k \rightarrow \infty$ , to the IR,  $k \rightarrow 0$ . This is the so-called *Wetterich equation*, or *Exact Renormalization Group flow equation*, or simply *FRG flow equation* [63, 83, 90],

$$\partial_k \Gamma_k[\phi] = \text{Tr} \left[ \left( \frac{1}{2} \partial_k R_k \right) (\Gamma_k^{(2)}[\phi] + R_k)^{-1} \right] = \text{Diagram}, \quad (3.13)$$


where the trace indicates an integral over momenta and a sum over all internal degrees of freedom of the theory, such as color, flavor, spin etc.. The FRG flow equation is the central object of the FRG approach and will be the starting point for any further investigation in this work. One of the first features one can point out from the FRG flow equation is that it has an exact one-loop structure, since it contains the full propagator  $G_k[\phi] = (\Gamma_k^{(2)}[\phi] + R_k)^{-1}$ . This one-loop structure of the flow equation is due to the fact that the regulator term we added to the classical action,  $\Delta S_k$ , is quadratic in the field operator  $\phi$ , and it is indicated by the Feynman-diagram representation on the right-hand side. Here, the black line represents the full propagator  $G_k[\phi] = (\Gamma_k^{(2)}[\phi] + R_k)^{-1}$  and the crossed circle stands for the insertion of the regulator via the term  $\frac{1}{2} \partial_k R_k$ .

One can also point out the fact that the RG-trajectory, i.e., the RG-time or RG-scale evolution of the effective average action governed by the Wetterich equation Eq. (3.13), can be also viewed as a trajectory in the so-called theory space, which is the space spanned by all possible operators which possess a symmetry compatible with the examined theory. This trajectory clearly depends on the choice of the regulator, but property Eq. (3.5) ensures that the ending point is always the full quantum effective action  $\Gamma$ . Anyway, as we will discuss later in much more detail, this reasoning is not valid anymore if we use approximations in solving the FRG flow equation, which may be, for example, the presence of a finite UV cutoff  $\Lambda$ , the use of truncations for the effective action and/or the existence of a finite IR scale  $k_{\text{IR}} > 0$  as the final point reachable during the RG-evolution.

We already pointed out the IR-regulation function of the regulator, but it also serves as a UV regularization, due to the term  $\partial_k R_k$  in Eq. (3.13). In fact,  $\partial_k R_k$  can usually be considered to be small except for values  $q^2 \sim k^2$ , implying also that the main contribution to the momentum integral comes from this momentum shell, thus also implementing the concept of the Wilsonian momentum-shell integration.

As a final consideration, for the sake of convenience, let us introduce the RG time  $t$  and the following abbreviations:

$$t = -\ln \left( \frac{k}{\Lambda} \right) \quad \Longleftrightarrow \quad k = \Lambda e^{-t}, \quad (3.14)$$

from which follows

$$\frac{\partial}{\partial t} = -k \frac{\partial}{\partial k}. \quad (3.15)$$

With respect to the standard literature definition, we added an extra minus sign in Eq. (3.14). This is just a convention chosen in order to have a positive RG-time evolution, which flows from  $t = 0$  (UV) to  $t \rightarrow \infty$  (IR), following the natural scaling of a variable which resembles time. This will be especially useful in the process of identifying the FRG flow equation as a hydrodynamic equation, as we will investigate in the following chapters.

### 3.3 Approximation schemes

The exactness of the FRG flow equation is a very striking feature, since it means that UV and IR quantities are linked in an exact way, and thus solving the flow equation corresponds to solving the theory. However, despite its deceptively simple form, the Wetterich equation is a functional integro-differential equation, and as such it cannot be solved exactly for an arbitrary  $\Gamma_k[\Phi]$ , because this would imply, in general, to find an exact generic solution for an infinite system of coupled integro-differential equations (one equation for each operator, compatible with the symmetry of the theory, that spans the theory space). Thus, it is clear that some approximation has to be made. Every kind of expansion of the effective action, in order to be reliable, should have two important properties:

1. systematicity, which means that there exists a hierarchy which establishes a definite order of relevance in the expansion;
2. consistency, in the sense that all the terms up to the chosen order in the expansion have to be taken into account.

We will introduce the two main approximation schemes used in literature, which are usually referred to as *method of truncations*: the *vertex expansion* and the *operator expansion*. Since none of these approximations rely on the existence of a small coupling parameter, the FRG approach retains its non-perturbative nature.

#### 3.3.1 Vertex expansion

The vertex expansion was developed by Tim R. Morris et al. [65, 91]. It represents a valid and widely used approach in condensed-matter physics and also in low-energy QCD studies [70, 71, 92, 93, 94]. The key idea is an expansion of the effective average action in powers of the field  $\phi$

$$\Gamma_k[\phi] = \sum_{n=0}^{\infty} \frac{1}{n!} \int d^D x_1 \cdots d^D x_n \Gamma_k^{(n)}(x_1 \cdots x_n) \phi(x_1) \cdots \phi(x_n), \quad (3.16)$$

where  $\Gamma_k^{(n)}$  are the scale-dependent 1PI vertex functions defined in Eq. (C.7). Once we insert this expansion into the Wetterich equation Eq. (3.13), we obtain a tower of coupled flow equations for the different  $\Gamma_k^{(n)}$ , which will then interpolate between the bare and the fully dressed vertex functions. The tower contains an infinite number of equations and, due to the structure of the Wetterich equation, each equation couples the evolution of  $\Gamma_k^{(n)}$  to the  $\Gamma_k^{(n+2)}$  vertex function. Thus, this tower needs to be truncated at some order via an approximation, in a similar fashion to the Dyson-Schwinger equations [95, 96, 97, 98]. One of the main advantages of this approximation consists of its relative simplicity, such that sometimes it is also used in combination with the derivative expansion to further simplify the solution of the flow equation [99, 100, 101, 102, 103, 104]. One of the downsides of using the vertex expansion is that it assumes regularity of  $\Gamma_k[\phi]$ , since  $\Gamma_k[\phi]$  has to be differentiable at least  $n + 2$ -times in order to obtain the vertex functions. Anyway, it has been shown that this property of analyticity may be violated near phase transitions, where the effective action develops discontinuities or points of non-analyticity during the FRG flow [32, 105, 106]. For this reason it is preferable to adopt a different truncation scheme when approaching this kind of phenomena in order to correctly capturing the non-analytic behavior of the effective action.



### 3.3.2 Operator and Derivative Expansion

A second popular scheme used in order to obtain approximate solutions of the flow equations is the operator expansion, which approximates the effective action using operators of increasing mass dimension. In particular we will focus on the derivative operators, obtaining the so-called *derivative expansion* of the effective action [71, 72, 107, 108], which consists of expanding the effective average action  $\Gamma_k[\phi]$  in terms of all composite operators constructed from space-time derivatives (in principle of arbitrary order) of the fields. These composite operators must be compatible with the symmetries of the theory.

As for the vertex-expansion case, one obtains an infinite system of coupled integro-differential equations which needs to be truncated at a certain order of space-time derivatives of the fields. As an example, for a theory with one real scalar field, a possible derivative-expansion truncation for the effective action would read

$$\Gamma_k[\phi] = \int d^D x \left[ V_k(\phi) + \frac{1}{2} \mathcal{Z}_k(\phi) (\partial_\mu \phi)^2 + \mathcal{O}(\partial^4) \right], \quad (3.17)$$

where

$$V_k(\phi) = \frac{1}{V_{ol}} \Gamma_k[\phi]_{\phi=\text{const}} \quad (3.18)$$

corresponds to the effective potential and  $\mathcal{Z}_k(\phi)$  is called *wave-function renormalization factor*.  $V_{ol}$  indicates the  $D$ -dimensional space-time volume.

In particular

$$\Gamma_k[\phi] = \int d^D x \left[ V_k(\phi) + \frac{1}{2} (\partial_\mu \phi)^2 \right] \quad (3.19)$$

is usually referred to as local potential approximation (LPA), since the only scale dependence of the effective average action comes from the effective potential, and the wave function renormalization factor is trivially set to one,  $\mathcal{Z}_k(\phi) = 1$ . The subsequent improvement of the LPA is the so-called LPA'

$$\Gamma_k[\phi] = \int d^D x \left[ V_k(\phi) + \frac{1}{2} \mathcal{Z}_k (\partial_\mu \phi)^2 \right] \quad (3.20)$$

in which the wave function renormalization factor is reintroduced in a non trivial way, since it is considered to be RG-scale but not field-dependent. Thanks to the presence of the non-trivial wave function renormalization function, this truncation is extremely useful when dealing with a large variety of physical phenomena, such as Mott regimes, (color-)superconductivity, inhomogeneous phases and in general all those systems which exhibit behavior characterized by a non-trivial dispersion relation [109, 110, 111, 112, 113, 114]. In general, the derivative expansion turns out to be very useful when used to understand, as we will see, the low-momentum (or, equivalently, long-wavelength) behavior, such as in critical phenomena. It is one of the most used approximation techniques in the literature and its features have been largely discussed (for example in [69, 71, 108, 115, 116]). In particular, since in this work we are interested in capturing the correct physical behavior of phase transitions and critical phenomena in general, as previously pointed out, we have to employ a method which allows to treat discontinuities and non-analyticities in the FRG flow of the effective action. The derivative expansion fulfills this requirement, even in the most simple truncation, the aforementioned LPA. Thanks to this feature and to the relatively simple calculations to which it leads, the LPA will be the main truncation we will use throughout this work. Naturally, one can check

the systematic error on the obtained results using higher-order truncations (LPA', full  $2^{nd}$ -order expansion etc...), but this is beyond the scope of the present thesis and part of an ongoing work.

## The $O(N)$ model

This chapter is mainly based on [117].

### 4.1 Introduction and motivation

In this chapter we begin our investigation of QCD effective field theories by studying the  $O(N)$  model and in particular its behavior close to a second-order phase transition and the related critical exponents.

Let us consider the  $O(N)$  model in  $D$ -dimensional Euclidean space-time. The theory describes a collection of  $N$  scalar fields  $\phi_a(x)$  with  $a = 1, \dots, N$  and the associated bare action is

$$S[\vec{\phi}] = \int d^D x \left\{ (\partial_\mu \phi_a)^2 + V(\rho) \right\}, \quad (4.1)$$

where  $\vec{\phi} = (\phi_1, \dots, \phi_N)$ ,  $V(\rho)$  is the self-interacting potential and  $\rho = \frac{1}{2} \phi_a \phi^a$ . The  $O(N)$  symmetry is represented on the field space as an orthogonal transformation

$$\phi_a \rightarrow O_{ab} \phi_b. \quad (4.2)$$

According to this symmetry, the  $O(N)$ -invariant terms are those constructed by the modulus of the fields  $\phi_a \phi^a$ . That is the reason why the potential is restricted to depend only on  $O(N)$ -invariant terms, namely the combination  $\rho = \frac{1}{2} \phi_a \phi^a$ .

Despite being a rather simple model, the  $O(N)$  model can describe a significantly large variety of physical systems at different energy scales. The reason behind such a wide range of applicability of this relatively simple model is due to the well-known universal behavior of physical systems close to criticality, i.e., close to a second-order phase transition. Under these circumstances, the microscopic degrees of freedom cease to be relevant and only the main features, like the symmetry of the model, play a role in the description of the physical behavior of the system.

For example, the main reason why we consider the  $O(N)$  model is that for  $N = 4$  it can describe the chiral phase transition in Quantum Chromodynamics (QCD) with two quark flavors [118]. Furthermore, for  $N = 3$  it belongs to the universality class of the Heisenberg model, describing a ferromagnetic phase transition [119]. The  $N = 2$  case can be used to describe the XY-model [120] and  $N = 1$  belongs to the Ising universality class [121].

For the previous reasons, the  $O(N)$  model can be effectively considered as a prototype model to study in detail the mechanisms that govern a phase transition.

The reason why we choose to investigate such a physical phenomenon via the FRG approach is fact that phase transitions involving a change in the degrees of freedom

at different scales are highly non-perturbative phenomena. Thus, thanks to the fact that it is non-perturbative and connects degrees of freedom at different scales, the FRG approach is well suited to address the issue of describing systems approaching criticality and phase transitions, and thus a tool for the computation of critical exponents, cf. Refs. [122, 123, 124, 125, 126, 127, 128, 129, 130].

As we stated at the beginning of this section, our goal is to study both the critical behavior and the critical exponents for this model. However, the critical exponents of the  $O(N)$  model have already been studied within the FRG approach several times, see, e.g., Refs. [124, 127, 128, 130, 131]. There are essentially two reasons why we chose to redo such a study. The first one is given by the recent development of a new approach to the solution of the FRG flow [32]. This approach is based on the key observation that the FRG flow equation, under specific approximations and truncations, can be rearranged into the form of a hydrodynamic advection-diffusion equation. This thus strongly pushes towards the use of specific numerical techniques, which are well-known from hydrodynamics, to solve that equation, see Refs. [80, 81, 105, 106, 132, 133, 134] as well as Refs. [135, 136, 137, 138, 139, 140, 141] for some early developments. To be more specific, a key feature of hydrodynamic conservation laws is that they allow for the formation of discontinuities or, more general, non-analyticities in the solution of the differential equation. This requires that the applied numerical scheme has to be able to capture and properly handle such non-analyticities. In the previously cited work, Ref. [32], a discontinuous Galerkin method was used to solve the FRG flow equation. In contrast here we will exploit a well-established finite-volume central scheme, the so-called Kurganov-Tadmor (KT) algorithm, which is designed to have a high-order accuracy, preserving stability and introducing negligible dissipation, while allowing to treat discontinuities in the solution (see App. E and Ref. [142] for more details). The second reason why we chose to repeat such an investigation is to provide a more systematic study of various sources of errors in determining the critical exponents of the  $O(N)$  model, since the previous studies which used the FRG approach in the LPA for such calculations lack this kind of extensive error study. It is also worth mentioning that, as already specified, there are more advanced truncations available for high-precision calculations of the critical exponents of  $O(N)$  models via the FRG, and/or different approaches (using, for example, fixed-point equations) [127, 128, 130, 131], and the scope of this chapter is not to provide results that can rival that precision. However, some of these works combine the use of fixed-point equations with the approach we employed, thus making the error analysis of wider interest.

We now proceed to analyze the flow equation that describes the  $k$  (or equivalently  $t$ ) evolution of the average effective action. As already mentioned in Chapter 3, to do so we need to truncate the effective action, i.e., we need to choose an ansatz. We will use a derivative expansion and in particular the LPA, where the only space-time derivatives of the fields appear in the kinetic term and the effective potential  $V_k(\rho)$  is the only scale-dependent quantity. In particular, as we stated in the introduction, we choose to use the derivative expansion over the vertex expansion since the latter assumes regularity of the effective action, which is clearly not the case in the proximity of phase transitions, where the effective action can develop discontinuities or points of non-analyticity during the FRG flow [32, 105, 106]. This requirement is particularly strict in our case, since the other goal of this chapter is the calculation of the critical exponents for a second-order phase transition, and discontinuities and non-analyticities in the effective action are expected in this case.

## 4.2 The flow equation in the LPA

As we established in the previous section, the first step to study the critical behavior of the  $O(N)$  model will be to derive the flow equation that describes the  $k$ -evolution of the effective average action. As already mentioned, we will consider the easiest approximation one can make for the effective action, i.e., the LPA. This approximation is really useful since it leads to simple expressions while capturing many features of the theory. Furthermore, it becomes exact in the limit  $N \rightarrow \infty$  [143]. The LPA ansatz for the effective action is given by

$$\Gamma_k[\vec{\phi}] = \int d^D x \left[ \frac{1}{2} (\partial_\mu \phi_a)^2 + V_k(\rho) \right], \quad (4.3)$$

where  $V_k(\rho)$  is the effective potential, which is the only quantity depending on the FRG momentum scale  $k$ , and  $\rho = \frac{1}{2} \phi_a \phi_a$  is the previously defined  $O(N)$  invariant. If one would try to improve the truncation, the next order in the derivative expansion would be the LPA', which includes a non-trivial scale-dependent wave-function renormalization factor. For different and better truncations in models with properties similar to the  $O(N)$  model, see, e.g., Refs. [144, 145, 146, 147]. In this chapter and in the whole thesis, the wave function renormalization factor is set to  $Z_k = 1$  identically.

Once the ansatz for the effective action is specified, we can insert it into the right-hand side of the Wetterich equation (3.13) to derive a PDE for the effective potential  $V_k(\rho)$ .

For a concrete result, we have to choose a regulator which satisfies the conditions (3.6)-(3.4). It is possible to prove (see [148]) that, in the case of the LPA, an optimal choice for the regulator, in terms of stability of the kernel of the FRG flow equation, is the Litim regulator

$$R_k(q, p) = (2\pi)^D \delta^{(D)}(q + p) p^2 r_k(p), \quad (4.4)$$

where  $r_k(p)$  is the corresponding regulator shape function

$$r_k(p) = \left( \frac{k^2}{p^2} - 1 \right) \Theta \left( \frac{k^2}{p^2} - 1 \right). \quad (4.5)$$

Once both the ansatz for the effective average action and the regulator have been fixed, one can plug them into the flow equation Eq.(3.13) and arrive at the flow equation for the effective potential in the LPA:

$$\partial_k V_k(\rho) = A_D k^{D+1} \left( \frac{N-1}{k^2 + V'_k(t, \rho)} + \frac{1}{k^2 + V'_k(t, \rho) + 2\rho V''_k(t, \rho)} \right), \quad (4.6)$$

where we introduced the notation

$$V'_k(\rho) = \partial_\rho V_k(\rho), \quad V''_k(\rho) = \partial_\rho V'_k(\rho) = \partial_{\rho\rho}^2 V_k(\rho). \quad (4.7)$$

Furthermore, we defined the factor

$$A_D = \frac{\Omega_D}{(2\pi)^D D}, \quad (4.8)$$

where

$$\Omega_D = \frac{2\pi^{D/2}}{\Gamma(\frac{D}{2})} \quad (4.9)$$

is the volume of a  $D - 1$  dimensional sphere. In this context,  $\Gamma$  indicates the usual Gamma function. More details about the steps we followed for the derivation of the flow equation Eq. (4.6) are provided in App. D.1.

As we stated in the introduction, the choice of the UV cutoff  $\Lambda$  in Eq. (4.6) should be guided by the fact that  $\Lambda \gg$  any scale of the problem, such that in the limit  $k \rightarrow \Lambda \sim \infty$  one recovers  $\Gamma[\phi] \simeq S_{bare}[\phi]$ . In our calculation we will use  $\Lambda = 1 \text{ GeV}$ , which can be considered as sufficiently larger than the scales involved in the model.

Already at this level, we can point out some features of this flow equation and its structure, which are strictly related to the physical content of the theory.

1. First of all we can notice that the r.h.s. of Eq. (4.6) is independent of  $V_k(t, \rho)$ . We will take further advantage of this observation when discussing the conservative formulation of the flow equation.
2. The two terms that compose the r.h.s of the flow equation very closely resemble the structure of the propagator for a scalar field in momentum space:

$$G(p)_{scalar} \simeq \frac{1}{p^2 + m^2} . \quad (4.10)$$

However, this is not just a resemblance, since the two terms arise from the loop involved in the flow equation, which is specified by inversion of the regularized two-point function  $\Gamma_k^2 + R_k$ , which, by definition, represents the scale-dependent full propagator.

3. The previous point allows us to identify two different type of particles, the pions and the radial sigma mode, to which correspond two different masses whose values depend on the effective potential:

$$m_\pi^2 = V'_k(t, \rho) , \quad m_\sigma^2 = V'_k(t, \rho) + 2\rho V''_k(t, \rho) . \quad (4.11)$$

4. If the physical point, i.e., the global minimum of the effective potential, is located at  $\rho = 0$ , we can observe that both the sigma and the pion modes are massive and their masses coincide  $m_\pi^2 = m_\sigma^2$ . In this case the theory still possesses the  $O(N)$  symmetry and thus we will refer to this case as the symmetric phase.
5. When the radial sigma mode acquires a non-vanishing expectation value, which means that  $V'(t, \rho) = 0$  for  $\rho \neq 0$ , this leads to a spontaneous symmetry breaking of the  $O(N)$  symmetry, leaving an  $O(N - 1)$  residual symmetry. Thus we will refer to this case as the broken phase. Under these circumstances, the Goldstone theorem predicts the presence of exactly  $N - 1$  massless bosons, the so-called Goldstone bosons. Indeed in this case the pion modes become massless since  $V'(t, \rho) = 0$ , and we have exactly  $N - 1$  pion modes, which then play the role of the Goldstone bosons related to this spontaneous breaking of symmetry. From this discussion thus follows the original choice of naming the pion and the sigma loops in this way.

### 4.2.1 Formulation in terms of the field $\sigma$ and boundary conditions

The formulation we followed so far for the partial differential equation (PDE) Eq. (4.6) for the effective potential involves the use of the  $O(N)$ -invariant  $\rho$ . However, this specifically leads to some issues related to the boundary condition of the discretized version of Eq. (4.6). In particular, the numerical solution of a PDE with a scheme that requires a

discretization of the spatial dimension(s), exploits a stencil of points close to the considered one, where the value of the solution of the PDE is defined. When the considered points are located at the edge of the spatial domain, the knowledge of the (discretized version of the) boundary conditions is needed, which usually is provided by the physics underlying the PDE. In the analyzed case, in particular, this stencil is also required at the boundary  $\rho = 0$ , which means that the knowledge of the value of  $V_k(\rho)$  for some negative value of  $\rho$ , which does not exist, is demanded by the numerical scheme.

A possible solution is to reformulate the equations above in terms of the field expectation value

$$\sigma = \sqrt{2\rho} \quad (4.12)$$

Thus, we will consider  $V_k(\sigma)$ ,  $\partial_\sigma V_k(\sigma)$ , and  $\partial_{\sigma\sigma}^2 V_k(\sigma)$  instead of  $V_k(\rho)$ ,  $\partial_\rho V_k(\rho)$ , and  $\partial_{\rho\rho}^2 V_k(\rho)$ . With this change of notation we can put Eq. (4.6) in the following form:

$$\partial_k V_k(\sigma) = A_D k^{D+1} \left[ \frac{N-1}{k^2 + \frac{1}{\sigma} \partial_\sigma V_k(\sigma)} + \frac{1}{k^2 + \partial_\sigma^2 V_k(\sigma)} \right]. \quad (4.13)$$

This equation will be the reference point for our further investigations in the LPA for the  $O(N)$  model. Using this formulation the problem of the boundary conditions at  $\rho = 0$  is now easily solved, since we now have access to values of  $V_k(\sigma)$  at the points close to  $\sigma = 0$ : we just need to exploit the  $O(N)$  symmetry of the model and in particular the  $\mathbb{Z}_2$  symmetry of the effective potential:

$$V_k(\sigma) = V_k(-\sigma), \quad (4.14)$$

which leads to a  $\mathbb{Z}_2$  antisymmetry for  $\partial_\sigma V(\sigma)$

$$\partial_\sigma V_k(\sigma) = -\partial_\sigma V_k(-\sigma) \quad (4.15)$$

and to a  $\mathbb{Z}_2$  symmetry for  $\partial_{\sigma\sigma}^2 V(\sigma)$

$$\partial_{\sigma\sigma}^2 V_k(\sigma) = \partial_{\sigma\sigma}^2 V_k(-\sigma). \quad (4.16)$$

A second boundary condition that has to be specified is the one at large field values. This is related to the fact that it is not generally possible to numerically solve the flow equation on the whole domain  $\sigma \in [0, \infty)$ . Therefore, one has to choose a given maximum value of  $\sigma$ , that we will call  $\sigma_{\max}$ , and on this point we are also required to know the value of the effective potential, i.e., we need  $V_k(\sigma_{\max})$ .

The criterion according to which one should choose  $\sigma_{\max}$  can be obtained via some considerations on the symmetries of the model and on the structure of the flow equation Eq. (4.13). In particular at the UV cutoff scale,  $k \rightarrow \Lambda \rightarrow \infty$ , the effective action coincides with the bare action. This means that the effective potential  $V_k(\sigma)$  is given by the corresponding interaction term in the bare action  $S_{\text{bare}}$ , which is oftentimes parameterized as polynomial in powers of the field  $\sigma$ . If the theory, and thus the effective potential, is  $\mathbb{Z}_2$ -symmetric, this implies that the only allowed powers of  $\sigma$  are the even ones. Thus, in order for the theory to describe some non trivial interactions, the potential has to be at least of fourth order in  $\sigma$ , i.e.,  $V_{k=\Lambda}(\sigma) \sim \sigma^4$ . From this naturally follows that  $\partial_\sigma V_{k=\Lambda}(\sigma) \sim \sigma^3$  and  $\partial_{\sigma\sigma}^2 V_{k=\Lambda}(\sigma) \sim \sigma^2$ . From the structure of the FRG flow equation Eq. (4.13) we can thus observe that its right-hand side becomes smaller and smaller for larger values of  $\sigma$ , scaling with a power at least of order  $\sim \sigma^{-2}$ . From this piece of information we can thus deduce that we must choose  $\sigma_{\max}$  large enough to neglect the right-hand side of the flow equation Eq. (4.13). This implies that the evolution of the



effective potential at the boundary is negligible and thus one can assume that  $V_k(\sigma_{\max})$  does not change under the FRG flow and keeps its original UV value. A detailed discussion on the boundary conditions and how to implement them can also be found in Ref. [80].

### 4.2.2 Conservative formulation

As we already pointed out, Eq. (4.13) for the evolution of  $V_k(\sigma)$  is independent of the value of the potential itself, and this seems intuitive since the value of the potential is related to the undetectable zero-point energy and only the differences and derivatives of the effective potential are observable. This opens the possibility, from a mathematical point of view, for the flow equation to be expressed solely in terms of the derivative(s) of the effective potential. Before proceeding, it is convenient to replace the  $k$ -dependence of  $V_k(\sigma)$  by the equivalent dependence on the RG-time variable  $t$ . Thus, we define  $V(t, \sigma) = V_k(\sigma)$  and we use this convention in the following. So, as previously mentioned, we now introduce the derivative of the potential as new variable

$$u(t, \sigma) = \partial_\sigma V(t, \sigma) \quad (4.17)$$

and in an analogous way

$$u'(t, \sigma) = \partial_\sigma u(t, \sigma) = \partial_{\sigma\sigma}^2 V(t, \sigma). \quad (4.18)$$

As a next step, we thus take a derivative of Eq. (4.13) with respect to  $\sigma$  and rearrange the terms, obtaining

$$\partial_t u(t, \sigma) + \frac{\partial}{\partial \sigma} \left[ (N-1) A_D \frac{(\Lambda e^{-t})^{D+2}}{(\Lambda e^{-t})^2 + \frac{1}{\sigma} u(t, \sigma)} \right] = \frac{\partial}{\partial \sigma} \left[ A_D \frac{(\Lambda e^{-t})^{D+2}}{(\Lambda e^{-t})^2 + u'(t, \sigma)} \right]. \quad (4.19)$$

Thus, we obtained an equation for the derivative of the potential  $u(t, \sigma)$  of the form

$$\partial_t u(t, \sigma) + \partial_\sigma f(t, \sigma, u) = \partial_\sigma g(t, u'), \quad (4.20)$$

where we introduced the advection flux

$$f(t, \sigma, u) = (N-1) A_D \frac{(\Lambda e^{-t})^{D+2}}{(\Lambda e^{-t})^2 + \frac{1}{\sigma} u(t, \sigma)} \quad (4.21)$$

and the diffusion flux

$$g(t, u') = -A_D \frac{(\Lambda e^{-t})^{D+2}}{(\Lambda e^{-t})^2 + u'(t, \sigma)}, \quad (4.22)$$

which we will shortly analyze in more detail. For the sake of convenience in the notation, we omitted the explicit  $t$  and  $\sigma$  dependence of  $u(t, \sigma)$  and  $u'(t, \sigma)$  when considered as the flux arguments.

Equation (4.20) is exactly in the form of an advection-diffusion equation Eq. (E.11), a PDE which is typical of fluid dynamics and whose general features are presented in App. E. If we let us then guide by the interpretation of the FRG flow equation as an advection-diffusion equation,  $t$  can be considered as a time variable for the FRG flow, while  $\sigma$  can be interpreted as a spatial variable. It is clear that, once the association between the FRG flow equation and an advection-diffusion equation has been demonstrated, we are then allowed to exploit all the wide and well-established toolbox of powerful numerical methods that have been developed to solve hydrodynamic equations. This thus provides us with the main advantage of being sure to use a well-suited numerical method, specifically developed for this kind of equations. In particular we will use the so-called Kurganov and Tadmor scheme (KT), which is described in [142] and in App. E.



### Advection and diffusion fluxes

We now solidify the analogy between the FRG flow equation and an advection-diffusion equation by turning to a more detailed analysis of the previously defined fluxes. For similar studies and description of the properties of this equation in the FRG framework one can also refer to Refs. [32, 80, 81, 105, 106, 132, 133, 134]. We start noticing that Eq.(4.20) is in the conservative form (cf. Eq.(E.11)). In order to further deepen our study, we evaluate the  $\sigma$  derivatives, thus casting it into its primitive form (cf. Eq.(E.14)):

$$\partial_t u(t, \sigma) + \partial_u f(t, \sigma, u) u'(t, \sigma) + \partial_\sigma f(t, \sigma, u) = \partial_{u'} g(t, u') u''(t, \sigma), \quad (4.23)$$

where, intuitively,  $u''(t, \sigma) = \partial_\sigma u'(t, \sigma)$ . This form shows more clearly the structure of an advection-diffusion equation. In this specific case  $u(t, \sigma)$  plays the role of a fluid "density" whose transport properties are governed by the two contribution that we labeled as advection and diffusion.

Even though Eq. (4.23) is not a conservation law in a strict sense, since it involves also dissipative contributions, we will refer to  $u(t, \sigma)$  as the "conserved quantity" of this generalized conservation law.

We can now analyse in more detail the advection flux, which is due to the pion loop. If we want to isolate only this contribution in Eq. (4.23), this can be formally done by rescaling the equation by a factor  $N$  and then taking the limit  $N \rightarrow \infty$ , which is then regarded as the inviscid limit. In a more crude way, we can just neglect the diffusion term, and therefore we are left with an advection equation

$$\partial_t u(t, \sigma) + \partial_u f(t, \sigma, u) u'(t, \sigma) + \partial_\sigma f(t, \sigma, u) = 0, \quad (4.24)$$

where the advection coefficient is given by

$$\partial_u f(t, \sigma, u) = -A_D (\Lambda e^{-t})^{D+2} \frac{N-1}{\sigma [(\Lambda e^{-t})^2 + \frac{1}{\sigma} u(t, \sigma)]^2} < 0 \quad \forall \sigma > 0. \quad (4.25)$$

Following the analogy with the hydrodynamic framework, the advection term is responsible for the bulk motion of the conserved quantity. In particular the direction towards which this transport is oriented is given by the sign of the advection coefficient, which in general may change depending on the value of  $\sigma$ ,  $t$  and  $u(t, \sigma)$ . However, as it is already highlighted in Eq.(4.25), the sign of  $\partial_u f(t, \sigma, u)$  is simply the opposite of the  $\sigma$  one. This means that this contribution transports the conserved quantity from higher values (in absolute value) of  $\sigma$  toward  $\sigma = 0$ . Furthermore, the change in sign at  $\sigma = 0$ , and thus the change in the direction of the characteristic curves, may lead to the formation of shocks or rarefaction waves.

To a more careful analysis, one notices that actually Eq. (4.24) is not purely advective, since the flux  $f(t, \sigma, u)$  depends also explicitly on  $\sigma$ , thus producing an extra term  $\partial_\sigma f(t, \sigma, u)$  when taking the  $\sigma$  derivative. However, this term acts like a  $u(t, \sigma)$ -dependent sink or source, and it does not have a specific direction, i.e., it is not oriented. This means that the previous considerations hold without major changes.

We now move to a more detailed description of the diffusive term in Eq.(4.23), which arises from the  $\sigma$  loop. As can be seen from Eq. (4.19), Eq. (4.23) can be reduced to a purely diffusive equation, like the heat equation, considering the  $N = 1$  case, which thus is usually referred as the viscous limit. In this case Eq.(4.23) reduces to

$$\partial_t u(t, \sigma) = \partial_{u'} g(t, u') u''(t, \sigma), \quad (4.26)$$

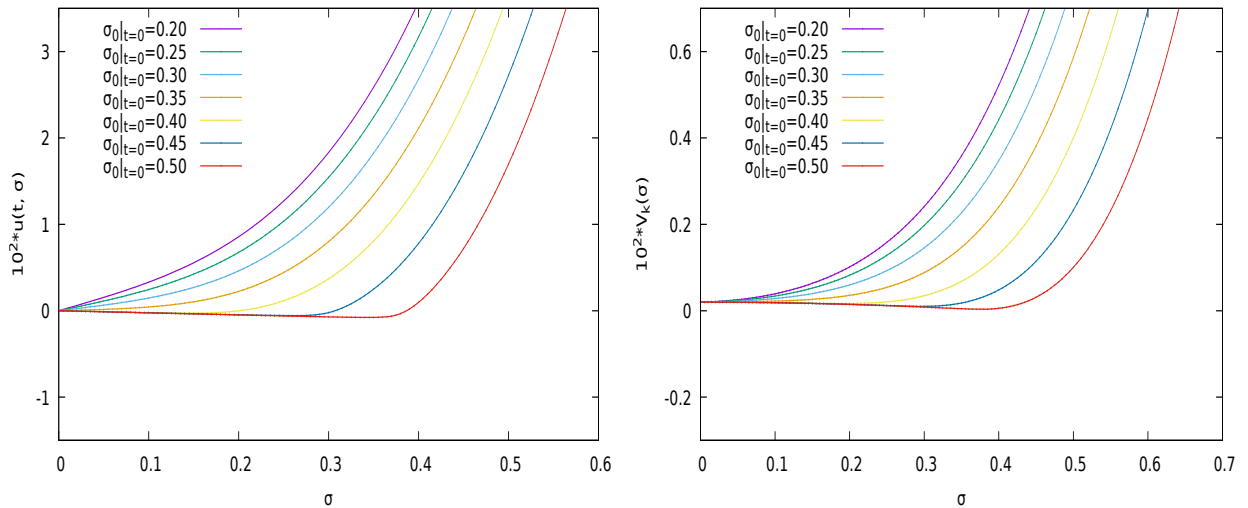


Figure 4.1: The effective potential  $V_k(\sigma)$  (right panel) and its derivative  $u(t, \sigma)$  (left panel), for  $N = 3$  at RG time  $t = 3$ , for different values of  $\sigma_0|_{t=0} = \sqrt{2\rho_0}|_{t=0}$  in the LPA. For lower values of  $\sigma_0|_{t=0}$  the system, in the IR limit, ends up in the symmetric phase ( $\sigma_0|_{IR} = 0$ ), while for higher values of  $\sigma_0|_{t=0}$  the symmetry is not restored ( $\sigma_0|_{IR} > 0$ ) and the potential exhibits a plateau. The UV cut-off scale is  $\Lambda = 1.0$ , the grid size is  $[0, \sigma_{\max}] = [0, 2.0]$ , while the grid spacing is  $\Delta\sigma = 0.005$  (corresponding to 400 grid points).

which, as anticipated, is a purely diffusive equation. From a fluid-dynamical perspective, diffusion is related to a smearing of the solution, since it depends on the gradient of the solution itself, thus transporting the conserved quantity from regions in the spatial domain where it is more concentrated, i.e., the value of the solution is high in absolute value, to regions where it is less concentrated, i.e., where it has a lower absolute value. The crucial aspect is that this line of reasoning can only be followed if the diffusion coefficient is positive, otherwise the solution would be concentrated instead of being smeared, thus leading to singularities. This means that having a positively defined diffusion coefficient is crucial in terms of both the (numerical) stability and the well-posedness of the problem. Advantageously for us, the diffusion coefficient in Eq. (4.26) is

$$\partial_{u'}g(t, u') = A_D (\Lambda e^{-t})^{D+2} \frac{1}{[(\Lambda e^{-t})^2 + u'(t, \sigma)]^2} > 0 \quad (4.27)$$

and thus clearly positively defined. As we will see in the next section, both the advection and the diffusion terms play a fundamental role in the symmetry-restoration dynamics.

As a final remark, one can easily check that, using the formulation of the flow equation in terms of the invariant  $\rho$  as in Eq. (4.13), we do not find a  $u$ -dependent source term in the advection contribution, since  $f(t, \sigma, u(t, \sigma)) \Leftrightarrow f(t, u(t, \rho))$ , where  $u(t, \rho) = V_k'(\rho)$ . However, the trade-off would be the appearance of a source-like and an advection-like term in the diffusive contribution, since now  $g$  would also depend on both  $u$  and  $\rho$  explicitly:  $g(t, u'(t, \sigma)) \Leftrightarrow g(t, \rho, u(t, \rho), u'(t, \rho))$ , where  $u'(t, \rho) = V_k''(\rho)$ .

The next section will be devoted to the analysis of the critical behavior of the  $O(N)$  model.

### 4.3 Critical behavior

The first thing we have to do, in order to study the critical behavior of the  $O(N)$  model, is to fix the UV potential at the cutoff scale  $\Lambda$ , which means to fix the initial condition for the RG flow equation at  $t = 0$ . In particular, we choose the well-known  $\phi^4$  potential:

$$V_{k=\Lambda}(\rho) = \frac{\lambda}{4} \left( \rho - \rho_{0|t=0} \right)^2, \quad (4.28)$$

where  $\rho_{0|t=0}$  is the minimum of the potential at the cutoff scale  $\Lambda$ . Whether or not the system is in the symmetric or spontaneously broken phase is indicated by  $\rho_{0|t=0}$ . In fact  $\rho_{0|t=0} = 0$  corresponds to the symmetric phase, while  $\rho_{0|t=0} > 0$  signals a symmetry-broken phase.

In particular, as we already pointed out, in the case of  $\rho_{0|t=0} > 0$ , the  $N$ -component  $\vec{\phi}$  field develops a non-vanishing expectation value and thus the theory exhibits a spontaneous symmetry breaking of the  $O(N)$  symmetry group. However, the symmetry is not completely broken since the rotations in field space in the  $N - 1$ -dimensional hyperplane perpendicular to the direction in which the field acquires a finite expectation value are still symmetries for the theory. Thus, the  $O(N)$  symmetry of the theory is spontaneously broken down to an  $O(N - 1)$  subgroup. This means that, out of the  $N(N - 1)/2$  generators of the  $O(N)$  group, or better the continuous counterpart  $SO(N)$ ,  $N - 1$  will generate a transformation under which the theory is not anymore invariant. These generator are the one belonging to  $SO(N)/SO(N - 1)$  and indeed are exactly  $N(N - 1)/2 - (N - 1)(N - 2)/2 = N - 1$ . According to the Goldstone theorem then, these generators will form a vector multiplet of the unbroken  $SO(N - 1)$  subgroup, to which will correspond exactly  $N - 1$  massless fields, which we identified as the pion modes, forming again a vector multiplet of  $SO(N - 1)$ . The remaining field then, the radial mode that we called sigma, will also be part of an  $SO(N - 1)$  multiplet, but in this case of the trivial scalar one, and develops a mass which is proportional to the minimum  $\rho_{0|t=0}$  [149].

What is more interesting from a physical perspective is that the  $O(N)$  symmetry is then restored at sufficiently high temperature via a second-order phase transition. The latter will be the focus of our study.

#### 4.3.1 Dimensional reduction

We mentioned that the phase transition should occur at a given finite temperature. This means that, in order to study the critical behavior of the system, we need to generalize the flow equation (4.13) to finite temperature. However, this step is actually not necessary since we can exploit the well-known phenomenon of dimensional reduction [150, 151, 152, 153]. We can justify this in many ways. For example, as we will investigate in the next chapters, the finite-temperature flow equation displays the discrete Matsubara sum over the discrete frequencies  $\omega_n$  instead of a continuous integral over  $p_0$ . If one then looks at the scale-dependent propagators at finite temperature, they have the following structure:

$$G_k(p; T) \sim \frac{1}{1 + \omega_n^2(T)/k^2 + \tilde{m}^2}, \quad (4.29)$$

where  $\tilde{m} = m/k$  and the bosonic Matsubara modes are given by  $\omega_n(T) = 2\pi nT$ . The propagators are then inserted into the loops, where a sum over the frequencies and a  $(D - 1)$ -momentum integral have to be performed. This means that, effectively, the finite-temperature generalization corresponds to an infinite number of copies of a

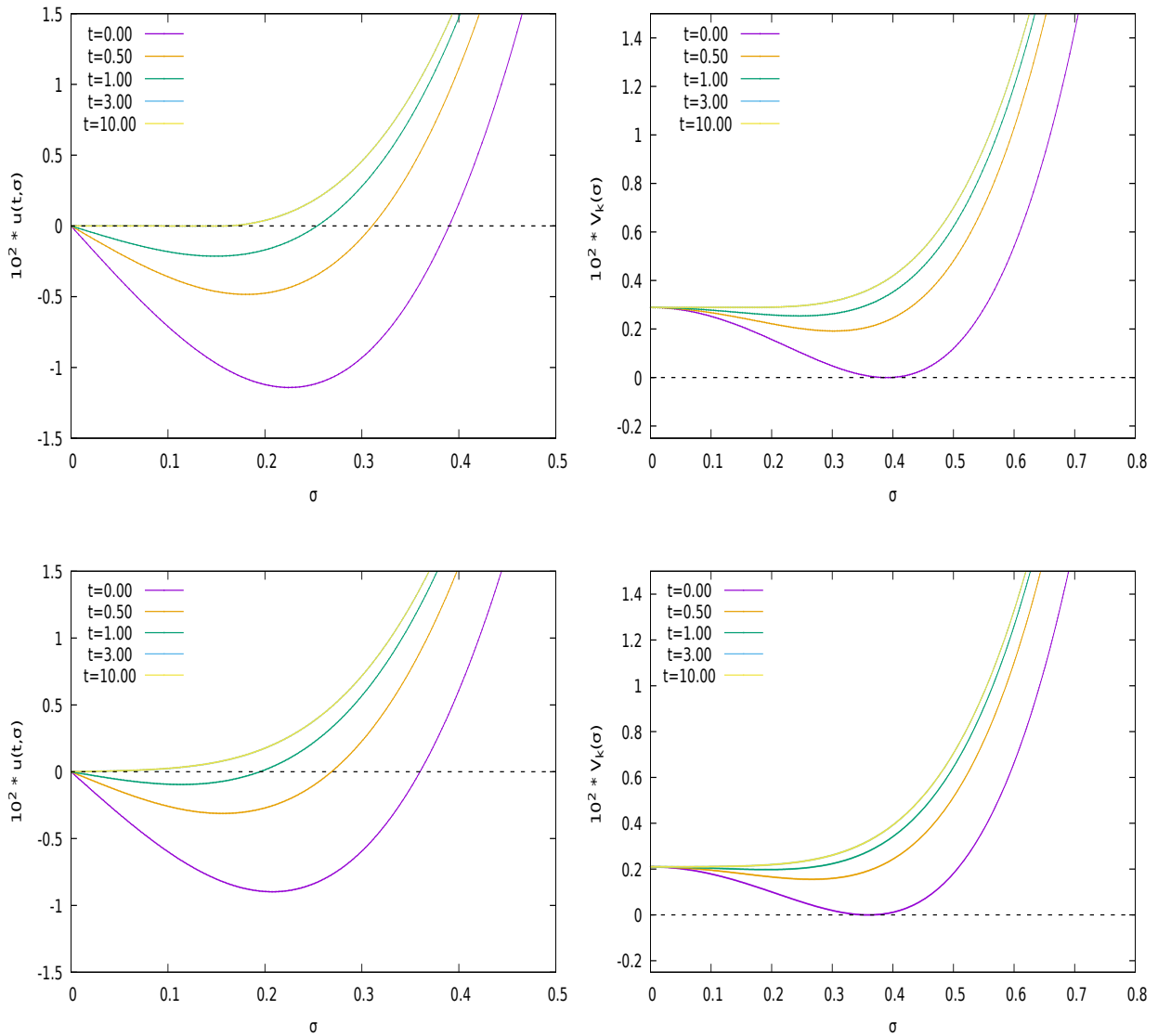


Figure 4.2: The effective potential  $V_k(\sigma)$  (right panels) and its derivative  $u(t, \sigma)$  (left panels), for  $N = 3$  in the LPA for different RG time values at  $\sigma_0|_{t=0} = 0.39$  (upper panels) and at  $\sigma_0|_{t=0} = 0.36$ . For  $\sigma_0|_{t=0} = 0.36$  the system, in the IR limit ( $t = 10$ ), ends up in the symmetric phase ( $\sigma_0|_{IR} = 0$ ), while for  $\sigma_0|_{t=0} = 0.39$  the symmetry is not restored ( $\sigma_0|_{IR} > 0$ ) and the potential exhibits a plateau. The UV cut-off scale is  $\Lambda = 1.0$ , the grid size is  $[0, \sigma_{\max}] = [0, 2.0]$ , while the grid spacing is  $\Delta\sigma = 0.000133$  (corresponding to 1500 grid points).

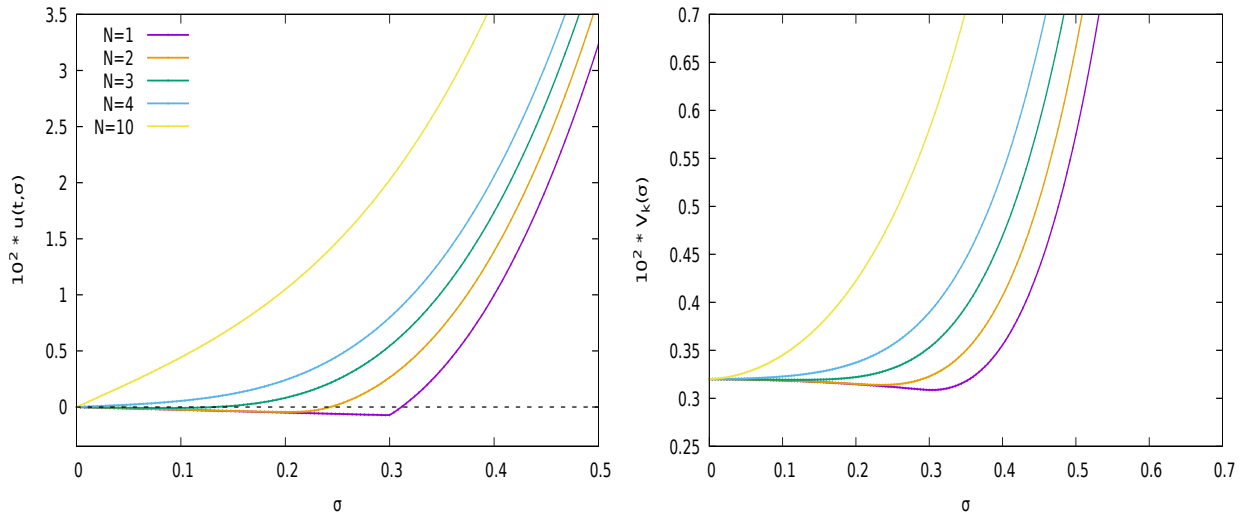


Figure 4.3: The effective potential  $V_k(\sigma)$  (right panel) and its derivative  $u(t, \sigma)$  (left panel), at RG time  $t = 3$ , for  $\sigma_0|_{t=0} = 0.38$  for different values of  $N$  in the LPA. For lower values of  $N$  the system, in the IR limit, ends up in the broken phase ( $\sigma_0|_{IR} > 0$ ) and the potential exhibits a plateau, while for higher values of  $N$  the symmetry is restored ( $\sigma_0|_{IR} = 0$ ). The UV cut-off scale is  $\Lambda = 1.0$ , the grid size is  $[0, \sigma_{\max}] = [0, 2.0]$ , while the grid spacing is  $\Delta\sigma = 0.004$  (corresponding to 500 grid points).

$(D - 1)$ -dimensional theory, each one differing by an extra temperature-dependent mass contribution given by  $\omega_n^2(T)/k^2$ . This leads to the fact that, in the limit of high temperatures, or more precisely, when the temperature is much larger than the FRG flow parameter,  $T \gg k$ , the non-zero Matsubara modes with mass  $\sim 2\pi nT/k$ ,  $n \neq 0$ , decouple from the evolution, leaving a  $(D - 1)$ -dimensional effective theory involving only the zero Matsubara mode. Changing the point of view, one can notice that the length scale associated with the system, the correlation length, diverges approaching criticality, and thus is much bigger than the inverse temperature, which gives the extent of the compactified Euclidean time dimension. This means that it is not possible to resolve the aforementioned compactified Euclidean time dimension, leading to a dimensionally reduced effective theory. Thus, in the particular case of interest for us, i.e., for  $D = 3 + 1$ , it is not necessary to use a finite-temperature  $D = 3 + 1$  flow equation in order to investigate the critical dynamics of the system and the related phase transition. Instead, it is sufficient to employ the  $D = 3$  zero-temperature flow equation (4.13).

### 4.3.2 Order parameter

It is well known, on the basis of universality-class arguments [154, 155, 156, 157], that the parameters that can bring the  $O(N)$  model towards criticality are, in general, two: temperature and external magnetic field. This can be immediately understood considering as an example the ferromagnetic spin Ising model with a discrete symmetry  $\mathbb{Z}_2 = O(1)$ , where we know that the parameters that drive the system towards the phase transition are precisely the temperature and external magnetic field. Since we are considering our theory in the chiral limit (no external sources or masses, i.e., no external field) only one relevant eigenvalue from the linearized RG equations is left, the temperature (see, e.g., [128] and references therein). However, we are exploiting the dimensional-reduction theorem and working with a zero-temperature field theory, thus we need to identify the temperature-like relevant variable. In our case the role of the temperature that decides whether the system ends up in the symmetric or broken phase at  $t = \infty$ , is the UV minimum of the potential  $\rho_0|_{t=0}$ : if  $\rho_0|_{t=0}$  is larger than a critical value  $\rho_0^c|_{t=0}$  (which is

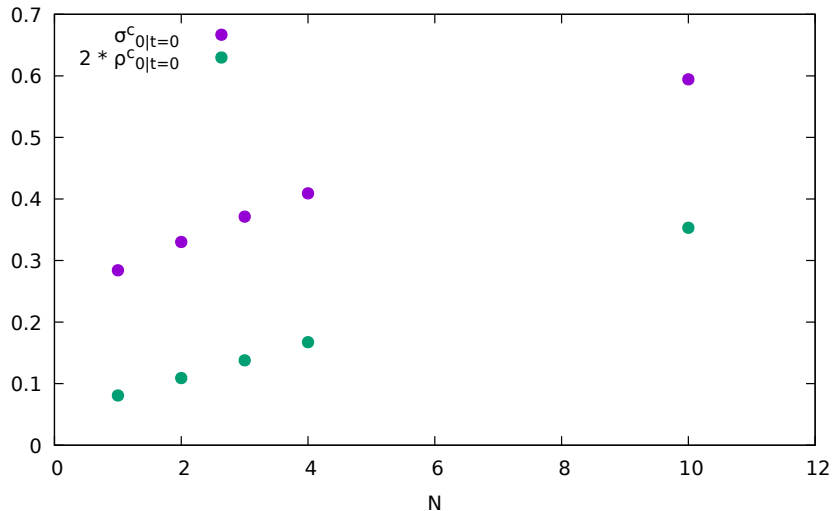


Figure 4.4: Scaling of  $\rho_0^c|_{t=0}$  (green dots) and  $\sigma_0^c|_{t=0} \sqrt{2\rho_0^c|_{t=0}}$  (purple dots) as a function  $N$  for  $D = 3$  in the LPA. The results are obtained for  $\Lambda = 1.0$ ,  $\sigma_{\max} = 2.0$ , and grid spacing  $\Delta\sigma = 0.0005$ .

equivalent to  $T < T_c$ ) the system will end up in the broken phase with a flat potential and a finite minimum  $\sigma_0|_{IR} > 0$ , otherwise if  $\rho_0|_{t=0} < \rho_0^c|_{t=0}$  (which corresponds to  $T > T_c$ ), the symmetry will be restored and  $\sigma_0|_{IR} = 0$ . This discussion thus allows us to identify  $\rho_0|_{t=0}$  as the temperature-like variable that drives the phase transition and  $\sigma_0|_{IR}$  as the *order parameter* of the phase transition, since  $\sigma_0|_{IR} > 0$  in the broken phase and  $\sigma_0|_{IR} = 0$  in the symmetric one. Solving the FRG flow equation, one can get a quantitative confirmation of the previous argument. The results of this numerical solution are displayed in Figs. 4.1, 4.2, and 4.3 where the effective potential  $V_k(\sigma)$  and its derivative  $u(t, \sigma)$  are shown as different parameters are changed. In particular, in Fig. 4.1 we show the effective potential  $V_k(\sigma)$  (right panel) and its derivative  $u(t, \sigma)$  (left panel) for different values of  $\sigma_0|_{t=0} = \sqrt{2\rho_0|_{t=0}}$  at the FRG time  $t = 3$ . This time has been chosen such that the related RG scale  $k$  is sufficiently small, i.e., we are sufficiently far in the IR, such that the evolution of the effective potential given by the flow equation does not change the position of the observables we are interested in, i.e., the minimum of the potential itself and the curvature mass at the minimum, by an appreciable amount. A more detailed discussion on the choice of the IR scale and the errors on the calculated quantities is given in Sec. 4.4. It is then possible to observe that small values of  $\sigma_0|_{t=0}$  will bring the system to the symmetric phase in the IR ( $\sigma_0|_{IR} = 0$ ), while for larger values of  $\sigma_0|_{t=0}$  the symmetry is not restored in the IR ( $\sigma_0|_{IR} > 0$ ) and, due to the convexity of the effective potential, see for example Ref. [158], the potential exhibits a plateau. Similar conclusions can be drawn by looking at Fig. 4.2, where the effective potential  $V_k(\sigma)$  (right panels) and its derivative  $u(t, \sigma)$  (left panels) are shown for different values of the FRG time  $t$  in the  $N = 3$  case. In particular we considered two different values of  $\sigma_0|_{t=0}$  around the critical value  $\sigma_0^c|_{t=0} \sqrt{2\rho_0^c|_{t=0}} = 0.37136655$ : the upper panel shows the result for  $\sigma_0|_{t=0} = 0.39 > \sigma_0^c|_{t=0}$ , leading to a broken phase, while in the lower panel we used  $\sigma_0^c|_{t=0} = 0.36 < \sigma_0^c|_{t=0}$ , meaning that the system will be in the symmetric phase in the IR. This figure also confirms that the differences between  $t = 3$  and  $t = 10$  are negligible since the two curves overlap almost perfectly in every depicted case. We can also notice that, due to the already described properties of the different fluxes that form the flow equation, the effect of time evolution on the effective potential is always a shift of the minimum of the potential towards smaller values of  $\sigma$  either reaching zero or freezing into a finite value of  $\sigma$ . Finally, in Fig. 4.3 we show the effective potential  $V_k(\sigma)$  (right



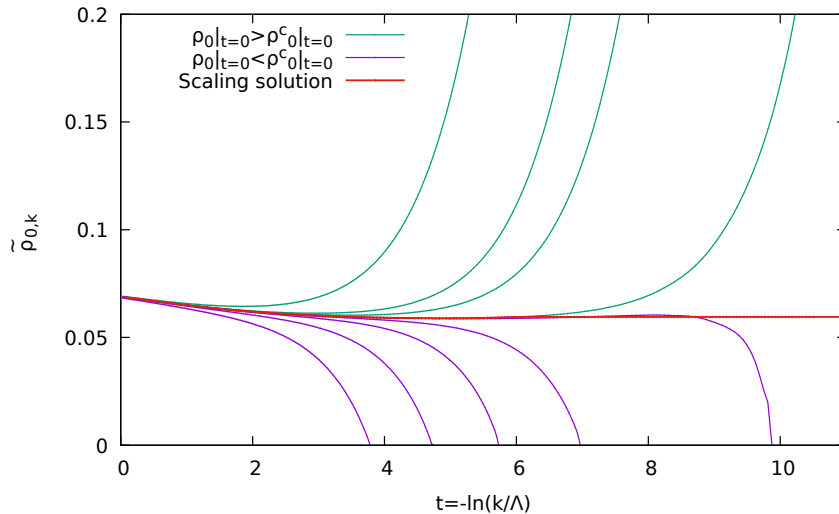


Figure 4.5: Scaling of  $\tilde{\rho}_{0,k}$  as a function of RG time  $t$  in the LPA for  $N = 3$  and  $d = 3$ . The green curves deviate upwards from the scaling value (red line), indicating that the system is in the broken phase ( $\rho_0|_{t=0} > \rho_0^c|_{t=0}$ ), while the purple curves deviate downwards towards the symmetric phase ( $\rho_0|_{t=0} < \rho_0^c|_{t=0}$ ). The results are obtained for  $\Lambda = 1.0$ ,  $\sigma_{\max} = 2.0$ , and grid spacing  $\Delta\sigma = 0.0005$ .

panel) and its derivative  $u(t, \sigma)$  (left panel), at a fixed RG time scale  $t = 3$ , for a given fixed value of  $\sigma_0|_{t=0} = 0.38$ , for different values of  $N$ . In particular we can observe that for lower values of  $N$ , the system ends up in the broken phase ( $\sigma_0|_{IR} > 0$ ) in the IR, while for higher values of  $N$  the symmetry is restored ( $\sigma_0|_{IR} = 0$ ). This is due to the fact that, increasing  $N$ , the advection flux becomes more dominant and tends to restore the symmetry in a stronger way, due to its structure. In order to contrast this effect, the critical value of  $\sigma_0^c|_{t=0}$  has to increase for higher values of  $N$ . This is depicted in Fig. 4.4, where we show the critical value  $\sigma_0^c|_{t=0}$  and the corresponding  $\rho_0^c|_{t=0}$  as function of  $N$ .

### 4.3.3 Critical scaling

Since we are treating a second-order phase transition, we expect an infrared fixed point of the renormalization group, close to which the theory is scale-invariant [154, 155, 156, 157]. Thus, the critical behavior has to be described by a scale-independent solution of the RG flow equation. Now, guided by the previous reasoning, we fix  $\lambda$  to an arbitrary value  $\lambda = 0.5$ , which is, however, an irrelevant quantity from the RG perspective (see, e.g., [128]), and adjust  $\rho_0|_{t=0}$  at  $t = 0$  in order to find the so-called *scaling solution*, i.e., a  $k$ -independent solution of the flow equations for sufficiently small  $k$ . In particular, the closer  $\rho_0|_{t=0}$  is to  $\rho_0^c|_{t=0}$  in the UV, the closer the solution will be to the scaling one towards the IR, where for the scaling solution the  $t$ -dependence vanishes. This implies that properly rescaled dimensionless quantities will exhibit a constant behavior at sufficiently large  $t$ . In particular, the dimensionless minimum

$$\tilde{\rho}_{0,k} = k^{2-D} \rho_{0,k} \quad (4.30)$$

tends to a constant (fixed-point) value as  $\rho_0|_{t=0}$  approaches  $\rho_0^c|_{t=0}$ . The previously described qualitative behavior can be quantitatively validated simply by solving the FRG flow equation, the result of which is depicted in Fig. 4.5 (cf. Ref. [128]). Here we plot the  $t$ -evolution of the dimensionless minimum Eq. (4.30) for different initial values  $\rho_0|_{t=0}$ . One observes that, during the FRG flow,  $\tilde{\rho}_{0,k}$  approaches the critical trajectory, the asymptotic fixed-point value of which is shown by the red line, thus meaning that the system reaches the scaling solution at a given RG time. However, the system will eventually



move out of the scaling phase, meaning that the rescaled minimum deviates either upwards or downwards. Let us try to give a better qualitative and quantitative description of this behavior specifying our results for the case  $D = 3$ . We can divide it into three regimes:

1.  $0 < t < t_G$ . Close to  $t = 0$  the minimum moves towards the critical value associated to the fixed-point. The scale at which the scaling regime is reached is  $t_G$ , the so-called *Ginzburg scale*. This corresponds to the scale at which the rescaled coupling  $\tilde{\lambda}_k = \lambda k^{D-4} = \lambda/k$  is of the order of one, i.e.,  $\tilde{\lambda}_k \sim 1$ , thus signaling the breaking of perturbation theory.
2.  $t_G < t < t^*$ . The value of the minimum is close to the fixed-point value and its time evolution is very slow. The scale  $t^*$ , and thus the corresponding value  $k^*$ , is the scale that signals the end of the scaling regime and it depends on the correlation length  $k^* \sim \xi^{-1}$ . In particular the time spent by the system on the scaling trajectory depends on how close the initial value  $\rho_0|_{t=0}$  is to the critical value  $\rho_0^c|_{t=0}$ , since the closer  $\rho_0|_{t=0}$  is to the critical value  $\rho_0^c|_{t=0}$ , the larger is the correlation length and thus the value of  $t^*$  where the deviation from the scaling solution occurs.
3.  $t > t^*$ . Once the fluctuations have been integrated up to the scale of the correlation length, the system can arrange itself into one of the following three possibilities:
  - (a) if  $\rho_0|_{t=0} > \rho_0^c|_{t=0}$ , the fluctuations will not be able to destroy the finite value of the minimum, thus resulting in the broken phase. In analogy to the behavior of the Ising model, this phase is called ferromagnetic. In this case  $\rho_{0,k}$  tends to a constant value  $\rho_0|_{IR} > 0$  while  $k \rightarrow 0$ , implying that  $\tilde{\rho}_{0,k} = (\rho_{0,k}/k) \rightarrow +\infty$ . So the broken phase corresponds to the curves deviating upwards (the green ones in Fig. 4.5).
  - (b) if  $\rho_0|_{t=0} < \rho_0^c|_{t=0}$ , the fields appear coarse-grained and a finite expectation value is present until the integration in fluctuations reaches the correlation length scale. Once this is reached, the fluctuations will destroy the finite value of the minimum, thus resulting in the symmetric phase. Following once again the analogy to the Ising model, one refers to this phase as the paramagnetic one. In particular  $\rho_{0,k}$  goes to 0 for a finite value of  $k \lesssim k^*$  and this means that  $\tilde{\rho}_{0,k} \rightarrow 0$ . This implies that the symmetric phase corresponds to the curves deviating downwards (the purple ones in Fig. 4.5). This is deeply in contrast with a naive mean-field analysis, since in that case the symmetric phase is reached only for  $\rho_0|_{t=0} = 0$ , while every finite value of  $\rho_0|_{t=0} > 0$  would result in a broken phase.
  - (c) if  $\rho_0|_{t=0} = \rho_0^c|_{t=0}$  exactly, then the rescaled minimum will follow the scaling behavior  $\rho_{0,k} \sim k$ . This implies that  $\tilde{\rho}_{0,k} = \frac{\rho_{0,k}}{k}$  will tend to a constant fixed-point value as  $k \rightarrow 0$ . In this case the correlation length diverges, corresponding to  $k^* = 0$ , which is associated to the so-called Wilson-Fisher fixed point of the RG. This is the case of the scaling solution, depicted in red in Fig. 4.5.

As one would expect, not only  $\tilde{\rho}_{0,k}$  exhibits a scaling behavior, but all other properly rescaled quantities reach and leave the critical trajectory at given RG times, which depends on  $\rho_0|_{t=0}$ . However, we choose to analyze the behavior of  $\tilde{\rho}_{0,k}$  since the minimum of the potential is the most striking feature that characterizes the phase transition, being the order parameter.

#### 4.3.4 Critical exponents

The physics of phase transitions has been extensively investigated due to its relevance for the description of the behavior of several physical systems. In particular, one of its most known aspects [70, 154, 155, 156, 157, 159] is the possible divergence of some of the physical quantities derived from the partition function, or equivalently from the free energy of the system, approaching a phase transition. In our dimensionally reduced system, the critical region corresponds to the case  $\rho_0|_{t=0} \rightarrow \rho_0^c|_{t=0}$ . In particular, one observes that the aforementioned observables exhibit a power-law behavior approaching criticality. This behavior is then characterized by specific exponents, which are usually referred to as *critical exponents*. Their most striking feature is that they do not depend on the specific microscopic details of the system, but on more general features, like the dimensionality and on the symmetries of the system itself. This well-known phenomenon is referred to as *universality* and the value of the set of the critical exponents defines the so-called *universality class* of the theory. In the standard formulation of the theory of scaling, one counts six critical exponents:  $\alpha$ , related to the specific heat,  $\beta$ , related to the order parameter,  $\gamma$ , related to susceptibility,  $\delta$ , related to the external field,  $\nu$ , related to correlation length and  $\eta$ , related to the correlation of critical fluctuations. One useful property of critical exponents is that only two of them are independent, since they are constrained by four relations, which can be obtained via scaling arguments. Indeed, these relations are called *scaling laws* or *scaling relations* and can be listed as:

$$\alpha = 2 - D\nu \quad \text{Josephson law ,} \quad (4.31)$$

$$\gamma = \nu(2 - \eta) \quad \text{Fisher law ,} \quad (4.32)$$

$$\gamma = \beta(\delta - 1) \quad \text{Widom law ,} \quad (4.33)$$

$$\alpha + 2\beta + \gamma = 2 \quad \text{Rushbrooke law ,} \quad (4.34)$$

where  $D$  represents the dimension of the system. We will now focus on the calculation of two of these six critical exponents:  $\beta$  and  $\nu$ . In particular, we will discuss how to extract them from the solution of the FRG flow equation. Since only two critical exponents are independent, one can calculate the remaining four using the scaling relations, or test if the scaling relations are satisfied or not and to which extent by assuming  $\eta = 0$  in the LPA.

##### 1. Critical exponent $\beta$

As we already hinted, the critical exponent  $\beta$  is associated to the critical behavior of the order parameter, which we already discussed being  $\sigma_0|_{IR}$  for the analyzed phase transition. In particular, close to criticality, it is described by the following behavior

$$\sigma_0|_{IR} = \begin{cases} 0 & \rho_0|_{t=0} < \rho_0^c|_{t=0} \\ \sim (\rho_0|_{t=0} - \rho_0^c|_{t=0})^\beta & \rho_0|_{t=0} > \rho_0^c|_{t=0} \end{cases} . \quad (4.35)$$

One can obtain the value on  $\beta$  by taking the logarithm of both sides of Eq.(4.35) when the value of the order parameter is finite, i.e., in the broken phase, and then the critical exponent can be read off from the slope of  $\ln(\sigma_0|_{IR})$  as a function of  $\ln(\rho_0|_{t=0} - \rho_0^c|_{t=0})$ :

$$\ln(\sigma_0|_{IR}) = \beta \ln(\rho_0|_{t=0} - \rho_0^c|_{t=0}) + \text{const} . \quad (4.36)$$

This procedure is shown in Fig. 4.6 using as an example the results obtained for  $N = 3$ . In particular, looking at Fig. 4.6, one can observe that, for small values of

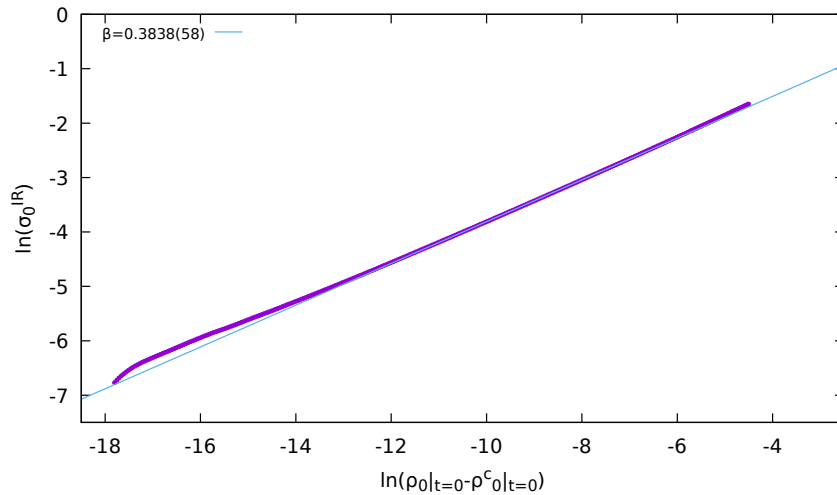


Figure 4.6: Double-logarithmic plot of Eq. (4.35) (violet dots) in the LPA case for  $N = 3$  and  $D = 3$ . The estimate for the value of the critical exponent  $\beta$  is given by the slope of the blue line. Other parameters of the calculation are the same as for Fig. 4.5.

$\ln(\rho_0|_{t=0} - \rho_0^c|_{t=0})$ ,  $\ln(\sigma_0|_{IR})$  deviates from the scaling behavior given by Eq. (4.36). This can be justified by the finite precision we have at our disposal in the determination of  $\rho_0^c|_{t=0}$ . In particular, the closer the initial  $\rho_0|_{t=0}$  is to the approximately determined critical value, the more the resulting  $\ln(\sigma_0|_{IR})$  is sensitive to deviations from the actual critical value caused by the finite numerical precision, and thus one simply does not follow the critical behavior anymore. On the other hand, the deviation observed for large values of  $\ln(\rho_0|_{t=0} - \rho_0^c|_{t=0})$  is due to the fact that one is simply too far away from the critical region, such that the scaling behavior of Eq. (4.36) does no longer apply. Before moving to the description of the critical exponent  $\nu$ , we can make a final remark: if we had worked with the finite-temperature theory,  $\sigma_0|_{IR}$  would have been a function of temperature. In particular, close to criticality it would have been proportional to  $(T - T_c)^\beta$ . Thus  $\rho_0^c|_{t=0}$  is what defines the critical temperature in three dimensions.

## 2. Critical exponent $\nu$

It is known that, given two points  $x$  and  $y$ , whose space-time distance is very large, the field correlator exhibits an exponential decay:

$$G(x - y) = \langle \phi(x)\phi(y) \rangle - \langle \phi(x) \rangle \langle \phi(y) \rangle \sim e^{-|x-y|/\xi} \quad \text{for } |x - y| \gg \xi, \quad (4.37)$$

where  $\xi$  is called *correlation length*, since it measures the range of correlations. Close to the criticality, it has the following divergent behavior

$$\xi(T) \sim (T - T_c)^{-\nu}, \quad (4.38)$$

In our three-dimensional reduced theory, this behavior translates into

$$\xi(\rho_0|_{t=0}) \sim (|\rho_0|_{t=0} - \rho_0^c|_{t=0}|)^{-\nu}. \quad (4.39)$$

Thus,  $\nu$  is the critical exponent which describes the divergence of the correlation length close to criticality. In order to compute  $\nu$ , one can take advantage of the link between the correlation length and the renormalized mass  $m$ . In particular,

$$\xi \sim m^{-1}. \quad (4.40)$$

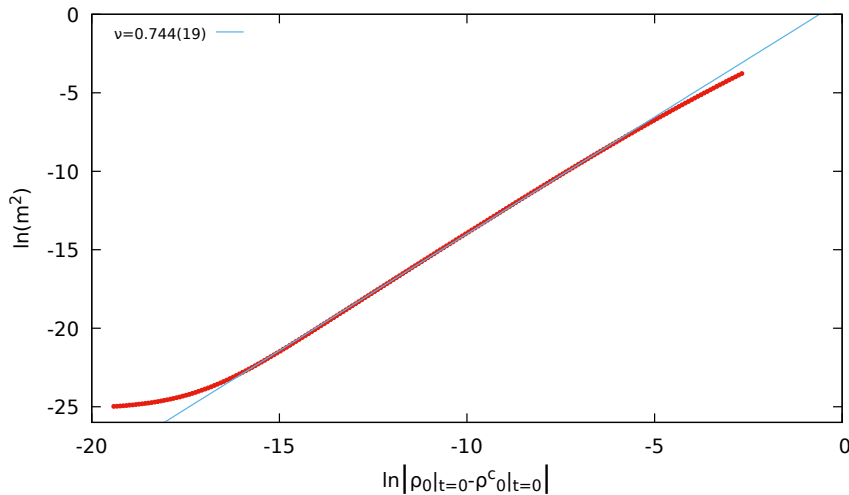


Figure 4.7: Double-logarithmic plot of Eq. (4.42) (red dots) in the LPA case for  $N = 3$  and  $D = 3$ . The estimation for the value of the critical exponent  $\nu$  is given by the slope of the blue line. Other parameters of the calculation are the same as for Fig. 4.5 .

If one considers the symmetric phase, the renormalized curvature mass is given by

$$m^2 = \lim_{k \rightarrow 0} u'(\sigma = 0, k) = \lim_{k \rightarrow 0} V''(\sigma = 0, k) . \quad (4.41)$$

In particular, Eq. (4.40) is fulfilled by the so-called *screening mass*, which is indeed the one responsible for spatial modulations of the two-point function. On the other hand, in Eq. (4.41) we are considering the *curvature mass*, arising from the second field derivative of the effective potential. In principle, curvature and screening mass do not have to coincide, but conveniently for us, they do coincide in the LPA for zero-temperature calculations [160]. In this case, the pole mass (given by the pole of the propagator in the case of vanishing 3-momenta), the curvature mass, and the screening mass are identical [160]. Thus, we will compute  $m^2$  via Eq. (4.41) and then combine it with Eq. (4.40) and Eq. (4.39), resulting in

$$m^2 \sim (|\rho_0|_{t=0} - \rho_0^c|_{t=0})^{2\nu} . \quad (4.42)$$

In this way we can obtain  $\nu$  as the slope of  $\ln m^2$  as a function of  $\ln(|\rho_0|_{t=0} - \rho_0^c|_{t=0})$ :

$$\ln m^2 = 2\nu \ln(|\rho_0|_{t=0} - \rho_0^c|_{t=0}) + \text{const} . \quad (4.43)$$

We have to notice that one has to make sure to reach the symmetric phase before stopping the  $t$ -evolution, because only in this way one can be sure that  $m^2 > 0$  at  $\sigma = 0$ .

In Tabs. 4.1 and 4.2 we show our results for  $\beta$  and  $\nu$ , respectively, obtained within the LPA for  $D = 3$  and various values of  $N$ , in comparison to results obtained within similar frameworks, as well as results from different approaches. Results obtained within the same FRG framework but including a non-trivial RG-scale dependent wave-function renormalization [128] are denoted as “RG’ ”. Results obtained from Monte Carlo (MC) simulations [161, 162] are listed under “MC”, those from perturbative RG are denoted as “PT” [163], while those from the  $\varepsilon$ -expansion at order  $\varepsilon^6$  are shown under “ $\varepsilon$ -exp.” [164]. Results from Conformal Bootstrap (CB) are denoted as “CB” [165, 166, 167], and finally those from a derivative expansion up to fourth order as “DE<sub>4</sub>” [127]. One can conclude that the results obtained in this work are overall in good agreement with the

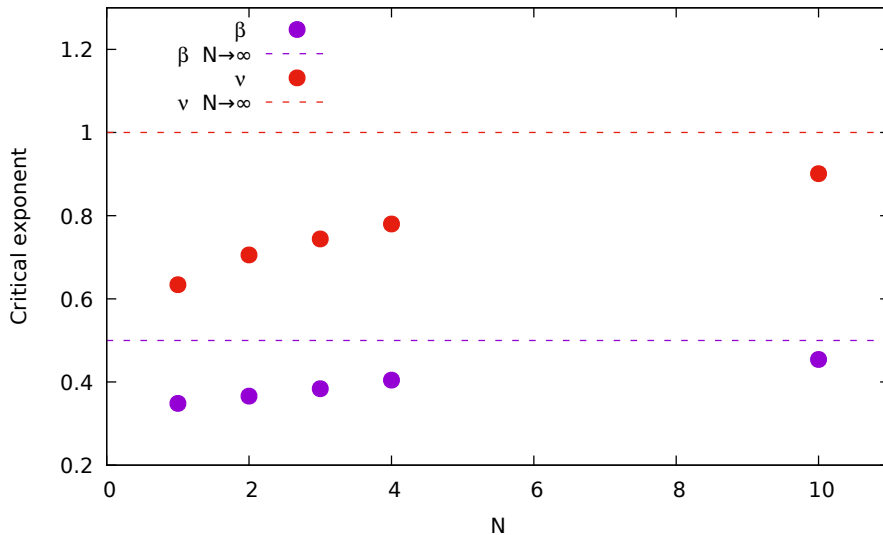


Figure 4.8: Critical exponents  $\beta$  (purple dots) and  $\nu$  (red dots) as a function of  $N$  and  $D = 3$ . The dashed lines correspond to the value of the corresponding critical exponent in the limit  $N \rightarrow \infty$ . Other parameters of the calculation are the same as for Fig. 4.5.

ones obtained with other approaches. As compared to the results of  $RG'$ , which is, from a technical perspective, the closest to our approach, we improve the precision by one order of magnitude and, in addition, we provide an error estimate. A more detailed analysis of the various error sources is presented in the next section. Although  $RG'$  includes a non-trivial wave-function renormalization, while our approach does not, our results for the values of the critical exponents are not significantly worse than  $RG'$  in comparison to the other methods. As a final remark for this section, we point out that the values we obtained for the critical exponents at finite  $N$  nicely tend to converge to the ones expected in the large- $N$  limit as  $N$  is increased. This is in agreement with the known fact that the LPA becomes exact in the limit  $N \rightarrow \infty$  [65]. This behavior can be clearly deduced from Fig. 4.8, where we show the value of the different calculated critical exponents as a function of  $N$  and the corresponding large- $N$  limit, reported in Tab. 4.3.

## 4.4 Testing the method: numerical precision and error estimates

As already pointed out, the critical exponents for the  $O(N)$  model have been extensively studied with the use of several techniques. However, we decided to use them as a test ground for the capabilities and limitations of our hydrodynamic method. Guided by this goal, in this section we discuss the numerical precision of our results and provide error estimates. One possible source of error, which we are not going to further discuss in this work, arises undoubtedly from the use of the LPA as a truncation [124, 127]. This is a systematic kind of error and the only way to estimate it is by improving the truncation beyond LPA [127, 128, 130, 131].

The other errors we will discuss and that can be put under better control are the following:

- general fit errors, which result from the way the critical exponents are determined

$N$	LPA	RG'	MC	PT	$\varepsilon$ -exp.	CB	DE <sub>4</sub>
1	0.3486(59)	0.32	0.32643(6)	0.3258(10)	0.32599(32)	0.326419(2)	0.3263(4)
2	0.3659(45)	0.35	0.34864(5)	0.3470(11)	0.3472(6)	0.34872(5)	0.3485(5)
3	0.3838(58)	0.37	0.3689(3)	0.366(2)	0.366(1)	0.3697(12)	0.3691(7)
4	0.4046(34)	0.40	0.3873(4)	0.3834(35)	0.3834(18)	0.3877(47)	0.3874(6)
10	0.4541(45)	0.45			0.4398(7)	0.4523(2)	0.4489(6)

Table 4.1: Order-parameter exponent  $\beta$  obtained via various methods, for different values of  $N$  and for  $D = 3$ .

$N$	LPA	RG'	MC	PT	$\varepsilon$ -exp.	CB	DE <sub>4</sub>
1	0.634(8)	0.64	0.63002(10)	0.6304(13)	0.6292(5)	0.629971(4)	0.62989(25)
2	0.7057(14)	0.69	0.67169(7)	0.6703(15)	0.6690(10)	0.6718(1)	0.6716(6)
3	0.744(19)	0.74	0.7112(5)	0.7073(35)	0.7059(20)	0.7120(23)	0.7114(9)
4	0.780(20)	0.78	0.7477(8)	0.741(6)	0.7397(35)	0.7472(87)	0.7478(9)
10	0.901(13)	0.91			0.859(1)	0.8842(3)	0.8776(10)

Table 4.2: Correlation-length exponent  $\nu$  obtained via various methods, for different values of  $N$  and for  $D = 3$ .

	$\beta$	$\nu$	$\eta$	$\delta$	$\alpha$	$\gamma$
Large $N$	0.5	1.0	0	5	-1.0	2.0

Table 4.3: Critical exponents in the large- $N$  case for  $D = 3$ .

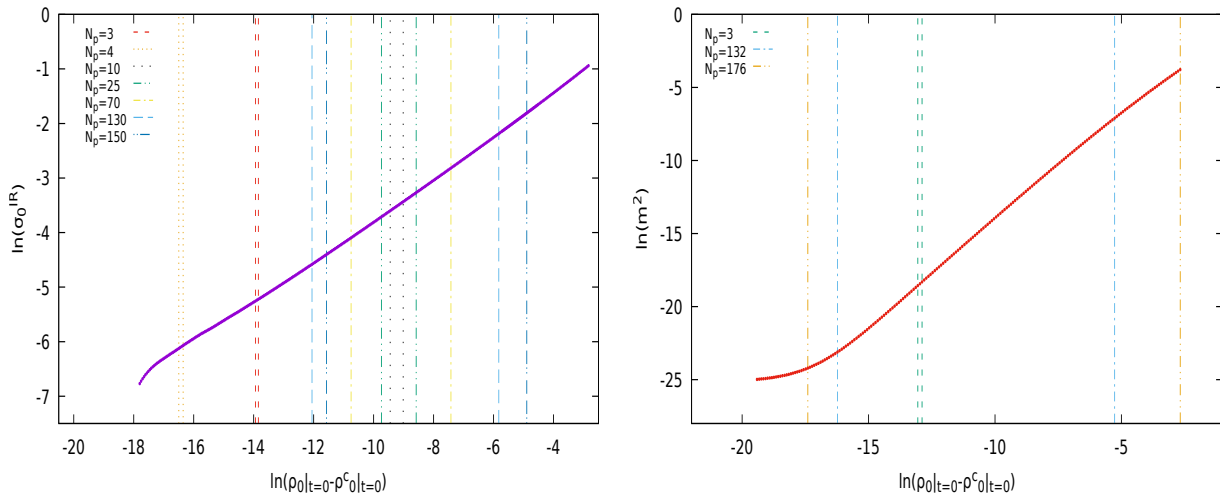


Figure 4.9: Different fitting regions corresponding to different numbers of most aligned consecutive points, for the extraction of the critical exponents  $\beta$  (left panel) and  $\nu$  (right panel). Here,  $N = 3$  and  $D = 3$ . Other parameters of the calculation are the same as for Fig. 4.5.

and thus affects both critical exponents;

- error on the determination of the curvature mass in the IR, which influences the value of  $\nu$ ;
- error on the determination of the position of the minimum in the IR  $\sigma_0^{\text{IR}}$ , which is inherent to the extraction of  $\beta$ .

Let us now analyze each contribution in detail.

#### 4.4.1 General fit error

As already discussed, a linear fit to the data is performed in order to extract the value of the critical exponents from the resulting slope. This procedure inevitably leads to some error due to the fact that, as mentioned in the previous section, some points do not follow the critical scaling and thus deviate from the linear fit. This implies the strict need for a criterion which enables us to select which points we should take into account for the fit. This is definitively a non-negligible issue, since, as can be seen from Figs. 4.10 and 4.12, the value of a particular critical exponent and the relative fit error may change a lot if only a single data point is added to (or subtracted from) the fit. So in order to find the aforementioned criterion, let the physics of phase transitions guide us. Since our goal is to extract the critical exponents from the scaling region, here a linear behavior of the observables (in case of the logarithm of the IR minimum and the logarithm of the curvature mass) as a function of  $\ln |\rho_0|_{t=0} - \rho_0^c|_{t=0}|$  is expected. This means that it seems reasonable to use for the fit those consecutive points which exhibit the highest degree of collinearity, which we can obtain using as a criterion, for example, the Pearson correlation coefficient. However, even considering the most collinear data points, the number of points which are taken into consideration still have a significant impact on the value of the critical exponents. This is exactly what can be deduced from Figs. 4.10 and 4.12, where the critical exponents are shown as a function of the number of consecutive most aligned points. This is mainly due to two factors. First of all, the region that we are supposed to use for the fit and where the consecutive most aligned points are contained can move while modifying the number of points. Secondly, the fitting region



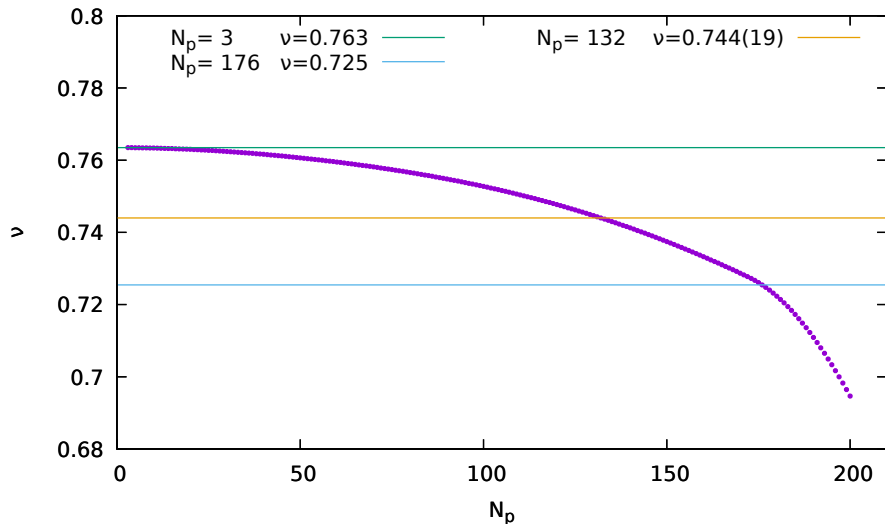


Figure 4.10: Critical exponent  $\nu$  as a function of the number of the most aligned points  $N_p$  taken into consideration in the fit, for the case  $N = 3$  and  $D = 3$ . Other parameters of the calculation are the same as for Fig. 4.5.

can include points which are increasingly further away from a desired straight fitting line. One can clearly realize this by looking Fig. 4.9, where we show how the fitting region changes if one modifies the corresponding number of most aligned consecutive points, for both  $\beta$  (left panel) and  $\nu$  (right panel).

This implies that we still have to establish a reliable criterion according to which the number of the consecutive most collinear points can be selected.

We also have to remark that the previously described behavior shown in Figs. 4.10 and 4.12 is not affected by the variation of what we can define as the point density, i.e., the number of points per unit interval of the fitting region. This feature can be deduced from Fig. 4.11, where we repeat the same procedure described in Figs. 4.10 and 4.12 but changing the point density, indicating that the values of the critical exponents depend on the size of the fitting region rather than on the number of points contained in it.

Ideally, if the scaling relations were perfectly satisfied, all points would belong to the scaling region since all of them would exhibit perfect collinearity. Thus, this implies that the critical exponents would become completely independent of the fitting region.

Guided by this piece of information, we can formulate our criterion for the selection of the points to consider in the fit. We will thus identify the scaling region by searching for the range on the abscissa in Figs. 4.10 and 4.12 where the critical exponent is least dependent on the number of consecutive collinear points and thus on the considered fitting region. Once this range is identified, we reasonably assume that the actual value of the critical exponent lies somewhere between the highest and the lowest value of the critical exponent in that range. Thus we identify the contribution to the total error on the critical exponent arising from the fitting procedure as being half the difference of the highest and the lowest value in that range. If we now analyze separately the case of  $\beta$  and  $\nu$ , we observe that finding such a range of consecutive collinear points is straightforward in the case of  $\beta$ : if the number of points in the range considered is too small, the range moves a lot along the abscissa when it is extended. Therefore, we discard the leftmost points in Fig. 4.12 (left panel). From a certain size onward the range does not move anymore, but merely grows within the critical region. However, if the range is too large, also points from outside the critical region are included, which is clearly seen by the jump in Fig. 4.12 (left panel) at  $N_p \simeq 130$ . Hence, this clearly restricts the size of the critical region.

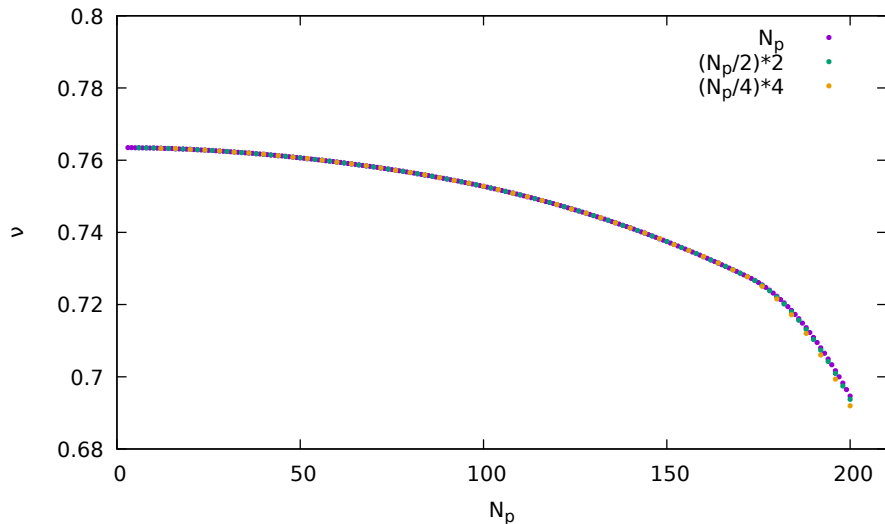


Figure 4.11: Critical exponent  $\nu$  as a function of the number of the most aligned points  $N_p$  taken into consideration in the fit, changing the density of points contained in the scaling region. Here for  $N = 3$  and  $D = 3$  while parameters of the calculation are the same as for Fig. 4.5.

On the other hand, in the case of  $\nu$ , if the fitting region is too large, the exponent starts to change more rapidly, indicating that the corresponding fitting region includes points which do not follow a straight line in Fig. 4.7. Thus, we can discard those points and restrict the fit to a maximum value of  $N_p \simeq 180$ . However, from Fig. 4.10 it is clearly visible that it is much harder, if not almost impossible, to identify a critical region, because  $\nu$  strongly depends on the fitting interval and the change is rather continuous.

As a final remark for this subsection, we state that the error originating from the choice of the fitting region is much larger than the error of the fit itself, i.e., the one extracted from the maximum deviation of the points in the fitting region from a straight line. Indeed, this error is at least one order of magnitude smaller than the error from the choice of the fitting region. Second, as we will soon discuss, the error coming from the KT scheme and the determination of the curvature mass, which is required for extracting  $\nu$  is much smaller than the previously described one obtained from choosing the correct fitting region. This statement will not hold for  $\beta$ , since the discretization error, which results in an uncertainty on the position of the minimum, is instead comparable to the error arising from the determination of the size of the critical region.

#### 4.4.2 Error on $m^2$

In order to obtain a numerical solution of the flow equation Eq. (4.19), or to a general PDE, we need a discretization in the field space. In this subsection we thus analyze how such a discretization in field space influences the value of the renormalized mass  $m^2$  and the corresponding error. In particular, since we chose a uniformly spaced grid whose spacing is  $\Delta\sigma$ , we will assess the impact of  $\Delta\sigma$  on our results. In Fig. 4.13, we show the squared curvature mass  $m^2$  (left panel) and its relative deviation (right panel)

$$\Delta m_{rel}^2(\Delta\sigma) = 1 - \frac{m^2(\Delta\sigma)}{m^2(\Delta\sigma_{min})} \quad (4.44)$$

from the value  $m^2(\Delta\sigma_{min})$  calculated for the smallest cell size  $\Delta\sigma_{min}$  (which in our case is  $10^{-4}$ ), as a function of  $\Delta\sigma$ . We should point out that each point in these figures corresponds to a result of the numerical solution of the FRG flow evolution, obtained

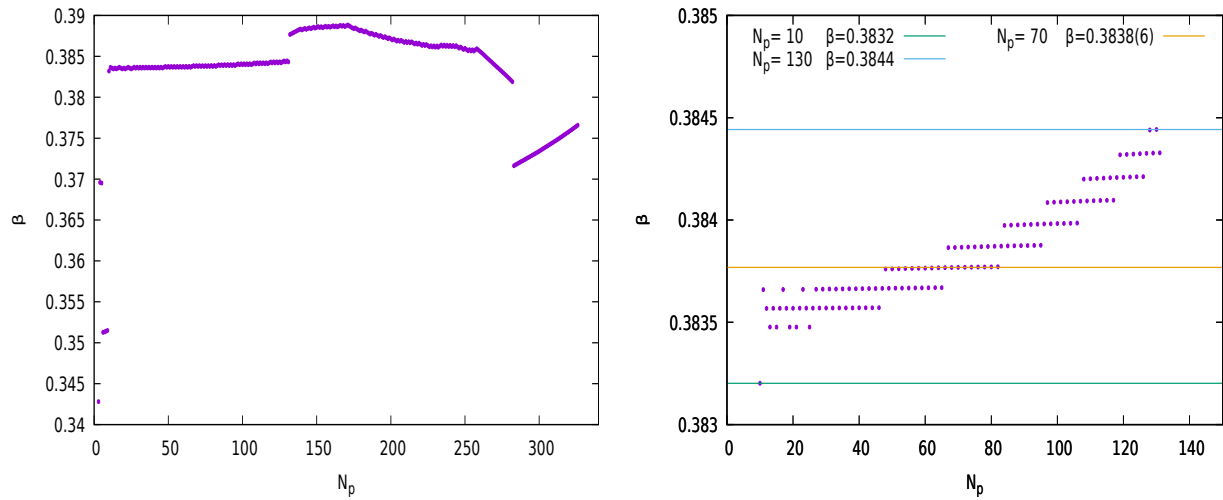


Figure 4.12: Critical exponent  $\beta$  as a function of the number of the most aligned points  $N_p$  taken into consideration in the fit (left panel). The right panel is zooming in on the region where the value of the critical exponent is least dependent on  $N_p$ . In both plots  $N = 3$  and  $D = 3$ . Other parameters of the calculation are the same as for Fig. 4.5.

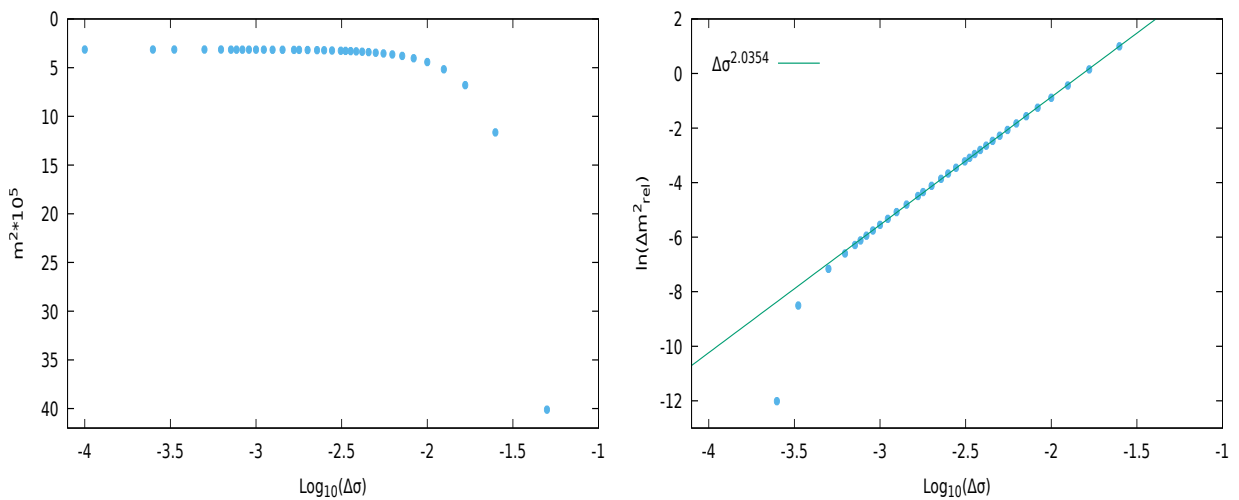


Figure 4.13: Squared curvature mass in the IR,  $m^2$  (left panel), and its relative deviation from the value calculated for the smallest cell size (right panel), as functions of the cell size  $\Delta\sigma$ . Here,  $N = 3$ ,  $D = 3$ ,  $\Lambda = 1.0$ , and  $\sigma_{\text{max}} = 2.0$ .

for  $\sigma_0|_{t=0} = 0.3$  in the symmetric phase ( $\sigma_0^{\text{IR}} = 0$ ) at final time  $t_{\text{IR}} = 25$  ( $k_{\text{IR}} \sim 10^{-11}$ ). Our goal is to determine the region in  $\Delta\sigma$  such that the value of  $m^2$  does not change anymore upon changing the value of  $\Delta\sigma$ , i.e., from a plateau region in Fig. 4.13. From Fig. 4.13 we observe that this happens for values of  $\Delta\sigma \lesssim 10^{-2.5}$ . Thus, in order to get a reasonable compromise between computational resources and needed precision, we use  $\Delta\sigma = 0.0005$  (corresponding to the fourth point from the left in the left panel of Fig. 4.13). Looking at the corresponding region in the right panel of Fig. 4.13, one concludes that this choice leads to a relative error in the determination of  $m^2$  of the order of  $\sim e^{-7} \simeq 10^{-3}$ .

As we have already hinted, from the right panel of Fig. 4.13 one can obtain an estimate of the order of magnitude of the relative errors on each point contained in the left panel. This is especially useful if one considers those points which belong to the plateau in the left panel of Fig. 4.13, since it gives us a possible criterion to select the value of  $\Delta\sigma$ . Still, from the right panel of Fig. 4.13, we can observe that the relative differences scale as  $\Delta\sigma^\alpha$ , with  $\alpha > 2$ . This is a direct consequence of the numerical scheme used, the KT scheme, which has second-order precision in the spatial resolution. In this way we have the possibility to significantly reduce the error in the determination of  $m^2$  by choosing a sufficiently small  $\Delta\sigma$ . We should also mention that there is no additional error from using a finite-difference stencil in Eq. (4.41) to extract the curvature mass at  $\sigma = 0$ , for details see Refs. [80, 106].

One could also argue that another contribution on the determination of  $m^2$  should be taken into account, namely the one related to the extrapolation of the value of  $m^2$  in the IR. As final value of  $t$  in the IR we have chosen  $t = 25$ , since at this point the FRG flow is effectively frozen in, i.e., no quantity changes anymore with RG time. We checked that this is true by computing  $m^2$ , e.g., for  $t = 50$  and  $t = 100$ . The values of  $m^2$  at these times were the same as at  $t = 25$  up to machine precision. Thus, one can conclude that in the symmetric phase it is possible to reach arbitrarily small momentum scales to obtain IR quantities, implying that no further error on the RG time extrapolation needs to be taken into account.

### 4.4.3 Error on $\sigma_0^{\text{IR}}$

One can highlight several aspects which have to be taken into account regarding the determination of the value of  $\sigma_0^{\text{IR}}$ . The first one derives from the structure of the flow equation itself. In fact, in the broken phase, the solution  $u(t, \sigma)$ , whose value vanishes at  $\sigma = 0$ , in the presence of a finite minimum  $\sigma_0$  is negative for  $\sigma < \sigma_0$  and approaches zero from below as  $t \rightarrow \infty$ . As a consequence, the denominator of the advection term in Eq. (4.19) becomes very small when approaching the IR, which leads to a stiff problem when solving the FRG flow equation numerically. This implies that the time step  $\Delta t$  has to become increasingly smaller when  $t \rightarrow \infty$  in order to avoid numerical instabilities. In practice, this prevents us to go arbitrarily far into the IR within our setup. For recent advances on this issue, we refer to Ref. [168]. In order to solve this problem, we can determine the position of the minimum  $\sigma_0^{\text{IR}}$  via extrapolating its IR value using the knowledge of  $\sigma_0$  at the earlier times at our disposal. Here, we decided to perform an exponential extrapolation of  $\sigma_0$  as a function of  $k$  via a linear extrapolation of the values of  $\ln \sigma_0$

$$\ln \sigma_0 = a k + b, \quad \iff \quad \sigma_0 = e^b e^{a k}, \quad (4.45)$$

as can be seen from Fig. 4.14.

This functional form of the extrapolation is motivated by the behavior of  $\sigma_0$  in the large- $N$  limit, where such an exponential scaling is exact, as can be shown by solving

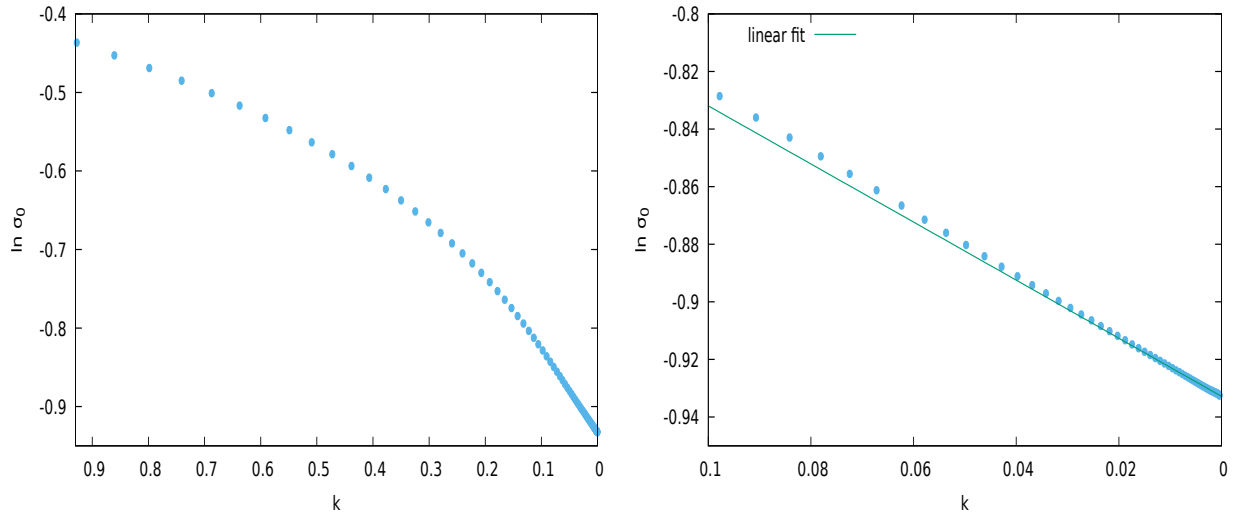


Figure 4.14: Logarithm of the minimum  $\sigma_0$  of the effective potential as a function of the momentum scale  $k$ , for  $N = 3$  and  $D = 3$ . The right panel shows the range  $0.1 \geq k \geq 0$  from the left panel in higher resolution, with the corresponding linear extrapolation to determine the minimum  $\sigma_0^{\text{IR}}$  at  $k = 0$ . Other parameters of the calculation are the same as for Fig. 4.5.

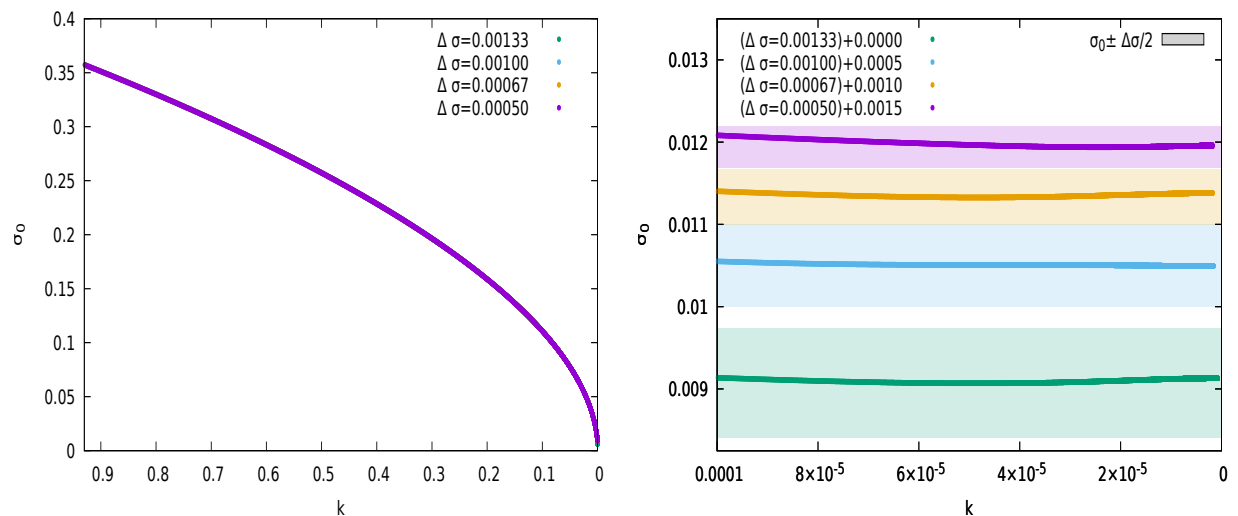


Figure 4.15: Position of the minimum of the effective potential  $\sigma_0$  as a function of the momentum scale  $k$  for different values of the cell size  $\Delta\sigma$ , for  $N = 3$  and  $D = 3$ . The right panel shows the range  $0.0001 \geq k \geq 0$  from the left panel in higher resolution, where the fluctuations in the value of  $\sigma_0$  can be seen. Each band around a line has a width  $\Delta\sigma$ . In order to avoid overlapping bands, we have performed a global shift of  $\sigma_0$  for the cases  $\Delta\sigma = 0.001$ ,  $0.00067$ , and  $0.0005$  by  $0.0005$ ,  $0.001$ , and  $0.0015$ , respectively. Other parameters of the calculation are the same as for Fig. 4.5.

the FRG flow equation analytically via the method of characteristics (see Refs. [32, 169]). This extrapolation is the reason for the small oscillations of  $\ln \sigma_0^{\text{IR}}$  observed in Fig. 4.6.

Even if the extrapolation procedure were to give the correct value, the uncertainty on  $\sigma_0^{\text{IR}}$  is still limited from below by the grid spacing  $\Delta\sigma$ . Assuming that the correct value lies within a cell, one can still determine whether  $\sigma_0$  lies to the left or the right of the cell center, such that the uncertainty is  $\Delta\sigma_0^{\text{IR}} \lesssim \Delta\sigma/2$ .

A clear explanation of our previous line of reasoning can be found in Fig. 4.15, where we observe that, starting with the same fixed  $\sigma_0^{\text{UV}}$ , the position of the minimum is independent of the cell size  $\Delta\sigma$  for larger momentum scales and becomes dependent on  $\Delta\sigma$  as  $k$  decreases. We should also point out that in Fig. 4.15 we shifted some of the curves in the right panel, in order to increase the visibility of the  $\Delta\sigma$  bands, but these shifts are anyway smaller than the actual differences between the curves. However, we observe that, for any given  $\Delta\sigma$ , for small  $k$  the numerical fluctuations of  $\sigma_0$  as a function of  $k$  stay within a band given by  $\pm\Delta\sigma/2$ , confirming the aforementioned assumption for the error on  $\sigma_0^{\text{IR}}$ . In addition, as one would expect, these fluctuations seem to decrease as  $\Delta\sigma$  is reduced.

Thus we justified the assumption of using  $\Delta\sigma/2$  as the error on every value of  $\sigma_0^{\text{IR}}$ . This implies that each point in Fig. 4.6 has an error given by

$$\Delta \ln \sigma_0^{\text{IR}} = \frac{\Delta\sigma_0^{\text{IR}}}{\sigma_0^{\text{IR}}} = \frac{\Delta\sigma}{2\sigma_0^{\text{IR}}}. \quad (4.46)$$

It is crucial noticing that this error depends on  $\sigma_0^{\text{IR}}$  itself. The error bands which originate from this contribution are depicted in Fig. 4.16. We now have to use this consideration in order to extract an error on  $\beta$ . In particular, it seems reasonable to construct the slopes with maximum deviation from the one defining  $\beta$  which originate from the previously described error bands. We then consider the value of  $\beta$  extracted from the line which passes through the points  $\left((q_0|_{t=0} - q_0^c|_{t=0})^{\text{left}}, \ln \sigma_0^{\text{IR, left}} - \Delta \ln \sigma_0^{\text{IR, left}}\right)$  and  $\left((q_0|_{t=0} - q_0^c|_{t=0})^{\text{right}}, \ln \sigma_0^{\text{IR, right}} + \Delta \ln \sigma_0^{\text{IR, right}}\right)$ , where  $\Delta \ln \sigma_0^{\text{IR, left}}$  and  $\Delta \ln \sigma_0^{\text{IR, right}}$  are the errors of the leftmost and rightmost points of the selected fit interval. The difference of this value of  $\beta$  and the one extracted from the slope of the straight line in Fig. 4.6 gives our estimate for  $\Delta\beta$ , which then reads

$$\Delta\beta = \frac{\Delta \ln \sigma_0^{\text{IR, left}} + \Delta \ln \sigma_0^{\text{IR, right}}}{\Delta q_{\text{fit}}}, \quad (4.47)$$

where  $\Delta q_{\text{fit}}$  is the range in  $\ln(q_0|_{t=0} - q_0^c|_{t=0})$  where the linear fit is performed.

Using typical values encountered during the calculations, i.e.,  $\Delta q_{\text{fit}} \simeq 3.5$ ,  $\Delta\sigma = 0.0005$  one finds

$$\Delta\beta \simeq 0.006. \quad (4.48)$$

We will assume this as the contribution to the error on the critical exponent  $\beta$  arising from  $\Delta\sigma_0^{\text{IR}}$ . It is worth noticing that this contribution is significantly larger than the one coming from the fit error, i.e., the one extracted from the maximum deviation of the points from the straight-line fit, which is usually of order

$$\Delta\beta_{\text{fit}} \sim 0.0002. \quad (4.49)$$

If one wants to have an upper and lower bound for the error, one can use the minimum and the maximum value for  $\sigma_0^{\text{IR}}$  in the fit region in Eq. (4.47). One gets

$$\Delta\beta_{>} = 0.024, \quad \Delta\beta_{<} = 0.007. \quad (4.50)$$

Thus, our estimate of the error seems a good compromise between the highest and the lowest possible errors.

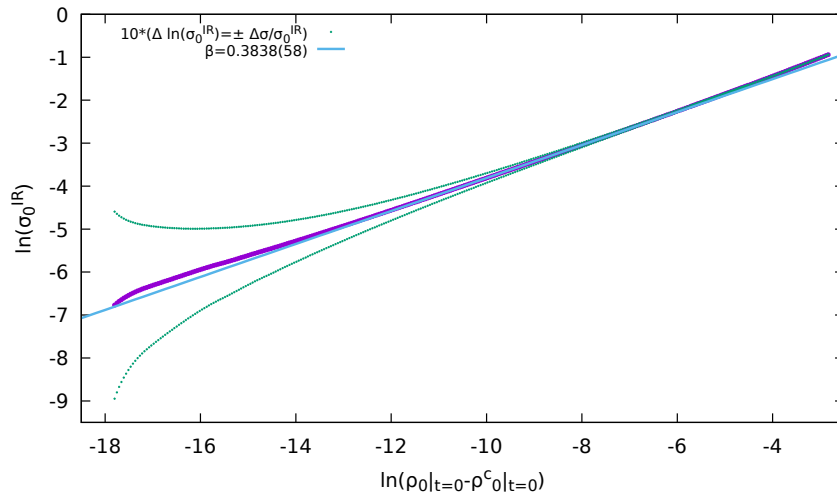


Figure 4.16: Same as Fig. 4.6. The green dots indicate the error  $\pm\Delta \ln(\sigma_0^{\text{IR}})$  on each purple dot obtained as a result.

## 4.5 Final remarks

In this chapter we chose to apply the FRG approach to the study of the critical behavior of the  $O(N)$  model and the related critical exponents. The critical exponents of the  $O(N)$  model are a well-established quantity and have been studied previously within several frameworks and especially in the FRG approach in LPA (for example in Ref. [128] one can see very similar kind of calculations). Anyway, there still can be seen a wide margin of novelty in this part of work, which is actually twofold. On one hand we chose to take advantage of the possibility to cast the FRG flow equation for the effective potential into the form of an advection-diffusion equation [32, 80, 81, 105, 106, 132, 133, 134]. This is of significant importance, since it allows for the possibility to exploit a broad range of widely used and well-tested hydrodynamic algorithms to solve it. On the other hand, and strictly related to the previous point, we showed how this novel hydrodynamic approach to solve the FRG flow equations allows for a better control on statistical errors. With this method, these errors can be more precisely determined and are of order  $10^{-2}$  to  $10^{-3}$ . They are thus comparable to the errors of other well-established methods like lattice calculations, perturbation theory, the  $\varepsilon$ -expansion, or CB.

As hydrodynamic algorithm, we used a finite-volume method, the so-called KT scheme (see Ref. [142] for the original work, or App. E.4 for a brief summary).

The range of applicability for the novel hydrodynamic method to solve FRG flow equations is very wide. Studies in the framework of the  $O(N)$  model were already carried out including higher-order terms in gradients, such as wave-function renormalization factors [127, 128, 130, 131]. Combining these high-precision studies with our developments is certainly a worthwhile future project for the estimation of systematic truncation errors. Furthermore, it is possible to study the system at finite temperature, without exploiting dimensional reduction. In particular, we expect that the non-zero Matsubara modes do not influence the exponents related to the singular part of the free energy (the effective action), that is  $\alpha, \gamma, \eta, \nu$ , while in principle they could give contributions to the order parameter, thus modifying  $\beta$ , and to the critical isotherm, changing the value of  $\delta$ .

In the next chapters of this work we also consider the extension of this model with the inclusion of fermions, the QM model. We can anticipate that, from a mathematical point of view, the FRG flow equations can still be cast into the form of an advection-diffusion equation, but the presence of fermions generates a source term [105, 106, 170].



However, this kind of equations can also be solved using the approach described above. This will be the focus of the next chapters.

# The two-flavor Quark-Meson model

## 5.1 Introduction and motivation

Following the discussion of the QCD Lagrangian, chiral symmetry breaking and QCD effective models in Chapter 2, we now dedicate our attention to a very well-established low-energy effective model for QCD: the Quark-Meson (QM) model. This model can be regarded as the extension of the well-known purely bosonic linear sigma model with the inclusion of fermionic degrees of freedom [47, 171, 172, 173]. In particular, we will consider the QM model with two quark flavors, which contains as fundamental degrees of freedom four mesons, the three pions and the sigma meson, coupled to the fermionic fields representing up and down quarks.

The reason why this model has been intensively studied is that it can qualitatively capture the essential features of the chiral phase transition of QCD, that we described in Chapter 2. As expected, we then find back those features in the framework of this model, with the possibility to have a better grasp on the leading physical quantities behind them. To this aim, it is then meaningful to recapitulate the general sketch of the well-known QM model phase diagram. We will then consider the model, first, in the chiral limit, i.e., with vanishing current quark masses, and then we observe the impact of the relaxation of this hypothesis. As we stated, the two-flavor QM model contains both fermionic d.o.f., namely the quarks, and mesons. In the chiral limit the mesonic sector is endowed with an  $O(4)$  symmetry, which is broken spontaneously in the vacuum. According to the Goldstone theorem this results in an isotriplet of massless pions and one massive sigma meson, which exhibits a non-vanishing expectation value. Due to the presence of a Yukawa coupling between the quarks and the mesons, the finite expectation value of the sigma gives rise to a non-vanishing chiral condensate. For small values of the chemical potential, the chiral symmetry is restored via a second-order phase transition at a given critical temperature, which depends on the chemical potential  $T_c(\mu)$ . For higher values of the chemical potential, the transition becomes of first order. The first- and second-order transition lines meet at a tricritical point, where the transition is of second order, with an order parameter that smoothly vanishes at the critical temperature [174, 175].

In the chiral limit, the mechanism of spontaneous chiral symmetry breaking and chiral symmetry restoration is exact. However, when one includes also a finite current mass term, it explicitly breaks the  $O(4)$  symmetry. This implies that the pions are now pseudo-Goldstone bosons, thus having a non-vanishing mass. As a first consequence, the chiral symmetry is never fully restored and the sigma expectation value never truly vanishes, turning the second-order phase transition at small chemical potentials into a smooth crossover. This occurrence is typical of statistical-mechanical models, for example when studying ferromagnetism. In this case, an external magnetic field acts in such

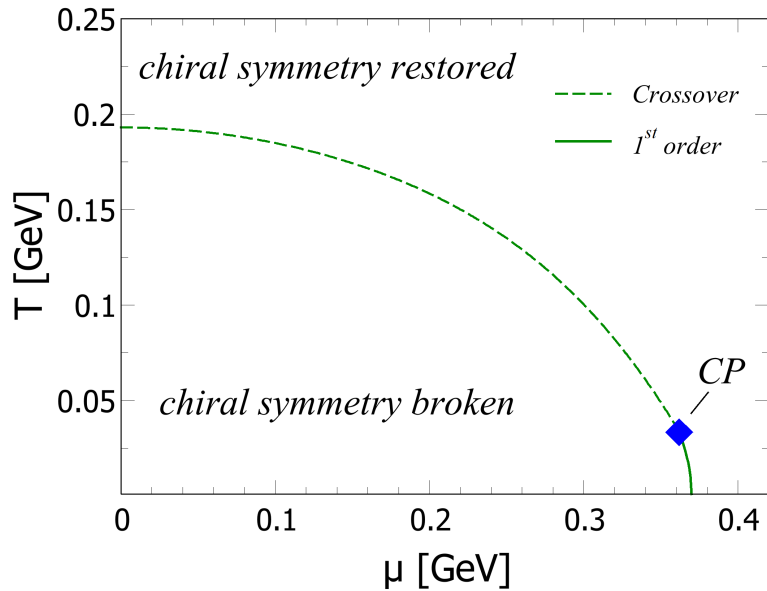


Figure 5.1: Sketch of the phase diagram of the Quark-Meson model at finite temperature  $T$  and chemical potential  $\mu$ . The chirally spontaneously (and explicitly) broken phase and the (approximately) chirally symmetric phase are indicated in the plot. The dashed line, indicating a crossover, and the first-order phase transition lines merge at the critical end point, labeled CP.

a way that the average spin magnetization never vanishes, even for temperatures higher than the Curie one. Following this analogy, valid both for the QM model as well as for QCD, the chiral condensate plays the role of the spontaneous magnetization while the mass term is equivalent to the applied external magnetic field.

At increasing chemical potential, as for the chiral limit, the transition turns into a sharp first-order one, with a jump in the quark condensate from a finite to a very small (but not vanishing) value. The crossover line and the first-order line once again meet in a critical end point, where the phase transition is truly second order. This is signaled by the fact that only at this point the susceptibilities diverge, as it should be the case for a second-order phase transition [11, 12, 115, 174]. What we described so far is illustrated in Fig. 5.1 where a sketch phase diagram of the QM model is shown as a function of the temperature  $T$  and the quark-number chemical potential  $\mu$ . Here, the regions where the chiral symmetry is broken and (approximately) restored are explicitly labeled. The dashed line denotes the crossover at lower values of the chemical potential while the solid line represents the sharp first-order phase transition at higher values of  $\mu$ . The critical end point where the two transition lines meet is labeled as CP.

As expected, the validity of the QM model is confirmed by the fact that the predicted phase diagram is in qualitative agreement with what is believed to be the phase diagram of full QCD, as we discussed in the introduction, Chapter 1.

The goal of this chapter is to study the QM model and its features. Specifically, we begin our analysis by describing how to construct the model starting from the symmetries of QCD Lagrangian. We then present an introductory mean-field (MF) Landau study to settle an expected picture of the model's phase diagram. We then improve the mean-field approximation and apply the FRG approach to the QM model, stressing the analogy with a fluid-dynamic interpretation of the resulting flow equation in the LPA truncation of the effective action. We use this approach to study how the phase diagram and the related physical observables are modified by the inclusion of quantum fluctu-

ations, both in the chiral and in the physical quark-mass limit. Finally, we analyze the critical behavior of the model in the chiral limit and present some results on the critical exponents.

As a final remark on the notation adopted, whenever we investigate the (effective) potential for the QM model we use the symbol  $U$  and not  $V$ , in contrast to the notation used when studying the  $O(N)$  model.

## 5.2 Approximate axial-vector symmetry and its consequences

In order to have at our disposal all the necessary tools to build the QM-model Lagrangian, it is useful to comment more on the approximate conservation of the  $SU_A(2)$  current in QCD and its consequences. For this section one can refer to, e.g., Refs. [47, 173, 176, 177, 178].

### 5.2.1 PCAC

We begin this subsection describing the implication of an exact SSB and an approximate one. In particular, in an exact SSB pattern, the axial-vector current Eq.(2.43) derived from the Noether theorem does not annihilate the vacuum, but produces particles, which must be spinless due to Lorentz invariance

$$A_\mu^k(q_\mu)|0\rangle \propto q_\mu|\pi^k\rangle, \quad (5.1)$$

where  $q_\mu$  represents the momentum of the created particle.

If the current is exactly conserved, then

$$0 = \partial_\mu A^{k,\mu}(q_\mu)|0\rangle \propto q^\mu q_\mu|\pi\rangle = m_\pi^2|\pi\rangle. \quad (5.2)$$

We can interpret this relation in two ways: on one hand, we can check that the pions are massless  $m_\pi^2 = 0$ , as stated by the Goldstone theorem; on the other hand, if we consider  $m_\pi^2$  sufficiently small we can assume the conservation of the axial-vector current with good approximation.

Changing slightly the point of view, we can look at the weak decay of charged pions, whose primary decay mode is

$$\pi^+ \rightarrow \mu^+ \nu_\mu, \quad (5.3)$$

$$\pi^- \rightarrow \mu^- \bar{\nu}_\mu. \quad (5.4)$$

If one considers a simple Fermi theory of the weak interaction, then the interaction term is of the current-current type, involving both the vector and the vector-axial currents defined in Eqs.(2.32) and (2.43) (see, e.g., [176]). Due to parity, the process is dominated by the matrix element of the axial current between the vacuum and the pion state

$$\langle 0|A_\mu^k|\pi^l(q)\rangle = -if_\pi q_\mu \delta^{kl} e^{-iq \cdot x}, \quad (5.5)$$

where  $q_\mu$  is the momentum of the pion. The relation Eq.(5.5) defines the proportionality constant  $f_\pi$ , which is the so-called pion decay constant and is determined experimentally. If we now take the divergence of Eq.(5.5) we obtain

$$\langle 0|\partial_\mu A^{k,\mu}|\pi^l(q)\rangle = -f_\pi q^2 \delta^{kl} e^{-iq \cdot x} = -f_\pi m_\pi^2 \delta^{kl} e^{-iq \cdot x}, \quad (5.6)$$

which is exactly what we expected from Eq.(5.2). So once again we can conclude that the fact that pions have a small mass can be seen as the consequence of the partial conservation of the axial current and the approximate  $SU_A(2)$  symmetry of QCD Lagrangian.

Equation (5.6) is what is usually referred to as *partially conserved axial current* (PCAC) relation. As a final statement, we can also deduce from Eqs. (5.5) and (5.6) the shape of the axial-vector current associated to the pion field  $\pi^k(x)$

$$A_{\mu,\pi}^k = f_\pi \partial_\mu \pi^k(x). \quad (5.7)$$

This relation will be useful in the next paragraph and sometimes it is also referred to as PCAC relation, since it follows from the combination of both Eqs. (5.5) and (5.6).

## 5.2.2 Goldberger-Treiman relation

We now explore another consequence of the approximate conservation of the axial current. We consider a nucleon, namely an isospin doublet  $\Psi_{Nuc}$  composed of the proton  $P$  and the neutron  $N$ :  $\Psi_{Nuc} = (\Psi_P, \Psi_N)^T$ . Recalling Eq. (2.43), we can write the axial-vector current related to the nucleon as

$$A_{\mu,Nuc}^k = g_A \bar{\Psi}_{Nuc} \gamma_\mu \gamma_5 \tau^k \Psi_{Nuc}, \quad (5.8)$$

where the factor  $g_a = 1.25$  is a normalization factor due to the fact that nucleons are not elementary particles. As we have seen from the PCAC relation, we expect the axial-vector current of the nucleon to be highly not conserved due to the big nucleon mass. However, nucleon interactions are mediated by pions. Therefore, it is reasonable to assume that the axial current which should be conserved arises from the sum of the nucleon and the pion currents:

$$A_{\mu,Tot}^k = A_{\mu,Nuc}^k + A_{\mu,\pi}^k = g_A \bar{\Psi}_{Nuc} \gamma_\mu \gamma_5 \tau^k \Psi_{Nuc} + f_\pi \partial_\mu \pi^k(x) \quad (5.9)$$

where we used Eqs. (5.7) and (5.8). Imposing the conservation of the total current  $\partial_\mu A_{\mu,Tot}^k = 0$  we obtain:

$$\partial_\mu \partial^\mu \pi^k(x) + i g_A \frac{M_{Nuc}}{f_\pi} \bar{\Psi}_{Nuc} \gamma_5 \tau^k \Psi_{Nuc} = 0, \quad (5.10)$$

where  $M_{Nuc}$  corresponds to the mass of the nucleon. Eq. (5.10) can be interpreted as a Klein-Gordon equation for the massless pion field, which is coupled to the nucleon via the coupling

$$g_{\pi Nuc Nuc} = g_A \frac{M_{Nuc}}{f_\pi}. \quad (5.11)$$

Equation (5.11) is the so-called *Goldberger-Treiman* relation. We also emphasize that in Eq. (5.10) we obtained that the pion has to be massless from the conservation of the axial-vector current. On the other hand, one can impose the PCAC relation Eq. (5.6) instead of the strict conservation of the axial-vector current allowing for a finite pion mass, thus finding

$$\left( \partial_\mu \partial^\mu + m_\pi^2 \right) \pi^k(x) + i g_A \frac{M_{Nuc}}{f_\pi} \bar{\Psi}_{Nuc} \gamma_5 \tau^k \Psi_{Nuc} = 0, \quad (5.12)$$

which is, once again, a Klein-Gordon equation for a massive pion coupled to the nucleon via the same coupling as given by the Goldberger-Treiman relation Eq. (5.11). Even though we derived it for the case of nucleons, this is still valid at the quark level setting  $g_A = 1$ . We will indeed use this version of the relation, where the quark mass term will be the one arising from the coupling to the chiral condensate, to construct the interaction term between quarks and meson in the QM model.

### 5.3 From QCD symmetries to the QM-model Lagrangian

In order to start building the QM-meson Lagrangian out of the symmetry of QCD, let us come back to the definitions of the transformations of the chiral group for two flavors  $SU_V(2) \otimes SU_A(2)$  defined in Eqs. (2.19) and (2.20). In particular, we will consider the infinitesimal transformations associated to the vector and axial-vector symmetries, that we indicate as  $\Lambda_V$  and  $\Lambda_A$  respectively. They act on the spinor doublet  $\Psi = (u, d)^T$  in the following way:

$$\Psi'_V = \Lambda_V \Psi = e^{-i\frac{\vec{\tau}}{2} \cdot \vec{\theta}_V} \Psi \simeq \left( \mathbb{I} - i\frac{\vec{\tau}}{2} \cdot \vec{\theta}_V \right) \Psi, \quad (5.13)$$

$$\Psi'_A = \Lambda_A \Psi = e^{-i\gamma_5 \frac{\vec{\tau}}{2} \cdot \vec{\theta}_A} \Psi \simeq \left( \mathbb{I} - i\gamma_5 \frac{\vec{\tau}}{2} \cdot \vec{\theta}_A \right) \Psi, \quad (5.14)$$

where  $\vec{\tau}$  indicates the Pauli matrices which generate the  $SU(N_f = 2)$  symmetry group. Analogously one finds the associated transformation for  $\bar{\Psi} = (\bar{u}, \bar{d})$ :

$$\bar{\Psi}'_V = \bar{\Psi} e^{i\frac{\vec{\tau}}{2} \cdot \vec{\theta}_V} \simeq \bar{\Psi} \left( \mathbb{I} + i\frac{\vec{\tau}}{2} \cdot \vec{\theta}_V \right), \quad (5.15)$$

$$\bar{\Psi}'_A = \bar{\Psi} e^{-i\gamma_5 \frac{\vec{\tau}}{2} \cdot \vec{\theta}_A} \simeq \bar{\Psi} \left( \mathbb{I} - i\gamma_5 \frac{\vec{\tau}}{2} \cdot \vec{\theta}_A \right). \quad (5.16)$$

In order to construct the model, we then introduce the combinations of quark fields which carry the quantum numbers of the pions and of the sigma meson, namely a (Lorentz) pseudo-scalar iso-triplet and a (Lorentz) scalar iso-singlet:

$$\sigma \equiv \bar{\Psi} \Psi, \quad (5.17)$$

$$\vec{\pi} \equiv i\bar{\Psi} \vec{\tau} \gamma_5 \Psi. \quad (5.18)$$

We can now check the isospin properties of the previously defined fields following the definitions of the infinitesimal transformations in Eqs. (5.13)-(5.16). We begin considering the  $SU_V(2)$  transformation for the  $\sigma$  field at first order in the infinitesimal parameter  $\theta_V$ :

$$SU_V(2): \quad \sigma \equiv \bar{\Psi} \Psi \rightarrow \bar{\Psi} \Psi \equiv \sigma, \quad (5.19)$$

meaning that the  $\sigma$  field is invariant under  $SU_V(2)$  transformations, which we already stated when analyzing the symmetries of the mass term  $\propto \bar{\Psi} \Psi$  in Chapter 2. From this trivially follows that also  $\sigma^2$  is invariant under  $SU_V(2)$  transformations.

We now move to the  $SU_V(2)$  transformation for the pions

$$\begin{aligned} SU_V(2): \quad \pi_i &\equiv i\bar{\Psi} \tau_i \gamma_5 \Psi \rightarrow i\bar{\Psi} \tau_i \gamma_5 \Psi + i\theta_{V,j} \epsilon_{ijk} \bar{\Psi} \tau_k \gamma_5 \Psi \\ &= \pi_i + i\theta_{V,j} \epsilon_{ijk} \pi_k, \end{aligned} \quad (5.20)$$

which in the iso-vector formalism can be indicated as

$$SU_V(2): \quad \vec{\pi} \rightarrow \vec{\pi} + i\vec{\theta}_V \times \vec{\pi}, \quad (5.21)$$

thus implying that the pions behave indeed as an iso-vector and that an  $SU_V(2)$  transformation acts on them as an isospin rotation. This means that the quantity

$$\pi^2 \equiv \vec{\pi} \cdot \vec{\pi} \quad (5.22)$$

is invariant under  $SU_V(2)$  transformations.

We can now consider how the  $\sigma$ -field transforms under the  $SU_A(2)$  symmetry group

$$\begin{aligned} \text{SU}_A(2) : \quad \sigma &\equiv \bar{\Psi}\Psi \rightarrow \bar{\Psi}\Psi + i\theta_{A,i}\bar{\Psi}\tau_i\gamma_5\Psi + \\ &= \sigma - \theta_{A,i}\pi_i, \end{aligned} \quad (5.23)$$

which in isospin vector notation translates to

$$\text{SU}_A(2) : \quad \sigma \rightarrow \sigma - \vec{\theta}_A \cdot \vec{\pi}. \quad (5.24)$$

Analogously, the pions transform under the axial transformation  $\text{SU}_A(2)$  as

$$\begin{aligned} \text{SU}_A(2) : \quad \pi_i &\equiv i\bar{\Psi}\tau_i\gamma_5\Psi \rightarrow +\bar{\Psi}\tau_i\gamma_5\Psi + \theta_{A,i}\bar{\Psi}\Psi \\ &= \pi_i + \theta_{A,i}\sigma \end{aligned} \quad (5.25)$$

and in isospin vector notation

$$\text{SU}_A(2) : \quad \vec{\pi} \rightarrow \vec{\pi} + \vec{\theta}_A\sigma. \quad (5.26)$$

This means that the effect of an  $\text{SU}_A(2)$  transformation is to rotate the pions into the  $\sigma$  meson and vice versa.

Since both  $\pi^2$  and  $\sigma^2$  are independently invariant under  $\text{SU}_V(2)$  transformations, we now check how they are affected by infinitesimal  $\text{SU}_A(2)$  transformations. In particular, it is easy to verify that, at first order in  $\theta_A$ ,  $\sigma^2$  transforms as

$$\text{SU}_A(2) : \quad \sigma^2 \rightarrow \sigma^2 - 2\sigma\vec{\theta}_A \cdot \vec{\pi} \quad (5.27)$$

and  $\pi^2$  as

$$\text{SU}_A(2) : \quad \pi^2 \rightarrow \pi^2 + 2\sigma\vec{\theta}_A \cdot \vec{\pi}. \quad (5.28)$$

Thus, we can conclude that we can construct the effective Lagrangian of the model starting from the combination  $\sigma^2 + \pi^2$ , which is invariant under the full chiral group  $\text{SU}_V(2) \otimes \text{SU}_A(2)$

$$\text{SU}_V(2) : \quad \sigma^2 + \pi^2 \rightarrow \sigma^2 + \pi^2, \quad (5.29)$$

$$\text{SU}_A(2) : \quad \sigma^2 + \pi^2 \rightarrow \sigma^2 + \pi^2. \quad (5.30)$$

From the previous discussion we can then conclude that the  $\text{SU}_V(2) \otimes \text{SU}_A(2)$  chiral symmetry translates into an  $\text{O}(4)$  rotational symmetry for the bosonic field

$$\Phi = \begin{pmatrix} \sigma \\ \pi^1 \\ \pi^2 \\ \pi^3 \end{pmatrix} \quad (5.31)$$

and

$$\Phi^2 = \sigma^2 + \pi^2 \quad (5.32)$$

is the  $\text{O}(4)$  invariant.

Since the kinetic term for fermions is invariant under the chiral group transformation, we can already construct the kinetic term of our low-energy effective model

$$\mathcal{L}_{kin} = i\bar{\Psi}\gamma_\mu\partial^\mu\Psi + \frac{1}{2}(\partial_\mu\Phi)^2. \quad (5.33)$$



The next ingredient is a potential which governs the interaction among mesons. The only requirement that this potential has to fulfill, in order to respect chiral symmetry, is that its only field dependence can come from the  $O(4)$  invariant  $\Phi^2$ :

$$U(\sigma, \pi) = U(\Phi^2). \quad (5.34)$$

No further specification is needed at this stage, and the potential can be an arbitrary function of  $\Phi^2$  (as long as the stability requirements are fulfilled and it is bounded from below).

Regarding the interaction term between mesons and fermions, it has to be built in order to retain both Lorentz and chiral symmetry. To fulfill the constraint of Lorentz symmetry, the pions must be coupled to a pseudo-scalar combination of Dirac fields while the  $\sigma$  field has to be coupled to a scalar one. As far as chiral symmetry is concerned, it is sufficient to recreate a combination which behaves like  $\sigma^2 + \pi^2$ , which is both Lorentz and chiral invariant. The easiest interaction term that fulfills both requirements is obtained by coupling each meson with the corresponding expression in terms of Dirac fields, and is given by

$$\mathcal{L}_{int} = h(\sigma \bar{\Psi} \Psi + \vec{\pi} \cdot (i \bar{\Psi} \gamma_5 \vec{\tau} \Psi)). \quad (5.35)$$

We can notice that the term  $h\sigma \bar{\Psi} \Psi$  acts as a mass term for the fermions. Even though a fermion mass term would explicitly break chiral invariance, the term  $h\sigma \bar{\Psi} \Psi$  does not, since it is inserted in the chirally invariant combination presented in Eq. (5.35). Thus the interaction with the  $\sigma$  meson gives the quarks a constituent mass given by

$$M_\Psi = h \langle \sigma \rangle, \quad (5.36)$$

where  $\langle \sigma \rangle$  indicates the expectation value of the  $\sigma$  field. Using the Goldberger-Treiman relation Eq. (5.11) for quarks, setting  $g_a = 1$ ,  $g_{\pi Nuc Nuc} = h$  and using as mass term the one in Eq. (5.36), one can fix the value of the  $\sigma$  condensate in vacuum:

$$\langle \sigma \rangle = f_\pi. \quad (5.37)$$

This means that the potential in Eq. (5.34) has to have a minimum located at  $\sigma = f_\pi$  in the vacuum. The fact that the  $\sigma$  field acquires a finite expectation value breaks the  $O(4)$  symmetry spontaneously, since the minimum is not invariant under this transformation. This means that the mechanism through which quarks get a finite constituent mass is indeed the SSB of chiral symmetry. When the minimum of the potential is located at  $\sigma = 0$ , i.e., the sigma condensate vanishes  $\langle \sigma \rangle = 0$ , the  $O(4)$  chiral symmetry is restored and the quarks are massless.

Associated to the SSB of the  $O(4)$  symmetry down to  $O(3)$ , the pions are the Goldstone modes and are massless, while the radial  $\sigma$  excitation is massive. When the symmetry is restored, both pions and  $\sigma$  turn massive and become degenerate.

Thus, collecting all the different terms we discussed, we can construct the (Euclidean) Lagrangian for the QM model which then reads:

$$\mathcal{L}_{QM}^E = \bar{\psi}(\gamma_\mu \partial^\mu + h(\sigma + i \gamma_5 \vec{\tau} \cdot \vec{\pi}))\psi + \frac{1}{2}(\partial_\mu \Phi)^2 + U(\Phi^2). \quad (5.38)$$

This will be the starting point for our following discussions, especially when considering the chiral limit.

## 5.4 Extensions of the model

In this section we will consider the extensions of the model to include the effects of finite quark mass, chemical potential and temperature on the structure of the model and on its predictions.

### 5.4.1 Explicit breaking of chiral symmetry

We stated multiple times that the presence of the small but finite current quark masses of the up and down quark breaks the axial-vector symmetry explicitly. In order to implement this feature in the QM model, we recall that the mass term for fermions looks like

$$\mathcal{L}_m = -m^2 \bar{\Psi} \Psi . \quad (5.39)$$

The fermionic content of this term is equal to the one of the definition Eq. (5.17) of the sigma meson. Thus, we can mimic the presence of a finite current quark mass by the insertion of a term

$$\mathcal{L}_m = -c\sigma \quad (5.40)$$

in the Lagrangian Eq. (5.38). The total Lagrangian then reads:

$$\mathcal{L}_{QM}^E = \bar{\psi}(\gamma_\mu \partial^\mu + h(\sigma + i\gamma^5 \vec{\tau} \cdot \vec{\pi}))\psi + \frac{1}{2}(\partial_\mu \Phi)^2 + U(\Phi^2) - c\sigma . \quad (5.41)$$

In this way the O(4) symmetry is also explicitly broken by the term  $-c\sigma$ , and the spontaneous symmetry-breaking pattern is not exact. As we discussed describing the PCAC relation, the pions then turn into massive pseudo-Goldstone mesons, acquiring a finite mass given by

$$M_\pi^2 = \left. \frac{\partial^2 (U(\Phi^2) - c\sigma)}{\partial \pi^2} \right|_{\langle \sigma \rangle = f_\pi} = \frac{c}{f_\pi} . \quad (5.42)$$

Furthermore, the expectation value  $\langle \sigma \rangle$  never truly vanishes and the O(4) symmetry is never restored, even though it can be considered approximately restored when  $\langle \sigma \rangle \ll f_\pi$ .

### 5.4.2 Finite temperature

In the case of finite temperature, we can use the standard Matsubara formalism introduced in textbooks, see, e.g., [179, 180, 181], and consider the model in the grand canonical ensemble at vanishing density. In this case the partition function is given by

$$Z(T) = \text{Tr} e^{-\beta \hat{H}} , \quad (5.43)$$

where Tr indicates the standard statistical-mechanical trace,  $\beta = 1/T$  and  $\hat{H}$  represents the Hamiltonian operator of the system. Via the standard procedure, one can express Eq. (5.43) in a path-integral formulation

$$Z(T) = \int_{\text{boundaries}} \mathcal{D}\bar{\Psi} \mathcal{D}\Psi \mathcal{D}\Phi e^{-S_E[\bar{\Psi}, \Psi, \Phi]} , \quad (5.44)$$

where the Euclidean action contains a standard 3-dimensional spatial integral and an integral over the compactified imaginary-time dimension  $x_0 \in [0, \beta)$ . In particular, for the QM model it reads

$$S_E[\bar{\Psi}, \Psi, \Phi; \mu] = \int_0^\beta dx^0 \int_{\mathbb{R}^3} d^3\mathbf{x} \left\{ \bar{\psi}(\gamma_\mu \partial^\mu + h(\sigma + i\gamma^5 \vec{\tau} \cdot \vec{\pi}))\psi + \frac{1}{2}(\partial_\mu \Phi)^2 + U(\Phi^2) \right\} . \quad (5.45)$$

In Eq. (5.44) we used the specification *boundaries* on the path integral. This indicates the boundary conditions in the imaginary-time dimension that the fields have to fulfill due to the presence of the trace in Eq. (5.43). In particular, the bosonic field has to be periodic,

$$\Phi(\beta, \mathbf{x}) = \Phi(0, \mathbf{x}) , \quad (5.46)$$

while, due to the anticommutation relations, the fermionic fields  $\bar{\Psi}$  and  $\Psi$  have to be anti-periodic,

$$\bar{\Psi}(\beta, \mathbf{x}) = -\bar{\Psi}(0, \mathbf{x}) , \quad (5.47)$$

$$\Psi(\beta, \mathbf{x}) = -\Psi(0, \mathbf{x}) . \quad (5.48)$$

The finite size of the imaginary temporal dimension and the periodicity reflects onto the Fourier expansion of the fields, where the  $p^0$  integral gets replaced by a discrete summation, the so-called *Matsubara sum*, over discrete frequencies  $\omega_n$ , the so-called *Matsubara frequencies*. In particular, for the bosonic field  $\Phi$  the Fourier expansion reads

$$\Phi(x_0, \mathbf{x}) = T \sum_{n=-\infty}^{\infty} \int_{\mathbb{R}^3} \frac{d^3 \mathbf{p}}{(2\pi)^3} e^{i(\omega_n x_0 + \mathbf{x} \cdot \mathbf{p})} \Phi(\omega_n, \mathbf{p}) , \quad (5.49)$$

where the bosonic Matsubara frequencies are given by

$$\omega_n = 2\pi n T \quad \text{Bosons} . \quad (5.50)$$

Analogously, for the fermionic fields  $\bar{\Psi}$  and  $\Psi$  one obtains

$$\bar{\Psi}(x_0, \mathbf{x}) = T \sum_{n=-\infty}^{\infty} \int_{\mathbb{R}^3} \frac{d^3 \mathbf{p}}{(2\pi)^3} e^{-i(\omega_n x_0 + \mathbf{x} \cdot \mathbf{p})} \bar{\Psi}(\omega_n, \mathbf{p}) , \quad (5.51)$$

$$\Psi(x_0, \mathbf{x}) = T \sum_{n=-\infty}^{\infty} \int_{\mathbb{R}^3} \frac{d^3 \mathbf{p}}{(2\pi)^3} e^{i(\omega_n x_0 + \mathbf{x} \cdot \mathbf{p})} \Psi(\omega_n, \mathbf{p}) \quad (5.52)$$

and the fermionic Matsubara frequencies are

$$\omega_n = (2n + 1)\pi T \quad \text{Fermions} . \quad (5.53)$$

This formalism, which is general and independent of the details of the QM model, will be used throughout this work whenever finite-temperature calculations have to be performed.

### 5.4.3 Finite quark-number density

We discussed in Chapter 2 that the baryon number represents a conserved Noether charge derived from the QCD Lagrangian's invariance under the  $U_V(1)$  symmetry. In this section we refer to the conserved charge as  $N$  indicating the quark number, and follow the standard convention that differs from Eq.(2.30) by a factor 3, namely

$$N = \int_{\mathbb{R}^3} d^3 x n(x) = \int_{\mathbb{R}^3} d^3 x \bar{\Psi}(x) \gamma_0 \Psi(x) , \quad (5.54)$$

where  $n(x)$  represents the quark-number density. If we then want to consider the system in presence of a finite quark-number density, we have to work in the grand canonical ensemble and we have to associate an energy cost per particle, the chemical potential, to the conserved charge. In this way the Hamilton operator of the system gets a shift given by the finite-density contribution

$$\hat{H} \rightarrow \hat{H} - \mu \hat{N} , \quad (5.55)$$

where  $\hat{N}$  represents the quantum operator associated to the conserved charge. In this way, the standard grand canonical partition function is given by

$$Z(T, \mu) = \text{Tr} e^{-\beta(\hat{H} - \mu \hat{N})} , \quad (5.56)$$

or in the path-integral formulation

$$Z(T, \mu) = \int \mathcal{D}\bar{\Psi} \mathcal{D}\Psi \mathcal{D}\Phi e^{-S_E[\bar{\Psi}, \Psi, \Phi]}, \quad (5.57)$$

where we neglected the sources for the fields and used the Euclidean action, which for the QM model then reads

$$S_E[\bar{\Psi}, \Psi, \Phi; T, \mu] = \int_0^\beta dx_0 \int_{\mathbb{R}^3} d^3x \left\{ \bar{\psi}(\gamma_\mu \partial^\mu + h(\sigma + i\gamma^5 \vec{\tau} \cdot \vec{\pi}) - \gamma_0 \mu) \psi + \frac{1}{2}(\partial_\mu \Phi)^2 + U(\Phi^2) \right\}. \quad (5.58)$$

Once again, the grand canonical formalism associated to the introduction of a finite density of a conserved charge is very general and can be applied to the study of systems which exhibit Noether symmetries and conserved charges, with the introduction of the associated chemical potentials.

## 5.5 Landau Mean-Field study

Before studying the full model with the inclusion of fluctuations, it can be very helpful to have a first grasp of what is expected to be the phase diagram of the QM model. This can easily be done by using the simple Landau theory of phase transitions [182].

We have to consider a theory which allows us to describe a system where a symmetry is spontaneously broken and where an order parameter can be identified. As we already stated, the order parameter has to vanish for temperatures bigger than some critical temperature  $T_c$  and be finite for temperatures lower than  $T_c$ . This approach, for example, can be used also to describe the Ising model, where the  $\mathbb{Z}_2$  symmetry is spontaneously broken by a finite magnetization. In the case we are studying, the order parameter is clearly the expectation value of the sigma field, which, when finite, gives rise to a finite value of the chiral condensate. If this happens then the  $O(4)$  symmetry of the model is spontaneously broken to an  $O(3)$  symmetry, as we discussed previously. So we can consider a potential that is  $O(4)$ -symmetric and whose parameters depend on the physical parameters of the original QM model, namely the temperature  $T$  and the chemical potential. We now distinguish the two cases, i.e., the chiral limit, where the  $O(4)$  symmetry is exact, and the finite current quark mass case, when the  $O(4)$  symmetry is explicitly broken.

### 5.5.1 Chiral limit

In the chiral limit, we consider an exactly  $O(4)$ -symmetric potential. To do so, the potential has to contain only terms that depend on the  $O(4)$  invariant of the theory  $\rho = (\pi^2 + \sigma^2)/2$

$$U(\rho) = 2m^2\rho + 2\lambda\rho^2 + \frac{8}{3}\gamma\rho^3. \quad (5.59)$$

As requested, if the minimum of the potential is located at  $\rho = 0$  then also the minimum is  $O(4)$ -invariant, otherwise a minimum at a finite value of  $\rho \neq 0$  would spontaneously break the  $O(4)$  symmetry down to  $O(3)$ . Without loss of generality, one can assume that the direction of the symmetry breaking is the  $\sigma$  one, and identify the pions as the Goldstone modes of the transition, with vanishing mass and expectation value. Thus one can just focus, as we already did in Eq.(4.12), on the expectation value  $\sigma = \sqrt{2\rho}$  and rewrite Eq.(5.59) as

$$U(\sigma) = m^2\sigma^2 + \frac{1}{2}\lambda\sigma^4 + \frac{1}{3}\gamma\sigma^6. \quad (5.60)$$

In general, one could also consider higher-order terms in the potential, but for our study is sufficient to stop at the sixth order. This approximation is justified as long as the order parameter can be considered to be small w.r.t. the scales of the theory. We now specify the dependence on the external parameters temperature  $T$  and chemical potential  $\mu$  of the various couplings in the potential. First of all, we assume  $\gamma$  to be independent of  $T$  and  $\mu$ , but to be positive and small compared to  $\lambda$ , in order to be sure to have a bounded-from-below potential regardless of the sign of the coupling  $\lambda$ . We also assume that  $m^2$  changes sign in the proximity of a critical temperature  $T_c(\mu)$ , which depends on the chemical potential, such that

$$m^2 \simeq m_0^2(T - T_c(\mu)) , \quad (5.61)$$

where  $m_0^2$  is a positive constant. We also assume that  $\lambda$  is a function of the chemical potential only, such that it decreases as  $\mu$  is increased, and also that  $\lambda(\mu = 0) > 0$ , implying a  $\bar{\mu}$  exists for which  $\lambda$  vanishes  $\lambda(\mu = \bar{\mu}) = 0$ . We now analyze the different regions in  $\mu$ .

1. For  $0 < \mu < \bar{\mu}$ , the quartic coupling is positive  $\lambda(\mu) > 0$  and sufficiently larger than  $\gamma$ ,  $\lambda(\mu) \gg \gamma$ , such that, in our hypothesis of a small order parameter, we can neglect the sixth-order term. So in the current case we are left with the potential

$$U(\sigma; T, \mu) = m_0^2(T - T_c)\sigma^2 + \frac{1}{2}\lambda(\mu)\sigma^4 . \quad (5.62)$$

We now want to obtain the position of the minimum of the potential  $\sigma_0$ :

$$\partial_\sigma U(\sigma; T, \mu) \Big|_{\sigma=\sigma_0} = 0 = 2m_0^2(T - T_c)\sigma + 2\lambda(\mu)\sigma^3 , \quad (5.63)$$

which gives the solutions

$$\sigma_0 = 0 , \quad \sigma_0 = \pm \sqrt{\frac{m_0^2}{\lambda(\mu)}(T_c - T)} . \quad (5.64)$$

For  $T > T_c$ , the only acceptable solution is  $\sigma_0 = 0$ , so in this case the minimum is invariant under the  $O(4)$  symmetry, and so is the system.

For  $T < T_c$ , the point  $\sigma_0 = 0$  is a local maximum, and the minimum of the potential is located at a finite value  $\sigma_0 \neq 0$ . In this case the  $O(4)$  symmetry is spontaneously broken down to  $O(3)$ . We point out that the presence of two opposite solutions is consistent with the  $\mathbb{Z}_2$  symmetry, which is part of the larger  $O(3)$  symmetry not broken by the finite minima.

We can notice that  $\sigma_0$  goes continuously to 0 as  $T$  approaches  $T_c$ , thus we can conclude that the system undergoes a second-order phase transition at this point. We can also extract the value of the critical exponent  $\beta$ , since

$$\sigma_0 \sim (T_c - T)^{1/2} \quad \text{for} \quad T \leq T_c . \quad (5.65)$$

Recalling the behavior of the order parameter described in Eq.(4.35), we can rewrite it for the finite-temperature case:

$$\sigma_0 = \begin{cases} 0 & T \geq T_c \\ \sim (T_c - T)^\beta & T \leq T_c \end{cases} . \quad (5.66)$$

Thus, we can conclude that  $\beta = 1/2$ , as expected from a mean-field calculation [182].

2. For  $\mu > \bar{\mu}$  the quartic coupling is negative,  $\lambda(\mu) < 0$ , thus, for the previously highlighted stability reasons, we cannot neglect the sixth-order term. So in the current case we consider the full potential in Eq. (5.60), specifying the  $T$  and  $\mu$  dependence of the parameters

$$U(\sigma; T, \mu) = m_0^2(T - T_c)\sigma^2 + \frac{1}{2}\lambda(\mu)\sigma^4 + \frac{1}{3}\gamma\sigma^6. \quad (5.67)$$

We proceed, as in the previous case, looking for the extrema of the potential:

$$\partial_\sigma U(\sigma; T, \mu) \Big|_{\sigma=\sigma_0} = 0 = 2m_0^2(T - T_c)\sigma + 2\lambda(\mu)\sigma^3 + 2\gamma\sigma^5. \quad (5.68)$$

Solving for  $\sigma_0^2$  one obtains

$$\sigma_{0;1}^2 = 0, \quad \sigma_{0;2}^2 = \frac{-\lambda(\mu)}{2\gamma} \left[ 1 + \sqrt{1 + 4\frac{\gamma m_0^2}{\lambda^2(\mu)}(T_c - T)} \right]. \quad (5.69)$$

However, we have to take into account that  $\sigma_{0;1}^2$  and  $\sigma_{0;2}^2$  correspond to local extremes of the potential, and our goal is to find the global minimum of the potential. To do so we need a more accurate analysis of the behavior of the potential as the temperature is changed.

For  $T < T_c$ ,  $\sigma_{0;1}^2$  is a local maximum, since  $\partial_{\sigma_0^2}^2 U(\sigma_{0;1}) = m_0^2(T - T_c) < 0$ , while  $\sigma_{0;2}^2$  is the global minimum. It is important to point out that in this case  $U(\sigma_{0;2}) < 0$ .

For  $T \gg T_c$ ,  $\sigma_{0;2}^2$  is not available, and  $\sigma_{0;1}^2$  is the only local and global minimum of the potential.

For  $T$  slightly bigger than  $T_c$ ,  $\sigma_{0;1}^2$  is still a local minimum, but also  $\sigma_{0;2}^2$  is a local minimum and we have a competition between the two minima. Since  $U(\sigma_{0;2}^2) < 0$  and  $U(\sigma_{0;1}^2) = 0$ ,  $\sigma_{0;2}^2$  is the global minimum of the potential.

Gradually increasing  $T$  above  $T_c$ ,  $U(\sigma_{0;2}^2)$  increases, up to the temperature  $T^*$  when  $U(\sigma_{0;2}^2) = 0$ . In this case we have a degeneracy of the minima, and further increasing  $T$  above  $T^*$  implies that the global minimum abruptly changes from  $\sigma_{0;2}^2$  to  $\sigma_{0;1}^2$ . This means that the system undergoes a sharp first-order phase transition at  $T = T^* > T_c$ . One can also determine  $T^*$  and the discontinuity of the order parameter at  $T^*$ , i.e.,  $\sigma_{0;2}^2(T = T^*)$ , by imposing that  $\sigma_{0;2}^2$  fulfills the minimization condition Eq. (5.68) and that  $U(\sigma_{0;2}^2(T = T^*)) = 0$ . One thus obtains

$$\sigma_{0;2}^2(T = T^*) = -\frac{3\lambda}{4\gamma} \quad (5.70)$$

and

$$T^* = T_c + \frac{3\lambda^2}{16\gamma}. \quad (5.71)$$

3. For  $\mu \rightarrow \bar{\mu}$ , the coupling  $\lambda(\mu) \rightarrow 0$ ,  $T^* \rightarrow T_c$  and the discontinuity in the order parameter in Eq. (5.70) becomes progressively smaller, implying that the first-order phase transition becomes weaker and weaker. When  $\mu = \bar{\mu}$  is reached,  $\lambda$  vanishes,  $\lambda(\mu = \bar{\mu}) = 0$ , and the phase transition turns into a smooth second-order one. Setting  $\lambda(\mu) = 0$  in Eq. (5.69), we can also deduce the behavior of  $\sigma_{0;2}^2$  as  $T$  approaches  $T_c$ :

$$\sigma_{0;2}^2 = \sqrt{\frac{m_0^2}{\gamma}(T_c - T)} \sim (T_c - T)^{\frac{1}{2}}. \quad (5.72)$$

This implies that, in this case,  $\beta = 1/4$ .



Summarizing what we obtained so far, the MF Landau model exhibits a line of second-order phase transitions for  $\mu < \bar{\mu}$ , a line of first-order transitions for  $\mu > \bar{\mu}$ , and the two lines merge into a single tricritical point for  $\mu = \bar{\mu}$  and  $T = T_c(\mu = \bar{\mu})$ , where the transition is of second order.

### 5.5.2 Finite quark mass

We now consider the case in which quark are massive fields. To mimic the presence of a finite current-quark mass in our model, we add to the potential Eq. (5.60) an external source term for the sigma field:

$$U(\sigma) = m^2\sigma^2 + \frac{1}{2}\lambda\sigma^4 + \frac{1}{3}\gamma\sigma^6 - c\sigma, \quad (5.73)$$

where  $c$  is an external,  $T$ ,  $\mu$  and  $\sigma$  independent source field. This is analogous to what happens to the Ising model in presence of an external magnetic field, which couples linearly with the magnetization. In this way the  $O(4)$  symmetry is also explicitly broken due to the introduction of the non-invariant term  $-c\sigma$ , as in full QCD a finite quark mass explicitly breaks chiral symmetry. We now consider the different cases separately, as we did in the chiral limit.

1. As previously, the case  $0 < \mu < \bar{\mu}$  corresponds to  $\lambda(\mu) > 0$  and sufficiently larger than  $\gamma$ ,  $\lambda(\mu) \gg \gamma$  so that once again we can neglect the sixth-order term. The potential then reads

$$U(\sigma; T, \mu) = m_0^2(T - T_c)\sigma^2 + \frac{1}{2}\lambda(\mu)\sigma^4 - c\sigma. \quad (5.74)$$

The minimization condition then results in

$$\partial_\sigma U(\sigma; T, \mu) = 0 = 2m_0^2(T - T_c)\sigma + 2\lambda(\mu)\sigma^3 - c. \quad (5.75)$$

We can then conclude that in this case the solution  $\sigma_0 = 0$  is not present anymore, implying that the minimization always lead to a finite minimum. Indeed, at  $T = T_c$  the minimum does not vanish and we have

$$\sigma_0(T = T_c) = \left(\frac{c}{2\lambda(\mu)}\right)^{1/3}. \quad (5.76)$$

From this expression one can also extract the critical exponent  $\delta$ , which is the one describing the behavior of the order parameter at the critical temperature as a function of the applied external field

$$\sigma_0(T = T_c) \sim c^{1/\delta}. \quad (5.77)$$

We can thus conclude that  $\delta = 3$ . The minimum smoothly decreases when  $T$  is increased but never reaches  $\sigma = 0$  unless  $c = 0$ . This destroys the second-order phase transition since no spontaneous symmetry breaking occurs at any temperature. So the second-order phase transition line is replaced by a smooth crossover.

2. The case  $\mu = \bar{\mu}$  and  $\lambda(\bar{\mu}) = 0$  actually does not correspond to the critical point but still to a crossover. As we will soon see, this is valid also for a small chemical potential interval  $\bar{\mu} < \mu < \mu^*$  up to the value  $\mu^*$  for which  $\lambda(\mu^*) < 0$ . In the  $\mu = \bar{\mu}$  case the potential reads

$$U(\sigma; T, \mu) = m_0^2(T - T_c)\sigma^2 + \frac{1}{3}\gamma\sigma^6 - c\sigma. \quad (5.78)$$



Once again, we look for the minimum of the potential:

$$\partial_\sigma U(\sigma; T, \mu) \Big|_{\sigma=\sigma_0} = 0 = 2m_0^2(T - T_c)\sigma + 2\gamma\sigma^5 - c. \quad (5.79)$$

The same considerations we did for the previous case still hold and we can easily determine the critical exponent  $\delta$ :

$$\sigma_0(T = T_c) = \left(\frac{c}{2\gamma}\right)^{1/5}, \quad (5.80)$$

concluding that  $\delta = 5$ .

3. For  $\mu > \mu^*$ ,  $\lambda(\mu) < 0$  and we keep the sixth-order term. So the potential reads

$$U(\sigma; T, \mu) = m_0^2(T - T_c)\sigma^2 + \frac{1}{2}\lambda(\mu)\sigma^4 + \frac{1}{3}\gamma\sigma^6 - c\sigma. \quad (5.81)$$

Imposing the minimization condition results in:

$$\partial_\sigma U(\sigma; T, \mu) \Big|_{\sigma=\sigma_0} = 0 = 2m_0^2(T - T_c)\sigma + 2\lambda(\mu)\sigma^3 + 2\gamma\sigma^5 - c. \quad (5.82)$$

Also in this case the solution  $\sigma_0 = 0$  is not available and a finite minimum is always present. The first-order phase transition still happens, but the minimum jumps from a larger value to a smaller but still finite one.

4. The first- and second-order lines meet once again in one point, the critical endpoint, located at  $(T^*(\mu = \mu^*), \mu^*)$  for which  $\lambda(\mu^*) < 0$ . The nature of this point can be understood considering the derivatives of the potential and the extreme-point location. We have seen that, in order to have a first-order phase transition, we need at least three extreme points, which in the chiral case were symmetric w.r.t.  $\sigma = 0$ . When  $c \neq 0$ , three extreme points are still present but the symmetry is broken and none of them is located at the origin. The existence of three extreme points implies by definition that, using the same potential as in Eq. (5.81),  $\partial_\sigma U(\sigma; T, \mu) \Big|_{\sigma=\sigma_0} = 0$  for three separate values of  $\sigma_0$ , which we call  $\sigma_{0;i}$  with  $i = 1, 2, 3$ . From this it follows that there exist two intermediate points, between those values of  $\sigma_{0;i}$ , which we call  $\sigma_{1;j}$ , with  $j = 1, 2$ , for which the second derivative vanishes  $\partial_{\sigma^2}^2 U(\sigma; T, \mu) \Big|_{\sigma=\sigma_{1;j}} = 0$ . This in turn implies the existence of a single point  $\sigma_2$ , which is located in between  $\sigma_{1;1}$  and  $\sigma_{1;2}$ , for which also the third derivative of the potential vanishes. As we have seen in the chiral limit, we can identify the critical point as the one in which the three different extreme points coincide at the critical temperature. In the current case this means that  $\sigma_{0;1} \equiv \sigma_{0;2} \equiv \sigma_{0;3}$ . Consequently, also the points  $\sigma_{1;1}$ ,  $\sigma_{1;2}$  and  $\sigma_2$  come to coincide with the three degenerate extreme points in a single point, that we call  $\sigma^*$ , namely  $\sigma_{0;1} \equiv \sigma_{0;2} \equiv \sigma_{0;3} \equiv \sigma_{1;1} \equiv \sigma_{1;2} \equiv \sigma_2 \equiv \sigma^*$ . This implies that

$$\partial_\sigma U(\sigma; T^*(\mu^*), \mu^*) \Big|_{\sigma=\sigma^*} = \partial_{\sigma^2}^2 U(\sigma; T^*(\mu^*), \mu^*) \Big|_{\sigma=\sigma^*} = \partial_{\sigma^3}^3 U(\sigma; T^*(\mu^*), \mu^*) \Big|_{\sigma=\sigma^*} = 0. \quad (5.83)$$

Therefore, the endpoint corresponds to a second-order phase transition. Imposing the conditions Eq. (5.83), one can easily determine  $\sigma^*$

$$\sigma^* = \sqrt{-\frac{\lambda(\mu^*)}{10\gamma}}, \quad (5.84)$$

from which we see that this point can only be found in the  $\lambda(\mu^*) < 0$  case. One can also calculate the value of  $\lambda(\mu^*)$

$$\lambda(\mu^*) = -5 \left( \frac{\gamma^3 c^2}{216} \right)^{1/5}. \quad (5.85)$$

Consistently with the chiral limit discussion, if  $c \rightarrow 0$  then  $\lambda(\mu^*) = 0$  and  $\sigma^* = 0$ . One can also check that, considering small deviations from the minimum  $\sigma^*$ , like  $\sigma^* + \delta\sigma$ , the critical exponent  $\beta$  is given by  $\beta = 1/2$ .

To recapitulate the behavior of the Landau MF model in the case of an explicit symmetry-breaking term, we find a crossover line in the  $0 < \mu < \mu^*$  interval, a first-order line for  $\mu > \mu^*$ , and the two lines meet in a critical endpoint  $(T^*(\mu = \mu^*), \mu^*)$ , where the transition is of second order.

This concludes the purely bosonic Landau MF analysis. We will shortly find that these results are qualitatively in agreement with the ones obtained considering also fermions in the model, and successively, with the ones obtained including bosonic fluctuations via the FRG.

## 5.6 Beyond mean field: FRG approach

In this and the following section, we extend the discussion on the properties of the QM model going beyond the mean-field approximation, including fluctuations. In particular we choose to use the FRG approach as a tool for the analysis of the effects of fluctuations on several properties of the model such as the phase diagram, the critical exponents, and the value of the condensate. A discussion of the thermodynamic properties of the model, with a comparison between MF and FRG calculation is presented in Chapter 6.

### 5.6.1 Flow equation

As we already stated, the central object of the FRG approach is the FRG flow equation Eq. (3.13). In particular, for a system which contains both fermionic ( $\bar{\Psi}, \Psi$ ) and bosonic ( $\Phi$ ) degrees of freedom, we have two separate loops that contribute to the flow equation:

$$\begin{aligned} \partial_t \Gamma_t[\Psi, \bar{\Psi}, \Phi] = & \frac{1}{2} \text{Tr} \left[ (\partial_t R_t^B) (\Gamma_{t, \Phi\Phi}^{(2)}[\Psi, \bar{\Psi}, \Phi] + R_t^B)^{-1} \right] \\ & - \text{Tr} \left[ (\partial_t R_t^F) (\Gamma_{t, \bar{\Psi}\Psi}^{(2)}[\Psi, \bar{\Psi}, \Phi] + R_t^F)^{-1} \right], \end{aligned} \quad (5.86)$$

where  $R_t^B$  and  $R_t^F$  represent the bosonic and the fermionic regulator, respectively. In the particular case of the QM model, we will soon observe that the contributions arising from the various bosonic modes, namely the pions and the sigma, can be disentangled due to diagonal structure of the bosonic two-point function in field space. This means that, once the trace is taken, the bosonic loop in the field  $\Phi = (\vec{\pi}, \sigma)$  in Eq. (5.86) further splits in the contribution of the pions (with multiplicity 3) and the sigma.

The next fundamental ingredient for the FRG machinery is the choice of the ansatz for the effective average action. In particular we adopt the LPA ansatz

$$\begin{aligned} \Gamma_t[\bar{\Psi}, \Psi, \phi] = & \int_0^{1/T} dx_0 \int d^3x \left\{ \bar{\psi}(\gamma_\mu \partial^\mu + h(\sigma + i\gamma^5 \vec{\tau} \cdot \vec{\pi}) - \mu\gamma_0)\psi \right. \\ & \left. + \frac{1}{2}(\partial_\mu \sigma)^2 + \frac{1}{2}(\partial_\mu \vec{\pi})^2 + U_t(\sigma^2 + \vec{\pi}^2) - c\sigma \right\}, \end{aligned} \quad (5.87)$$

which is similar to the action Eq. (5.58), but in this case the bosonic potential is scale-dependent. This truncation is relatively simple, since, for example, no running of the wave-function renormalization factor or of the Yukawa coupling is taken into account, but yet it still allows for a good qualitative insight into the model due to the fact that it captures every possible bosonic self-coupling that can be generated during the flow.

We will now proceed to illustrate the shape of the various contributions to the flow equation. In particular, for the moment we do not need to specify the regulator shape function, since most of the considerations can be performed without it.

### 5.6.2 Bosonic contribution to the flow equation

The final ingredient we need before performing the actual calculations is the regulator function. In this subsection we just state the result and leave the full calculations to App. D. In particular, we use a generic shape for the 3D regulator, which is diagonal in momentum and field space

$$R_t^B(\mathbf{q}, \mathbf{p}) = (2\pi)^3 \delta^{(3)}(\mathbf{q} + \mathbf{p}) \mathbf{p}^2 r_t^B(\mathbf{p}), \quad (5.88)$$

where  $r_t^B(\mathbf{p})$  represents the generic regulator shape function.

Plugging Eq. (5.88) into the first term on the r.h.s. of Eq. (5.86), we get the bosonic contribution to the flow equation in the LPA

$$\begin{aligned} \frac{1}{2} \text{Tr} \left[ (\partial_t R_t^B) (\Gamma_{t, \Phi\Phi}^{(2)}[\Psi, \bar{\Psi}, \Phi] + R_t^B)^{-1} \right] = & \frac{1}{8\pi^2} \int_0^\infty dq q^4 \partial_t r_t^B(q) \\ & \times \left\{ \frac{3}{E_{k,\pi}(q)} \coth\left(\frac{E_{k,\pi}(q)}{2T}\right) + \frac{1}{E_{k,\sigma}(q)} \coth\left(\frac{E_{k,\sigma}(q)}{2T}\right) \right\}, \end{aligned} \quad (5.89)$$

where  $q = |\mathbf{q}|$  and we have introduced the energies for the pions and the sigma modes as

$$E_{k,\pi}(q) = \sqrt{q^2 \left(1 + r_t^B(q)\right) + \frac{\partial_\sigma U_t(\sigma)}{\sigma}} \quad (5.90)$$

and

$$E_{k,\sigma}(q) = \sqrt{q^2 \left(1 + r_t^B(q)\right) + \partial_{\sigma\sigma}^2 U_t(\sigma)}. \quad (5.91)$$

We can then define the effective masses of the two particle species:

$$M_\pi^2(\sigma) = \frac{\partial_\sigma U_t(\sigma)}{\sigma}, \quad M_\sigma^2(\sigma) = \partial_{\sigma\sigma}^2 U_t(\sigma). \quad (5.92)$$

We can notice that, coherently with the discussion we made on the role of the pions as (pseudo) Goldstone bosons associated to the SSB of the  $O(4)$  symmetry, the mass of the pion mode vanishes when evaluated at the physical point, i.e., at the minimum of the effective potential (since the explicit symmetry breaking term is linear in the sigma field, it does not contribute to the flow equation and it is just added to the IR potential).

### 5.6.3 Fermionic contribution to the flow equation

We now introduce the fermionic loop contribution to the flow equation. Following the choice we made for the bosonic case, we do not specify the regulator and simply state a generic momentum-diagonal shape:

$$R_t^F(\mathbf{p}, \mathbf{q}) = i (2\pi)^3 \delta^{(3)}(\mathbf{q} + \mathbf{p}) \mathbf{p} r_t^F(x), \quad (5.93)$$

where we defined the variable

$$x = |\mathbf{p}|/k. \quad (5.94)$$

In Chapter 7, we will also investigate a different class of regulators which does not belong to the one indicated in Eq. (5.93), and in particular it will depend explicitly on the chemical potential.

Inserting Eq. (5.93) into the second term on the r.h.s. of Eq. (5.86), performing the inversion of the full fermionic two-point function and taking the trace one obtains

$$\begin{aligned} -\text{Tr} \left[ (\partial_t R_t^F) (\Gamma_{t, \Psi \Psi}^{(2)}[\Psi, \bar{\Psi}, \Phi] + R_t^F)^{-1} \right] &= -\frac{N_c}{4\pi^2} \int_0^\infty dp p^4 (1 + r_t^F(x)) \partial_t r_t^F(x) \times \\ &\frac{1}{E_{k, \Psi}(p)} \left[ 1 - n_F \left( \frac{E_{k, \Psi}(p) + \mu}{T} \right) - n_F \left( \frac{E_{k, \Psi}(p) - \mu}{T} \right) \right], \end{aligned} \quad (5.95)$$

where  $N_c$  is the number of color d.o.f., that for the moment we leave indicated as a parameter. We also used  $p = |\mathbf{p}|$  and we introduced the Fermi-Dirac distribution

$$n_F(x) = \frac{1}{e^x + 1} \quad (5.96)$$

and the energy of the fermions

$$E_{k, \Psi}(p) = \sqrt{p^2 (1 + r_t^F(x))^2 + (h\sigma)^2}. \quad (5.97)$$

We can then correctly emphasize that, as anticipated, thanks to the Yukawa coupling, the fermions obtain a dynamically generated mass

$$M = h\langle\sigma\rangle, \quad (5.98)$$

where  $\langle\sigma\rangle$  indicates the chiral condensate.

### 5.6.4 Full flow equation and hydrodynamic formulation

Summing up the two contributions Eq. (5.89) and Eq. (5.95) from the bosonic and the fermionic loop, respectively, we obtain the full flow equation for the QM model in the

LPA truncation:

$$\begin{aligned} \partial_t U_t(\sigma) = & \frac{1}{8\pi^2} \int_0^\infty d q q^4 \left\{ \partial_t r_t^B(q) \left[ \frac{3}{E_{k,\pi}(q)} \coth\left(\frac{E_{k,\pi}(q)}{2T}\right) + \frac{1}{E_{k,\sigma}(q)} \coth\left(\frac{E_{k,\sigma}(q)}{2T}\right) \right] \right. \\ & \left. - 2 N_c \left(1 + r_t^F(x)\right) \partial_t r_t^F(x) \frac{1}{E_{k,\Psi}(q)} \left[ 1 - n_F\left(\frac{E_{k,\Psi}(q) + \mu}{T}\right) - n_F\left(\frac{E_{k,\Psi}(q) - \mu}{T}\right) \right] \right\}. \end{aligned} \quad (5.99)$$

Following the steps in Sec. 4.2.2, we notice that Eq. (5.99) does not depend explicitly on the effective potential  $U_t(\sigma)$  but only on its first and second derivatives w.r.t. the  $\sigma$  field. So it comes natural to introduce the new variables

$$u_t(\sigma) = \partial_\sigma U_t(\sigma) \quad (5.100)$$

and

$$u_t'(\sigma) = \partial_\sigma u_t(\sigma) = \partial_{\sigma\sigma}^2 U_t(\sigma) \quad (5.101)$$

and express the flow equation Eq. (5.99) in terms of these variables. To do so, as we proceeded in Sec. 4.2.2, we now take the derivative w.r.t.  $\sigma$  of Eq. (5.99) and so we obtain

$$\partial_t u_t(\sigma) + \partial_\sigma f(t, \sigma, u_t(\sigma)) = \partial_\sigma g(t, u_t'(\sigma)) + N_c \partial_\sigma S(t, \sigma), \quad (5.102)$$

which can be classified once again as a non-linear advection-diffusion equation with a source term induced by the fermions.

As we stressed in Sec. 4.2.2, in this framework the derivative of the potential  $u(t, \sigma)$  plays the role of a conserved quantity, in the sense that it satisfies a generalized conservation law [32, 80, 168] with a source term. As we are about to see, each of the contributions that appear in Eq. (5.102) arises from the various particle species involved in the model.

More in detail, the advection flux is given by

$$f(t, \sigma, u) = -\frac{1}{8\pi^2} \int_0^\infty d q q^4 \partial_t r_t^B(q) \frac{3}{E_{k,\pi}(q)} \coth\left(\frac{E_{k,\pi}(q)}{2T}\right) \quad (5.103)$$

and it is responsible of the bulk motion of the conserved quantity  $u_t(\sigma)$ . This contribution originates from the pions, and this is confirmed by the factor 3 that appears in Eq. (5.103), signaling the multiplicity of this term. Furthermore, as we already pointed out when defining the pion energy  $E_{k,\pi}$  in Eq. (5.90), the mass term for the pions,  $u_t(\sigma)/\sigma$ , vanishes at the minimum of the effective potential, in agreement with the nature of the pions as Goldstone bosons. One can verify that the speed of characteristics is given by

$$\frac{\partial f(t, \sigma, u)}{\partial u} = \frac{1}{32 \pi^2 T \sigma} \int_0^\infty d q q^4 \partial_t r_t^B(q) \frac{3}{E_{k,\pi}(q)^3} \operatorname{csch}\left(\frac{E_{k,\pi}(q)}{2T}\right) \left[ E_{k,\pi}(q) + T \sinh\left(\frac{E_{k,\pi}(q)}{2T}\right) \right] \quad (5.104)$$

and it is positive if  $\sigma < 0$  and negative if  $\sigma > 0$  (since  $\partial_t r_t^B(q) < 0$  and the other functions are positive if their argument is positive), implying that the conserved quantity  $u_t(\sigma)$  and the minimum of the potential is always transported towards smaller values of  $|\sigma|$  by the

advection. This is analogous to the results obtained within the  $O(N)$ -model framework and is due to the similarity of the two models in the bosonic sector.

On the other hand, the radial sigma mode produces the diffusion term,

$$g(t, u') = \frac{1}{8\pi^2} \int_0^\infty dq q^4 \partial_t r_t^B(q) \frac{1}{E_{k,\sigma}(q)} \coth \frac{E_{k,\sigma}(q)}{2T}, \quad (5.105)$$

which depends on the curvature mass  $u'_t(\sigma)$ . The diffusion has no specific direction since it depends on the local gradients of the conserved quantity, meaning that it smears out peaks and discontinuities. Once again, this is totally analogous to the  $O(N)$ -model case, thus one can refer to Sec. 4.2.2 for a more detailed discussion of the bosonic sector.

The real aspect of novelty is given by the fermionic loop, which gives rise to a time- and  $\sigma$ -dependent source term,

$$S(t, \sigma) = - \frac{N_c}{4\pi^2} \int_0^\infty dp p^4 \left(1 + r_t^F(x)\right) \partial_t r_t^F(x) \times \\ \frac{1}{E_{k,\Psi}(p)} \left[ 1 - n_F \left( \frac{E_{k,\Psi}(p) + \mu}{T} \right) - n_F \left( \frac{E_{k,\Psi}(p) - \mu}{T} \right) \right], \quad (5.106)$$

which we identify as such since it is independent of the conserved quantity  $u_t(\sigma)$ . According to this observation, the fermionic contribution turns out to be completely independent of the effective potential and of its time evolution, so it receives no feedback from the bosonic sector. This observation will turn out very useful in the next subsection, since it suggests that there should exist a limit in which the fermionic loop can be decoupled and isolated.

If one considers the case of vanishing chemical potential,  $\mu = 0$ , and performs the  $\sigma$  derivative of Eq. (5.106), as indicated in Eq. (5.102), one finds a source-like, positive contribution to the flow equation for  $\sigma < 0$  and a sink-like negative contribution for  $\sigma > 0$ . This is not trivially true at finite values of the chemical potential, and also some high peaks and shocks in field space may develop, especially in the low-temperature case [183].

### 5.6.5 Large- $N_c$ limit: MF reduction

In the previous section, we pointed out that the source term is independent, by definition, of the variable  $u_t(\sigma)$ . This implies that, if a certain limit is taken such that the source term is the only one left to contribute to the flow equation Eq. (5.99), then it would lose the property of being a PDE to become a much simpler ordinary differential equation (ODE). This can be achieved, for example, in the mean-field (MF) approximation, which corresponds to the limit  $N_c \rightarrow \infty$ . In order to correctly perform such a limit, we need to introduce the following rescaling of the field and of the effective potential:

$$\sigma \rightarrow \sqrt{N_c} \sigma, \quad U_t(\sigma) \rightarrow N_c U_t(\sigma), \quad u_t(\sigma) \rightarrow \sqrt{N_c} u_t(\sigma). \quad (5.107)$$

In this way, we get the rescaled flow equation

$$\partial_t u_t(\sigma) + \frac{1}{\sqrt{N_c}} \partial_{u_t} f(t, \sigma, u_t(\sigma)) u'_t(\sigma) = \frac{1}{\sqrt{N_c}} \partial_\sigma g(t, u'_t(\sigma)) + \partial_\sigma S(t, \sigma). \quad (5.108)$$

The mean-field flow equation is then obtained in the  $N_c \rightarrow \infty$  limit, that is

$$\partial_t u_t(\sigma) = \partial_\sigma S(t, \sigma). \quad (5.109)$$

So we are left with just the fermionic source contribution. This type of equation will be our starting point for any further investigation of the MF behavior of the QM model.

## 5.7 Comparison of the results in MF and in FRG

In this section, we compare the results obtained in the MF with the ones derived from FRG calculations. In particular, as anticipated, we will highlight the impact of the fluctuations on the various observables that play a crucial role in the model, such as the chiral condensate (and thus the dynamically generated quark mass) or the critical exponents. In particular we will show the results obtained using the simple Litim regulator [124, 85] for both the fermionic and bosonic contributions to the flow equation. We will then dedicate a wider discussion of the effects of taking into account different regulator shape functions, on the model phase diagram, to Chapter 7.

### 5.7.1 Litim FRG setup

As we stated, we now specify our calculation considering both the fermionic and the bosonic 3D Litim regulator shape functions

$$r_t^B(\mathbf{p}) = \left( \frac{k^2}{\mathbf{p}^2} - 1 \right) \Theta(k^2 - \mathbf{p}^2), \quad (5.110)$$

$$r_t^F(\mathbf{p}) = \left( \sqrt{\frac{k^2}{\mathbf{p}^2}} - 1 \right) \Theta(k^2 - \mathbf{p}^2). \quad (5.111)$$

One of the main advantages of the Litim regulator lies in its simplicity, since it allows to perform the momentum integral analytically, significantly shortening the calculation time for the numerical solution of the flow PDE. Furthermore, as we already pointed out in Chapter 4, the Litim regulator is an optimal choice in the LPA truncation (see [148]).

Using then the Litim regulator, the flow equation still keeps the shape of the advection-diffusion equation with a source term Eq. (5.102), where the advection and diffusion fluxes are given by

$$f(k, \sigma, u_t(\sigma)) = \frac{k^5}{4\pi^2} \frac{1}{E_{k,\pi}} \coth\left(\frac{E_{k,\pi}}{2T}\right) \quad (5.112)$$

and

$$g(k, u'_t(\sigma)) = -\frac{k^5}{12\pi^2} \frac{1}{E_{k,\sigma}} \coth\left(\frac{E_{k,\sigma}}{2T}\right), \quad (5.113)$$

respectively, and the source term is

$$N_c S_k(\sigma) = \frac{N_c k^5}{3\pi^2} \frac{1}{E_{k,\Psi}} \left[ \tanh\left(\frac{E_{k,\Psi} - \mu}{2T}\right) + \tanh\left(\frac{E_{k,\Psi} + \mu}{2T}\right) \right]. \quad (5.114)$$

In particular, we defined the energies of the sigma and the pion modes as

$$E_{k,\sigma} = \sqrt{k^2 + M_\sigma^2}, \quad E_{k,\pi} = \sqrt{k^2 + M_\pi^2}. \quad (5.115)$$

with

$$M_\sigma^2 = \partial_\sigma^2 U_k(\sigma), \quad M_\pi^2 = \frac{\partial_\sigma U_k(\sigma)}{\sigma}. \quad (5.116)$$

Moreover, the energy of the fermions is given by

$$E_{k,\Psi} = \sqrt{k^2 + M^2}, \quad (5.117)$$



	$c$ (GeV <sup>3</sup> )	$m_{UV}^2$ (GeV <sup>2</sup> )	$\lambda_{UV}$	$f_\pi$ (GeV)	$M$ (GeV)
MF <sub><math>\chi</math></sub>	0	0.851	2.55	0.088	0.3168
MF	$1.78 \times 10^{-3}$	0.812	3.08	0.093	0.3348
FRG <sub><math>\chi</math></sub>	0	0.919	1.08	0.088	0.3168
FRG	$1.78 \times 10^{-3}$	0.762	1.05	0.093	0.3348

Table 5.1: Parameters of the QM model for MF in the chiral limit (MF <sub>$\chi$</sub> ), MF with explicit symmetry breaking (MF), FRG in the chiral limit (FRG <sub>$\chi$</sub> ) and FRG with explicit symmetry breaking (FRG).

with  $M = h\langle\sigma\rangle$  denoting the constituent quark mass, previously defined in Eq.(5.98).

Once again, the MF reduction is obtained formally in the large- $N_c$  limit and, from a practical point of view, just dropping the bosonic contributions to the flow equation and considering only the fermionic source term rescaled by a factor  $N_c$ . For the full LPA calculations, the number of colors is fixed,  $N_c = 3$ .

### 5.7.2 Initial condition and model parameters

Once the MF and FRG frameworks have been discussed, we have to choose the initial condition for the FRG flow equation. In particular we need to fix the shape of the bare potential in the UV ( $k = \Lambda$  or  $t = 0$ ). To this end, we choose a quartic potential

$$U_\Lambda(\sigma) = \frac{m_{UV}^2}{2}\sigma^2 + \frac{\lambda_{UV}}{4}\sigma^4. \quad (5.118)$$

The choice of the initial condition and of the parameters which appear in it is a very delicate issue and we will discuss it in much more detail in Chapter 7. We will also add further corrections to it in Chapter 6 in order to have thermodynamically correct results at high temperatures. For the purpose of this section, it is sufficient to consider Eq.(5.118) and tune the parameters to a couple of values of  $m_{UV}^2$  and  $\lambda_{UV}$  such that vacuum observables match with the experimentally known ones. In particular, we want the Goldberger-Treiman relation Eq.(5.11), i.e.,  $M = hf_\pi$  to be fulfilled, and also require that  $\langle\sigma\rangle = f_\pi$  and  $\partial_{\sigma\sigma}^2 U(\langle\sigma\rangle) = M_\sigma^2 = 0.36 \text{ GeV}^2$  in the vacuum. For all the calculations we also fixed the UV-cutoff  $\Lambda = 1 \text{ GeV}$  and the Yukawa coupling  $h = 3.6$ . The other model parameters are indicated in Tab.5.1 for the different cases of MF and FRG, both in the chiral limit (which we indicate with MF <sub>$\chi$</sub>  and FRG <sub>$\chi$</sub> ) and in the explicit chiral symmetry-breaking case (which we simply indicate as MF and FRG).

### 5.7.3 MF vs FRG phase diagram

We already pointed out the expected structure of the phase diagram in the MF case, both in the chiral limit and in the case of explicit symmetry breaking. This is confirmed

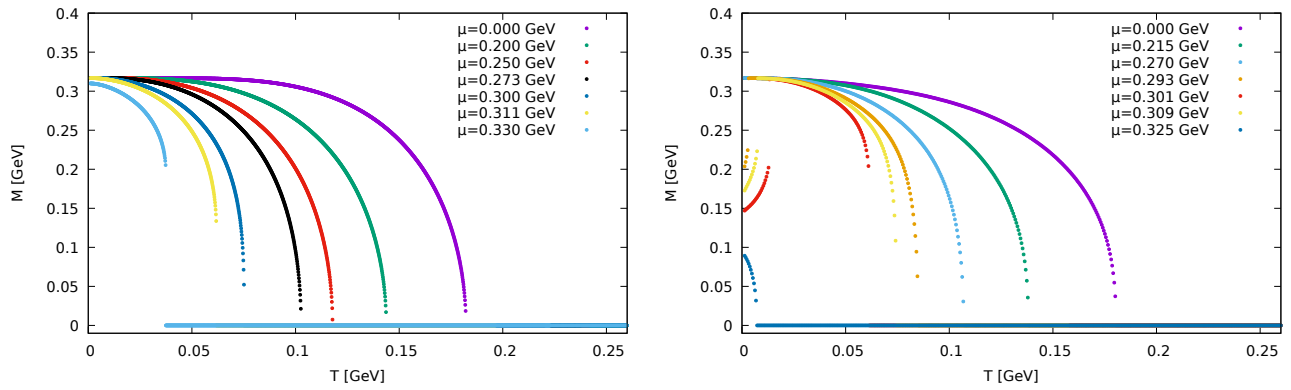


Figure 5.2: Dynamically generated quark mass  $M = h\langle\sigma\rangle$  in the chiral limit as a function of the temperature  $T$  for various values of the chemical potential, both in the MF case (left panel) and with the inclusion of fluctuations via FRG (right panel).

by the phase diagram obtained within our fermionic-loop MF approach. First of all, if we consider the chiral limit, we can refer to the left panel of Fig. 5.6, where the phase diagram of the QM model in the chiral limit and in the MF case is shown. We also consider the left panels of Fig. 5.2 and Fig. 5.8, in which we present the behavior of the dynamically generated quark mass  $M = h\langle\sigma\rangle$  as a function of the temperature  $T$  for different values of the chemical potential and as a function of the chemical potential  $\mu$  for various values of the temperature  $T$ , respectively. In particular, we point out the expected features of the phase diagram by looking at all the aforementioned plots.

- For lower values of the chemical potential, the minimum of the potential (and thus the dynamically generated mass of the quarks) smoothly goes from a finite value at  $T = 0$  to 0 at a given critical temperature  $T_c$ . Thus, this gives rise to a smooth second-order phase transition between the chirally broken and the chirally restored phases. Furthermore, the slope of the minimum close to the critical temperature seems to be vertical, meaning that the thermal susceptibility

$$\chi_T \simeq \frac{\partial\langle\sigma\rangle}{\partial T} \quad (5.119)$$

diverges, in agreement with the hypothesis of a second-order phase transition. In particular, at  $\mu = 0$  one finds  $T_c \sim 0.182$  GeV.

- At high values of the chemical potential, the minimum of the potential jumps abruptly from a finite value to 0 at the critical temperature  $T_c$ , producing a discontinuous first-order phase transition.
- the first- and second-order lines meet at a critical point at  $(T_c \sim 0.08$  GeV,  $\mu_c \sim 0.28$  GeV), where the transition still belongs to the second-order class.

We now move to the case of explicit chiral symmetry breaking, in the MF. We can refer to the left panel of Fig. 5.10, where we show the obtained phase diagram of the model in the case of explicit symmetry breaking and in the MF approximation, and to the left panels of Fig. 5.5 and Fig. 5.9 in which the behavior of the dynamically generated quark mass  $M = h\langle\sigma\rangle$  as a function of the temperature  $T$  for different values of the chemical potential  $\mu$  and as a function of the chemical potential  $\mu$  for various values of the temperature  $T$  are depicted, respectively. Once again, we can verify our expectations for the phase diagram.

- For lower values of the chemical potential, the minimum of the potential smoothly decreases but never truly vanishes. This means that chiral symmetry is never restored and that the second-order phase transition has been replaced by a smooth crossover. Since the system does not experience a real phase transition, only a pseudo-critical temperature can be identified, for example, from the peak of the absolute value of the susceptibility, and the crossover manifests around this pseudo-critical temperature.
- At high values of the chemical potential, the minimum of the potential jumps abruptly from a finite value to another value, which is still non-vanishing. So the first-order phase transition is still present for high chemical potentials.
- The first-order line and the crossover meet at a critical point at ( $T_c \sim 0.045$  GeV,  $\mu_c \sim 0.336$  GeV). At this point, and only at this point, the phase transition is of second order and the susceptibility diverges. Comparing this result to the one obtained for the tri-critical point in the chiral limit, we can observe that the finite current quark mass shifts the critical point towards higher value of the chemical potential and lower temperatures, reducing the extent of the first-order line.

We can now move our focus to the results obtained including the fluctuations via the FRG. In particular, before analyzing the resulting phase diagram, we want to directly compare the quark constituent mass and the critical temperature between the MF and the FRG case, thus testing the effect of fluctuations on these observables. In particular we will focus, for the moment, on the case of explicit symmetry breaking, since the results in the chiral limit are qualitatively similar and can be observed from the calculated phase diagrams. Fig. 5.3 shows the constituent quark condensate,  $M = h\langle\sigma\rangle$ , versus temperature, for  $\mu = 0$  and  $\mu = 0.3$  GeV. We note that there is a range of temperatures in which the condensate decreases from its zero-temperature value to a smaller one, signaling the crossover from the low-temperature phase, in which chiral symmetry is spontaneously broken to the high-temperature phase, in which the symmetry is (approximately) restored. The picture remains qualitatively the same also after fluctuations are included; quantitatively, fluctuations lower the temperature range in which the chiral crossover takes place. We also note that increasing the chemical potential results in the hardening of the crossover, since changes in  $\langle\sigma\rangle$  occur in a smaller range of temperature.

The results shown in Fig. 5.3 allow us, as previously hinted, to define a (pseudo-)critical temperature,  $T_c$ , as the temperature at which the highest change of  $\langle\sigma\rangle$  occurs. In Fig. 5.4 we plot  $T_c$  versus  $\mu$  for both the mean-field case and the full FRG calculation. Below the critical lines the chiral symmetry is spontaneously broken, while above the lines chiral symmetry is approximately restored. For both cases the lines are stopped at the critical endpoint, where the crossover changes into a real second-order phase transition; for larger values of  $\mu$  the phase transition is of first order. Furthermore, according to our previous qualitative reasoning, the critical temperature is lowered by the addition of the fluctuations.

We can now finally investigate the results for the phase diagram of the QM model and the dynamically generated quark mass obtained using the FRG calculation in LPA for both the chiral limit and case of explicit breaking of chiral symmetry.

We begin this discussion by focusing on the chiral limit. In the right panel of Fig. 5.6 we show the phase diagram of the two flavor quark-meson model in the chiral limit, while in the right panels of Fig. 5.2 and Fig. 5.8 the dynamically generated quark mass as a function of temperature  $T$  for various values of the chemical potential  $\mu$  and as a function of the chemical potential  $\mu$  for various values of the temperature  $T$ , are depicted, respectively, obtained in the chiral-limit FRG framework.

- At  $\mu = 0$ , the second-order phase transition behavior persists even with the addition of fluctuations. The critical temperature at which the spontaneously broken chiral symmetry is restored is  $T_c \sim 0.18$  GeV and, as anticipated, it is slightly lower than the one obtained in the MF case. One should point out that the value of the critical temperature depends on the chosen value for the pion decay constant and thus it is not a universal quantity. As we will see in the next section, the universality class in this case corresponds to the O(4) one.
- Increasing the chemical potential, one still finds a second-order phase transition, which belongs, once again, to the O(4)-universality class.
- Further increasing the chemical potential, a tri-critical point is found. The reason why we identify this point as a tri-critical one is that, for even greater values of the chemical potential, one finds a first-order phase transition, which meets with the second-order line at the tri-critical point. In our calculation, the tri-critical point is located at  $T_c \sim 0.033$  GeV and  $\mu_c = 0.313$  GeV. Comparing this result with the one obtained in the MF approximation, we can conclude that the inclusion of fluctuations results in the critical point to be shifted to higher values of chemical potential and to lower temperatures, coherently with our previous discussion on the chiral condensate. It has been shown that the tri-critical point exhibits a trivial Gaussian fixed-point with mean-field universality-class behavior [174], and we will calculate the related critical exponents in the next section. We point out that also the location of the tri-critical point is non-universal, being initial-condition and thus model-parameter dependent. However, both its existence and the universality class of the surrounding phase transitions can be considered as predictions of the model.
- As we stated previously, increasing the chemical potential beyond the value of the tri-critical point we find a first-order phase transition, where the condensate jumps abruptly from a finite value to 0.
- After this small line of first order transition, for  $\mu \sim 0.305$  GeV and for temperatures below  $T \sim 0.025$  GeV the transition line splits into two separate phase transitions, which create a triangular zone in between the lines. This can be seen from Fig. 5.7, where a zoomed version of the phase diagram is presented. The transition line which is located at smaller values of the chemical potential consists of a first-order phase transition, at which the condensate jumps abruptly from a bigger to a smaller, but still finite value. In this way chiral symmetry is not restored and still remains spontaneously broken. This first-order line extends up to  $T = 0$  and the peculiarity is that it bends backwards, in the sense that, if one considers the curvature of the phase diagram  $dT_c/d\mu$ , this is positive, in contrast to what happens in the rest of the phase diagram, where it is negative. This is a feature which is absent in the MF phase diagram and it is typical of FRG LPA calculations, and in the literature it is referred to as the "back-banding" problem. The emergence of this problem can be deduced from the Clausius-Clapeyron relation for a first-order phase transition

$$\frac{dT_c}{d\mu} = -\frac{\Delta n}{\Delta s}, \quad (5.120)$$

where  $\Delta n$  represents the change in quark number density, which is supposed to be positive in a liquid-gas-like transition, and  $\Delta s$  is the change of entropy density. This implies that, if the slope of the phase diagram  $dT_c/d\mu$  is positive, then  $\Delta s < 0$  and it has been shown [184] that this may lead to the triangular region having

negative entropy density with an associated thermodynamic instability. We will not investigate this issue further but it has been conjectured that this may be a regulator-related issue [185], or may be related to the appearance of new physics, such as inhomogeneous phases or di-quark condensates [184].

On the right side of the transition, for higher values of the chemical potential, the chiral condensate vanishes smoothly, giving rise to another second-order transition line, which in this case, bends in a way which does not lead to further complications, since  $dT_c/d\mu < 0$ . The presence of a second-order phase transition suggests that there should exist another tri-critical point, where the second-order line connects to the first-order one, in the region where the transition bifurcation happens. However, due to the finite numerical resolution, it is very hard to identify it and we can state that it could be located around  $T_c \sim 0.023$  GeV and  $\mu_c \sim 0.309$  GeV.

Finally, we focus on the case of finite pion masses, for which the related results of the phase diagram and of the dynamically generated quark mass are shown in the right panels of Figs. 5.10, 5.5, and 5.9, respectively.

- As expected from the MF results, we can observe that the second-order phase transition at low chemical potential is washed out and becomes a smooth crossover and the chiral condensate never truly vanishes.
- For increasing chemical potential, the first-order line is still present and the condensate jumps from a bigger value to a smaller but finite one.
- the two lines meet at a critical point which has been shown to belong to the  $\mathbb{Z}_2$ -universality class [174].
- The problematic triangular region is still present, since we can identify a bifurcation of the first-order transition line into two separate lines, even though it is significantly less extended than the one in the chiral limit. This is coherent with the observation we made in the MF case, when we pointed out that the presence of a finite quark mass reduces the extent of the first-order line.

The left line (for smaller values of the chemical potential) is still a first-order line, while the right second-order line (for higher chemical potential) has been turned into a smooth crossover. Also in this case, this region should contain a critical point associated to the meeting of the crossover and the first-order lines, but the limited numerical resolution does not allow us to locate it exactly.

#### 5.7.4 Critical exponents

We dedicate this final section to the analysis of the universality class of the QM model. In particular we will focus on the model in the chiral limit, such that we can investigate the second-order phase transition, which occurs for values of the chemical potential which are lower than the tri-critical one. In order to reconstruct the universality class, we just need to calculate two independent critical exponents, since we can then extract the remaining four using the scaling relations Eqs.(4.31)-(4.34). In this work we then choose to consider the critical exponent  $\eta$  (which is trivially vanishing both in mean-field approximation and in the FRG within the LPA truncation, since no non-trivial wave function renormalization factor is taken into account) and the correlation-length exponent  $\nu$ . In particular, as an example, we will perform the calculation for vanishing chemical potential  $\mu = 0$  in the FRG framework to identify the universality class of this phase transition. In agreement to what we stated in the previous section, we also verified

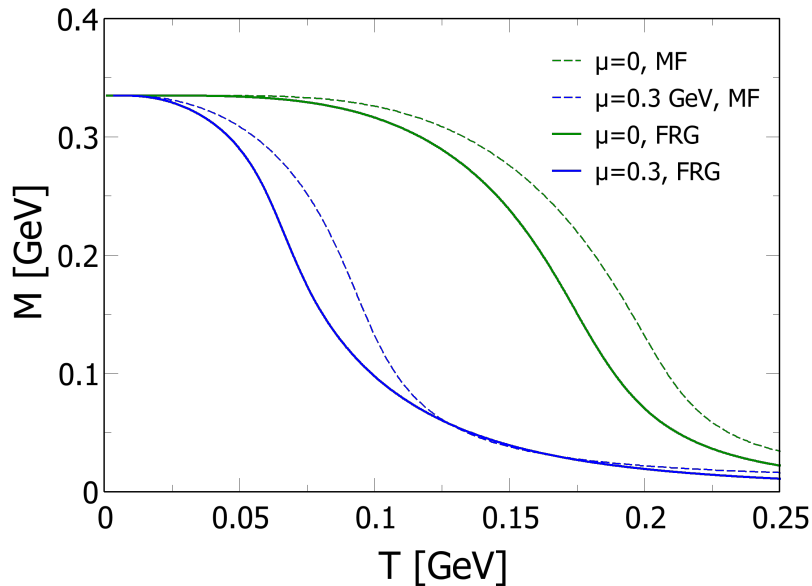


Figure 5.3: Constituent quark mass,  $M = h\langle\sigma\rangle$ , versus temperature  $T$ , for  $\mu = 0$  and  $\mu = 0.3$  GeV. MF and FRG stand for mean-field approximation and functional renormalization group, respectively.

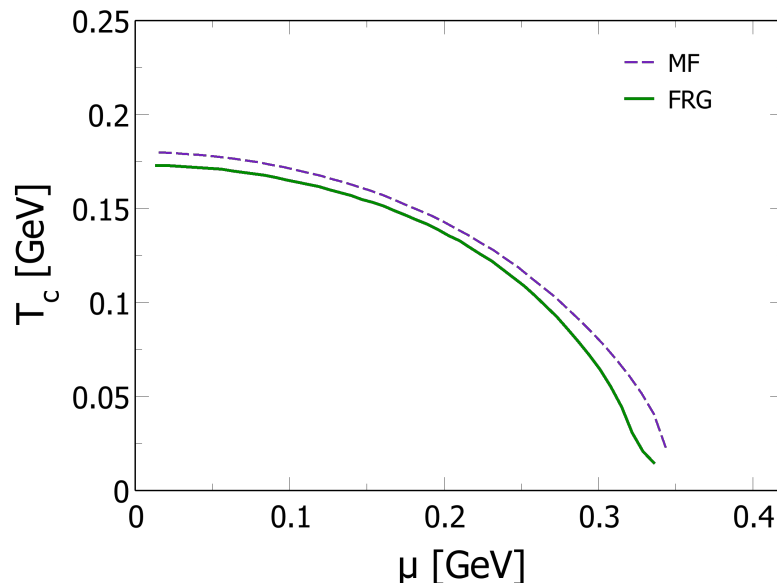


Figure 5.4: Critical temperature,  $T_c$ , versus  $\mu$ , for the MF (dashed line) and the full FRG (solid line) calculations.

that the universality class obtained in the  $\mu = 0$  case does not change for another value of the chemical potential  $\mu = 0.2$  GeV, which is still smaller than the tri-critical one. We also repeated the calculation in the MF approximation, in order to verify the results stated in Sec. 5.5 and to calculate the universality class of the tri-critical point.

Following what we did in the case of the  $O(N)$  model in Chapter 4, in order to study a second-order phase transition, we will be looking for a RG-time independent scaling solution, which is scale-independent and associated to an infrared fixed point of the renormalization group. Compared to what we did in Chapter 4, we will work at finite temperature and thus we will not exploit the dimensional-reduction theorem.



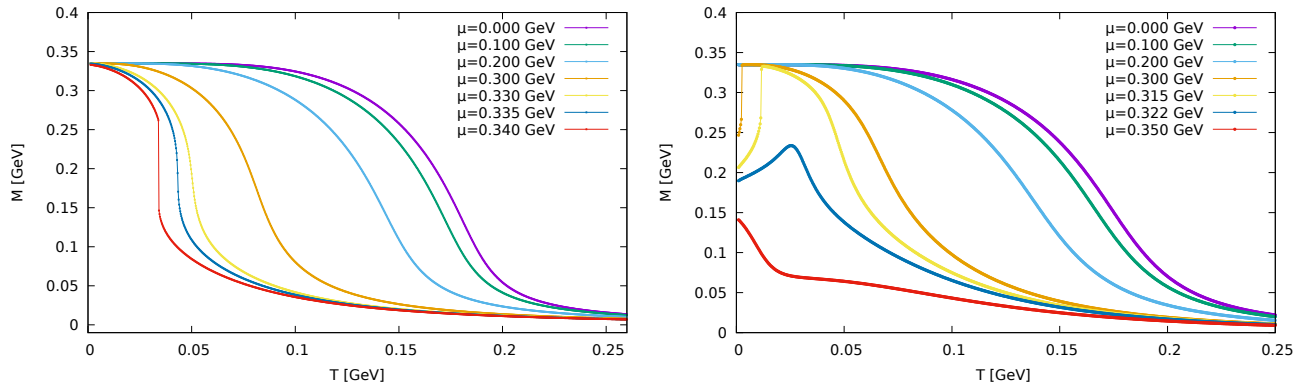


Figure 5.5: Dynamically generated quark mass  $M = h\langle\sigma\rangle$  in the case of explicit symmetry breaking, as a function of the temperature  $T$  for various values of the chemical potential  $\mu$ , both in the MF case (left panel) and with the inclusion of fluctuations via FRG (right panel).

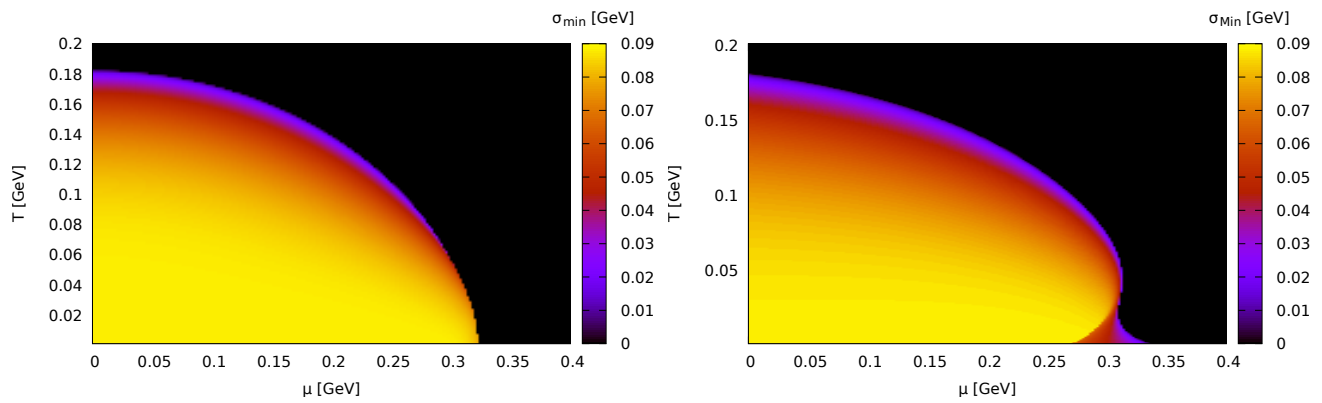


Figure 5.6: Phase diagram of the QM model in the chiral limit as a function of the chemical potential  $\mu$  and the temperature  $T$ , both in the MF approximation (left panel) and in the FRG (right panel).

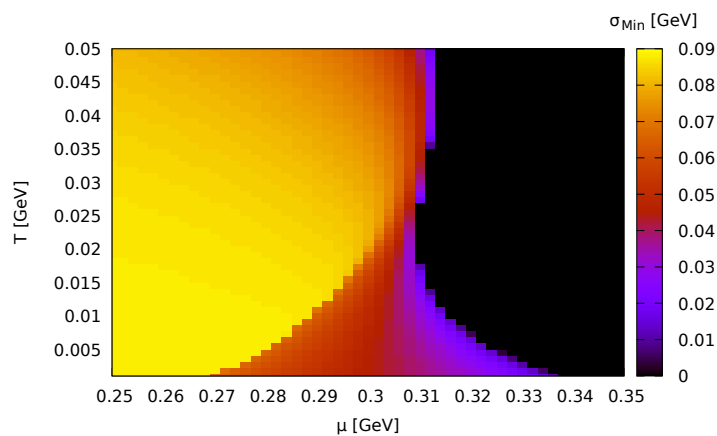


Figure 5.7: Zoom of the phase diagram of the QM model in the chiral limit and within the FRG approach, around the region where the phase transition splits into two separate transition lines.



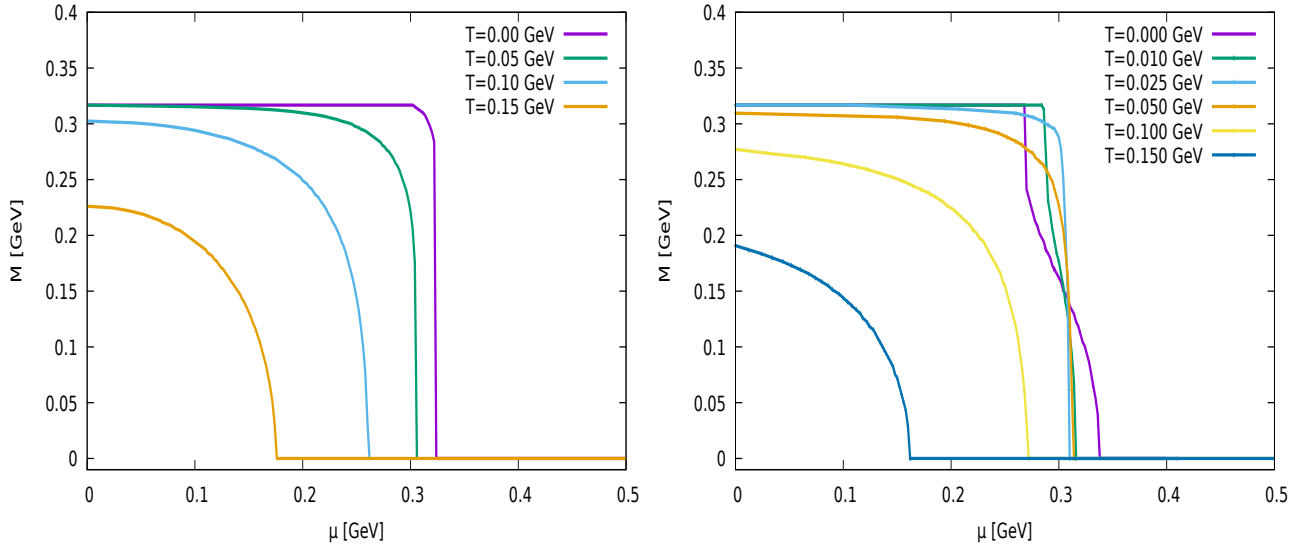


Figure 5.8: Dynamically generated quark mass  $M = h\langle\sigma\rangle$  in the chiral limit, as a function of the chemical potential  $\mu$  for various values of the temperature  $T$ , both in the MF case (left panel) and with the inclusion of fluctuations via FRG (right panel).

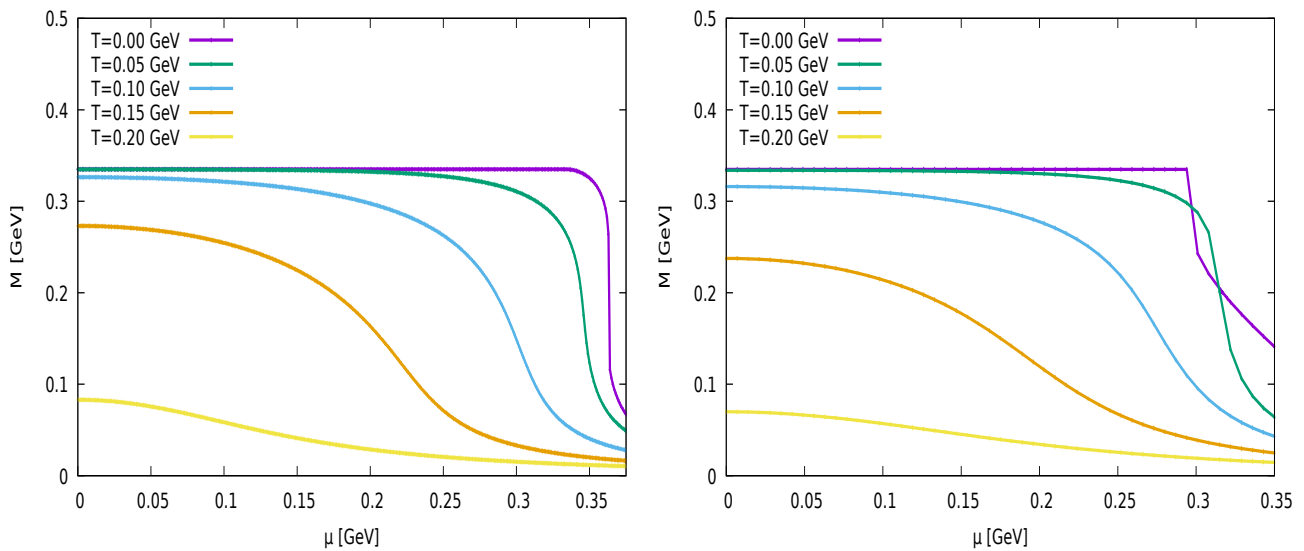


Figure 5.9: Dynamically generated quark mass  $M = h\langle\sigma\rangle$  in the case of explicit symmetry breaking, as a function of the chemical potential  $\mu$  for various values of the temperature  $T$ , both in the MF case (left panel) and with the inclusion of fluctuations via FRG (right panel).

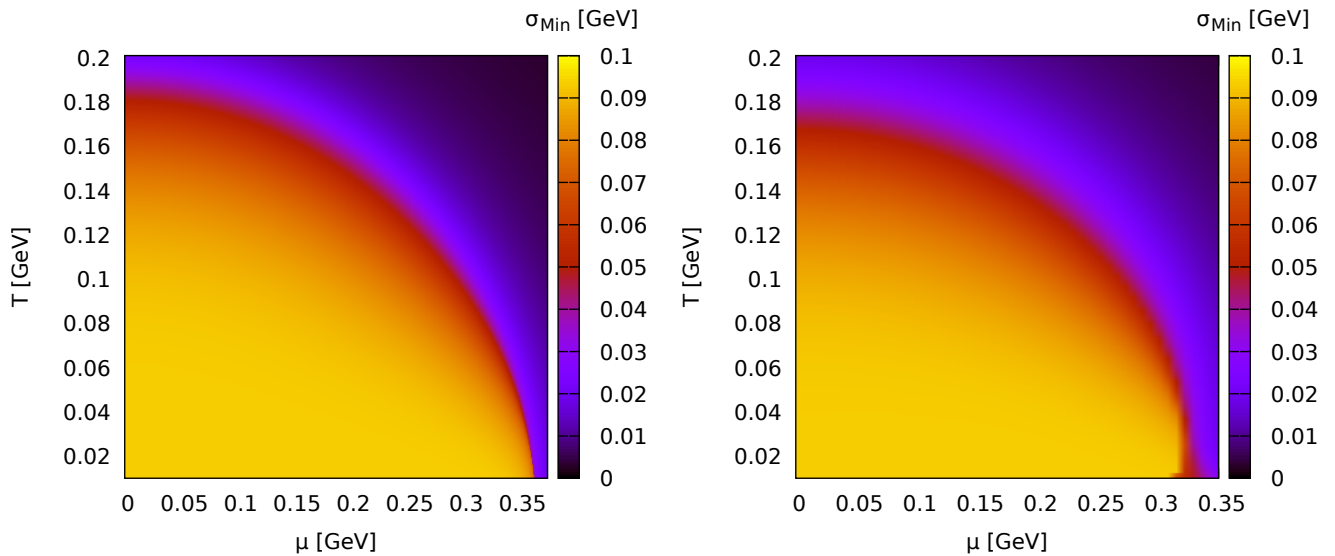


Figure 5.10: Phase diagram of the QM model in the case of explicit chiral symmetry breaking as a function of the chemical potential  $\mu$  and the temperature  $T$ , both in the MF approximation (left panel) and in the FRG (right panel).

This means that, in order to reach the scaling solution, we will tune the temperature  $T$  as the external parameter which drives the phase transition. In particular, the closer the temperature will be to the critical one  $T_c$ , the more time the system will spend on the scaling solution. We will then look to properly rescaled dimensionless quantities, which should exhibit, for temperatures sufficiently close to the critical one, a constant behavior at sufficiently large RG times  $t$ . As in Chapter 4, we choose, as observable, the dimensionless minimum

$$\tilde{\rho}_{0,k} = \rho_{0,k}/k, \quad (5.121)$$

which we expect to tend to the fixed-point value as  $T \rightarrow T_c$ . The behavior of the dimensionless minimum as a function of the RG time  $t$  is depicted in Fig. 5.11 for different values of the temperature  $T$ . One observes that, during the FRG flow,  $\tilde{\rho}_{0,k}$  approaches the critical trajectory, the scaling solution, which is shown by the red line, at a given RG time. However the system will eventually deviate from the scaling phase, meaning that the rescaled minimum will deviate either upwards in the broken phase, which corresponds to the case  $T < T_c$ , or downwards in the symmetric phase, in correspondence to  $T > T_c$ . The behavior of the rescaled minimum is analogous to the one described in Chapter 4, so one can refer to Chapter 4 for a more detailed discussion. The difference w.r.t what is presented in Chapter 4 is that, in the case we are currently discussing, the system is in the symmetric phase at the initial time  $t = 0$ , and a finite minimum is developed only at a later finite RG time. In agreement with our discussion in Sec. 5.6.4, this is possible thanks to the presence of fermionic degrees of freedom in the system, which act like a source/sink term that makes the potential develop a finite minimum, which is then smeared and transported towards smaller values by the bosonic fluxes.

Our result for the critical temperature is then  $T_c = 0.142484$  GeV.

Once we determined the critical temperature, we can now move to the actual determination of the critical exponents. In particular, in order to calculate  $\nu$  we need the curvature mass, i.e., the  $\sigma$  mass, evaluated at the physical point, i.e., at the minimum of the potential

$$M_\sigma^2 = \lim_{k \rightarrow 0} u'(\sigma = 0, k) = \lim_{k \rightarrow 0} U''(\sigma = 0, k). \quad (5.122)$$

Following the analogy to the approach used in Chapter 4, we have to make sure to reach the symmetric phase before stopping the  $t$ -evolution, because only in this way one can

be sure that the minimum is located at  $\sigma = 0$  and  $M_\sigma^2 > 0$  at  $\sigma = 0$ . We then follow the procedure illustrated in Chapter 4, and in particular, in order to extract the critical exponent, we will exploit a logarithmic relation corresponding to the finite-temperature equivalent of the one presented in Eq.(4.43). Namely, we consider the scaling relation

$$M_\sigma^2 \sim (T - T_c)^{2\nu} \quad (5.123)$$

and then take the logarithm of both sides

$$\ln M_\sigma^2 = 2\nu \ln(T - T_c) + \text{const} . \quad (5.124)$$

We can notice that in the symmetric phase  $T > T_c$ , so that we can omit the absolute value in  $|T - T_c|$  in both Eqs.(5.123) and (5.124). Based on Eq.(5.124), we can then extract  $\nu$  from the slope of  $\ln M_\sigma^2$  as a function of  $\ln(T - T_c)$ . The result of this procedure is shown in Fig.5.12, where the logarithm of the curvature mass is plotted as a function of  $\ln(T - T_c)$ , both in the FRG LPA at  $\mu = 0$  (purple dots) and in the mean-field approximation (light blue dots). We also show the resulting estimation for the value of the critical exponent  $\nu$  through the slope of the green line in the FRG case and of the orange line in the MF. We specify that the critical temperature used in the MF case is just determined as the one at which the thermal susceptibility Eq.(5.119) diverges, since no fixed-point behavior is expected beside the trivial Gaussian one.

The most reliable value for the critical exponent is then obtained following the procedure illustrated in Sec.4.4. In particular, we neglect the error on the determination of  $M_\sigma^2$ , as explained in Sec.4.4.2 due to the second-order precision in the adopted numerical KT scheme.

We then proceed, as shown in Fig.5.13, by plotting the critical exponent  $\nu$  as a function of the number of the most aligned points  $N_p$  taken into consideration in the fit. In this way, the most reliable value of the critical exponent can be extracted from the region where the value of the critical exponent is least dependent on  $N_p$ . The selected region in  $N_p$  from which the critical exponent is obtained provides us with a component of the total error, namely the half-width of the selected band in  $\nu$ . The total error on the critical exponent is then obtained by the square root of the sum of the squared different independent contributions to the error, which in our case consist of the aforementioned half-width of the interval in  $\nu$  and of the proper fitting error due to the linear regression performed to calculate the value of the critical exponent.

The final result for the MF case is then

$$\nu_{MF} = 0.9986(8) , \quad (5.125)$$

which is extremely precise if we consider the rigid procedure we followed in the error determination. This value is compatible with the expected value in the mean-field approximation, which is  $\nu_{MF} = 1$ , as can be obtained using the scaling relations Eqs.(4.31)-(4.34) and taking the results presented in Sec.5.5.1, where we calculated  $\beta = 1/2$  and  $\eta = 0$ .

Finally, we present the result obtained for the critical exponent  $\nu$  in the FRG framework within the LPA approximation:

$$\nu_{LPA} = 0.814(2) . \quad (5.126)$$

From this value we can then conclude that the phase transition of the QM at  $\mu = 0$  belongs to the  $O(4)$ -universality class. This result is indeed also compatible with the one obtained in Chapter 4 for the  $O(N)$  model in the case of  $N = 4$ , and it is also in agreement with the previous results obtained in this framework [174].

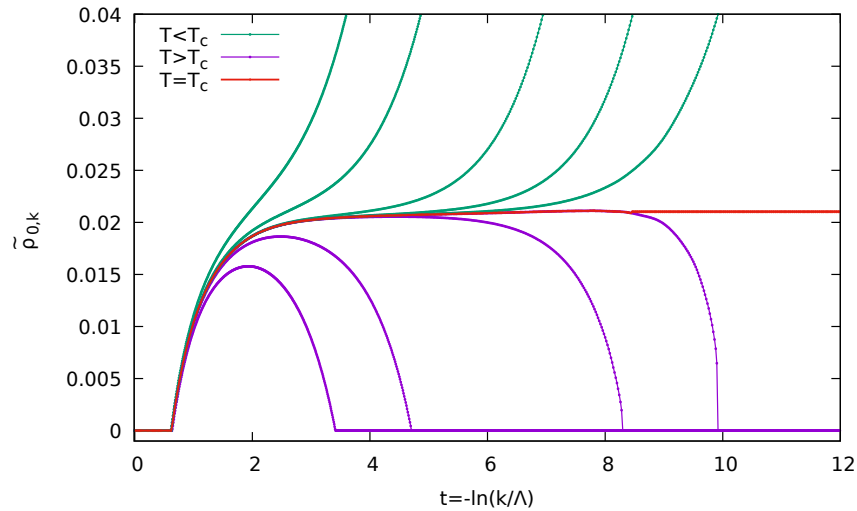


Figure 5.11: Scaling of  $\tilde{\rho}_{0,k}$  as a function of RG time  $t$  in the LPA for the QM model at  $\mu = 0$ . The green curves deviate upwards from the scaling value (red line), indicating that the system is in the broken phase ( $T < T_c$ ), while the purple curves deviate downwards towards the symmetric phase ( $T > T_c$ ).

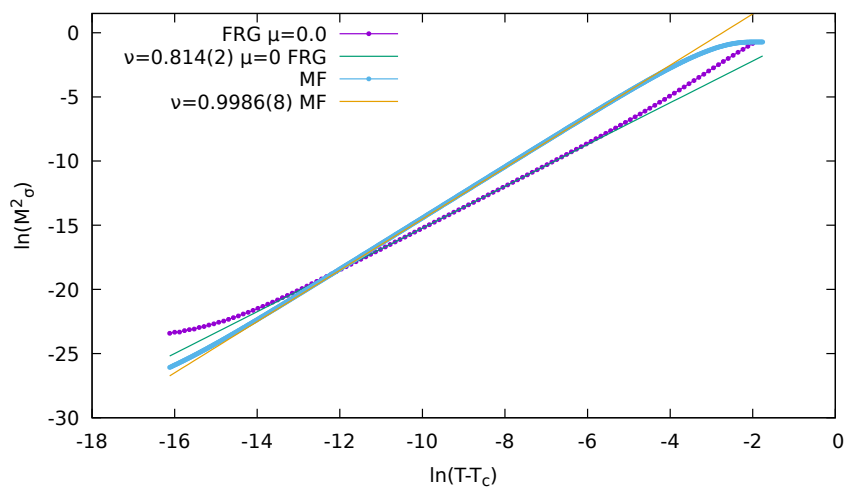


Figure 5.12: Double-logarithmic plot of Eq. (5.123) both in the FRG LPA for  $\mu = 0$  (purple dots) and in the mean-field approximation (light blue dots). The estimation for the value of the critical exponent  $\nu$  is given by the slope of the green line in the FRG case and of the orange line in the MF.

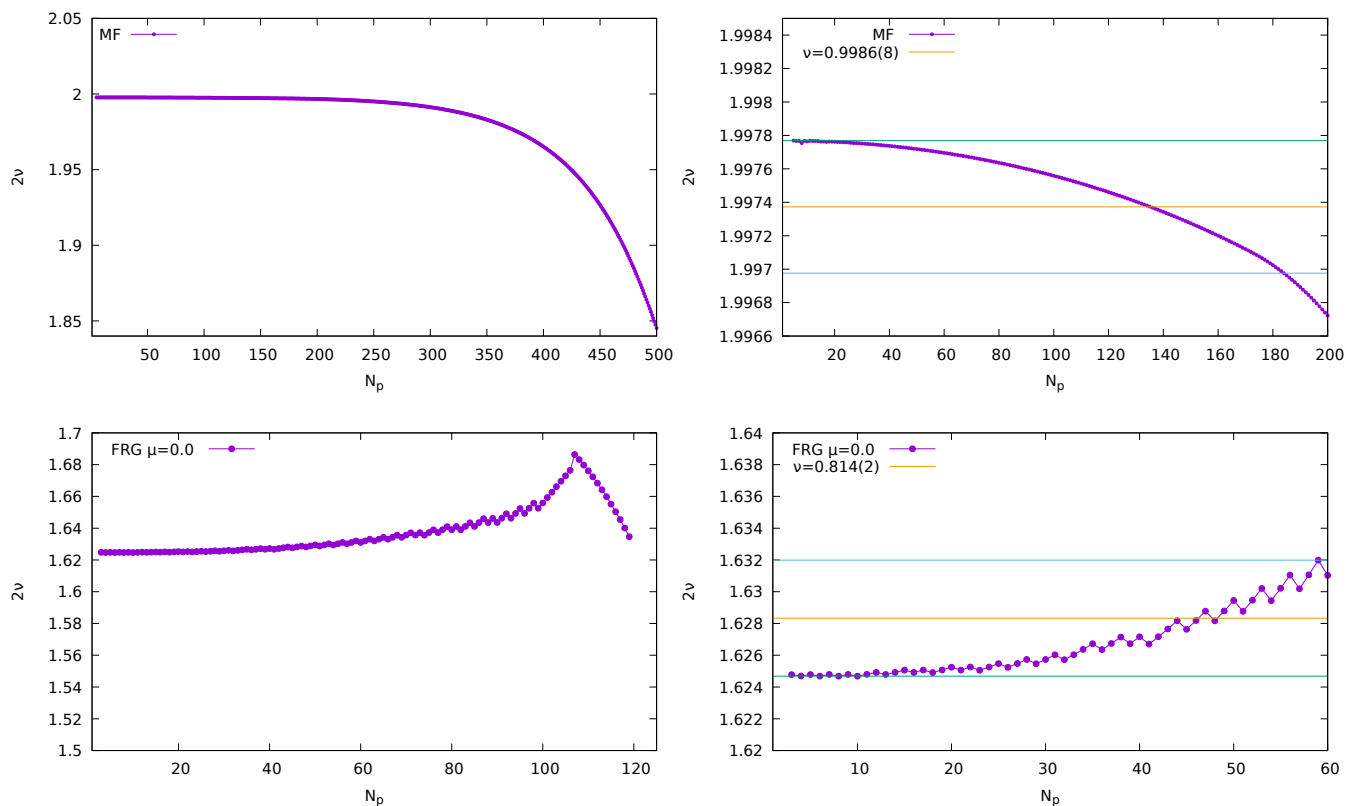


Figure 5.13: Critical exponent  $\nu$  as a function of the number of the most aligned points  $N_p$  taken into consideration in the fit (left panels) in the FRG LPA  $\mu = 0$  case (upper left panel) and in the MF approximation (lower left panel). The right panels are zoomed versions of the corresponding left plots, magnifying the region where the value of the critical exponent is least dependent on  $N_p$ .

# Quark Meson model: thermodynamic geometry

This chapter is mainly based on Ref. [186].

## 6.1 Introduction and motivation

In the previous chapter we validated the QM model by seeing that its phase diagram should be in qualitative agreement with what is believed to be the phase diagram of full QCD. In particular, our interest lies in the chiral symmetry breaking/restoration and the related phase transition and critical point. However, due to lack of certain answers from first-principle calculations because of the sign problem, it is not certain if this kind of observations hold also at finite baryon chemical potential for full QCD. This is the reason behind the great success of effective models like the QM, which allow to study the phase structure of QCD at finite  $\mu$ . This means that the more methods we have at our disposal to study the phase diagram of strongly interacting matter and to locate the critical point, the better will be the gain we can obtain in our knowledge on the topic. Moved by this motivation, one can consider the phase space spanned by the temperature  $T$  and the chemical potential  $\mu$  as a two-dimensional manifold and study its geometry, the metric and the curvature: this approach leads to the so-called *thermodynamic geometry*. One can refer to previous works on this subject [187, 188, 189, 190, 191, 192, 193, 194, 195, 196, 197, 198, 199] and [200, 201, 202, 203, 204, 205, 206, 207, 208, 209, 210, 211, 212].

The reason behind the use of the thermodynamic-geometry approach lies in the information one can extract on the system. As a first consideration, it has been argued that the sign of the thermodynamic curvature is connected to the dominance of a fermionic- or bosonic- like behavior of the system [195, 200, 201, 213]. This means that, through the thermodynamic geometry one can extract the information on which degrees of freedom are relevant for the system at a given temperature and chemical potential, and, combining it with the functional renormalization group, the momentum scale at which this happens.

The other interesting feature of the thermodynamic curvature is linked to the presence of a peak structure close to the crossover temperature for small values of  $\mu$ , which eventually should turn into a divergence when the critical point is reached. This feature is a consequence of the fact that the determinant of the metric exactly vanishes when a second-order phase transition is approached. Thus, the thermodynamic geometry can be understood as interesting additional tool to shed light on the ever-lasting quest on the location (and existence) of the CP.

In this chapter we apply the thermodynamic-geometry approach to the QM model

at finite density and temperature, as it has been done previously in [214, 215] or in [216] where a similar study has been performed for the Nambu-Jona-Lasinio (NJL) model. The choice of the QM model over the NJL model is due to its renormalizability [11], which makes the obtained results independent of the effective ultraviolet cutoff, that is instead part of NJL calculations [11, 217]. Compared to previous results in the QM framework [214, 215], in this work we include quantum fluctuations via using the functional renormalization group approach (FRG). As we stated in the previous chapters, the advantage of the use of the FRG method is that it belongs to the class of non-perturbative approaches to quantum field theories and it is built in such a way to link different energy scales and the associated degrees of freedom. Thus, it is a suitable tool to deal with second-order phase transitions and critical long-wavelength phenomena in general, whose nature is highly non-perturbative.

## 6.2 The thermodynamic geometry

We consider a thermodynamic system in the grand canonical ensemble, whose equilibrium state is characterized by the pair  $(\mu, T)$ , where  $T$  is the temperature and  $\mu$  is the quark-number chemical potential (conjugated to quark number density). Thermodynamic geometry is more conveniently defined in terms of the variables  $(\beta = 1/T, \gamma = -\mu/T)$ . A thermodynamic system at equilibrium at the point  $(\beta, \gamma)$  can fluctuate to another equilibrium state  $(\beta', \gamma')$ , and the probability of this fluctuation can be computed within the standard thermodynamic fluctuation theory. In fact, we firstly define a distance in the two-dimensional manifold spanned by  $(\beta, \gamma)$ ,

$$dl^2 = g_{\beta\beta}d\beta d\beta + 2g_{\beta\gamma}d\beta d\gamma + g_{\gamma\gamma}d\gamma d\gamma, \quad (6.1)$$

where the metric tensor is

$$g_{ij} = \frac{\partial^2 \log \mathcal{Z}}{\partial \beta^i \partial \beta^j} = \frac{\partial^2 \phi}{\partial \beta^i \partial \beta^j} \equiv \phi_{,ij}, \quad (6.2)$$

with  $\phi = \beta P$ ,  $P = -\Omega$  and  $\Omega$  denotes the grand canonical thermodynamic potential density; moreover, we used the standard notation  $\beta^1 = \beta$  and  $\beta^2 = \gamma$ . Given these, the fluctuation probability is

$$\frac{dp}{d\beta d\gamma} \propto \sqrt{g} \exp\left(-\frac{dl^2}{2}\right), \quad (6.3)$$

where

$$g = g_{\beta\beta}g_{\gamma\gamma} - g_{\beta\gamma}^2 \quad (6.4)$$

is the determinant of the metric. Large probability of a fluctuation corresponds to small  $dl^2$  and vice versa. Therefore, a large thermodynamic distance between two equilibrium states means a small probability to fluctuate between the two states. According to these considerations, Eq. (6.1) measures both the distance in the  $(\beta, \gamma)$  plane and the transition probability between two thermodynamic states in equilibrium.

Thermodynamic stability requires that  $g_{\beta\beta} > 0$  and  $g > 0$ , while  $g = 0$  corresponds to a phase boundary and regions with  $g < 0$  are thermodynamically unstable: hence, the stability conditions ensure that  $dl^2 > 0$ .

Furthermore, the second-order momenta of  $\phi$  w.r.t.  $\gamma$  and  $\beta$  measure fluctuations of the conjugated observables:

$$V\phi_{,\beta\beta} = \langle (U - \langle U \rangle)^2 \rangle, \quad (6.5)$$

$$V\phi_{,\beta\gamma} = \langle (U - \langle U \rangle) \rangle \langle (N - \langle N \rangle) \rangle, \quad (6.6)$$

$$V\phi_{,\gamma\gamma} = \langle (N - \langle N \rangle)^2 \rangle, \quad (6.7)$$



where  $U$  and  $N$  denote the internal energy and the particle number, respectively, while  $V$  stands for the volume of the system.

Once the manifold has been provided with the metric tensor, one can define the Riemann tensor as

$$R_{klm}^i = \frac{\partial \Gamma_{km}^i}{\partial x^l} - \frac{\partial \Gamma_{kl}^i}{\partial x^m} + \Gamma_{nl}^i \Gamma_{km}^n - \Gamma_{nm}^i \Gamma_{kl}^n, \quad (6.8)$$

with the Christoffel symbols

$$\Gamma_{kl}^i = \frac{1}{2} g^{im} \left( \frac{\partial g_{mk}}{\partial x^l} + \frac{\partial g_{il}}{\partial x^k} - \frac{\partial g_{kl}}{\partial x^m} \right). \quad (6.9)$$

The standard contraction procedure gives the Ricci tensor  $R_{ij} = R_{ikj}^k$ , and the scalar curvature  $R = R_i^i$ : within thermodynamic geometry,  $R$  is called the *thermodynamic curvature*. For the two-dimensional manifold that we consider in this study, the expression of  $R$  considerably simplifies, namely  $R = 2R_{1212}/g$  [198], where  $R_{1212}$  corresponds to the only independent component of the Riemann tensor for a two-dimensional manifold. So we can explicitly write  $R$  as

$$R = -\frac{1}{2g^2} \begin{vmatrix} \phi_{,\beta\beta} & \phi_{,\beta\gamma} & \phi_{,\gamma\gamma} \\ \phi_{,\beta\beta\beta} & \phi_{,\beta\beta\gamma} & \phi_{,\beta\gamma\gamma} \\ \phi_{,\beta\beta\gamma} & \phi_{,\beta\gamma\gamma} & \phi_{,\gamma\gamma\gamma} \end{vmatrix}, \quad (6.10)$$

where  $||$  indicates the determinant of the matrix. The curvature diverges for  $g \rightarrow 0$ , namely on a phase boundary, unless the numerator of Eq. (6.10) vanishes on the same boundary. We can observe that  $R$  depends on the second- and third-order moments of the thermodynamic variables that are conjugated to  $(\beta, \gamma)$ , thus it carries information about the fluctuation of the physical quantities.

Let  $\xi$  denote the correlation length of the order parameter: then,  $|R| \propto \xi^3$  near a second-order phase transition [187], which naturally results from hyperscaling. Theoretical calculations based on different models confirm this hypothesis [187, 198, 218, 219, 220]; therefore, the study of  $R$  in the  $(\mu, T)$  plane allows to estimate the correlation volume based only on the thermodynamic potential: this is one of the merits of the thermodynamic geometry. It has also been suggested that the sign of  $R$  conveys details about the nature of the interaction, attractive or repulsive, at a mesoscopic level in proximity of the phase transition.

Within our sign convention,  $R > 0$  indicates an attractive interaction while  $R < 0$  corresponds to a repulsive one. These interactions include not only real interactions [203, 205, 210, 221, 222], but also the statistical attraction and repulsion that ideal quantum gases feel in phase space [223, 224, 225, 226, 227]: an ideal fermion gas has  $R < 0$  due to the statistical repulsion, while an ideal boson gas has  $R > 0$  due to the statistical attraction. The thermodynamic curvature is known to be identically zero only for the ideal classical gas. Other fields of application of thermodynamic geometry include Lennard-Jones fluids [203, 221, 222], ferromagnetic systems [228], black holes [229, 230, 231, 232, 233, 234, 203, 235, 236, 237, 238, 239, 240, 213, 241, 242, 243], strongly interacting matter [214, 244, 245] and others [246, 247].

### 6.3 FRG setup

We use this section to specify the FRG setup we adopt in this chapter of this work and we also establish the procedure to obtain consistent finite-temperature thermodynamic observables.

### 6.3.1 Flow equation in the LPA for the Litim regulator

Proceeding as we did in Sec. 5.6.1, we begin this section by considering the LPA ansatz for the effective action of the QM model at finite temperature and quark number density

$$\Gamma_k[\bar{\Psi}, \Psi, \phi] = \int_0^{1/T} dx_0 \int d^3x \left\{ \bar{\psi}(\gamma_\mu \partial^\mu + h(\sigma + i\gamma^5 \vec{\tau} \cdot \vec{\pi}) - \mu\gamma_0)\psi \right. \\ \left. + \frac{1}{2}(\partial_\mu \sigma)^2 + \frac{1}{2}(\partial_\mu \vec{\pi})^2 + U_k(\sigma^2 + \vec{\pi}^2) - c\sigma \right\}. \quad (6.11)$$

Using the three-dimensional momentum-diagonal regulators Eqs. (5.88) and (5.93) and the Litim regulator for both fermions and bosons given in Eqs. (5.110) and (5.111), we get the flow equation for the effective potential

$$\partial_t U_k(\sigma) = -\frac{k^5}{12\pi^2} \left\{ \left[ \frac{3}{E_{k,\pi}} \coth\left(\frac{E_{k,\pi}}{2T}\right) + \frac{1}{E_{k,\sigma}} \coth\left(\frac{E_{k,\sigma}}{2T}\right) \right] \right. \\ \left. - 4N_c \frac{1}{E_{k,\Psi}} \left[ \tanh\left(\frac{E_{k,\psi} - \mu}{2T}\right) + \tanh\left(\frac{E_{k,\psi} + \mu}{2T}\right) \right] \right\}, \quad (6.12)$$

where the energies of the pions, sigma and fermionic modes are given by Eq. (5.115)-Eq. (5.117).

We notice that the choice of expressing the flow equation in terms of the  $\sigma$  expectation value instead of the  $O(4)$  invariant of the theory  $\rho = (\pi^2 + \sigma^2)/2$  is, once again, due to the correct identification of the boundary conditions for the solution of the flow equation as a partial differential equation. We argued more on this issue in Sec. 4.2.1 when studying the  $O(N)$  model, and it is still valid also in QM model case due to the  $O(4)$  bosonic symmetry.

Analogously to Sec. 4.2.2 we introduce the following variables

$$u_k(\sigma) = \partial_\sigma U_k(\sigma), \quad u'_k(\sigma) = \partial_\sigma u_k(\sigma). \quad (6.13)$$

Taking the derivative of Eq. (6.12) with respect to  $\sigma$ , the FRG flow equation is cast again in the form of an advection-diffusion equation with a source term, thus obtaining

$$\partial_t u_k(\sigma) + \partial_\sigma f_k(\sigma, u_k(\sigma)) = \partial_\sigma g_k(u'_k(\sigma)) + N_c \partial_\sigma S_k(\sigma), \quad (6.14)$$

where the advection flux, the diffusion flux and the source term are given by Eqs. (5.112) to (5.114), respectively.

As we stated in the previous section, thermodynamic quantities are extracted from the grand canonical thermodynamic potential  $\Omega$ . This is obtained considering the value of the IR effective potential evaluated at its global minimum  $\sigma_0$ :

$$\Omega(T, \mu) \equiv U_{k=0}(\sigma = \sigma_0; T, \mu) - c\sigma_0. \quad (6.15)$$

This means that, in order to compute thermodynamic quantities, we need to solve the FRG flow equation to obtain the effective potential. Anyway, the solution of the flow equation in the hydrodynamic formulation (6.14) provides us with the derivative of the effective potential w.r.t.  $\sigma$ . This leads to the fact that the solution  $u(\sigma; T, \mu)$  has to be integrated in the  $\sigma$  variable, implying that the effective potential would be defined up to an arbitrary integration constant, which is  $\sigma$ -independent but in principle  $T$  and  $\mu$ -dependent

$$U(\sigma; T, \mu) = \int_{\bar{\sigma}}^{\sigma} d\sigma' u(\sigma'; T, \mu) + U(\bar{\sigma}; T, \mu), \quad (6.16)$$

where  $\bar{\sigma} \in [0, \sigma_{\max}]$  is an arbitrary grid point. Thus, in order to obtain the correct thermodynamic properties, we need to calculate this constant using directly the flow equation for the effective potential (6.12), evaluated in the generic grid point  $\bar{\sigma}$ . The most convenient choice in this case is to select  $\bar{\sigma} = 0$ . Thus, in order to obtain the correct temperature and chemical-potential dependence of the effective potential, we also solve the equation

$$\begin{aligned} \partial_t U_k(0) = & -\frac{k^5}{12\pi^2} \left\{ \left[ \frac{4}{E_{k,\sigma}(\sigma=0)} \coth \left( \frac{E_{k,\sigma}(\sigma=0)}{2T} \right) \right] \right. \\ & \left. - 4N_c \frac{1}{k} \left[ \tanh \left( \frac{k-\mu}{2T} \right) + \tanh \left( \frac{k+\mu}{2T} \right) \right] \right\}, \end{aligned} \quad (6.17)$$

which is coupled to the standard flow equation Eq.(6.14).

### 6.3.2 UV initial condition

We dedicate this subsection to the description of the methodology we use to build the initial condition. In the case of the FRG flow equation, the choice of the initial condition corresponds to assign a shape to the bare potential in the UV ( $k = \Lambda$  or  $t = 0$ ). In particular, we choose a quartic potential

$$U_\Lambda(\sigma) = \frac{m_{UV}^2}{2}\sigma^2 + \frac{\lambda_{UV}}{4}\sigma^4. \quad (6.18)$$

We also need to take one more factor into account in the determination of the initial condition. In particular, due to the presence of a finite cutoff  $\Lambda$ , when the Matsubara sum is performed, thermal modes with  $2\pi T > \Lambda$  are factually excluded. This is a problem which needs to be assessed especially for the calculation of thermodynamic quantities at high temperatures. This issue can be fixed including the missing high-momentum modes in the effective potential in a proper way. In particular, since one expects the fermionic degrees of freedom to be relevant at higher temperature, a standard procedure consists of integrating the fermionic part of Eq. (6.12) from  $k \rightarrow \infty$  to  $k = \Lambda$  and add it to the effective potential. So we calculate

$$U_\Lambda^\infty(\sigma) = \int_\infty^\Lambda S_k(\sigma) dk \quad (6.19)$$

and then we add it to the effective potential at the UV scale

$$U_\Lambda(\sigma) \rightarrow U_\Lambda(\sigma) + U_\Lambda^\infty(\sigma). \quad (6.20)$$

Thus, we use Eq. (6.20) as the corrected initial condition for the solution of the flow equation.

We now have the freedom to tune the parameters in the model and in the initial condition in order to fulfill the Goldberger-Treiman relation Eq. (5.11), i.e.,  $M = hf_\pi$  for the fermionic mass in the vacuum. We also set the parameters in order to have  $\partial_{\sigma\sigma}^2 U(\langle\sigma\rangle) = M_\sigma^2 = 0.36 \text{ GeV}^2$ . Then we choose  $\Lambda = 1 \text{ GeV}$  for the UV-cutoff and  $h = 3.6$  for the Yukawa coupling. Other model parameters are the same as in the second and fourth lines of Tab. 5.1.

## 6.4 QM model thermodynamics

In this section we begin our investigation of the thermodynamic properties of the QM model, comparing the results which are given by the MF approximation with the one obtained in the FRG framework. In this way we will be able to compare the corresponding results, in order to appreciate the effects of the inclusion of the fluctuations.

In particular, we analyze the behavior of the pressure  $P$  and the entropy density  $s$ , as  $T$  and  $\mu$  are changed. As anticipated in Sec. 6.2, the pressure is given by

$$P(T, \mu) = -\Omega(T, \mu) + \Omega(0, 0), \quad (6.21)$$

where  $\Omega(T, \mu)$  is the grand canonical potential defined in Eq. (6.15), and we normalized the pressure such that it vanishes in the vacuum.

On the other hand, the entropy density is defined as the derivative of the pressure w.r.t. the temperature:

$$s = \frac{\partial P(T, \mu)}{\partial T}. \quad (6.22)$$

In particular, the pressure has the dimension of an energy to the fourth power,  $[P] = [\text{GeV}]^4$ , and thus, clearly, the entropy density scales as an energy to the third power,  $[s] = [\text{GeV}]^3$ . This implies that we can use this information to show the behavior of properly rescaled, dimensionless quantities. Following this line of reasoning, in Fig. 6.1 we show the behavior of the pressure and of the entropy density in units of  $T^3$  as a function of temperature, for two values of the chemical potential, both in the MF and in the FRG cases. What we can observe is that, for both MF and FRG individually, the pressure increases as  $T$  is increased, in agreement with standard thermodynamic arguments (see, e.g., [156, 157, 179]), and analogously, it increases when the density is increased, increasing  $\mu$ . On the other hand, when comparing the behavior of the pressure for a fixed value of the chemical potential, we can observe that the curves obtained within the FRG approach lie below the corresponding MF ones. This means that the effect of the inclusion of the fluctuations is to lower the pressure of the system. A possible interpretation of this result is that the presence of the bosonic fluctuations introduces an extra overall effective interaction among quarks and the bosons, which lowers the total pressure. This feature will be also investigated when analyzing the behavior of the thermodynamic curvature and the positions of its peaks. As far as the rescaled entropy density is concerned, we can observe that, coherently with the observed behavior of the pressure, it increases if one increases either the temperature or the chemical potential. An absolutely non-trivial feature of the rescaled entropy density is that it saturates at a given temperature, meaning that it stays almost constant as  $T$  increases. This is far more evident in the  $\mu = 0$  case w.r.t. the finite  $\mu$  one. This feature is found for both the MF and the FRG calculation even if, coherently with the previous discussion on the pressure, the entropy density in the FRG case is lower than the MF one. The saturation of the rescaled entropy can be understood if one considers that, at high temperatures, due to asymptotic freedom, QCD should behave like a gas of massless quarks and gluons. This is the so-called Stefan-Boltzmann limit (SB) (see, e.g., [179]), and the corresponding pressure is given, according to Dalton's law, by the sum of the quark contribution  $P_{SB}^Q$  and the one of the gluons:

$$P_{SB} = P_{SB}^Q + P_{SB}^G, \quad (6.23)$$

where the quark contribution is given by

$$P_{SB}^Q = T^4 \frac{\pi^2}{45} \left\{ \frac{7d_F}{4} \left[ 1 + \frac{30}{7\pi^2} \left( \frac{\mu}{T} \right)^2 + \mathcal{O} \left( \frac{\mu}{T} \right)^4 \right] \right\} \quad (6.24)$$

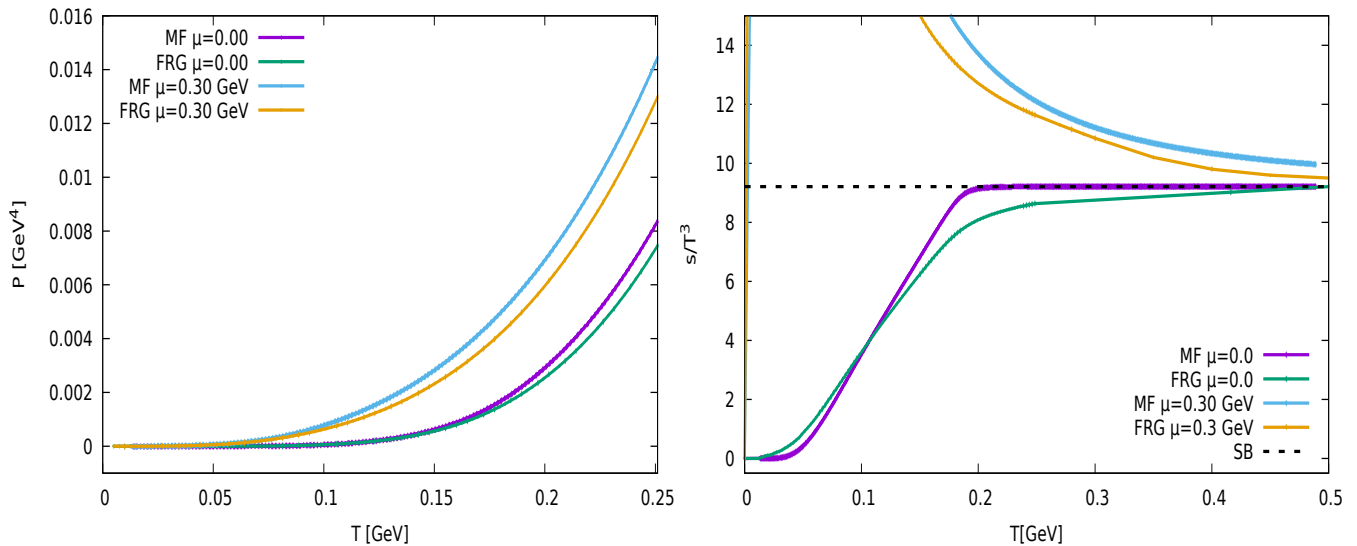


Figure 6.1: Pressure (left panel) and the rescaled entropy density (right panel) as a function of temperature  $T$  for two values of the chemical potential  $\mu$ , both in the MF and FRG cases. The dashed horizontal black line in the right panel corresponds to the SB limit.

and the gluonic one is

$$P_{SB}^Q = T^4 \frac{\pi^2}{45} d_A. \quad (6.25)$$

Furthermore we defined  $d_A = N_c^2 - 1$ ,  $N_c$  is the number of colors,  $d_F = N_c N_f$  and  $N_f$  is the number of flavors.

In the case of the QM model, at high temperature the main contribution to the pressure comes from the (nearly) massless quarks, while both the pions and the sigma bosons are massive due to the (partial) restoration of chiral symmetry and so effectively decouple. Thus, in the QM model, the Stefan-Boltzmann limit corresponds to the purely fermionic contribution. In particular, in the case we are examining, i.e., for  $N_f = 2$  and  $N_c = 3$ , the Stefan-Boltzmann pressure is given by

$$P_{SB}^{QM} = T^4 \frac{7\pi^2}{30} \left[ 1 + \frac{30}{7\pi^2} \left( \frac{\mu}{T} \right)^2 + \mathcal{O} \left( \frac{\mu}{T} \right)^4 \right] \quad (6.26)$$

and the associated rescaled entropy density is

$$\frac{s_{SB}^{QM}}{T^3} = \frac{14\pi^2}{15} \left[ 1 + \frac{30}{7\pi^2} \left( \frac{\mu}{T} \right)^2 + \mathcal{O} \left( \frac{\mu}{T} \right)^4 \right]. \quad (6.27)$$

From now on we will refer to the SB limit considering the constant, temperature and chemical-potential independent part of Eq.(6.27), namely

$$\frac{s_{SBI}^{QM}}{T^3} = \frac{14\pi^2}{15}. \quad (6.28)$$

The SB limit is depicted in the right panel of Fig. 6.1 as the black dashed horizontal line. Equation (6.27) justifies then the observed behavior of the rescaled entropy density in Fig. 6.1 for high temperatures: in the  $\mu = 0$  case the rescaled entropy density tends to the SB limit from below while, due to the positive finite chemical-potential correction, the SB limit is approached from above in the  $\mu = 0.3$  GeV case, and  $s_{SB}^{QM}/T^3 - s_{SBI}^{QM}/T^3 \propto 1/T^2$  as suggested by Eq.(6.27).

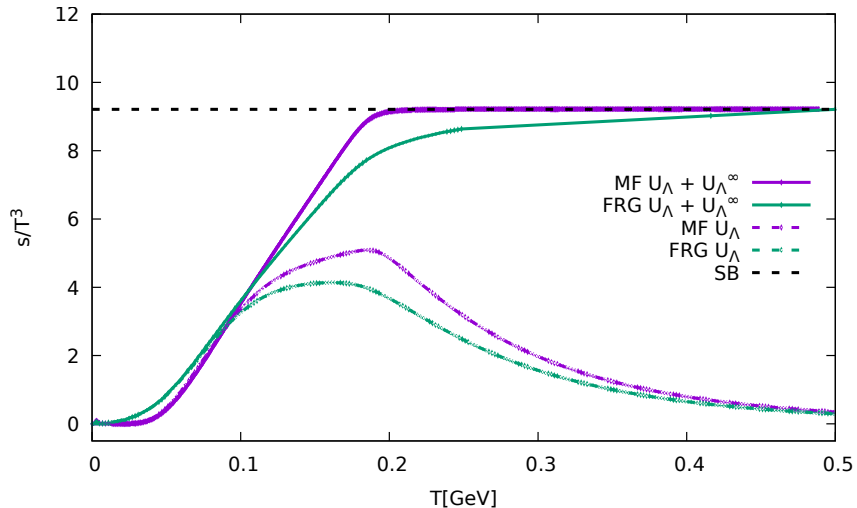


Figure 6.2: Rescaled entropy density as a function of temperature  $T$ , both in the case of MF (purple lines) and FRG (green lines). The solid lines represent the results obtained including the UV correction Eq. (6.20) to the UV initial condition, while the dashed lines are obtained neglecting those corrections. The black dashed horizontal line corresponds to the SB limit.

Finally, we point out the importance of the inclusion of the UV corrections to the initial condition described in Eq. (6.20) for the correct calculation of thermodynamic quantities at high temperatures. In particular, Fig. 6.2 contains a comparison between the results for the rescaled entropy density obtained including the UV corrections (solid lines) and neglecting them (dashed lines). The results are shown for  $\mu = 0$  and for both the MF and the FRG cases. One can clearly observe that only the results which include the UV corrections exhibit the correct asymptotic high-temperature behavior, reaching the SB limit (black dashed line), while the results for which the UV corrections have not been included start deviating at a temperature which is  $T \sim \Lambda/2\pi$ , in agreement with the discussion in Sec. 6.3.2 on the inclusion of the high-energy Matsubara modes.

## 6.5 Thermodynamic geometry results

In this section we will finally turn to the main focus of this chapter: the thermodynamic geometry of the QM model. In particular, as we did in the previous section, we compare the results obtained within the mean-field approximation, neglecting the bosonic fluctuations, with the results of calculations that take into account the fluctuations by solving the full FRG flow equation for the average effective action, emphasizing the effect of fluctuations on the studied quantities. In particular, we will focus on the determinant of the metric  $g$  and on the thermodynamic curvature  $R$ . We then study what happens to these quantities when approaching the chiral limit ( $c=0$ ) and how they evolve as the RG scale  $k$  is lowered, i.e., following their RG time  $t$  evolution.

### 6.5.1 Finite pion mass

We begin our analysis of the thermodynamic geometry of the QM model considering the physical limit, i.e., the one in which the explicit symmetry breaking term  $c$  is finite and has the physical value  $c = M_\pi^2 f_\pi$ . Firstly, we discuss the determinant of the metric  $g$ . In Fig. 6.3 we show the determinant of the thermodynamic metric,  $g$ , versus  $T$ , computed for two values of the chemical potential,  $\mu = 0$  and  $\mu = 0.3$  GeV. We present the results



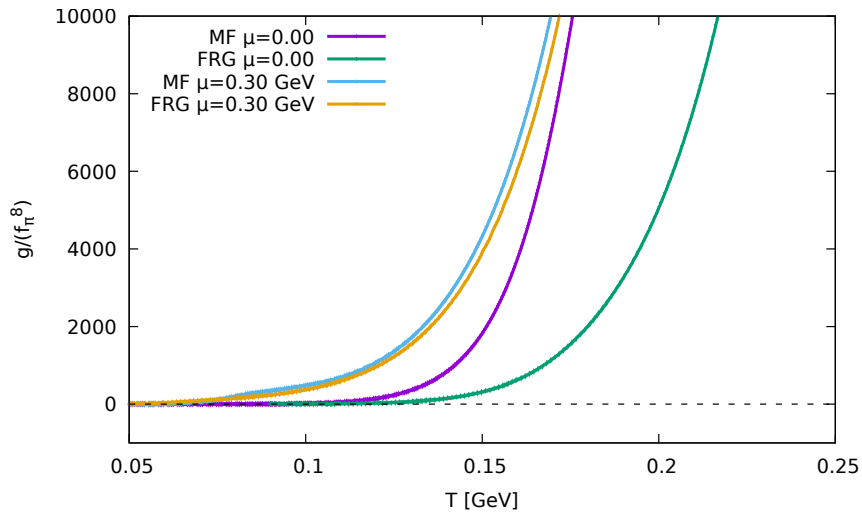


Figure 6.3: Determinant of the metric  $g$ , normalized by  $f_\pi^8$ , as a function of temperature  $T$  for different values of the chemical potential  $\mu$ , both in the case of MF and FRG. The dashed black horizontal line indicates 0.

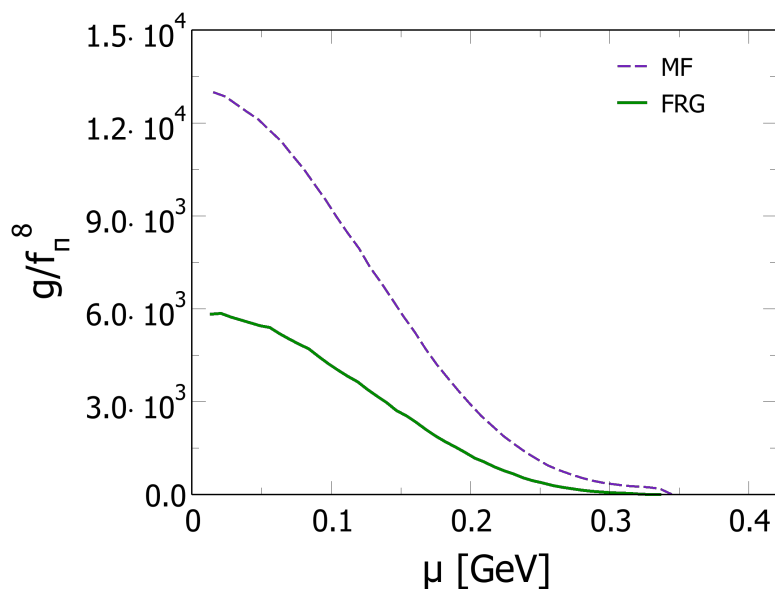


Figure 6.4: Determinant of the thermodynamic metric,  $g$ , versus  $\mu$  computed at  $T = T_c$ , within the mean-field approximation (dashed line) and FRG (solid line).

obtained within the mean-field approximation and within the FRG. We point out that  $[g] = [T]^8$ , that is why in Fig. 6.3 and Fig. 6.4 we normalize  $g$  by dividing it by the energy scale  $f_\pi^8$ . We can observe that  $g$  increases both with temperature and chemical potential, but FRG leads to smaller values compared to the MF ones. The results are in qualitative agreement with [215], where fluctuations were introduced within a Gaussian approximation.  $g = 0$  corresponds to the thermodynamic instability of the system, that is to a phase transition. What we can observe then is that, since for small values of the chemical potential the system is very far from criticality, and a smooth crossover takes place,  $g$  is not sensitive enough to exhibit any modification at the crossover temperature and keeps its monotonic increasing behavior. This is not the case for  $\mu = 0.30$  GeV, because we can see a rapid decrease of  $g$  close to the critical temperature  $T_c|_{\mu=0.3 \text{ GeV}} \sim 0.09$  GeV for the MF and  $T_c|_{\mu=0.3 \text{ GeV}} \sim 0.07$  GeV for FRG. This signals that the system is getting closer to the critical point, where  $g = 0$  exactly.



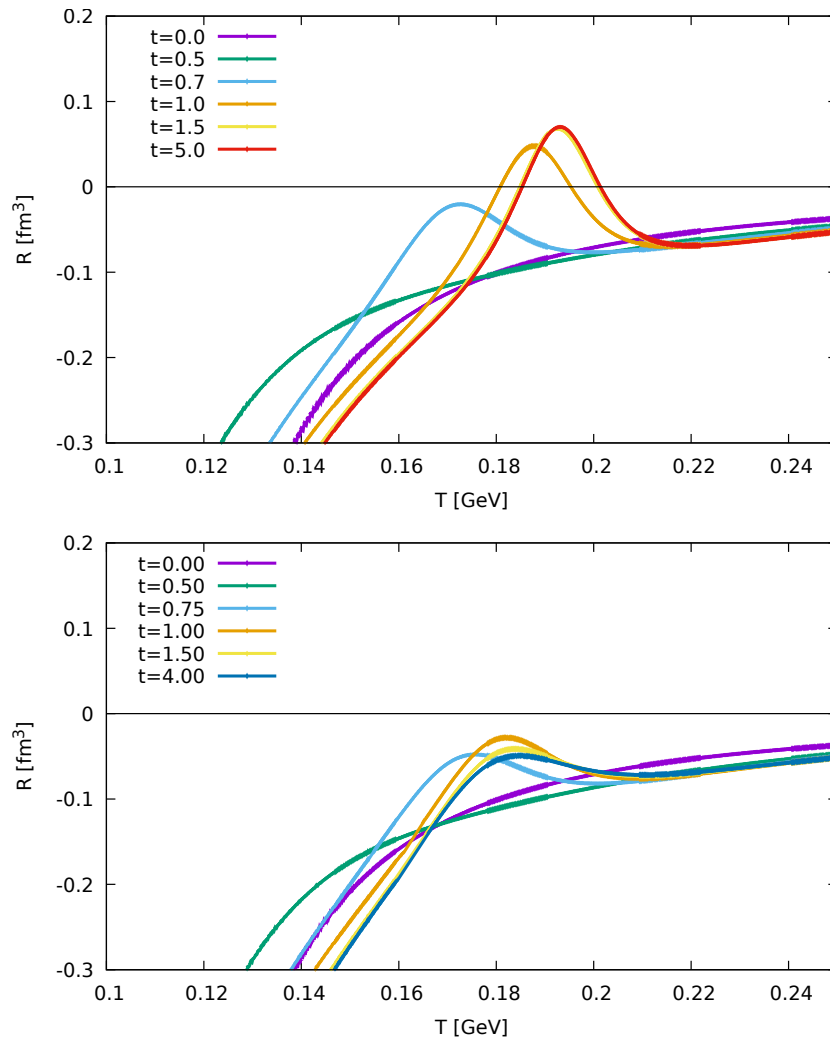


Figure 6.5: Thermodynamic curvature,  $R$ , versus  $T$ , at  $\mu = 0$ , for different values of the RG time  $t$ . Calculations correspond to the mean-field approximation (upper panel) and the FRG scheme (lower panel).

To complete the study of the determinant of the metric  $g$ , we show in Fig. 6.4  $g$ , as a function of  $\mu$ , computed at the critical temperature  $T = T_c$ . We present the results obtained within the mean-field approximation (dashed line) and in the FRG approach (solid line). Once again, the results are in qualitative agreement with a previous work [215], where fluctuations were introduced within a Gaussian approximation. We do not find  $g = 0$  exactly, which corresponds to the real second-order phase transition, because in this model chiral symmetry is explicitly, albeit softly, broken by the finite quark mass, hence a phase transition is replaced by a smooth crossover. However,  $g(T_c)$  decreases with  $\mu$ , signaling that the system is approaching criticality, that is the critical endpoint, in agreement with our previous observations. Moreover, we note that including fluctuations results in the lowering of  $g$ , in agreement with what we observed previously and with other works [215].

We now discuss the thermodynamic curvature,  $R$ . It is expected that  $R$  diverges at a second-order phase transition, while it is not obvious the behavior of  $R$  near a smooth crossover. However, as stated in the introduction, we expect a peak structure in the proximity of the crossover temperature.

In order to better understand the results on  $R$  obtained within the FRG at finite chemical potential, we preliminary analyze the curvature versus  $T$  at  $\mu = 0$ , with and without fluctuations, for several values of the RG time  $t$ , which regulates the scales of the integration of the fluctuations. In Fig. 6.5 we show  $R$  as a function of the temperature

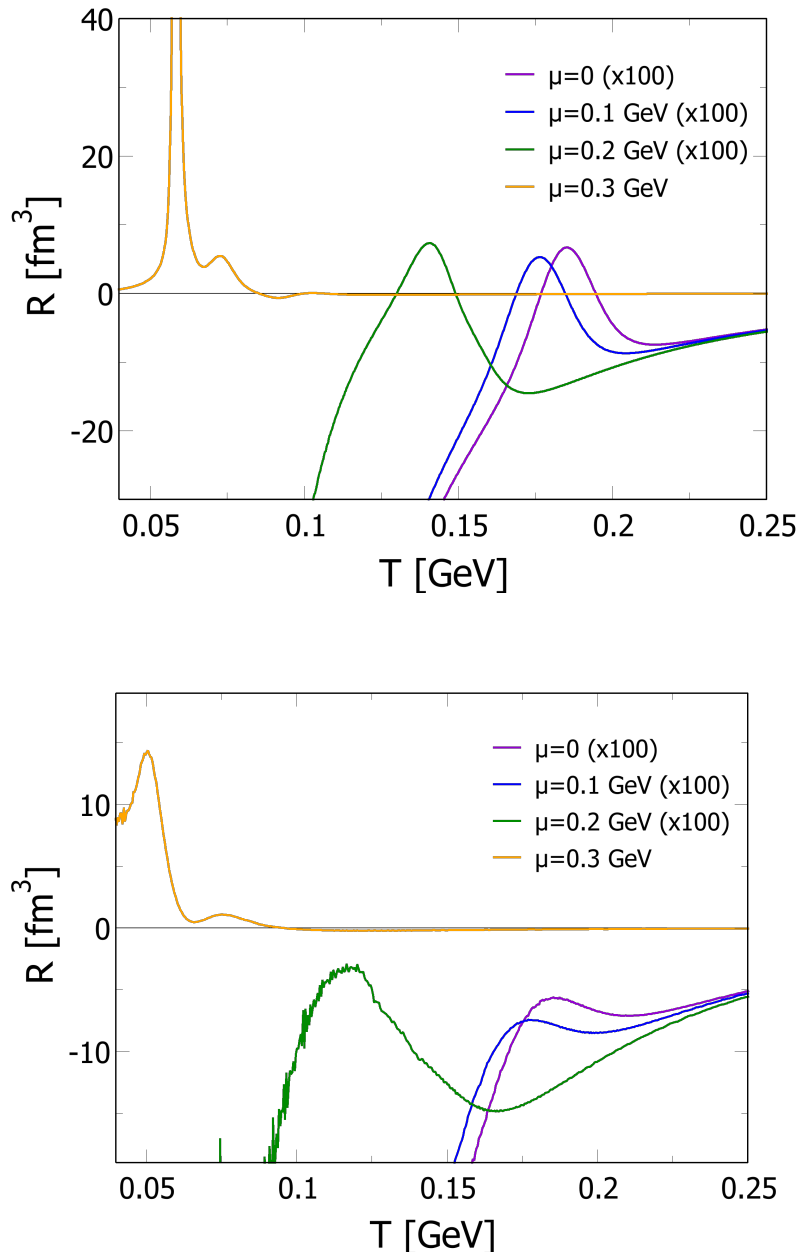


Figure 6.6: Thermodynamic curvature,  $R$ , versus  $T$ , for several values of  $\mu$ . Calculations correspond to the mean-field approximation (upper panel) and the FRG scheme (lower panel).

$T$ , at  $\mu = 0$  for different RG times  $t$ , both in the MF (upper panel) and in the FRG (lower panel) case. In both cases we observe that the peak close to the crossover temperature forms as  $t$  is increased. The MF calculations show that this peak monotonously grows as the fluctuations are integrated out. In particular, at a given scale, the peak becomes positive and then stays constant in time, since a sufficiently low scale is reached and the  $t$ -evolution freezes. This positive peak, which forms in the IR, can be interpreted as the emergence of a boson-like behavior of the system around  $T_c$ , namely of a statistical attraction in phase space due to long-range correlations that develop around  $T_c$  that overcome the statistical fermionic repulsion. This implies the existence of a scale  $\bar{t} \sim 0.8$ , and corresponding  $\bar{k} \sim 0.45$  GeV, at which this behavior begins to appear and that signals the dominance of the boson-like behavior over the fermionic one close to the crossover temperature.

The formation of a peak in  $R$  as time is increased is also found when fluctuations are

included within the FRG. However, we note that fluctuations lower the overall magnitude of  $R$ , in agreement with [215]. We also note that, despite the peaks of  $R$  become more prominent initially as  $t$  is increased, this behavior changes at a given RG time  $t^* \sim 1$ , and the associated momentum scale  $k^* \sim 0.37$  GeV, where the peak starts to decrease once again. At later times,  $t > 3$ , the results do not change in a way we can appreciate, thus we can consider the IR limit to be reached. The inversion of the behavior at  $t^*$  may signal the scale at which the bosonic fluctuations become dominant over the fermionic ones, lowering the peak. As a consequence  $R$  does not change sign as it does in the mean-field calculations. Hence, it is likely that, although the qualitative behavior of  $R$  is independent of the approximation used (mean field versus FRG), in the IR, the change of nature from fermion-like to boson-like depends on the calculation scheme adopted. The results shown in Fig. 6.5 will be useful to interpret the behavior of  $R$  we discuss below.

In Fig. 6.6 we plot  $R$  versus  $T$  for several values of  $\mu$ , obtained within the mean-field approximation and the full FRG calculation. In both the upper MF panel and the lower FRG one of Fig. 6.6, we multiplied times 100 the obtained  $R$  for  $\mu = 0$ ,  $\mu = 0.1$  GeV and  $\mu = 0.2$  GeV, in order to make the results more readable. Firstly, we note that the trend of  $R$  is qualitatively similar in both calculations. Within the mean-field approximation, at  $\mu = 0$  the curvature locally develops a peak in correspondence of the chiral crossover, signaling that  $R$  is capable to capture the pseudo-critical behavior of the quark condensate. Increasing the chemical potential,  $R$  maintains its local peak structure, but as the critical endpoint is approached, the peaks become more pronounced. This is in agreement with the general understanding of  $R$ , which is expected to diverge at a second-order phase transition. Moreover, we note that, at large  $\mu$  the thermodynamic curvature develops several peaks in the temperature range of the chiral crossover, although the most pronounced peak does not necessarily show up at the critical temperature. This behavior, already noticed in [214], shows that  $R$  is not necessarily as sensitive as other quantities, like the chiral susceptibility or  $|dM/dT|$ , on the changes of the quark condensate at  $T = T_c$ , but it is still capable to measure sensible deviations in the pressure around the chiral crossover.

Including fluctuations does not change the qualitative behavior of  $R$ . Therefore, we conclude that the fact that  $R$  is sensitive to the chiral crossover is not an artifact of the mean-field approximation, rather it is a quite solid statement. However, as already remarked in Fig. 6.5, the inclusion of fluctuations lowers the value of  $R$  around the chiral crossover; particularly, when  $\mu$  is small,  $R$  remains negative also around the crossover, while in the mean-field approximation it changes sign. Therefore, it is likely that the change of nature of the interaction at the mesoscopic level, from fermion-like to boson-like, depends on the approximation used in the calculation when the system is far from criticality. Hence, this implies that, at small  $\mu$ , the fluctuations substantially change the geometry of the manifold. On the other hand, when the critical endpoint is approached at large  $\mu$ , we find that  $R$  changes sign also in the FRG calculation, and the mean-field results do not qualitatively differ from those obtained within the FRG. Hence, we conclude that when this system approaches criticality,  $R$  changes sign and locally develops a marked peak: this conclusion was anticipated in previous mean-field calculations [214, 216] and stands also in case fluctuations are taken into account via FRG.

### 6.5.2 Towards the chiral limit

In order to make the results on  $R$  obtained within the FRG even more understandable, we now analyze the curvature versus  $T$ , with and without fluctuations, for several values of the parameter  $c$  that regulates the explicit breaking of chiral symmetry in the model at

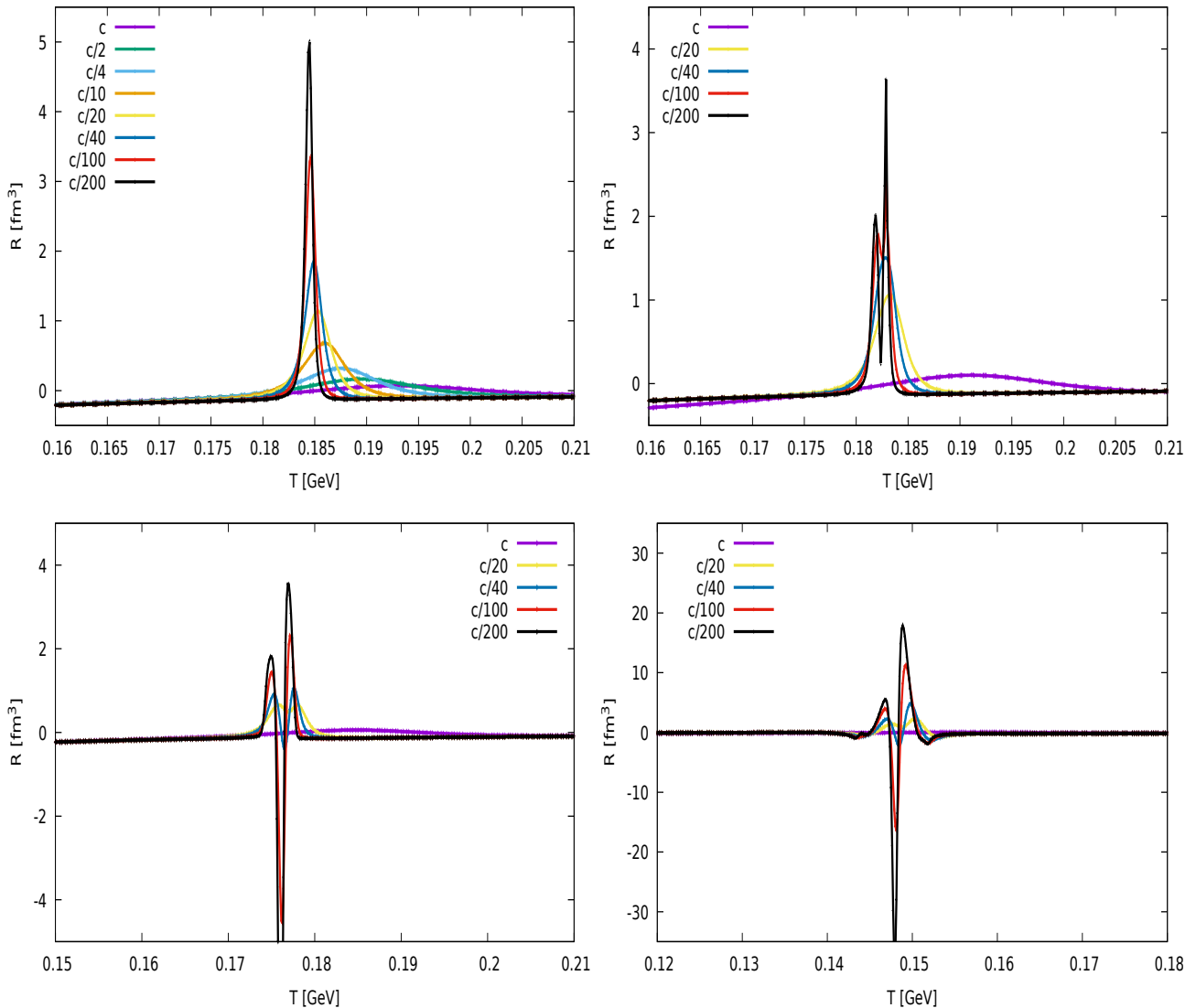


Figure 6.7: Thermodynamic curvature  $R$  as a function of temperature  $T$ , in the MF approximation, for four values of the chemical potential,  $\mu = 0$  (upper left panel),  $\mu = 0.05$  GeV (upper right panel),  $\mu = 0.1$  GeV (lower left panel) and  $\mu = 0.2$  GeV (lower right panel). In each plot, results are shown for several values of the parameter  $c$ , which is artificially lowered from  $c = M_\pi^2 f_\pi$ , corresponding to the physical limit, to  $c/200$ . The case  $c = 0$ , not shown, would correspond to the chiral limit.

hand.

In order to understand the general behavior of the thermodynamic geometry as the pion mass is lowered, i.e., as the system approaches the chiral limit, we begin our investigation with an explorative MF study. In this way, we will have more information at our disposal when comparing the MF and the FRG results. In Fig. 6.7 we plot  $R$  versus  $T$ , within the mean-field approximation, for four different values of the chemical potential,  $\mu = 0$ ,  $\mu = 0.05$  GeV,  $\mu = 0.1$  GeV and  $\mu = 0.2$  GeV. We show results for several values of the parameter  $c$ , considering that  $c = M_\pi^2 f_\pi$  leads to the physical limit while  $c = 0$  corresponds to no explicit breaking of chiral symmetry, i.e., to the chiral limit. Performing calculations of  $R$  at  $c = 0$  is numerically demanding near the phase transition, hence we stop at  $c/200$ . In order to avoid confusion, from now on we denote as  $c$  solely the value of the parameter at the physical point, namely  $c = M_\pi^2 f_\pi$ ; we then artificially lower the value of this parameter. We can observe that, in all panels of Fig. 6.7, for small values of  $c$  (almost chiral limit) the curvature is enhanced in the pseudo-critical region, while the peak of  $R$  becomes smoother as  $c$  approaches the physical limit. This

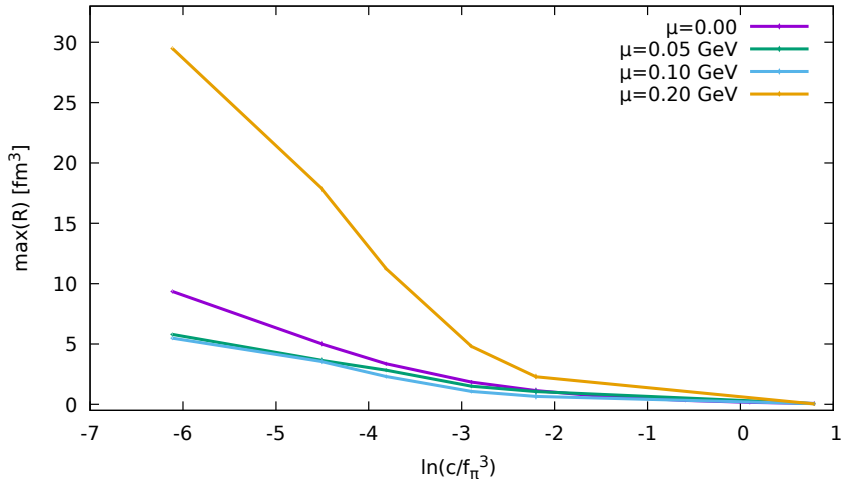


Figure 6.8: Maximum of  $R$ , as a function of the logarithm of the rescaled artificially lowered explicit symmetry breaking parameter  $c/f_\pi^3$ , for the same values of the chemical potential used in Fig. 6.7.

is more clearly depicted in Fig. 6.8, where we show the value of the maximum of  $R$ , as a function of the logarithm of the artificially lowered explicit symmetry breaking rescaled parameter  $c/f_\pi^3$ , for the same values of the chemical potential used in Fig. 6.7. The parameter  $c$  has been rescaled by a factor of  $f_\pi^3$  since it has the dimensions  $[c] = [\text{GeV}^3]$ . We can clearly observe that the value of the maximum of  $R$  increases as  $c$  is lowered, in agreement with our previous discussion. Furthermore, in analogy to what we observed commenting Fig. 6.6, the value of the peak of  $R$  is significantly higher for higher values of the chemical potential, signaling that also the chiral limit feels the influence of the critical endpoint, where the transition is of second order both in the physical and in the chiral limits. We can also point out that for all the values of the chemical potential in Fig. 6.7,  $R$  changes sign around the crossover temperature  $T_c$ , in agreement with previous results [214, 215, 216] and confirming the emergence of a boson-like behavior of the system around  $T_c$ . As a final comment about the results shown in Fig. 6.7, we can observe the emergence of a multi-peak structure in  $R$  around the crossover temperature  $T_c$ . This could be explained by considering that  $R$  takes into account several momenta of the thermodynamic potential, up to the third order both in temperature and chemical potential. Since, even at small but finite  $c$ , the transition still remains a crossover, different observables can exhibit peaks at different pseudo-critical temperatures, which do not necessarily coincide with the crossover one identified via the chiral condensate.

Due to the absence of multiple peaks for  $\mu = 0$ , we can conclude that the results obtained at vanishing chemical potential provide more straightforward information for the investigation of the features that  $R$  exhibits approaching the chiral-limit compared to the finite  $\mu$  ones. Thus, in this last part of this section, we focus on the  $\mu = 0$  case.

As a last result for our mean-field investigation, in Fig. 6.9 we show the behavior of the  $3 \times 3$  determinant (upper panel), which can be obtained from Eq. (6.10) as  $-2Rg^2$ , and the inverse of the square of the determinant of the metric  $g^{-2}$  (lower panel) as a function of temperature for different values of the explicit symmetry breaking parameter  $c$ , for  $\mu = 0$ . We restricted the plot to the range in temperature around the chiral crossover temperature. We can notice that the appearance of the peak in the thermodynamic curvature  $R$  around the crossover temperature we observed in Fig. 6.7 originates from the combination of two different effects: on one hand the  $3 \times 3$  determinant  $-2Rg^2$  develops a peak, in correspondence of the crossover temperature, which increases in magnitude as  $c$  is lowered; on the other hand  $g^{-2}$  exhibits a local maximum and a

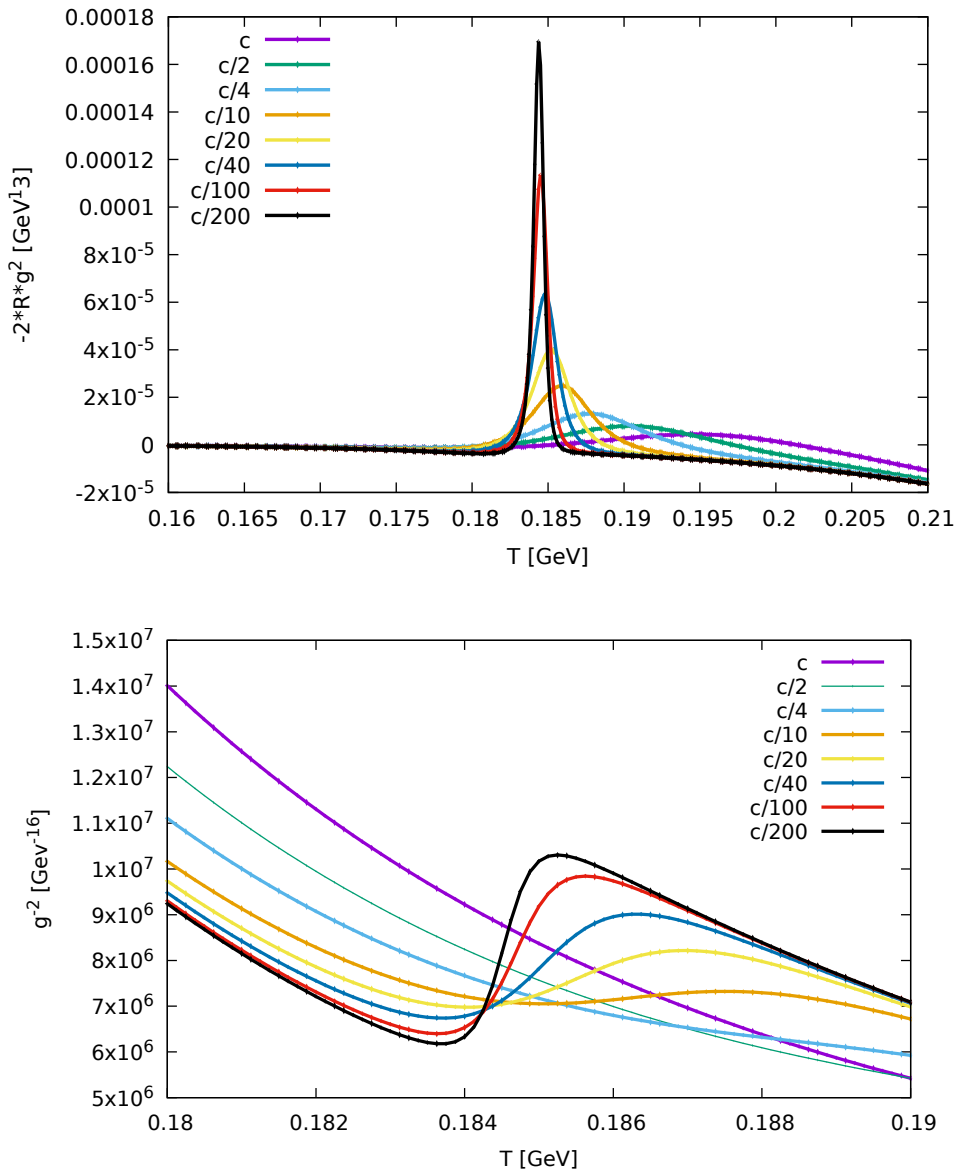


Figure 6.9:  $3 \times 3$  determinant  $-2Rg^2$  (upper panel), and the inverse of the square of the determinant of the metric  $g^{-2}$  (lower panel) as a function of temperature  $T$  for different values of the explicit symmetry breaking parameter  $c$ , in the MF and for  $\mu = 0$ .

local minimum, which seem to become closer and closer in temperature but further in magnitude (the minimum gets deeper and the maximum gets higher) as  $c$  approaches the chiral limit. This is in agreement with what one would expect approaching the chiral limit and the associated change of the phase transition from a crossover to a second-order phase transition, since in that case  $g \rightarrow 0$  and thus  $g^{-2} \rightarrow \infty$ . Furthermore, this structure seems to tend to a discontinuity as  $c$  vanishes, with the maximum turning into a single-point divergence, confirming how hard and numerically expensive the chiral limit is. We can also point out that, as previously observed, in the case of  $\mu = 0$  the different momenta of the thermodynamic potential, which enter both in  $-2Rg^2$  and in  $g^{-2}$ , exhibit the analyzed behavior at the same crossover temperature, in agreement with the absence of a multiple-peak structure in  $R$  for vanishing chemical potential.

Finally, in Fig. 6.10 we plot  $R$  versus  $T$  at  $\mu = 0$  within the mean-field approximation (upper panel) and with the inclusion of fluctuations via FRG (lower panel). We show results for several values of  $c$ . We note that, in both panels of Fig. 6.10, the curvature is enhanced in the pseudo-critical region for small values of  $c$  (almost chiral limit), while the peak of  $R$  becomes smoother as  $c$  approaches the physical limit. Moreover, as we

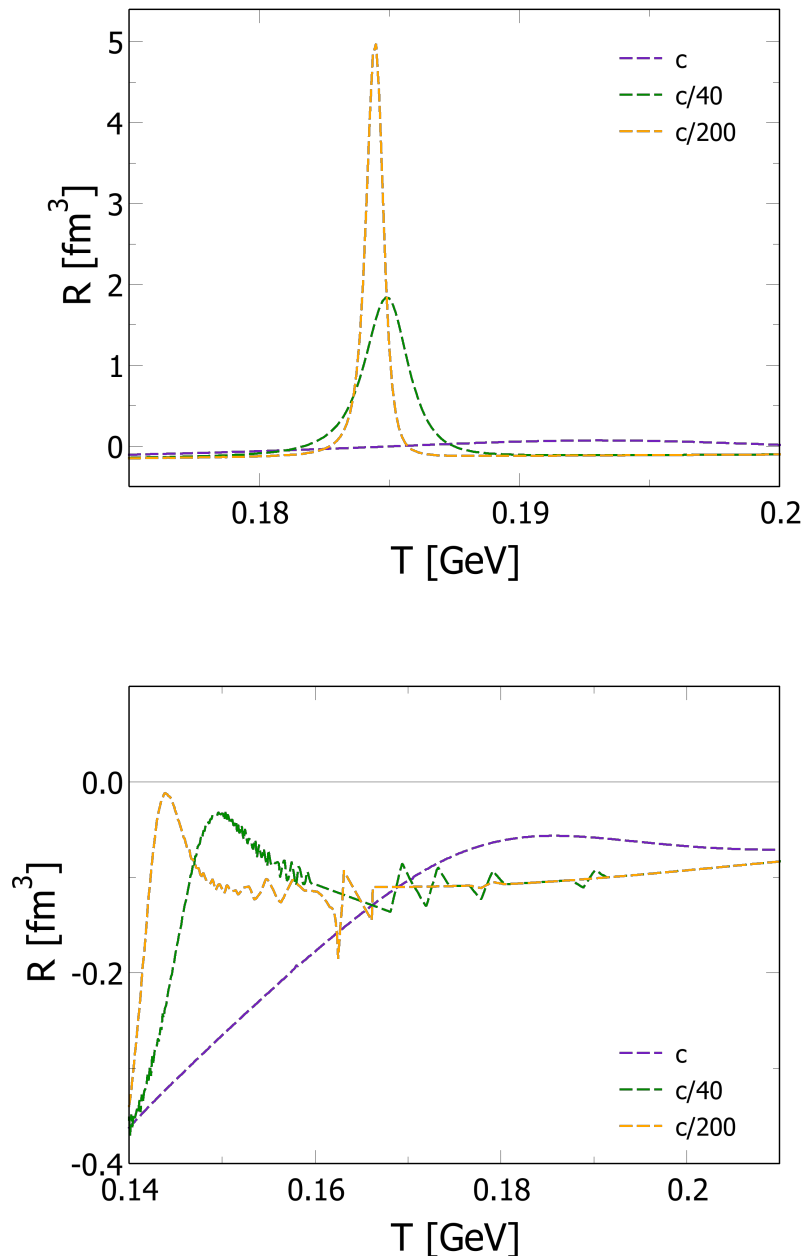


Figure 6.10: Thermodynamic curvature,  $R$ , versus  $T$ , for several values of  $c$ . The upper panel corresponds to the mean-field approximation, while the lower panel to the calculations within the FRG.

already pointed out, the inclusion of fluctuations results in the lowering of the peaks of  $R$  in the pseudo-critical region. Within the mean-field approximation,  $R$  changes sign around  $T_c$ , as expected from previous results [214, 215, 216]: this, as previously discussed, was interpreted as the emergence of a boson-like behavior of the system around  $T_c$ . This behavior of  $R$  is also found when fluctuations are included within the FRG (lower panel of Fig. 6.10). However, we note that fluctuations lower the overall magnitude of  $R$ , in agreement with [215]. We also note that, despite the fact that the peaks of  $R$  become more prominent as  $c$  is lowered, hence approaching the chiral limit,  $R$  does not change sign as it does in the mean-field calculations. Hence, this confirms our previous statement, i.e., that the qualitative behavior of  $R$  is independent of the approximation used (mean field versus FRG) at the physical point ( $c = M_\pi^2 f_\pi$ ) while the change of nature from fermion-like to boson-like depends on the calculation scheme



adopted.

As a final remark, we point out that the peak of  $R$  moves towards smaller temperatures as the chiral limit is approached, i.e., as  $c$  is lowered. This is in agreement with the fact that the critical temperature is lower in the chiral limit, when the real second-order phase transition takes place, in comparison to the smooth-crossover temperature in the finite pion mass case.

## 6.6 Conclusions and outlook

We studied the thermodynamic geometry, and in particular computed the thermodynamic curvature  $R$ , of the chiral phase transition of Quantum Chromodynamics, within the quark-meson model and the functional renormalization group method. The advantage of this method is that it allows to exactly include fluctuations, differently from previous approaches [215] in which fluctuations were introduced only within a Gaussian approximation.

We found that the qualitative behavior of  $R$  is not very different from the one previously computed within mean-field calculations, as well as within calculation schemes that include fluctuations by a Gaussian approximation. In particular,  $R$  seems to keep its local peak structure in the proximity of the chiral crossover at small chemical potential; moreover, it is enhanced at the critical point, signaling that when the system approaches criticality  $R$  could diverge, supporting the arguments of hyperscaling [187].

We also found that the change of sign of  $R$  near the chiral crossover, discussed previously in the literature [214, 215, 216, 244, 245], does not always happen when fluctuations are taken into account within the functional renormalization group approach; however, as the system approaches criticality, the change of sign from negative (fermion-like behavior) to positive (boson-like behavior) takes place. Hence, we conclude that the change of sign of  $R$  near the critical endpoint seems to be quite a robust prediction of the chiral effective models.

It would be interesting to analyze if the behavior of  $R$  we highlighted in this chapter does not change when the truncation adopted in the functional renormalization group approach is improved; for example, the inclusion of the scale-dependent wave function renormalization factors of the boson and the quark fields is worth further investigation, due to the possible link of this to the formation of inhomogeneous phases at large chemical potential. Another possible improvement is the introduction of other condensation channels, which could include diquarks or meson condensates. A potential application would be the QM model with a finite isospin chemical potential,  $\mu_I$ , at vanishing (or small)  $\mu$ . This would be extremely interesting, due to the opportunity to directly compare the obtained results with lattice-QCD calculations, since a finite  $\mu_I$  does not lead to a sign problem, and would give the opportunity to study  $R$  in presence of potentially two condensates, namely a pion condensate beside the standard chiral one.



# Quark-Meson model: regulator-dependence study

This chapter is based on an ongoing project in collaboration with Jonas Stoll, Niklas Zorbach, Lutz Kiefer, Jens Braun and Dirk H. Rischke. Most of the results and parts of the text are taken from a preliminary version of a publication in preparation. Moreover, the results will also be used in PhD theses of my collaborators.

## 7.1 Introduction and motivation

In the previous chapters we pointed out the relevance of the choice of the effective theories, which model the low-energy degrees of freedom of QCD and inherit their respective symmetries, since the phase structure of these theories might qualitatively agree with the QCD expected one. In particular we focused on the two-flavor quark-meson model, which we already extensively discussed and whose chiral symmetry-breaking/restoration pattern may serve as an effective description for the QCD behavior in a moderate-density regime.

In general, within the used functional approach, if the path integral of any QFT is solved exactly it is possible to arrive at the same effective action independently of the regularization scheme. However, effective theories, even though they are build on easier to handle degrees of freedom, are still interacting quantum field theories in their own right. Thus their full solution is highly non-trivial and most of the times directly impossible. In particular, we already discussed how, in the context of the FRG, this difficulty translates into the need of the choice of a truncation for the effective average action. In principle, the FRG machinery predicts a trajectory in theory space spanned as the RG scale  $k$  changes from the cutoff scale  $\Lambda \rightarrow \infty$ , where the effective average action should coincide with the bare action, to  $k = 0$ , where the full quantum effective action should be recovered. These trajectories are clearly dependent on the choice of the regulator used in the FRG flow equation, but the properties of the regulator Eqs. (3.4)-(3.6) guarantee that both the initial and final points of these trajectories are regulator-independent.

However, the outcome of truncated FRG calculations depends, in general, on many factors such as the truncation, the choice of the regulator and the UV-cutoff scale present both in the regulator and in the truncated-effective action. In fact, a truncation restricts the flow of the scale-dependent effective-average action to a subspace of the theory space, which is not guaranteed to contain the desired IR limit. Since to different regulators are associated different flows in theory space, it is not trivial that those flows will lead to the same IR limit. Furthermore, oftentimes it is not possible to reach arbitrarily low IR

scales, and the RG flow has to be interrupted at a finite IR scale. This implies that also the finite IR-cutoff scale may influence the final outcome of the result and thus it has to be taken into account carefully.

In order to restrict the number of elements which play a role in the determination of the final outcome of the FRG evolution, in this work we focus on the study of the regulator dependence, and on the impact that the regulator choice has on the IR observables and on the phase diagram of the model. In particular, we try to reduce the UV-cutoff dependence by exploiting the so called *RG consistency* (see, e.g., [248]), which, by construction, enables us to fix the UV-cutoff-independent RG flows via UV-cutoff-dependent initial conditions. We also decide to fix the truncation, and thus we face these problems in the mean-field (MF) approximation (or one-loop approximation or large- $N_c$  approximation) first, where we can have more control on the parameters and also comparison with semi-analytic results is possible, and then in the local potential approximation (LPA).

The regulator dependence of the FRG results, and in particular for us, of the phase diagram of the QMM, is a very delicate topic (see, e.g., Refs. [185, 184]). In this chapter we give our contribution to this ongoing discussion by analyzing several aspects associated to the regulator dependence of IR-FRG results, namely:

- the choice of different regulator classes, such as the standard one defined in Eq.(3.7) and the quasi-particle or Fermi-surface one, which is presented in more details in [87] and in App. D.2.3;
- the possibility to use different shape functions for the regulators, and in particular the Litim, exponential squared and the newly introduced "smooth Litim" one [249];
- the impact on the IR observables, and in particular on the phase diagram of the choice of the UV-cutoff scale.

Our goal is thus to present a systematic discussion on all this different issues, exploiting, as already mentioned, the QM model both in the simplified MF, large- $N_c$  approximation, and in the full LPA. In this way, the choice of this rather simple model can give us more flexibility in this study, allowing us to fully focus on the FRG-related and especially regulator-related issues we previously highlighted.

## 7.2 Model and setup

### 7.2.1 Quark-Meson model

We already introduced the quark-meson model and we extensively discussed its properties in the previous chapters. Thus, proceeding as we did in Sec. 5.6.1, we begin this section by considering the LPA ansatz for the effective-average action of the QM model at finite temperature and quark-number density in the chiral limit

$$\Gamma_k[\bar{\Psi}, \Psi, \phi] = \int_0^{1/T} dx_0 \int d^3x \left\{ \bar{\psi}(\gamma_\mu \partial^\mu + h(\sigma + i\gamma^5 \vec{\tau} \cdot \vec{\pi}) - \mu\gamma_0)\psi + \frac{1}{2}(\partial_\mu \sigma)^2 + \frac{1}{2}(\partial_\mu \vec{\pi})^2 + U_k(\sigma^2 + \vec{\pi}^2) \right\}. \quad (7.1)$$

Once again, in this study we focus on the global chiral symmetry of the QMM and its spontaneous symmetry breaking (SSB), indicated by a non-zero expectation value of one of the mesonic fields.

As previously, the next step for our FRG setup is the choice of an initial condition for the FRG flow equation, which corresponds to assign a shape to the bare potential in the UV ( $k = \Lambda$  or  $t = 0$ ). In particular, for the moment we choose a quartic potential

$$U_\Lambda(\sigma) = \frac{m_{\text{UV}}^2}{2}\sigma^2 + \frac{\lambda_{\text{UV}}}{4}\sigma^4, \quad (7.2)$$

where  $m_{\text{UV}}^2$  and  $\lambda_{\text{UV}}$  are coupling constants. We dedicate a much wider and detailed discussion on the choice of the initial condition, and actually on its construction via the RG consistency, in the following sections.

### 7.2.2 RG consistency and parameter dependence

As we discussed in Chapter 3, a solution  $\Gamma_k[\Phi]$  of the Wetterich equation can be regarded as a trajectory in the space of all possible actions, i.e., the theory space. The flow starts from the UV action towards the full-quantum-effective (IR) action  $\Gamma[\Phi]$  in the IR-limit  $t \rightarrow \infty$ .

As we pointed out, the choice of different regulators leads to different flows in theory space, and in principle also the choice of different initial condition in the UV has the same effect, due to the finite value of the UV cutoff. However, one can ensure that different flows originated by different regulators approach the same full quantum-effective action  $\Gamma[\Phi] = \Gamma_{k=0}[\Phi]$  in the IR limit  $k \rightarrow 0$ , within the given truncation, by choosing a proper initial conditions  $\Gamma_{k=\Lambda}[\Phi]$  for the respective flows at the cutoff-scale  $\Lambda$ . Flows with this property are called *RG-consistent flows* [248]. This property can be formulated as follows:

$$\Lambda \frac{\Gamma_{k=0}[\Phi]}{\partial \Lambda} = 0, \quad (7.3)$$

Which implies that the final outcome of the FRG flow evolution, i.e., the full quantum-effective action, has to be independent of the choice of the UV-cutoff. To satisfy the latter requirement, the UV initial condition  $\Gamma_\Lambda[\Phi] \equiv \Gamma_{k=\Lambda}[\Phi]$  has to be modified, in the form of a parameter tuning, in order to counter the change in the Wetterich equation under the variation of the UV cutoff. For specific classes of theories, depending on the field content, the symmetries of the theory and the choice of the truncation and of the regulator, it may be enough, in order to ensure the RG consistency (at least locally around the minimum of  $\Gamma[\Phi]$ , as we will detail in the following), to initialize the Wetterich equation with  $S_\Lambda^{\text{ren}}[\Phi]$  instead of  $\Gamma_\Lambda[\Phi]$ , where  $S_\Lambda^{\text{ren}}[\Phi]$  consists of a standard kinetic term and a low order polynomial in the fields with a few  $\Lambda$ -dependent couplings. If this is the case, we call the model in this specific setup *renormalizable*. A renormalizable model can then be meaningfully defined by a simple bare action, if the latter is identified with  $S_\Lambda^{\text{ren}}[\Phi]$ . Thus, for our study it is convenient to focus on this class of theories, to which the QM-model belongs. This justifies the choice of the form of the initial condition defined in Eq.(7.2).

In the presence of external parameters in the model, such as the temperature and the chemical potential, one should in general check that the choice of the RG-consistent initial condition is independent of these parameters. This implies that the tuning of UV parameters has to be performed only once, at a given fixed value of the parameters. For convenience, one can choose what we will refer to as the vacuum in the following, i.e., the case of vanishing external parameters. In order for this to be true, i.e. for a proper regulator choice, the Wetterich equation has to become independent of the external parameters for sufficiently large-RG scales. It immediately follows that an RG-consistent vacuum flow, to a desired vacuum full-quantum effective action, is also an RG-consistent flow with external parameters at sufficiently high RG scales. Thus, once

the RG-flow has been properly initialized at a sufficiently large-RG scale in the vacuum, one can then get a prediction for the full quantum-effective action in the IR also in the presence of the external parameters. This implies that, in order to avoid cutoff-artifacts, one has to be sure of initializing the RG-flow at RG scales which are significantly larger compared to the external parameters (and also to the scales which are internal to the theory, such as the mass of the particles).

According to the previous discussion, one has also to keep in mind that cutoff artefacts can (and most probably do) differ for different regulators, especially if the flows involving them are initialized at not sufficiently high RG-scales. As we pointed out, the choice of the vacuum flow as the one evaluated at vanishing external parameters is just a convention and a convenient choice for practical calculations, but the previous line of arguments does not rely on it and is still valid for different choices.

The previous argumentation is rigorously valid in the case of an exact solution of the Wetterich equation, i.e., if we were able to compute the full-effective action. However, as stated multiple times, this is often not possible, especially in the case of rich theories in terms of field content and symmetries. This is mainly due to the absolutely non-trivial structure of the Wetterich equation, which is a highly nonlinear functional differential equation. The natural simplification to this problem is the introduction of truncations for the effective-average action, i.e., reduce  $\Gamma_k[\Phi]$  to only a few terms which fulfill the symmetry constraints of the theory and which are then feed back into the Wetterich equation. However, truncations have a drastic impact on our previous discussion: in fact, already considering just the vacuum case, a full quantum-effective action that was accessible in the exact calculation might not be accessible in the truncated calculation, because the structure of the flow equation changed significantly. Furthermore, a quantum-effective action in vacuum that is accessible with one regulator must not be accessible with other regulators, since RG consistency in general applies only to exact calculations. However, one can still achieve cutoff independence for a specific regulator by constructing proper initial conditions, but the task of matching the IR results for different regulators is highly non-trivial. If we then include external parameters in the model and assume that the truncated flow equation can still be considered as independent of them for sufficiently large RG scales, then a vacuum flow leading to a cutoff-independent quantum-effective action will also lead to a cutoff-independent quantum-effective action in presence of external parameters, if it is used as an initial condition at sufficiently large-RG scales. One has to notice then that, choosing different regulators, the previously obtained cutoff-independent quantum-effective actions in presence of external parameters are in general not guaranteed to agree, even if it was possible to access the same vacuum quantum-effective action with all of them by independently tuning the different UV-initial conditions. This implies that the differences one observes in the finite-parameter case are caused by the used truncation. This is the reason why the choice of the regulator enters as a fundamental element of the resolution of the FRG flow equation, not only in order of stability of the flow itself, but also in terms of the obtained IR results. Finally, it has to be pointed out that if it is not possible to access the same vacuum quantum-effective action for the different considered regulators, even after the proper choice of the UV initial condition, then a comparison of the results obtained in the presence of the external parameters is not meaningful.

Once we gave this overview on what are the difficulties, our goal is to set a well-defined comparison, according to our previous discussion, of the IR results obtained for the different regulator, in order to truly appreciate their impact on the FRG computations. More precisely, we will study if it is possible to arrive at the same vacuum effective action with different regulators in the mean-field approximation and in the LPA, which would enable a fair comparison of results at non-zero  $T$  and  $\mu$ . If this is possible, the

differences in the obtained results could be traced back to the truncation itself or to a too low-cutoff scale. We will see that it is indeed possible to construct such initial conditions and that regulator dependencies are eventually small in LPA.

### 7.2.3 Preparation and regulators-shape functions

As for the previous chapters, we study the spontaneous symmetry breaking (SSB) of the chiral symmetry in the quark-meson model (QMM) in the presence of the external parameters  $T, \mu$ . A proper order parameter is the homogeneous<sup>1</sup> bosonic condensate which corresponds to the minimum of the effective potential  $U_{k=0}(\phi)$ . As we did in the previous chapters, in order to study the behavior of the condensate, we project the flow equation into the respective truncation of the scale dependent effective potential, which in the LPA case corresponds to

$$U_k(\sigma) = V^{-1} \Gamma_k[\bar{\Psi} = \Psi = 0, \phi = (\sigma, 0, 0, 0)] \quad (7.4)$$

where  $V$  is a volume factor and we used the  $SO(4)$  symmetry of the problem, such that we obtain the effective potential in the IR limit  $U(\phi = (\sigma, 0, 0, 0)) = U_{k=0}(\sigma)$ .

For simplicity, we choose regulators such that the right-hand side of the flow equation separates into a fermionic and a bosonic contribution. Furthermore, in the fermionic sector, we also classify the regulator choice by introducing two regulator classes. In particular, as regulator classes we consider the 3-dimensional standard regulator (SR) class, introduced in Eq. (3.7), as well as the 3-dimensional quasi-particle regulator (QPR) class [87], which we discuss in more detail in App. D.2.3. For general regulator shape functions  $r(y)$ , with  $y = p^2/k^2$ , the regulator contribution to the effective-average action for fermions reads:

$$\Delta S_{k,\text{SR}}^{\text{F}}[r, \phi] = -\frac{1}{\beta} \sum_{p_0} \int \frac{d^3 \mathbf{p}}{(2\pi)^3} \bar{\Psi}_{p_0, \mathbf{p}} \not{p} r_{\text{F}}(y) \Psi_{p_0, \mathbf{p}}, \quad (7.5)$$

$$\Delta S_{k,\text{QPR}}^{\text{F}}[r, \phi] = -\frac{1}{\beta} \sum_{p_0} \int \frac{d^3 p}{(2\pi)^3} \bar{\Psi}_{p_0, \mathbf{p}} \left( \sum_{z=\pm} (-\mu + z|\mathbf{p}|) r_{\text{F}} \left( \frac{(-\mu + z|\mathbf{p}|)^2}{k^2} \right) P_z \gamma_0 \right) \Psi_{p_0, \mathbf{p}}, \quad (7.6)$$

where  $\Psi_{p_0, \mathbf{p}} = \Psi(p_0, \mathbf{p})$ ,  $p_0 = \omega_n^{\text{F}} = (2n+1)\pi T$  are the discrete fermionic-Matsubara frequencies, and  $P_{\pm}$  are projectors defined in Eq. (D.33), which project onto the positive- and negative-energy solutions of the Dirac equation. For a more detailed discussion, one can refer to Ref. [87] or to App. D.2.3.

As far as the bosonic-regulator contribution is concerned, for reasons that we specify in the following, we just use the SR class, which reads:

$$\Delta S_k^{\text{B}}[r, \phi] = \frac{1}{\beta} \sum_{p_0} \int \frac{d^3 \mathbf{p}}{(2\pi)^3} \frac{1}{2} |\mathbf{p}|^2 r_{\text{B}}(y) \phi_{p_0, \mathbf{p}} \phi_{-p_0, -\mathbf{p}}, \quad (7.7)$$

where  $\phi_{p_0, p} = \phi(p_0, \mathbf{p})$  and  $p_0 = \omega_n^{\text{B}} = 2n\pi T$  are the discrete bosonic-Matsubara frequencies.

The relation between fermionic- and bosonic-shape functions is given by

$$r_{\text{F}}(y) = \sqrt{r_{\text{B}}(y) + 1} - 1. \quad (7.8)$$

<sup>1</sup>Considering only a homogeneous (spatially constant) order parameter is sufficient but not necessary for SSB, see, e.g., Ref. [250].



However, the relation used here is just one of the possible choices. As we will see in the following, this choice leads to remarkably similar vacuum effective potentials obtained using different shape functions, and therefore it is particularly suitable for a meaningful comparison of the associated phase diagrams.

It is worth mentioning that, by definition, the QPR only modifies the structure of the fermionic regulator, while leaving the structure of the bosonic regulator unchanged. For reasons that we explain once we establish the procedure we follow in order to obtain an RG-consistent initial condition in the MF approximation/leading order in the large- $N_c$  expansion, we do not use the QPR in the full LPA calculation, but we just use it as an extra-comparison element in the MF approximation.

For this study we use several regulator-shape functions. In particular we focus on the Litim (L) regulator [148, 251], an exponential (E) regulator and the smooth Litim-like (SL) regulator introduced in [249]. For the bosonic-shape functions they can be written as

$$r_{B,L}(y) = \left(\frac{1}{y} - 1\right) \Theta(1 - y), \quad (7.9)$$

$$r_{B,E}(y) = \frac{1}{1 - e^{-y-y^2}} - 1, \quad (7.10)$$

$$r_{B,SL}(y) = \exp\left(-\frac{1}{y - \frac{1}{2}}\right) \theta\left(y - \frac{1}{2}\right) + \frac{1}{y} - 1,$$

and the corresponding fermionic-shape functions are obtained using Eq.(7.8).

As we stated multiple times, the flow equations for the scale-dependent effective potential arising from the LPA truncation or from the mean-field approximation, and for the different regulator shapes, are either non-linear partial differential equations (PDEs) in the RG scale  $k$  and in the field variable  $\sigma$  or just ordinary differential equations (ODEs) in  $k$  for each of the values of  $\sigma$ . This will be a very important point in the following.

In both cases, the flow equations can be reformulated in terms of  $u(t, \sigma) := \partial_\sigma U_t(\sigma)$ , where  $t = -\ln\left(\frac{k}{\Lambda}\right)$  is the RG time. In this reformulation, the flow equation becomes an advection-diffusion equation with a source term and is reminiscent of PDEs from fluid dynamics. Solving numerically these PDEs is a challenging task since shocks and kinks might occur and stable numerical tools are required to treat them. Guided by the form of our flow equations, we use a finite-volume method, the aforementioned KT scheme.

### 7.3 Effective potential at leading order in large- $N_c$ expansion: mean-field approximation

Once the set-up has been fixed, we now move to the main focus of our discussion, i.e., how we can compare the different results obtained from different regulators in a consistent way. It is important to state that the reason why we chose to use the MF approximation is to test our method and to verify that one obtains the well known results in this approximation. In particular, the MF (one-loop) approximation is very similar to the untruncated/exact case: given a vacuum quantum effective action and regulators for which the one-loop Wetterich equation becomes independent of some considered external parameters at sufficiently large-RG scales, one can predict a unique quantum-effective action for external parameters, independently of the regulator choice and of the cutoff (for sufficiently large-cutoff scales). This useful property of the one-loop approximation is called one-loop universality (see, e.g., Ref. [70]). From a mathematical point of view this translates into the fact that the FRG flow equation loses the feature of

being a PDE, to become just a trivial ODE where the r.h.s is independent of the unknown function. This means that the task of finding the IR-effective potential is just reduced to a  $k$ - (or equivalently a  $t$ -) integration, where all the scales are included, leaving thus no dependence on the specific regulator function utilized. In this section we will also include discussions on the problems of implementing RG-consistency and fixing the UV-initial conditions.

We can have an intuitive point of view on the one-loop universality using the following argumentation. We start from the one-loop Wetterich equation in the presence of a set of external parameters, which we summarize under the variable  $e$ , and, for convenience, we also suppress the field dependence of the functionals

$$k\partial_k\Gamma_k(e) = \frac{1}{2}\text{STr}\left[(S^{(2)}(e) + R_k)^{-1} \cdot k\partial_k R_k\right],$$

where, because of the one-loop approximation, we substituted  $\Gamma_k^{(2)}(e)$  with  $S^{(2)}(e)$ , where  $S$  is the bare action associated to the respective theory. Since  $S^{(2)}(e)$  is  $k$ -independent, we have

$$(S^{(2)}(e) + R_k)^{-1} \cdot k\partial_k R_k = k\partial_k \ln(S^{(2)}(e) + R_k),$$

which can trivially be integrated. Note that the supertrace  $\text{STr}$  and the  $k$ -derivative do not commute in general, but the  $k$ -integral does. In this way we arrive at<sup>2</sup>

$$\Gamma(e) = \frac{1}{2}\text{STr}\left[\ln\left(\frac{S^{(2)}(e)}{S^{(2)}(e) + R_\Lambda}\right)\right] + \Gamma_\Lambda(e),$$

where we used  $R_{k=0} = 0$  and we defined  $\Gamma_{k=0}(e) \equiv \Gamma(e)$ . Note that all terms on the right-hand side are finite since the term inside the logarithm approaches the identity for large momenta  $p^2 \gg \Lambda^2$ , where  $R_\Lambda(p^2)$  tends to zero (since the regulator  $R_\Lambda$  acts as an IR regulator). Given a vacuum quantum effective action  $\Gamma = \Gamma(0)$ , we can rearrange the previous equation to  $\Gamma_\Lambda = \Gamma_\Lambda(0)$  and use it as an initial condition in the case of nonvanishing external parameters, i.e.,

$$\Gamma(e) = \Gamma + \frac{1}{2}\text{STr}\left[\ln\left(\frac{S^{(2)}(e)}{S^{(2)}(0)}\right) - \ln\left(\frac{S^{(2)}(e) + R_\Lambda}{S^{(2)}(0) + R_\Lambda}\right)\right].$$

The last logarithmic term vanishes for sufficiently large  $\Lambda$  if  $R_\Lambda(p^2)$  dominates over  $S^{(2)}(p^2, e)$  for all  $p^2 < \Lambda^2$  and loses its dependence on the external parameters, which is the case, for example, for regulators of the SR class with external parameters  $T, \mu \ll \Lambda$ . In that case we are left with

$$\Gamma(e) = \Gamma + \text{STr}\left[\ln\left(\frac{S^{(2)}(e)}{S^{(2)}(0)}\right)\right],$$

i.e., a regulator and in particular  $\Lambda$ -independent quantum effective action for external parameters.

In the following, we use this property as a guideline; in particular, once we build an RG-consistent initial condition, we test it for the case of the QMM.

In contrast to the previous general calculation for the quantum effective action, we now project the flow equation onto the truncation which contains only the scale-dependent effective potential as a flowing operator. More precisely, for regulators of the SR class the flow equation for  $u(t, \sigma)$  reads

<sup>2</sup>Here the denominator is meant as the inverse matrix.

$$\begin{aligned} \partial_t u(t, \sigma) \Big|_{\text{Fermions}} &= -\frac{N_c}{4\pi^2} \int_0^\infty d p p^4 \left(1 + r_t^F(p)\right) \partial_t r_t^F(p) \frac{\partial}{\partial \sigma} \left\{ \frac{1}{E_{k,\Psi}(p)} \times \right. \\ &\quad \left. \times \left[ 1 - n_F \left( \frac{E_{k,\Psi}(p) + \mu}{T} \right) - n_F \left( \frac{E_{k,\Psi}(p) - \mu}{T} \right) \right] \right\}, \end{aligned} \quad (7.11)$$

where  $t$  is the RG time,  $n_F(x) = 1/(e^x + 1)$  is the Fermi-Dirac distribution function,

$$E_{k,\Psi}(p) = \sqrt{p^2(1 + r_F(p))^2 + h^2\sigma^2}, \quad (7.12)$$

and the reformulation in  $u(t, \sigma)$  is used for convenience. As we previously hinted, Eq.(7.11) is an ODE in the RG time  $t$ , or equivalently in the RG scale  $k$ , since the spatial-like variable  $\sigma$  plays just the role of a parameter.

One can easily check that the flow equation becomes independent of the external parameters  $T, \mu$ , at large RG scales. This implies that, in order to perform a meaningful comparison of the IR observables at nonzero  $T, \mu$ , we have to establish a procedure to fix the vacuum effective potential  $U_{\text{vac}}(\sigma)$  for the different regulator shape functions.

Thus, once established the need for different initial conditions, our primary concern is to ensure that they produce RG-consistent results. The step-by-step procedure we used in order to achieve this goal is elucidated in Fig.7.1.

It is worth mentioning that, within our truncation (and also in the full-LPA case), the RG-consistency criterion translates into

$$\Lambda \frac{\partial U_{k=0}(\sigma)}{\partial \Lambda} = 0, \quad (7.13)$$

which encodes the independence of the IR-effective potential on the UV cutoff  $\Lambda$ .

Before explaining how we use this procedure, we should specify what we mean by flowing "backwards" in the RG flow. In the case of the mean-field, in particular, this is pretty straightforward since the only change that has to be done consists in switching the initial time with the final one in the RG-integration, meaning that the time derivative of the effective potential changes sign (or alternatively the source term changes sign). This naturally implies that the initial condition has also to be matched with the new initial time of the evolution, meaning, how one would expect, that the initial condition used in a backflow is actually just the result of a previous "standard" FRG-time evolution. Now that we have settled this aspect, we can proceed in explain in detail how this procedure is performed, following the various steps schematically presented in Fig.7.1.

1. The first step consists in solving the flow equation with a fixed-shape function. This step is usually performed using the standard Litim regulator-shape function  $r_{F,L}$  due to its simple form and to its numerical flexibility. The flow equation is initialized at the cutoff scale  $\Lambda = 1$  GeV, with a quartic potential

$$U_{k=\Lambda}(\sigma) = \frac{1}{2} m_{\text{UV}}^2 \sigma^2 + \frac{1}{4} \lambda_{\text{UV}} \sigma^4. \quad (7.14)$$

The UV parameters  $m_{\text{UV}}^2$  and  $\lambda_{\text{UV}}$  are then tuned in such a way that the vacuum effective potential at  $k = 0$  provides the chosen values for the IR observables, namely the chiral condensate, i.e., the position of the minimum of the IR potential, and the

sigma mass, i.e., the curvature of the IR potential evaluated at the minimum. In particular the used values are

$$\langle \sigma \rangle = f_\pi = 0.088 \text{ GeV} \quad m_{\text{IR}}^2 = m_\sigma^2 = \partial_\sigma u(t, \sigma) \Big|_{\sigma=\langle \sigma \rangle} = 0.2 \text{ GeV}^2, \quad (7.15)$$

where  $f_\pi$  is the pion decay constant. The last parameter of the model one can tune is the Yukawa coupling  $h$ . However, in order to have meaningful comparisons, we choose to fix it to a constant value that will be used in all the calculations presented in this chapter, namely

$$h = \frac{m_\Psi}{f_\pi} = 3.4, \quad (7.16)$$

where  $m_\Psi = hf_\pi = 0.3 \text{ GeV}$  is the dynamically-generated quark mass in the vacuum. The previously described step 1 corresponds to the first light-blue arrow in Fig. 7.1.

2. As a second step, we use the obtained IR-effective potential as the initial condition and solve the flow equation backwards from the infrared to a new UV cutoff  $\Lambda' \gg \Lambda$ . Here we choose  $\Lambda' = 100 \text{ GeV}$ . This step ensures that the RG-consistency condition Eq. (7.13) is fulfilled at the new UV cutoff  $\Lambda'$  by construction. This procedure is then performed for every regulator-shape function used in the SR class. The resulting scale-dependent effective potentials for the various regulators at  $k = \Lambda'$  are then proper initial conditions that can be used to calculate the effective potential at finite values of  $T, \mu \ll \Lambda$ , where one expects SSB. This step corresponds to the second light-blue arrow in Fig. 7.1. One can notice that, due to the already discussed simple structure of the flow equation in the MF, if for steps 1 and 2 one uses the same regulator-shape function, then these two steps can be also grouped into a single one, which consists in tuning the UV parameters at the scale  $\lambda_{\text{UV}}$  by flowing to the vacuum and then simply flowing upward from the scale  $\Lambda$  to the higher scale  $\Lambda'$ .

These two steps, as already stated, are sufficient to construct an RG-consistent and parameter-independent initial condition for the flow equation in the case of standard regulators, meaning that one can then just flow from the scale  $\Lambda'$  to the IR for any value of  $T$  and  $\mu$  simply using the chosen regulator and the obtained RG-consistent initial condition.

However, as we stated previously, we also investigate another class of regulators, the quasi-particle regulator class. In this case the flow equation reads:

$$\partial_t u(t, \sigma) = -\partial_t \left( 4N_c N_f (h^2 \sigma) \int \frac{d^3 p}{(2\pi)^3} \frac{1}{2\tilde{E}} \left[ 1 - n_f \left( \frac{\tilde{E} - \tilde{\mu}}{T} \right) - n_f \left( \frac{\tilde{E} + \tilde{\mu}}{T} \right) \right] \right), \quad (7.17)$$

with

$$\tilde{E} = \sqrt{\left( \frac{\omega_+ - \omega_-}{2} \right)^2 + h^2 \sigma^2}, \quad \tilde{\mu} = \frac{\omega_+ + \omega_-}{2}, \quad (7.18)$$

and

$$\omega_\pm = (\mu \mp |\vec{p}|)(1 + r_\pm). \quad (7.19)$$

Finally

$$r_\pm = r_F(x_\pm), \quad (7.20)$$

are the previously defined regulator-shape functions for the fermions, which depend on the dimensionless variables

$$x_{\pm}k^2 = (-\mu \pm |\mathbf{p}|)^2. \quad (7.21)$$

More details on the derivation of Eq. (7.17) and the meaning of the previously defined quantities can be found in App. D.2.3. From a mathematical point of view, Eq. (7.17) is still an ODE as for the SR case. However, it can be easily shown that it does not become independent of  $\mu$  for large-RG scales. This implies that we cannot use a vacuum flow at large RG scales to produce cutoff-independent results at non-zero  $\mu$ . This regulator class therefore has no predictive power with regard to the external parameter  $\mu$ , i.e., we cannot predict the behavior of IR observables as  $\mu$  is changed. However, it still has predictive power with regard to the temperature  $T$ . In fact, if we take the effective potentials resulting from RG flows which use regulators from the standard regulator class for every value of  $\mu$  at some arbitrary temperature, we can flow backwards from there with the quasi-particle regulator flow equation, to construct initial conditions at  $\Lambda = 100\text{GeV}$ , each for every  $\mu$ , see also Fig. 7.1. The predictions at other temperatures should then be in agreement with the regulators from the standard-regulator class.

Guided by this observation, we perform the previously described steps 1-2 with a SR, and we now detail the additional steps required to produce a suitable initial condition for the QPR class.

3. In the case of the Fermi-surface/quasi-particle class of regulators then, the next required step is to flow down to the IR starting from the scale  $\Lambda'$ , using the initial condition produced via steps 1-2 and exploiting a standard-class regulator. Crucially, this step has to be performed at a fixed temperature (usually  $T = 0$ ), for every value of the chemical potential one wants to obtain results for. This step corresponds to the third blue arrow depicted in Fig. 7.1.
4. The last step consists then in flowing back up with the in medium flow-equation obtained with the fermi-surface or quasi-particle regulator class, in order to generate a new RG-consistent UV-initial condition at scale  $\Lambda'$  for every value of the chemical potential  $\mu$ . This initial condition can then be used to solve the flow in medium at all different temperature values. This final step is represented by the black arrow in Fig. 7.1.

A crucial aspect that is worth stressing once again is that steps 1-2 have to be performed for a single point in the phase diagram, e.g., in the vacuum  $T = \mu = 0$ . Once steps 1-2 have been fulfilled, then the obtained initial condition is valid for every other value of the  $T - \mu$  space if using a SR. On the contrary, as already highlighted, when using the QPR, steps 3-4 have to be performed for every value of the chemical potential, meaning that the obtained RG-consistent initial condition is valid only for that specific  $\mu$ , but can be used for every value of the temperature one wants to investigate.

We then conclude this section stating that, as one would expect, the highlighted procedure correctly generates absolutely equivalent results for the different regulator-shape functions and regulator classes. The result of this comparative study is then shown in Fig. 7.2, where the phase diagrams, for both regulator classes and various regulator-shape functions are shown. We can observe that, as expected from the one-loop universality, all the possible combinations of regulator classes and regulator-shape functions lead to results that are in perfect agreement, proving that with our construction we achieved regulator-independent results.

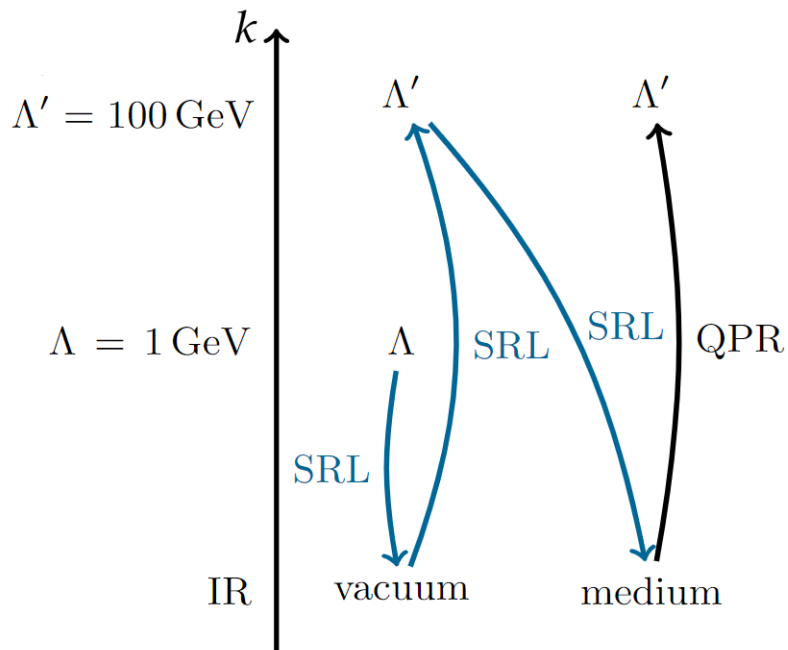


Figure 7.1: RG-consistency construction.

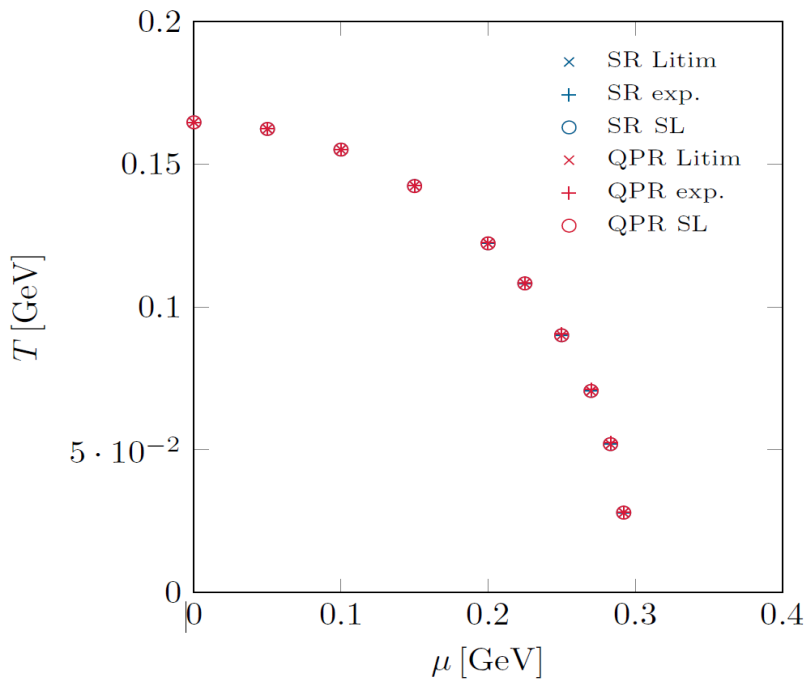


Figure 7.2: Comparison of the MF phase diagram for different regulator-shape functions and different regulator classes.



## 7.4 Beyond the large- $N_c$ approximation: LPA

Once we established our procedure for the testing ground of the MF/large- $N_c$  approximation, it is now time to go beyond it and approach the full-LPA case. one of the challenging aspects is that for LPA, in contrast with the one-loop case, there is no guaranteed universality of the results, and therefore it is absolutely not-trivial that results obtained in presence of finite external parameters agree for different regulators, even if the corresponding vacuum effective potentials are matched. The LPA flow equation for the standard-regulator class used for both fermions and bosons, reads

$$\begin{aligned} \partial_t u(t, \sigma) = & \frac{1}{8\pi^2} \int_0^\infty d p p^4 \left\{ \partial_t r_B(p) \frac{\partial}{\partial \sigma} \left[ \frac{3}{E_{k,\pi}(p)} \coth \left( \frac{E_{k,\pi}(p)}{2T} \right) + \frac{1}{E_{k,\sigma}(p)} \coth \left( \frac{E_{k,\sigma}(p)}{2T} \right) \right] \right. \\ & \left. - 2 N_c \left( 1 + r_F(p) \right) \partial_t r_F(p) \frac{\partial}{\partial \sigma} \left\{ \frac{1}{E_{k,\Psi}(p)} \left[ 1 - n_F \left( \frac{E_{k,\Psi}(p) + \mu}{T} \right) - n_F \left( \frac{E_{k,\Psi}(p) - \mu}{T} \right) \right] \right\} \right\}, \end{aligned} \quad (7.22)$$

where

$$E_{k,\pi} = \sqrt{p^2(1 + r_B(p)) + \frac{u(t, \sigma)}{\sigma}}, \quad E_{k,\sigma} = \sqrt{p^2(1 + r_B(q)) + \partial_\sigma u(t, \sigma)} \quad (7.23)$$

and  $E_{k,\Psi}$  is defined in Eq. (7.12).

In this case, the reformulation in terms of the conserved quantity  $u(t, \sigma)$  is a necessary consequence of the numerical approach we choose. In particular, as we stated multiple times, in this way the flow equation can be put in the form of an advection-diffusion equation with a source term. Thus we use a tool developed to solve PDEs from fluid dynamics, i.e., the KT finite-volume scheme ([142], or see App. E).

Due to the presence of both a fermionic and a bosonic loop in the LPA-flow equation, we can now choose up to nine different total regulator functions by using all possible combinations of the three shape functions we considered.

Similarly to the one-loop flow equation for the standard regulator, it can be easily shown that also the LPA-flow equation becomes independent of  $T$  and  $\mu$  for sufficiently large-RG scales. However, the flow equation has now the form of a non-linear partial differential equation in the field variable  $\sigma$  and the RG time  $t$ . Thus it can not be solved backwards, because of the presence of diffusion terms, which are source of irreversibility and entropy production [81]. Therefore, the task of finding a proper scale-dependent effective potential at large RG scales, i.e., an initial condition for the flow equation which leads to a fixed vacuum effective potential, is not as trivial as in the one-loop case. A possible strategy consist of making an ansatz for the initial condition

$$U_{k=\Lambda}(\sigma) = \frac{1}{2} m_{UV}^2 \sigma^2 + \frac{1}{4} \lambda_{UV} \sigma^4, \quad (7.24)$$

using  $m_{UV}^2$  and  $\lambda_{UV}$  as parameters and study to which extent it is feasible to tune these parameters such that the vacuum effective potential in the IR limit matches with the same desired one for all the various regulator-shape functions. This is the core of the next subsection.



### 7.4.1 Parameter space and UV independence of the IR observables

As we stated previously, our ansatz for the initial condition for the flow equation is built in such a way that we can tune two free parameters. Note that, within our restriction of the UV potential, it is clear that it is not guaranteed to find an exact match of the IR potentials for the various regulators. That is why we tune  $m_{\text{UV}}^2$  and  $\lambda_{\text{UV}}$  in order to fix the minimum and the curvature of the potential (the sigma mass), such that we are able to at least fix the local structure of the effective potential around its minimum in the IR. Since physical information is extracted from the derivatives of the potential at its minimum, this choice of observables provides suitable candidates for a meaningful comparison of the results obtained with different regulators. In particular, we make their value be the same (as far as possible, as we argue in the following) in the vacuum by fixing the initial conditions, and then compare the obtained results for the finite external-parameters case.

In practice, we scan the parameter space spanned by  $m_{\text{UV}}^2$  and  $\lambda_{\text{UV}}$ , which is however restricted by the following bounds  $\lambda_{\text{UV}} \geq 0$  (if  $\lambda_{\text{UV}} = 0$  then  $m_{\text{UV}}^2 > 0$ ) and  $m_{\text{UV}}^2 > -\Lambda^2$ . The former bound simply comes from the fact that the UV potential has to be bounded from below. The latter one prevents the LPA flow equation from being invalid right at the beginning of the RG flow. It is worth noticing that, while in order to ensure stability  $\lambda_{\text{UV}}$  has to be positive also in the mean-field approximation, the last limitation on the value of  $m_{\text{UV}}^2$  is not present in the mean-field approximation due to the simpler form of the flow equation. We can now make the condition  $m_{\text{UV}}^2 > -\Lambda^2$  more clear by considering the bosonic contribution in the LPA for the Litim regulator-shape function. However, the same line of reasoning holds with minor changes also for the other regulator-shape functions. In particular, as we demonstrated several times, in the case of the Litim-shape function we have

$$E_{k,\sigma} = \sqrt{k^2 + \partial_\sigma u(t,\sigma)}. \quad (7.25)$$

The initial condition at  $k = \Lambda$ , i.e., at  $t = 0$ , for the derivative of the effective potential then reads

$$u(t = 0, \sigma) = m_{\text{UV}}^2 \sigma + \lambda_{\text{UV}} \sigma^3. \quad (7.26)$$

Then its  $\sigma$ -derivative is

$$\partial_\sigma u(t = 0, \sigma) = m_{\text{UV}}^2 + 3\lambda_{\text{UV}} \sigma^2. \quad (7.27)$$

If we now evaluate it at  $\sigma = 0$  we trivially obtain

$$\partial_\sigma u(t = 0, \sigma = 0) = m_{\text{UV}}^2. \quad (7.28)$$

If we substitute it in Eq.(7.25) and evaluate it at  $k = \Lambda$  we obtain

$$E_{k=\Lambda,\sigma}|_{\sigma=0} = \sqrt{\Lambda^2 + m_{\text{UV}}^2}, \quad (7.29)$$

from which the condition  $m_{\text{UV}}^2 > -\Lambda^2$  trivially follows.

After this brief explanation we can come back to the main topic of the section, i.e., the compatibility of the vacuum results obtained using different regulators. What we find is that it is indeed possible to tune  $m_{\text{UV}}^2$  and  $\lambda_{\text{UV}}$  for any regulator combination and any cutoff scale  $\Lambda$ , such that the minimum takes the desired value of  $\sigma_{\text{min}} = 0.088 \text{ GeV}$ . This can be seen from Fig.7.3, where we show the accessible parameter space in the vacuum for different cutoffs and different regulator combinations. Here  $m_{\text{UV}}^2$  has been rescaled, and is expressed in units of the cutoff squared,  $\Lambda^2$ . Each solid curve corresponds to the parameter sets for which the IR-chiral condensate is fixed at  $\langle \sigma \rangle = 0.088 \text{ GeV}$ , while the IR-curvature mass changes along the curves. From this plot we clearly see that, as one would expect, in order to tune the IR minimum of the potential to the same fixed value,  $m_{\text{UV}}^2$  has to be increased when  $\lambda_{\text{UV}}$  is decreased and vice versa. Thus, the existence of a

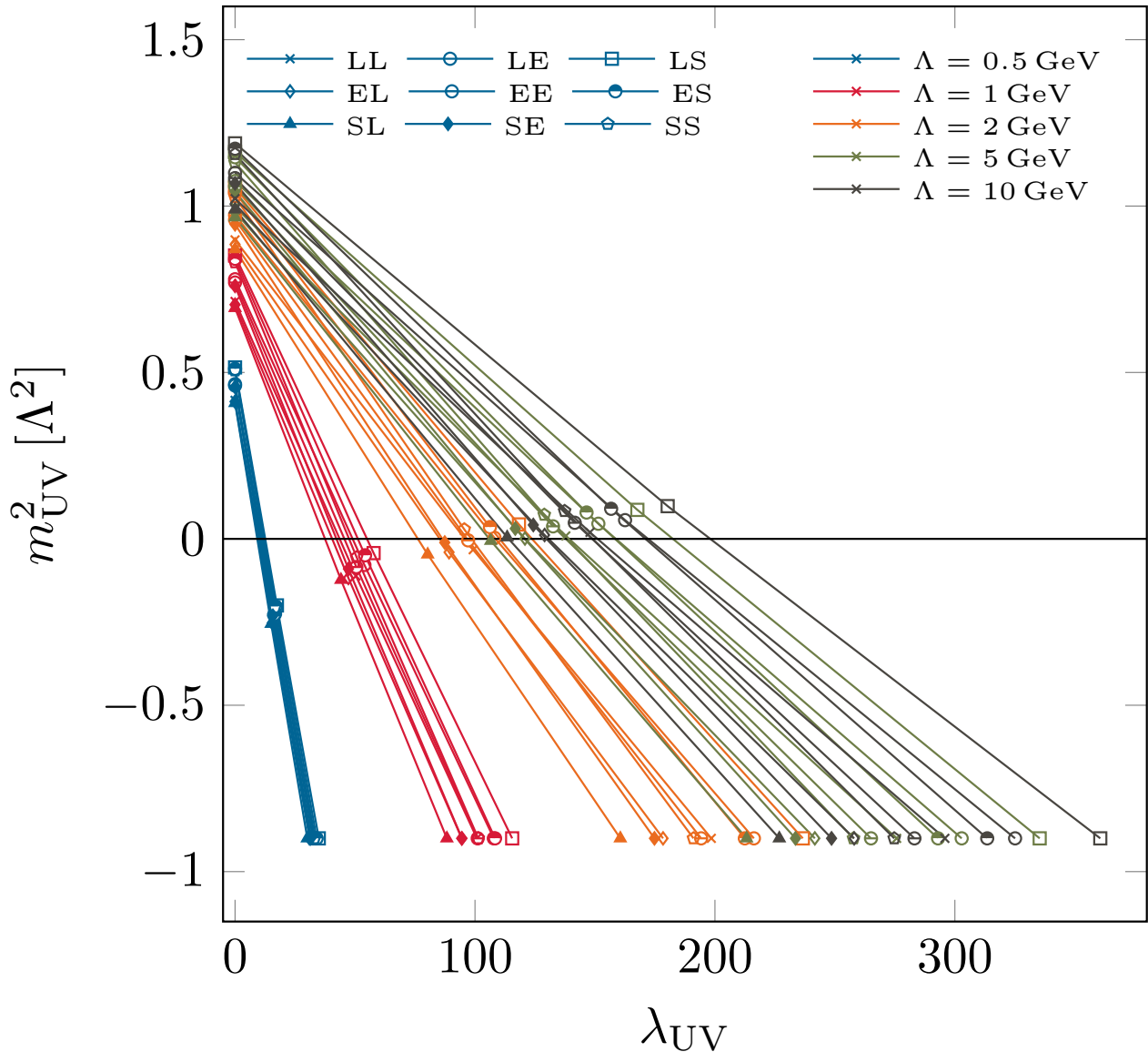


Figure 7.3: Complete parameter space in the vacuum for different cutoffs and different regulator combinations. On each solid curve the IR-chiral condensate is fixed at  $\langle\sigma\rangle = 0.088 \text{ GeV}$ .

minimal value for both  $m_{UV}^2$  and  $\lambda_{UV}$  translate into a maximal value for  $\lambda_{UV}$  and  $m_{UV}^2$ , respectively. These boundaries restrict the whole parameter space.

This is the reason why we find that it is not possible to obtain an arbitrary value for the curvature  $m_{IR}^2$  at the desired minimum. The associated results are depicted in Fig. 7.4, where we show the accessible values of  $m_{IR}^2$  for different regulator combinations and different values of the UV cutoff  $\Lambda$ . In particular, as expected,  $m_{IR}^2$  increases as  $\lambda_{UV}$  is increased. Thus we find bands of accessible  $m_{IR}^2$ , where the lower bound is obtained for the lowest possible value of  $\lambda_{UV}$ , i.e.,  $\lambda_{UV} = 0$ , and the upper bound corresponds to the maximal possible  $\lambda_{UV}$ , associated with  $m_{UV}^2 = -\Lambda^2$ .

We observe that the bands of the accessible values of  $m_{IR}^2$  are similar for different regulators, but not the same. For low enough  $\Lambda$  all bands overlap, allowing for a comparison of the phase diagrams in the sense we previously defined. However, we are more interested in the case of large  $\Lambda$ , because only for large enough cutoff scales the phase diagram is expected to be independent of the cutoff scale itself. For large  $\Lambda$  we observe a very interesting behavior for all regulators: with increasing cutoff, the bands become more narrow and lay inside the bands produced by lower cutoffs. Furthermore,

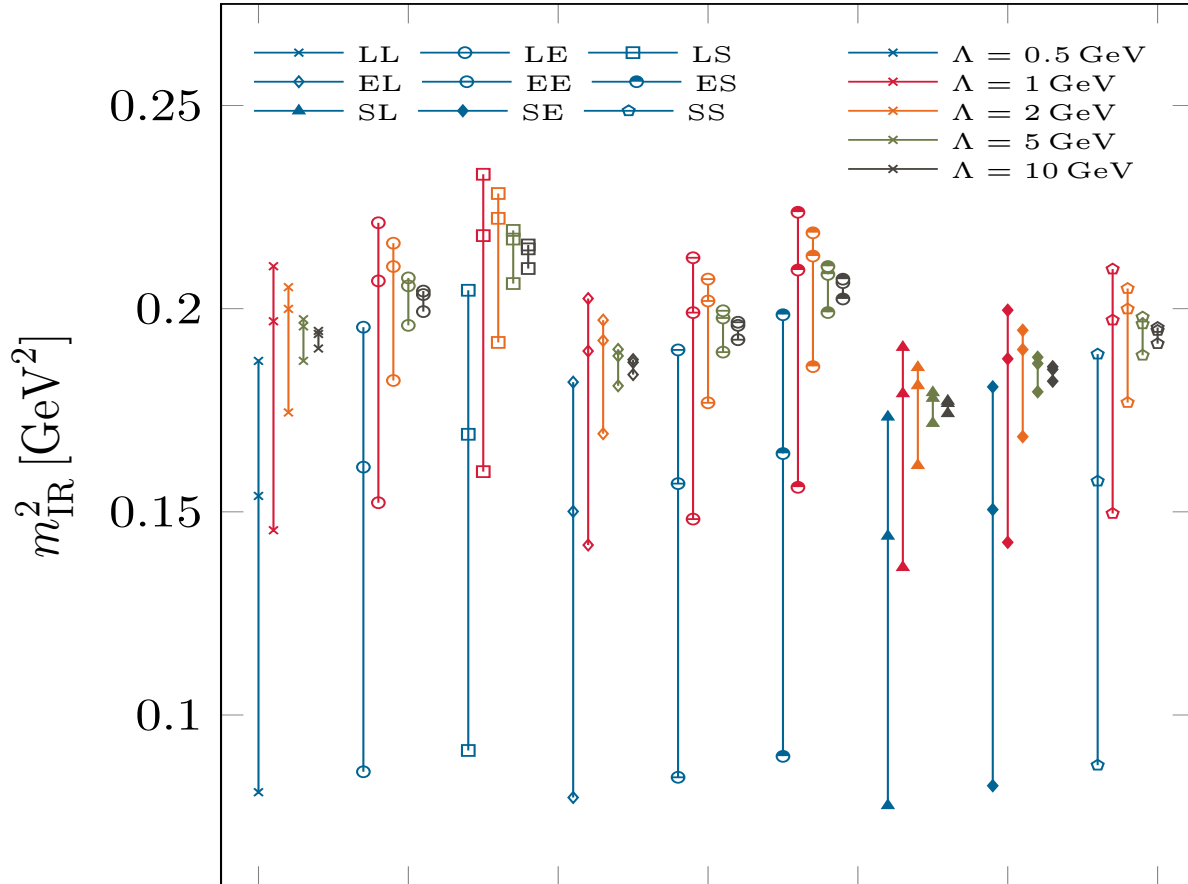


Figure 7.4: Accessible values of  $m_{\text{IR}}^2$  obtained for different regulator combinations and different values of the UV cutoff  $\Lambda$ . For each depicted value, the IR-chiral condensate is fixed at  $\langle\sigma\rangle = 0.088 \text{ GeV}$ .

these bands tend to collapse into a single point when  $\Lambda \rightarrow \infty$ , approaching a given limit. More precisely  $m_{\text{IR}}^2$  is not affected by the choice of  $m_{\text{UV}}^2$  and  $\lambda_{\text{UV}}$  in the limit  $\Lambda \rightarrow \infty$ , as long as they lead to  $\sigma_{\text{min}} = 0.088 \text{ GeV}$ . This happens alongside the fact that the allowed range of values for  $m_{\text{UV}}^2$  and  $\lambda_{\text{UV}}$  increases as the cutoff is increased, which is in agreement with our previous statement that the IR results get more UV-insensitive as  $\Lambda$  gets bigger. In other words, both  $m_{\text{IR}}^2$  and the effective-IR potential in a broader vicinity around the minimum are prediction of our calculation. This can be seen in Fig. 7.5, where we show the local enclosing of the IR-effective potentials, via the bands in the IR-effective potentials produced by the different choices of the UV couplings which lead to the bands of Fig. 7.4, for two values of the IR cutoff  $\Lambda$  and for two combinations of the regulator-shape functions. We note that this implies that many different quartic initial conditions will lead to the same effective potential in the neighborhood of the minimum, which is deeply in contrast to one-loop case, where only a unique parameter-set choice leaves the IR-effective potential invariant. As a consequence, it suffices to choose a very simple form for  $U_{k=\Lambda}$ , e.g., purely quadratic or purely quartic, as far as we use an arbitrary but sufficiently large  $\Lambda$ , in order to keep the vacuum-effective potential locally  $\Lambda$ -independent around its minimum. In this sense, we can state that the QMM in LPA is renormalizable.

The  $\Lambda \rightarrow \infty$  limits of  $m_{\text{IR}}^2$  however do not seem to agree for any two different regulator combinations, but the results are very similar if the fermionic and bosonic shape functions are chosen such that they fulfill the condition Eq. (7.8). Perfect comparability is

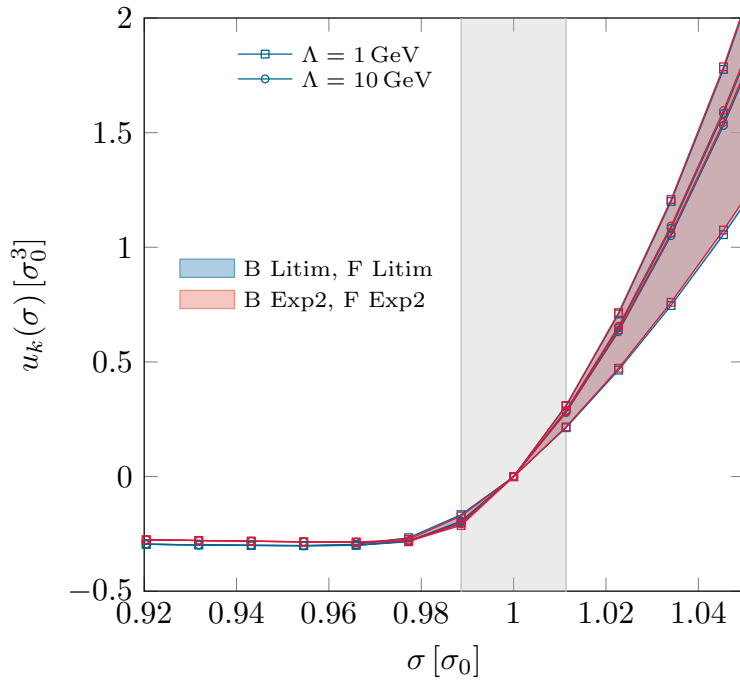


Figure 7.5: Local enclosing of IR-effective potentials for two values of the IR cutoff  $\Lambda$  and two combinations of the regulator-shape functions. The bands in the IR-effective potentials are produced by the different choices of the UV couplings which lead to the bands in Fig. 7.4.

therefore not given, but approximately achieved for some of the considered regulators. It is important to notice that the bands in Fig. 7.4 might depend on the chosen quartic form of  $U_{k=\Lambda}$ . If we would include a  $\sigma^6$ , it might be possible to arrive at values of  $m_{\text{IR}}^2$  outside the bands even in the limit  $\Lambda \rightarrow \infty$ , although we do not expect this to neither provide a relevant contribution to the size of the  $m_{\text{IR}}^2$  bands nor to impact our argumentation. However, the fact that the simple initial conditions that we found lead to a unique, cutoff-independent limit for the potential in the vicinity of its minimum (renormalizability) is true even if we enhance the ansatz for  $U_{k=\Lambda}$ .

As a final remark, we did not include the quasi-particle regulator class in the LPA analysis, since we would have to find initial conditions at every  $\mu$  using as an input the results obtained from a regulator belonging to the standard class, just as in the one-loop case. However, this is not trivial since the results for different regulators belonging to the standard regulator class are not unique in LPA. On top of that, during our investigation we did not find satisfying agreement between the possible  $m_{\text{IR}}^2$  obtained for a chosen QPR and SR at some chosen  $\mu$ , so, for the moment, we dropped this part of the study.

## 7.4.2 Cutoff Dependence Of Phase Diagram: Quartic Initial Condition

The next step of our comparison study consists in the investigation of the impact of the UV cutoff and the regulator choice on the results at finite values of the external parameters  $T$  and  $\mu$ , thus, as a main example, on the phase diagram of the model. More in detail, we can now use the results from the vacuum-parameter study in order to choose, for a given cutoff, parameter sets for different regulators that lead to equal (or similar) values of  $m_{\text{IR}}^2$ , in order to compare the resulting phase diagrams at non-zero  $\mu$  and  $T$ . However, since we emphasize that we found bounds for the possible values of  $m_{\text{IR}}^2$ , we now expect that the corresponding parameters might lead to an upper and lower limit for the phase boundary as well. This is indeed the case. In particular, we observe that the maximal value of  $m_{\text{IR}}^2$ , for a given regulator and cutoff, leads to an "outer" phase

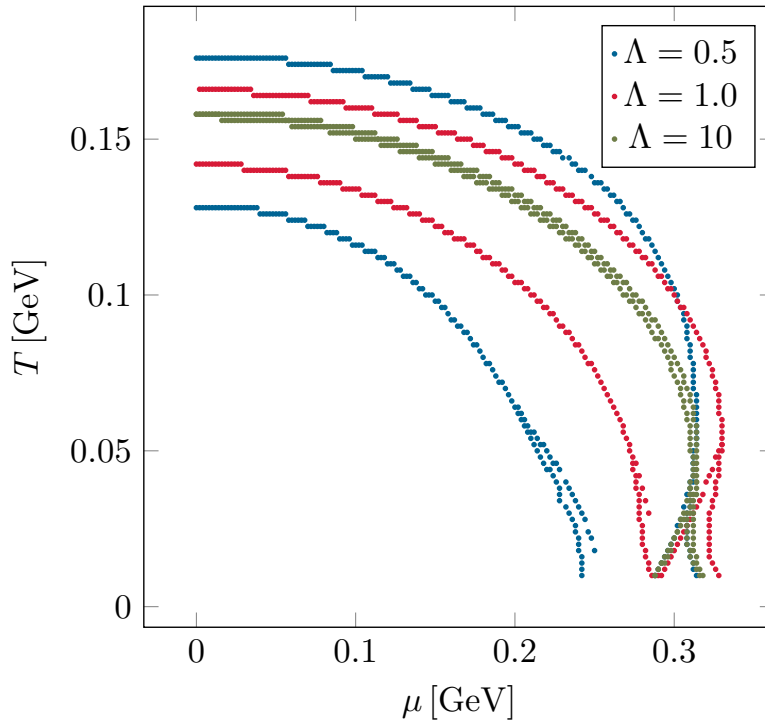


Figure 7.6: Phase boundaries of the QM model obtained with FRG in the LPA for different choices of the UV cutoff  $\Lambda$ . The used regulator combination for the shape functions in the bosonic and fermionic regulators is Litim-Litim. For a given cutoff, the lower and upper bounds correspond to the lowest and highest value allowed for  $m_{\text{IR}}^2$ , respectively.

boundary, located at larger values of  $T$  and  $\mu$ , while the corresponding minimal value of  $m_{\text{IR}}^2$  provides an "inner" phase boundary, which can instead be found at lower values of the external parameters. The resulting limiting phase boundaries for the Litim regulator-shape function, used both in the bosonic and fermionic loops, are shown in Fig. 7.6 for different cutoffs. Each of the points presented is the result of the calculation of the effective potential in the IR, from which we extract the value of the sigma-condensate. In particular, as points of the phase boundary we consider those points in a given  $T - \mu$  discretization, for which the minimum of the effective potential  $\sigma_{\text{min}}$  is non-zero, but becomes zero at a neighboring grid point in  $T$  or  $\mu$  direction. The phase boundaries have then been obtained by spreading an uniform grid over the region in the  $\mu, T$  plane we are interested in, using a grid spacing of  $\Delta\mu = 2\text{MeV}$  and  $\Delta T = 2\text{MeV}$ .

As we discussed in Chapter 5, the phase boundary close to  $T = 0$  and at high values of  $\mu$  splits up into two separate phase boundaries. The line at smaller  $\mu$  represents what we called the back-bending in the phase boundary, while the other one is the standard phase boundary, where  $\sigma_{\text{min}}$  changes from non-zero to zero. No order parameter changes from non-zero to zero at the back-bending phase boundary, but a rapid change of  $\sigma_{\text{min}}$  occurs, which can more easily be seen in a 3D plot, see Fig. 7.7.

Points are regarded as back-bending phase boundary points in this discretized  $T - \mu$  grid space, if the discrete derivative  $\partial_T \mu > 0$  along the phase boundary.

Before going any further in the analysis of the results, we point out that in Fig. 7.6 we used the Litim regulator shape function as an example, but a similar behavior is found for all tested regulator shape functions.

As a first observation, we can see that the back-bending phase boundary does not seem to be an UV-cutoff artifact, since it is present also for  $\lambda = 10 \text{ GeV}$ , in both of the phase boundaries.

One of the most interesting aspects is that all possible phase boundaries one can



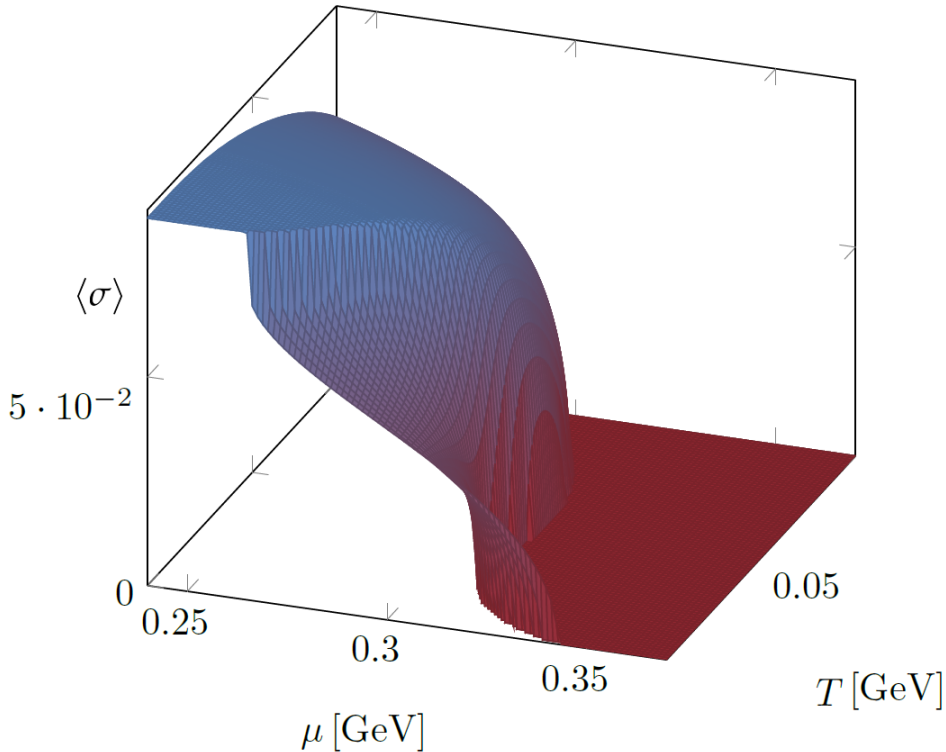


Figure 7.7: 3D-phase diagram of the QM model obtained with the FRG in the LPA. The used regulator combination for the shape functions in the bosonic and fermionic regulators is Litim-Litim.

obtain in LPA using a quartic initial condition are contained in between the previously described limiting phase boundaries, since all the possible available parameters lie inside the parameter-space boundaries for which the phase diagrams have been calculated.

We can then observe that, for low values of the UV cutoff, the range of possible phase boundaries is significantly wide but still finite, as long as we keep  $\sigma_{\min} = 0.088\text{GeV}$  fixed in the vacuum. This is worth emphasizing since the existence of these ranges, which strongly depend on the quartic initial condition, show that the results that are usually obtained in the literature, where the initial condition is fixed at what is often identified as a model scale,  $\Lambda_{\text{model}}$ , typically in the range  $0.5\text{GeV} - 1\text{GeV}$ , are also strongly dependent on the choice of the parameter, even if the value of the chiral condensate is fixed in the vacuum. Furthermore, we crucially observe that the region of obtainable phase diagrams, associated to the available portion of the parameter space, reduces significantly as the UV cutoff  $\Lambda$  is increased, since the two limiting phase boundaries tend to collapse onto each other. This is exactly what we expected from our previous considerations, since we observed the same behavior in the available bands of  $m_{\text{IR}}^2$  in vacuum. We thus conclude that, in agreement with the previously described behavior of  $m_{\text{IR}}^2$ , we expect an unique phase boundary in the limit  $\Lambda \rightarrow \infty$ . From this then follows that, as we already guessed, many different quartic initial conditions lead to the same phase boundary in this limit. Even though we do not expect so, it might be possible to obtain other phase boundaries, if one would allow for other terms of order higher than the fourth in the initial conditions, even in the limit  $\Lambda \rightarrow \infty$ . However, the fact that we found a set of simple initial conditions at arbitrarily large cutoffs, that lead to a unique, cutoff-independent IR result, remains correct even if other initial conditions are regarded.

Finally, we conclude this section pointing out that a comparison of outer and inner phase boundaries for different regulators, in the sense of RG consistency, is not meaningful if we are not able to match the corresponding  $m_{\text{IR}}^2$  in the vacuum.

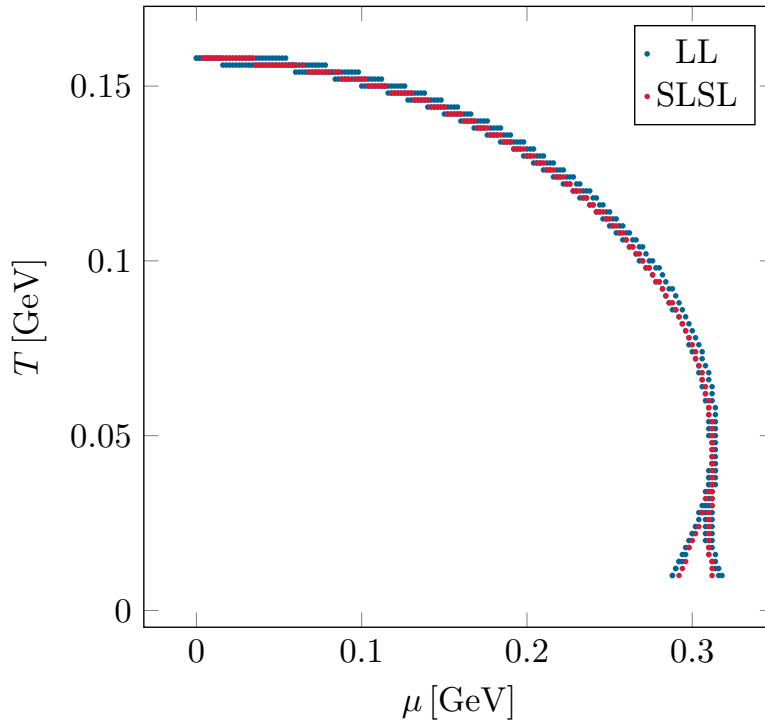


Figure 7.8: Phase boundaries of the QM model obtained with FRG in the LPA for  $\Lambda = 10$  GeV. The used regulator combinations for the shape functions in the bosonic and fermionic regulators are Litim-Litim and Smooth Litim-Smooth Litim. For the Litim-Litim combination, the lower and upper bounds correspond to the lowest and highest value allowed for  $m_{\text{IR}}^2$ , respectively, while we plot only the lower bound for the Smooth Litim-Smooth Litim case.

### 7.4.3 Cutoff And Regulator Dependence Of Phase Diagram: regulator comparison

We now turn back to what we defined as the meaningful comparison of the phase diagrams of QMM obtained in the LPA for different regulators. To this end we established in the previous sections that we need to properly initialize the vacuum-RG flows for the different regulators, such that they start at sufficiently high cutoff scales and lead to locally similar effective potentials in the IR limit. From Fig. 7.4 we know that the minimally accessible values of  $m_{\text{IR}}^2$  for the regulator-shape function combinations which use shape functions for bosons and fermions related by Eq. (7.8), i.e., Litim-Litim, SmoothLitim-SmoothLitim and Exp2-Exp2, are very similar for  $\Lambda = 10\text{GeV}$ . Since minimal  $m_{\text{IR}}^2$  values correspond to  $\lambda_{\text{UV}} = 0$  and since  $10\text{GeV}$  is much greater than the interesting  $\mu, T$  values, the purely quadratic initial conditions at  $\Lambda = 10\text{GeV}$  can be used to generate the desired vacuum flows and the associated comparable phase diagrams.

As an example, in Fig. 7.8 we show the phase boundaries obtained using as UV cutoff  $\Lambda = 10$  GeV. The used regulator combination for the shape functions in the bosonic and fermionic regulators are Litim-Litim and Smooth Litim-Smooth Litim. For the Litim-Litim combination, the lower and upper bounds correspond to the lowest and highest value allowed for  $m_{\text{IR}}^2$ , respectively, while we plot only the lower bound for the Smooth Litim-Smooth Litim case. We clearly see that the Smooth Litim-Smooth Litim phase boundary is completely included in the limiting phase boundaries obtained in the Litim-Litim case, and that it almost coincides with the lower bound obtained in the Litim-Litim case. This was expected, due to the overlap in Fig. 7.4 of the values of  $m_{\text{IR}}^2$  for the two combinations of regulator, but it is still absolutely not trivial, since in principle the initialization of the flow and the flow equations themselves are completely different. So



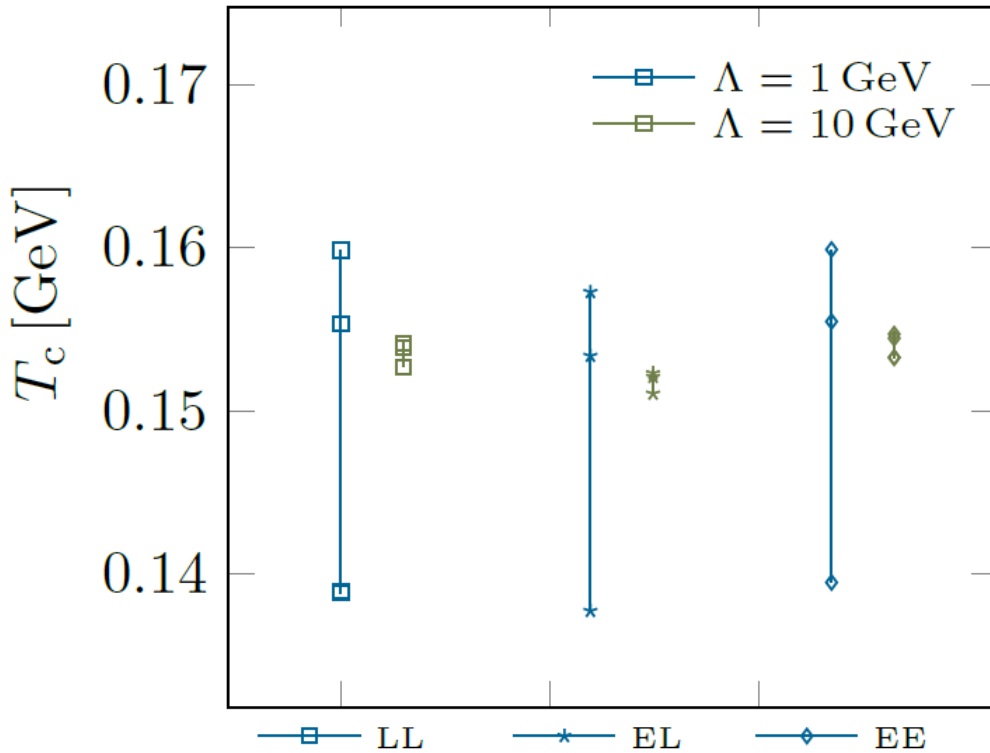


Figure 7.9: Range of critical temperatures at  $\mu = 0$  obtained changing the UV couplings, for different regulator-shape combinations and for two different values of the UV cutoff  $\Lambda$ .

we can consider these results as achievements of our RG-consistent procedure. In fact, in the vast majority of the literature on the topic, the phase diagrams naively produced with different regulators and initial conditions are very different, which we can now interpret as an effect of both the choice of a too low UV cutoff and the absence of an RG-consistent procedure to determine the initial condition for the flows associated to different regulators. In order to give a more complete view on the obtained results, in Fig. 7.9 we show the range of possible critical temperatures at  $\mu = 0$  obtained changing the UV couplings in the accessible region of the parameter space, for different regulator combinations, namely Litim-Litim, Litim-Exponential and Exponential-Exponential, and for two different values of the UV cutoff  $\Lambda$ , i.e.,  $\Lambda = 1$  GeV and  $\Lambda = 10$  GeV. The reason why we decided to show such a comparison is that in this way we fix one of the external parameters,  $\mu = 0$ , and so we can already have a clear idea of the result of the comparison without needing to perform the whole phase-diagram calculation. As we observed both for  $m_{\text{IR}}^2$  and for the phase boundaries, the range of possible critical temperatures shrinks significantly as the UV cutoff is increased, up to turn into a single point in the  $\Lambda \rightarrow \infty$  limit.

Naturally, we see a clear overlap for all the considered regulator combinations in the case of  $\Lambda = 1$  GeV. However, as we specified several times, we are particularly interested in the high UV-cutoff region. In this case we can observe that the overlap is still present and almost complete for the regulator combinations that use same shape functions, namely LL and EE, while the mixed combination LE is slightly off. From this we can then conclude that, guided also by our previous results, the resulting phase boundaries for the regulator combinations we tested are in significantly good agreement, once the RG-consistent procedure to tune the initial conditions has been used, if the regulator shape functions are chosen according to the relation Eq. (7.8). On the other hand, we see that, already at  $\mu = 0$ , the results obtained with mixed combinations seem not to agree in the large- $\Lambda$  limit. This may be related to a mismatch of the fermionic and

bosonic scales that are singled out by the presence of the regulator and then integrated during the RG flows, thus further studies can be carried out in this direction.

As a final remark, we can see from Fig.7.8 that the back-bending region is also present using another regulator-shape choice, signaling that this region may not be neither a regulator- nor a UV-cutoff artifact. Thus one could investigate whether this effect derives from the choice of the truncation of it is an established feature of the QM model, which cannot correctly describe the high-density regime.

## 7.5 Conclusions and outlook

In this chapter we discussed the quark-meson model in the mean-field and local-potential approximation within the FRG framework. In particular we analyzed the dependency on the regulator choice and on the UV cutoff of the IR observables and of the phase diagram of the model. The main guideline that we followed is the property of RG consistency of the RG flow and how to exploit it in order to construct external parameter-independent UV-initial conditions.

In the MF approximation we were able to investigate two different regulator classes, the standard and the quasi-particle one, besides three different regulator-shape functions. As expected from the one-loop universality property, the results for the phase diagrams obtained using all the possible regulator-shape and regulator-class combinations perfectly agreed. This solidifies the validity of the procedure we used to determine the UV-initial condition.

In LPA case we discussed only the standard regulator class because the UV potential depends non-trivially on the chemical potential, which makes this class of regulator inconvenient. However, this issue is definitively interesting and deserves further investigation. Our take on this problem is, as we stated previously and in analogy to the procedure we followed in the MF approximation, to tune the UV parameters at a sufficiently high UV scale in such a way that the obtained IR results agree with the one obtained using a standard-class regulator, e.g., the Litim one. Note that this procedure would need to be performed at a fixed temperature but for every value of the chemical potential, since the QPR regulator class has no predictive power as  $\mu$  is concerned. On the other hand, each of the obtained initial conditions could be used to obtain prediction in the temperature direction.

Coming back to our main work in the LPA with standard-class regulators, we showed that, in order to compare different regulators, one has to match the IR potentials, at least locally close to the minimum, in the vacuum. This match is necessary to find the UV potential for all the possible values of the external parameters. In contrast to the MF case, where flowing upwards is allowed due to the easy ODE-structure of the flow equation, in the LPA this is impossible due to the presence of diffusive contributions which lead to irreversibility of the flow.

One possible way is then tune the parameters in the UV potential at a sufficiently high UV-scale such that they lead to the correct IR-vacuum physics. We then choose to use a quartic potential with two independent couplings.

Due to the structure of the LPA flow equations and to stability constraints, we found some restrictions on the values of the UV parameters, meaning that not the whole parameter space is accessible, but just a finite portion of it. In this way we found that there are bands of allowed values for the IR-curvature mass which, together with the position of the IR minimum, are the observables that we decided should be fixed in the different vacuum IR-potentials. This thus leads to the presence of phase boundaries in the phase diagrams, corresponding to the highest and lowest possible values of the  $m_{\text{IR}}^2$ . Interest-

ingly, we found that the bands in  $m_{\text{IR}}^2$  tend to converge to a single point in the limit  $\Lambda \rightarrow \infty$ . We found the same occurrence also in the boundaries of the phase diagram and in the critical temperatures at  $\mu = 0$ . We then found an almost perfect agreement between the LL and SLSL phase diagram, signaling that our comparison procedure was indeed meaningful. We also found that the results obtained with mixed combinations seem not to agree in the large- $\Lambda$  limit. As we already pointed out, this may be due to a mismatch of the fermionic and bosonic scales that are involved in the regulator, and thus in the scale-integration during the RG flow. This is then another possible direction for further studies. One can also try to extent this study to other regulator-shape functions (even if we also tested a polynomial one and the results do not differ significantly from the presented ones). It would also be extremely interesting to extend our discussion to higher order truncation, in order to systematically investigate how the parameter dependence is influenced by the choice of the truncation.

## Conclusions

In this thesis we focused on the application of the nonperturbative Functional Renormalization Group (FRG), to study the critical behavior of effective field theories, with the ultimate goal of understanding the critical properties of Quantum Chromodynamics (QCD) and in particular of the chiral phase transition. We provided a general introduction to QCD and to the Renormalization Group, and then discussed the effective average action formalism and the Wetterich equation. Due to the functional nature of the FRG approach and of the Wetterich equation, an ansatz for the effective action is generally needed. In this work we choose to adopt the local-potential approximation (LPA), where one stops at zeroth order in the expansion in derivative operators of the quantum effective action, including only the quantum effective potential.

The key idea used in this work lies in the observation that the FRG flow equation in the LPA can be cast, for specific models and truncation schemes, in the form of an advection-diffusion equation [32, 80, 81, 105, 106, 132, 133, 134], possibly with a source term. This type of equation is typical of viscous hydrodynamics, and therefore, using a method developed specifically for its resolution constitutes an innovative approach to the solution of the FRG flow equation. In particular, the Kurganov-Tadmor [142] finite-volume scheme is adopted and details are presented in App. E. We thus showed the reliability and the flexibility of this approach by applying it to the study of different systems.

The first physical case discussed is the well-known  $O(N)$  model, where we applied the hydrodynamic formulation of the FRG flow equation in the LPA truncation to study the critical behavior of the system and calculate the corresponding critical exponents. Particular attention is given to the error estimation in the extraction of critical exponents, which is a needed and not widely explored aspect. The results are well compatible with others in the literature, obtained with different perturbative and nonperturbative methods, which validates the procedure.

The second part of the thesis begins with a brief review of the quark-meson model as a low-energy effective model of QCD, since it exhibits chiral symmetry breaking and quark-mass generation. The model is studied at finite temperature and quark chemical potential, using the Matsubara formalism. The LPA flow equations are also of the advection-diffusion type, with an extra source term arising from the inclusion of fermionic degrees of freedom [105, 106, 170]. We thus adopted the previously described numerical techniques to derive the phase diagram of the model, which is in agreement with the one obtained with other techniques in the literature.

We also exploited the numerical advancement to assess one of the most delicate issues which arise when using approximations to solve the FRG flow equation, i.e., the choice of the regulator. In particular we performed a vacuum-parameter study and used the RG-consistency requirement to determine the impact of the choice of the regulator

on the physical observables and on the phase diagram of the model. This study is particularly interesting since it develops in a systematic way a comparison of the results obtained via different regulators, showing both the importance of the choice of the UV-cutoff and consequently the fundamental role that the RG consistency, the truncation of the effective average action and the choice of the regulator play in the determination of IR observables. In particular, in the MF approximation we found a perfect agreement of the results obtained within different regulator classes and regulator-shape functions, as expected from the one-loop universality property. This solidifies the procedure we used to develop an RG-consistent UV-initial condition. In the LPA case, we studied the UV parameter space. The latter is not totally accessible and has some boundaries, which translate into band in the accessible  $m_{\text{IR}}^2$  and on the phase diagrams obtained for different regulator-shape functions. We also observed that these bands tend to converge to a single point in the limit  $\Lambda \rightarrow \infty$ , indicating that one should choose a sufficiently large UV cutoff in order to get a parameter-independent initial condition and thus a regulator-independent IR potential. We also found that the LL and SL SL phase diagram are in significantly good agreement, signaling that our comparison procedure was indeed successful. Finally, we found that the results obtained with mixed combinations of regulator shape functions seem not to agree in the large- $\Lambda$  limit, due to possible scales mismatch in the FRG-scale integration.

Finally, the second-last chapter is devoted to the study of thermodynamic geometry of the quark-meson model, which is based on the interpretation of the parameter space of the system as a differential manifold. One then can obtain relevant information about the phase transitions from the Ricci scalar. We studied the chiral crossover investigating the behavior of the Ricci scalar up to the critical point, featuring a peaking behavior in the presence of the crossover. We then repeated this analysis in the chiral limit, where the phase transition is expected to be of second order. Moreover, for low values of the chemical potential, the Ricci scalar remains negative, indicating that bosonic fluctuations reduce the system's ability to completely overcome the fermionic statistical repulsion of quarks. On the other hand, as the chemical potential increases and approaches the critical point, we found that  $R$  is increased and changes sign, in agreement with mean-field studies. This geometric technique appears to be particularly interesting, and promising for new applications, since it can shed light on the (chiral) phase transition of QCD via quantities which are influenced by higher-order momenta of the thermodynamic potential, thus allowing us to analyze the transition in a more comprehensive way.

Possible developments of the work performed in this thesis can include the study of the stability of the obtained results under the improvement of the truncation adopted in the functional renormalization group approach. For example, the inclusion of the scale-dependent wave function renormalization factors both for the boson and the quark fields can be particularly interesting, especially due to the possible formation of inhomogeneous phases at large chemical potential. We begin to assess this issue by conducting preliminary studies of the  $O(N)$  model in the so-called LPA' approximation, which are not presented in this thesis, which show that the flow equations can be cast once again into the form of an advection-diffusion equation for the RG evolution of the effective potential, which is then coupled to an ODE for the RG evolution of the wave function renormalization factor. The resulting system of differential equations can then be solved using the same numerical technique we adopted in this thesis, thus opening the possibility to a detailed study of the impact of the wave function renormalization factor on the results discussed in this work.

Another possible direction for improvements and further studies can involve the inclusion of other condensation channels, as for example diquarks or meson condensates. This would mean the change of the model with the inclusion of different degrees of

freedom, which would give us the possibility to analyze different phenomena and transitions w.r.t. the chiral one, resulting in a wider mapping of the QCD phase diagram. This was ultimately the goal of this thesis and obviously still is (and will definitely be for the years that come) the goal of a wide sector of the high-energy physics research.





# Bibliography

- [1] David J. Gross and Frank Wilczek, *Phys. Rev. Lett.* **30**, 1343 (1973).
- [2] H. David Politzer, *Phys. Rev. Lett.* **30**, 1346 (1973).
- [3] D. T. Son and M. A. Stephanov, *Physical Review Letters* **86**, 592–595 (2001).
- [4] Bastian B. Brandt, Gergely Endrődi, and Sebastian Schmalzbauer, *EPJ Web of Conferences* **175**, 07020 (2018).
- [5] A. Bazavov, H.-T. Ding, P. Hegde, O. Kaczmarek, F. Karsch, N. Karthik, E. Laermann, Anirban Lahiri, R. Larsen, S.-T. Li, Swagato Mukherjee, H. Ohno, P. Petreczky, H. Sandmeyer, C. Schmidt, S. Sharma, and P. Steinbrecher, *Physics Letters B* **795**, 15–21 (2019).
- [6] Christian Schmidt and Sayantan Sharma, *J. Phys. G* **44**, 104002 (2017).
- [7] M. D’Agostino, M. Bruno, F. Gulminelli, F. Cannata, P. Chomaz, G. Casini, E. Geraci, F. Gramegna, A. Moroni, and G. Vannini, *Nucl. Phys. A* **749**, 55 (2005).
- [8] Stefan Floerchinger and Christof Wetterich, *Nuclear Physics A* **890–891**, 11–24 (2012).
- [9] L. G. Moretto, A. C. Larsen, F. Giacoppo, M. Guttormsen, S. Siem, and A. V. Voinov, *J. Phys. Conf. Ser.* **580**, 012048 (2015).
- [10] Len Brandes, Norbert Kaiser, and Wolfram Weise, *The European Physical Journal A* **57**, (2021).
- [11] Marco Ruggieri, Motoi Tachibana, and Vincenzo Greco, *JHEP* **07**, 165 (2013).
- [12] M. Ruggieri, L. Oliva, P. Castorina, R. Gatto, and V. Greco, *Phys. Lett. B* **734**, 255 (2014).
- [13] V. Skokov, B. Friman, E. Nakano, K. Redlich, and B.-J. Schaefer, *Phys. Rev. D* **82**, 034029 (2010).
- [14] Leonid Ya. Glozman, Owe Philipsen, and Robert D. Pisarski, *The European Physical Journal A* **58**, (2022).
- [15] Larry McLerran and Robert D. Pisarski, *Nuclear Physics A* **796**, 83–100 (2007).
- [16] Larry McLerran, *Nuclear Physics A* **830**, 709c (2009), quark Matter 2009.
- [17] Nils Strodthoff, Bernd-Jochen Schaefer, and Lorenz von Smekal, *Physical Review D* **85**, (2012).

- [18] Nils Strodthoff and Lorenz von Smekal, *Physics Letters B* **731**, 350–357 (2014).
- [19] Michael Buballa, *Physics Reports* **407**, 205 (2005).
- [20] Naseemuddin Khan, Jan M. Pawłowski, Fabian Rennecke, and Michael M. Scherer, *The Phase Diagram of QC2D from Functional Methods*, 2015.
- [21] Gaopei Pan and Zi Yang Meng, in *Encyclopedia of Condensed Matter Physics* (Elsevier, ADDRESS, 2024), p. 879–893.
- [22] C. R. Allton, S. Ejiri, S. J. Hands, O. Kaczmarek, F. Karsch, E. Laermann, Ch. Schmidt, and L. Scorzato, *Phys. Rev. D* **66**, 074507 (2002).
- [23] Owe Philipsen, *PoS ConfinementVIII*, 011 (2012).
- [24] K. N. Anagnostopoulos and J. Nishimura, *Physical Review D* **66**, (2002).
- [25] Wei-jie Fu, Jan M. Pawłowski, and Fabian Rennecke, *Physical Review D* **101**, (2020).
- [26] Christian S. Fischer, Jan Luecker, and Christian A. Welzbacher, *Physical Review D* **90**, (2014).
- [27] Fei Gao, Jing Chen, Yu-Xin Liu, Si-Xue Qin, Craig D. Roberts, and Sebastian M. Schmidt, *Physical Review D* **93**, (2016).
- [28] Jonas Wilhelm, Lukas Holicki, Dominik Smith, Björn Wellegehausen, and Lorenz von Smekal, *Phys. Rev. D* **100**, 114507 (2019).
- [29] B.-J. Schaefer, J. M. Pawłowski, and J. Wambach, *Physical Review D* **76**, (2007).
- [30] Xiang Li, Wei-jie Fu, and Yu-xin Liu, *Physical Review D* **99**, (2019).
- [31] Prabal Adhikari, Jens O. Andersen, and Patrick Kneschke, *Phys. Rev. D* **98**, 074016 (2018).
- [32] Eduardo Grossi and Nicolas Wink, *Resolving phase transitions with Discontinuous Galerkin methods*, 2019.
- [33] Hongxia Huang, Chengrong Deng, Xuejie Liu, Yue Tan, and Jialun Ping, *Symmetry* **15**, 1298 (2023).
- [34] Richard F. Lebed, *PoS FPCP2023*, 028 (2023).
- [35] R. A. Fini, *Acta Phys. Polon. Supp.* **16**, 8 (2023).
- [36] Pedro Bicudo, *Phys. Rept.* **1039**, 1 (2023).
- [37] Greig Cowan and Tim Gershon, (2018).
- [38] Biagio Lucini, David Mason, Maurizio Piai, Enrico Rinaldi, and Davide Vadacchino, *Phys. Rev. D* **108**, 074517 (2023).
- [39] Suraj Kumar Rai and Vivek Kumar Tiwari, (2023).
- [40] Kenji Fukushima and Vladimir Skokov, *Progress in Particle and Nuclear Physics* **96**, 154–199 (2017).
- [41] Markus Quandt and Hugo Reinhardt, *Physical Review D* **106**, (2022).
- [42] Murray Gell-Mann, (1961).

- [43] Yuval Ne'eman, *Nucl. Phys.* **26**, 222 (1961).
- [44] G. Zweig, (1964).
- [45] G. Zweig, in *DEVELOPMENTS IN THE QUARK THEORY OF HADRONS. VOL. 1. 1964 - 1978*, edited by D. B. Lichtenberg and Simon Peter Rosen (PUBLISHER, ADDRESS, 1964), pp. 22–101.
- [46] J. F. Donoghue, E. Golowich, and Barry R. Holstein, *Dynamics of the standard model* (CUP, ADDRESS, 2014), Vol. 2.
- [47] Steven Weinberg, *The Quantum Theory of Fields* (Cambridge University Press, ADDRESS, 1996), Vol. 2.
- [48] Stephen L. Adler, *Phys. Rev.* **177**, 2426 (1969).
- [49] J. S. Bell and R. Jackiw, *Nuovo Cim. A* **60**, 47 (1969).
- [50] Jeffrey Goldstone, Abdus Salam, and Steven Weinberg, *Phys. Rev.* **127**, 965 (1962).
- [51] Daniel Naegels, *An introduction to Goldstone boson physics and to the coset construction*, 2021.
- [52] Alan Durrant, *Quantum Physics of Matter*, 1 ed. (CRC Press, Location Boca Raton, 2000).
- [53] John Bardeen, L. N. Cooper, and J. R. Schrieffer, *Phys. Rev.* **106**, 162 (1957).
- [54] B.-J. Schaefer, M. Wagner, and J. Wambach, *Phys. Rev. D* **81**, 074013 (2010).
- [55] Takeru Yokota, Teiji Kunihiro, and Kenji Morita, *PTEP* **2016**, 073D01 (2016).
- [56] M. Reuter, *Phys. Rev. D* **57**, 971 (1998).
- [57] Roberto Percacci and Gian Paolo Vacca, *Eur. Phys. J. C* **75**, 188 (2015).
- [58] Kenneth G. Wilson and J. Kogut, *Physics Reports* **12**, 75 (1974).
- [59] Andrea Pelissetto and Ettore Vicari, *Physics Reports* **368**, 549 (2002).
- [60] Martin Hasenbusch, *Phys. Rev. B* **82**, 174433 (2010).
- [61] Massimo Campostrini, Martin Hasenbusch, Andrea Pelissetto, Paolo Rossi, and Ettore Vicari, *Phys. Rev. B* **65**, 144520 (2002).
- [62] John L. Cardy, *Nuclear Physics B* **389**, 577 (1993).
- [63] Christof Wetterich, *Phys. Lett. B* **301**, 90 (1993).
- [64] Ulrich Ellwanger, *Z. Phys. C* **62**, 503 (1994).
- [65] Tim R. Morris, *Phys. Lett. B* **334**, 355 (1994).
- [66] M. Reuter and C. Wetterich, *Nucl. Phys. B* **417**, 181 (1994).
- [67] Christof Wetterich, *Physics Letters B* **301**, 90 (1993).
- [68] Jan M. Pawłowski, *Annals Phys.* **322**, 2831 (2007).
- [69] Holger Gies, *Lect. Notes Phys.* **852**, 287 (2012).

- [70] Peter Kopietz, Lorenz Bartosch, and Florian Schütz, *Introduction to the functional renormalization group* (Springer Berlin, Heidelberg, ADDRESS, 2010), Vol. 798.
- [71] N. Dupuis, L. Canet, A. Eichhorn, W. Metzner, J. M. Pawłowski, M. Tissier, and N. Wschebor, *Phys. Rept.* **910**, 1 (2021).
- [72] Juergen Berges, Nikolaos Tetradis, and Christof Wetterich, *Phys. Rept.* **363**, 223 (2002).
- [73] Leo P. Kadanoff, *Physics Physique Fizika* **2**, 263 (1966).
- [74] Kenneth G. Wilson, *Phys. Rev. B* **4**, 3184 (1971).
- [75] Kenneth G. Wilson, *Phys. Rev. B* **4**, 3174 (1971).
- [76] Kenneth G. Wilson, *Rev. Mod. Phys.* **47**, 773 (1975).
- [77] K. G. Wilson, *Sci. Am.* **241**, 140 (1979).
- [78] Joseph Polchinski, *Nucl. Phys. B* **231**, 269 (1984).
- [79] Anna Hasenfratz and Peter Hasenfratz, *Nucl. Phys. B* **270**, 687 (1986).
- [80] Adrian Koenigstein, Martin J. Steil, Nicolas Wink, Eduardo Grossi, Jens Braun, Michael Buballa, and Dirk H. Rischke, *Phys. Rev. D* **106**, 065012 (2022).
- [81] Adrian Koenigstein, Martin J. Steil, Nicolas Wink, Eduardo Grossi, and Jens Braun, *Phys. Rev. D* **106**, 065013 (2022).
- [82] Martin J. Steil and Adrian Koenigstein, *Phys. Rev. D* **106**, 065014 (2022).
- [83] C. Wetterich, *Nuclear Physics B* **352**, 529 (1991).
- [84] Jens Braun, Marc Leonhardt, and Jan M. Pawłowski, *SciPost Phys.* **6**, 056 (2019).
- [85] Daniel F. Litim, *Phys. Rev. D* **64**, 105007 (2001).
- [86] Jan M. Pawłowski, Michael M. Scherer, Richard Schmidt, and Sebastian J. Wetzel, *Annals Phys.* **384**, 165 (2017).
- [87] Jens Braun, Timon Dörfeld, Benedikt Schallmo, and Sebastian Töpfel, *Phys. Rev. D* **104**, 096002 (2021).
- [88] Jens Braun et al., *Renormalised spectral flows*, 2022.
- [89] C. Wetterich, *Z. Physik C Particles and Fields* **57**, 451 (1993).
- [90] Tim R. Morris, *Int. J. Mod. Phys. A* **9**, 2411 (1994).
- [91] Bastian Bergerhoff and Christof Wetterich, *Phys. Rev. D* **57**, 1591 (1998).
- [92] B.-J. Schaefer, O. Bohr, and J. Wambach, *Phys. Rev. D* **65**, 105008 (2002).
- [93] Nils Strodthoff, *Physical Review D* **95**, (2017).
- [94] Kazuhiko Kamikado, Nils Strodthoff, Lorenz von Smekal, and Jochen Wambach, *The European Physical Journal C* **74**, (2014).
- [95] F. J. Dyson, *Phys. Rev.* **75**, 1736 (1949).

- [96] Julian S. Schwinger, *Proc. Nat. Acad. Sci.* **37**, 452 (1951).
- [97] Craig D. Roberts and Anthony G. Williams, *Progress in Particle and Nuclear Physics* **33**, 477–575 (1994).
- [98] Carl M. Bender, Christos Karapoulitidis, and S. P. Klevansky, *Phys. Rev. Lett.* **130**, 101602 (2023).
- [99] Bernd-Jochen Schaefer and Hans-Jürgen Pirner, *Nuclear Physics A* **660**, 439 (1999).
- [100] Léonie Canet, Bertrand Delamotte, Dominique Mouhanna, and Julien Vidal, *Phys. Rev. D* **67**, 065004 (2003).
- [101] Jan M. Pawłowski and Fabian Rennecke, *Phys. Rev. D* **90**, 076002 (2014).
- [102] Jan M. Pawłowski, Nils Strodthoff, and Nicolas Wink, *Phys. Rev. D* **98**, 074008 (2018).
- [103] Naseemuddin Khan, Jan M. Pawłowski, Fabian Rennecke, and Michael M. Scherer, *The Phase Diagram of QC2D from Functional Methods*, 2015.
- [104] G. Papp, B.-J. Schaefer, H.-J. Pirner, and J. Wambach, *Phys. Rev. D* **61**, 096002 (2000).
- [105] Eduardo Grossi, Friederike J. Ihssen, Jan M. Pawłowski, and Nicolas Wink, *Phys. Rev. D* **104**, 016028 (2021).
- [106] Jonas Stoll, Niklas Zorbach, Adrian Koenigstein, Martin J. Steil, and Stefan Rechenberger, *Bosonic fluctuations in the  $(1 + 1)$ -dimensional Gross-Neveu(-Yukawa) model at varying  $\mu$  and  $T$  and finite  $N$* , 2021.
- [107] Jennifer A. Adams, J. Berges, S. Bornholdt, F. Freire, N. Tetradis, and C. Wetterich, *Mod. Phys. Lett. A* **10**, 2367 (1995).
- [108] Bertrand Delamotte, Matthieu Tissier, and Nicolás Wschebor, *Phys. Rev. E* **93**, 012144 (2016).
- [109] Adrian Koenigstein, Laurin Pannullo, Stefan Rechenberger, Martin J. Steil, and Marc Winstel, *J. Phys. A* **55**, 375402 (2022).
- [110] Fabian Rennecke, Robert D. Pisarski, and Dirk H. Rischke, *Phys. Rev. D* **107**, 116011 (2023).
- [111] Fabian Rennecke and Robert D. Pisarski, *Moat Regimes in QCD and their Signatures in Heavy-Ion Collisions*, 2021.
- [112] Laurin Pannullo, *Phys. Rev. D* **108**, 036022 (2023).
- [113] Friederike Ihssen, Jan M. Pawłowski, Franz R. Sattler, and Nicolas Wink, (2023).
- [114] Jens Braun, Felix Karbstein, Stefan Rechenberger, and Dietrich Roscher, *Phys. Rev. D* **93**, 014032 (2016).
- [115] B.-J. Schaefer and J. Wambach, *Nuclear Physics A* **757**, 479 (2005).
- [116] C. WETTERICH, *International Journal of Modern Physics A* **09**, 3571 (1994).
- [117] Fabrizio Murgana, Adrian Koenigstein, and Dirk H. Rischke, (2023).

- [118] Hildegard Meyer-Ortmanns, *Rev. Mod. Phys.* **68**, 473 (1996).
- [119] H. Kleinert, *Gauge Fields in Condensed Matter*, 1 ed. (World Scientific, Singapore, 1989).
- [120] Leon Hostetler, Jin Zhang, Ryo Sakai, Judah Unmuth-Yockey, Alexei Bazavov, and Yannick Meurice, *PoS LATTICE2021*, 353 (2022).
- [121] Robert B. Griffiths Barry Simon, *Communications in Mathematical Physics* **33**, 145 (1973).
- [122] Jens Braun, Holger Gies, and Daniel D. Scherer, *Phys. Rev. D* **83**, 085012 (2011).
- [123] Lukas Janssen and Holger Gies, *Phys. Rev. D* **86**, 105007 (2012).
- [124] Daniel F. Litim, *Nucl. Phys. B* **631**, 128 (2002).
- [125] Julia Borchardt and Benjamin Knorr, *Phys. Rev. D* **91**, 105011 (2015), [Erratum: *Phys.Rev.D* 93, 089904 (2016)].
- [126] Julia Borchardt and Astrid Eichhorn, *Phys. Rev. E* **94**, 042105 (2016).
- [127] Gonzalo De Polsi, Ivan Balog, Matthieu Tissier, and Nicolás Wschebor, *Phys. Rev. E* **101**, 042113 (2020).
- [128] O. Bohr, B. J. Schaefer, and J. Wambach, *Int. J. Mod. Phys. A* **16**, 3823 (2001).
- [129] Andrzej Chlebicki and Pawel Jakubczyk, *SciPost Phys.* **10**, 134 (2021).
- [130] Ivan Balog, Hugues Chaté, Bertrand Delamotte, Maroje Marohnic, and Nicolás Wschebor, *Phys. Rev. Lett.* **123**, 240604 (2019).
- [131] Gonzalo De Polsi, Guzmán Hernández-Chifflet, and Nicolás Wschebor, *Phys. Rev. E* **104**, 064101 (2021).
- [132] Martin J. Steil and Adrian Koenigstein, *Phys. Rev. D* **106**, 065014 (2022).
- [133] Friederike Ihssen and Jan M. Pawłowski, *Functional flows for complex effective actions*, 2022.
- [134] Friederike Ihssen, Jan M. Pawłowski, Franz R. Sattler, and Nicolas Wink, *Local Discontinuous Galerkin for the Functional Renormalisation Group*, 2022.
- [135] A. B. Zamolodchikov, *JETP Lett.* **43**, 730 (1986).
- [136] G. Zumbach, *Nucl. Phys. B* **413**, 754 (1994).
- [137] N. Tetradis and D. F. Litim, *Nucl. Phys. B* **464**, 492 (1996).
- [138] D. Litim and N. Tetradis, (1995).
- [139] Oliver J. Rosten, *Phys. Rept.* **511**, 177 (2012).
- [140] Ken-Ichi Aoki, Shin-Ichiro Kumamoto, and Daisuke Sato, *PTEP* **2014**, 043B05 (2014).
- [141] Ken-Ichi Aoki, Shin-Ichiro Kumamoto, and Masatoshi Yamada, *Nucl. Phys. B* **931**, 105 (2018).

- [142] Alexander Kurganov and Eitan Tadmor, *Journal of Computational Physics* **160**, 241 (2000).
- [143] Marco D'Attanasio and Tim R. Morris, *Phys. Lett. B* **409**, 363 (1997).
- [144] Leonie Canet, Bertrand Delamotte, Dominique Mouhanna, and Julien Vidal, *Phys. Rev. D* **67**, 065004 (2003).
- [145] Jürgen Eser, Florian Divotgey, Mario Mitter, and Dirk H. Rischke, *Phys. Rev. D* **98**, 014024 (2018).
- [146] Florian Divotgey, Jürgen Eser, and Mario Mitter, *Phys. Rev. D* **99**, 054023 (2019).
- [147] Niklas Cichutek, Florian Divotgey, and Jürgen Eser, *Phys. Rev. D* **102**, 034030 (2020).
- [148] Daniel F. Litim, *Phys. Rev. D* **64**, 105007 (2001).
- [149] Sidney R. Coleman, R. Jackiw, and H. David Politzer, *Phys. Rev. D* **10**, 2491 (1974).
- [150] Aleksandar Kocic and John B. Kogut, *Nucl. Phys. B* **455**, 229 (1995).
- [151] E. Cavalcanti, J. A. Lourenço, C. A. Linhares, and A. P. C. Malbouisson, *Phys. Rev. D* **99**, 025007 (2019).
- [152] D. U. Jungnickel and C. Wetterich, in *Workshop on the Exact Renormalization Group* (PUBLISHER, ADDRESS, 1998), pp. 41–113.
- [153] Arttu K. Rajantie, *Nucl. Phys. B* **480**, 729 (1996), [Erratum: *Nucl.Phys.B* 513, 761–762 (1998)].
- [154] Shang keng Ma, *Modern Theory Of Critical Phenomena*, 1st ed. (Imprint Routledge, New York, 2001).
- [155] Nigel Goldenfeld, *Lectures on phase transitions and the renormalization group* (CRC Press, Boca Raton, 2018).
- [156] John Cardy, *Scaling and Renormalization in Statistical Physics, Cambridge Lecture Notes in Physics* (Cambridge University Press, Cambridge, 1996).
- [157] Giuseppe Mussardo, *Statistical field theory: an introduction to exactly solved models in statistical physics* (Oxford Univ. Press, New York, NY, 2010).
- [158] Marcela Peláez and Nicolás Wschebor, *Phys. Rev. E* **94**, 042136 (2016).
- [159] Kerson Huang, *Statistical Mechanics*, 2 ed. (John Wiley & Sons, New York, USA, 1987).
- [160] Alexander J. Helmboldt, Jan M. Pawłowski, and Nils Strodthoff, *Phys. Rev. D* **91**, 054010 (2015).
- [161] Martin Hasenbusch, *Phys. Rev. B* **82**, 174433 (2010).
- [162] Massimo Campostrini, Martin Hasenbusch, Andrea Pelissetto, Paolo Rossi, and Ettore Vicari, *Phys. Rev. B* **65**, 144520 (2002).
- [163] Riccardo Guida and Jean Zinn-Justin, *J. Phys. A* **31**, 8103 (1998).
- [164] Mikhail V. Kompaniets and Erik Panzer, *Phys. Rev. D* **96**, 036016 (2017).



- [165] Hirohiko Shimada and Shinobu Hikami, *J. Statist. Phys.* **165**, 1006 (2016).
- [166] Shai M. Chester, Walter Landry, Junyu Liu, David Poland, David Simmons-Duffin, Ning Su, and Alessandro Vichi, *JHEP* **06**, (2020).
- [167] Filip Kos, David Poland, and David Simmons-Duffin, *JHEP* **06**, (2014).
- [168] Friederike Ihssen, Franz R. Sattler, and Nicolas Wink, *Numerical RG-time integration of the effective potential: Analysis and Benchmark*, 2023.
- [169] J. W. Thomas, *Numerical partial differential equations: conservation laws and elliptic equations* (Springer, New York, 1999).
- [170] Nicolas Wink, Ph.D. thesis, U. Heidelberg, ITP, 2020.
- [171] Murray Gell-Mann and M Levy, *Nuovo Cim.* **16**, 705 (1960).
- [172] Volker Koch, *Int. J. Mod. Phys. E* **6**, 203 (1997).
- [173] Michael Edward Peskin and Daniel V. Schroeder, *An Introduction to Quantum Field Theory* (Westview Press, ADDRESS, 1995), reading, USA: Addison-Wesley (1995) 842 p.
- [174] N. Tetradis, *Nucl. Phys. A* **726**, 93 (2003).
- [175] N. Tetradis, *Adv. Nucl. Phys.* **15**, 15 (2020).
- [176] E. D. Commins and P. H. Bucksbaum, *Weak Interactions of Leptons and Quarks* (PUBLISHER, ADDRESS, 1983).
- [177] M. Procura, B. U. Musch, T. Wollenweber, T. R. Hemmert, and W. Weise, *Phys. Rev. D* **73**, 114510 (2006).
- [178] Reilly Atkinson, *Phys. Rev.* **162**, 1488 (1967).
- [179] Joseph I. Kapusta, *Finite Temperature Field Theory, Cambridge Monographs on Mathematical Physics* (Cambridge University Press, Cambridge, 1989).
- [180] Mikko Laine and Aleksi Vuorinen, *Basics of Thermal Field Theory: A Tutorial on Perturbative Computations* (Springer International Publishing, ADDRESS, 2016).
- [181] Munshi G. Mustafa, *The European Physical Journal Special Topics* **232**, 1369–1457 (2023).
- [182] L. D. Landau, *Zh. Eksp. Teor. Fiz.* **7**, 19 (1937).
- [183] Jonas Stoll, Niklas Zorbach, Adrian Koenigstein, Martin J. Steil, and Stefan Rechenberger, (2021), arXiv:2108.10616 [hep-ph].
- [184] Ralf-Arno Tripolt, Johannes Weyrich, Lorenz von Smekal, and Jochen Wambach, *Phys. Rev. D* **98**, 094002 (2018).
- [185] Konstantin Otto, Christopher Busch, and Bernd-Jochen Schaefer, *Phys. Rev. D* **106**, 094018 (2022).
- [186] Fabrizio Murgana, Vincenzo Greco, Marco Ruggieri, and Dario Zappalà, (2023).
- [187] George Ruppeiner, *Phys. Rev. A* **20**, 1608 (1979).

- [188] George Ruppeiner, *Phys. Rev. A* **24**, 488 (1981).
- [189] George Ruppeiner, *Phys. Rev. A* **27**, 1116 (1983).
- [190] G. Ruppeiner, *Phys. Rev. Lett.* **50**, 287 (1983).
- [191] George Ruppeiner, *Phys. Rev. A* **31**, 2688 (1985).
- [192] George Ruppeiner, *Phys. Rev. A* **32**, 3141 (1985).
- [193] George Ruppeiner, *Phys. Rev. A* **34**, 4316 (1986).
- [194] George Ruppeiner and Christopher Davis, *Phys. Rev. A* **41**, 2200 (1990).
- [195] George Ruppeiner and Jerry Chance, *The Journal of Chemical Physics* **92**, 3700 (1990).
- [196] George Ruppeiner, *Phys. Rev. A* **44**, 3583 (1991).
- [197] George Ruppeiner, *Phys. Rev. E* **47**, 934 (1993).
- [198] George Ruppeiner, *Rev. Mod. Phys.* **67**, 605 (1995), [Erratum: *Rev. Mod. Phys.* **68**, 313–313 (1996)].
- [199] George Ruppeiner, *Phys. Rev. E* **57**, 5135 (1998).
- [200] George Ruppeiner, *Phys. Rev. E* **72**, 016120 (2005).
- [201] George Ruppeiner, *American Journal of Physics* **78**, 1170 (2010).
- [202] George Ruppeiner, *Phys. Rev. D* **78**, 024016 (2008).
- [203] George Ruppeiner, Anurag Sahay, Tapobrata Sarkar, and Gautam Sengupta, *Phys. Rev. E* **86**, 052103 (2012).
- [204] George Ruppeiner, *J. Phys. Conf. Ser.* **410**, 012138 (2013).
- [205] George Ruppeiner, *Phys. Rev. E* **86**, 021130 (2012).
- [206] Helge-Otmar May, Peter Mausbach, and George Ruppeiner, *Phys. Rev. E* **88**, 032123 (2013).
- [207] George Ruppeiner, *Springer Proc. Phys.* **153**, 179 (2014).
- [208] George Ruppeiner, *Journal of Low Temperature Physics* **174**, 13 (2014).
- [209] George Ruppeiner and Stefano Bellucci, *Phys. Rev. E* **91**, 012116 (2015).
- [210] Helge-Otmar May, Peter Mausbach, and George Ruppeiner, *Phys. Rev. E* **91**, 032141 (2015).
- [211] George Ruppeiner, *Journal of Low Temperature Physics* **185**, 246 (2016).
- [212] George Ruppeiner, Nathan Dyjack, Abigail McAloon, and Jerry Stoops, *The Journal of Chemical Physics* **146**, 224501 (2017).
- [213] George Ruppeiner, *Phys. Rev. D* **75**, 024037 (2007).
- [214] Bonan Zhang, Shen-Song Wan, and Marco Ruggieri, *Phys. Rev. D* **101**, 016014 (2020).

- [215] Paolo Castorina, Daniele Lanteri, and Marco Ruggieri, *Phys. Rev. D* **102**, 116022 (2020).
- [216] P. Castorina, D. Lanteri, and S. Mancani, *Eur. Phys. J. Plus* **135**, 43 (2020).
- [217] P. Ferstl, M. Schaden, and E. Werner, *Nucl. Phys. A* **452**, 680 (1986).
- [218] H. Janyszek and R. Mrugala, *Phys. Rev. A* **39**, 6515 (1989).
- [219] H Janyszek, *Journal of Physics A: Mathematical and General* **23**, 477 (1990).
- [220] H. Janyszek R. Mrugala, *Open Systems & Information Dynamics* **1**, 379 (1992).
- [221] Helge-Otmar May and Peter Mausbach, *Phys. Rev. E* **85**, 031201 (2012).
- [222] Helge-Otmar May, Peter Mausbach, and George Ruppeiner, *Phys. Rev. E* **88**, 032123 (2013).
- [223] Behrouz Mirza and Hosein Mohammadzadeh, *Phys. Rev. E* **78**, 021127 (2008).
- [224] Hiroshi Oshima, Tsunehiro Obata, and Hiroaki Hara, *Journal of Physics A: Mathematical and General* **32**, 6373 (1999).
- [225] Marcelo R. Ubriaco, *Physica A: Statistical Mechanics and its Applications* **392**, 4868 (2013).
- [226] M R Ubriaco, *Journal of Physics: Conference Series* **766**, 012007 (2016).
- [227] Hossein Mehri-Dehnavi and Hosein Mohammadzadeh, *Journal of Physics A: Mathematical and Theoretical* **53**, 375009 (2020).
- [228] Anshuman Dey, Pratim Roy, and Tapobrata Sarkar, *Physica A: Statistical Mechanics and its Applications* **392**, 6341 (2013).
- [229] Gautam Sengupta Pankaj Chaturvedi, Anirban Das, *The European Physical Journal C* **77**, 110 (2017).
- [230] Anurag Sahay and Rishabh Jha, *Phys. Rev. D* **96**, 126017 (2017).
- [231] Tapobrata Sarkar Anurag Sahay, Gautam Sengupta, *Journal of High Energy Physics* **82**, (2010).
- [232] Narit Pidokrajt Jan E. Åman, Ingemar Bengtsson, *General Relativity and Gravitation* **35**, 1733 (2003).
- [233] JIANYONG SHEN, RONG-GEN CAI, BIN WANG, and RU-KENG SU, *International Journal of Modern Physics A* **22**, 11 (2007).
- [234] Jan E. Aman and Narit Pidokrajt, *Phys. Rev. D* **73**, 024017 (2006).
- [235] Tapobrata Sarkar, Gautam Sengupta, and Bhupendra Nath Tiwari, *Journal of High Energy Physics* **2008**, 076 (2008).
- [236] Stefano Bellucci and Bhupendra Nath Tiwari, *Entropy* **14**, 1045 (2012).
- [237] Shao-Wen Wei and Yu-Xiao Liu, *Phys. Rev. D* **87**, 044014 (2013).
- [238] Shao-Wen Wei and Yu-Xiao Liu, *Phys. Rev. Lett.* **116**, 169903 (2016).
- [239] Anurag Sahay, *Phys. Rev. D* **95**, 064002 (2017).

- [240] George Ruppeiner, *Entropy* **20**, (2018).
- [241] Pavan Kumar Yerra and Chandrasekhar Bhamidipati, *International Journal of Modern Physics A* **35**, 2050120 (2020).
- [242] Pavan Kumar Yerra and Chandrasekhar Bhamidipati, *Physics Letters B* **819**, 136450 (2021).
- [243] Daniele Lanteri, Shen-Song Wan, Alfredo Iorio, and Paolo Castorina, *The European Physical Journal C* **81**, (2021).
- [244] P. Castorina, M. Imbrosciano, and D. Lanteri, *Phys. Rev. D* **98**, 096006 (2018).
- [245] P. Castorina, D. Lanteri, and S. Mancani, *The European Physical Journal Plus* **135**, (2020).
- [246] L. Diósi, *Physics Letters A* **120**, 377 (1987).
- [247] L. Diósi, B. Lukács, and A. Rácz, *The Journal of Chemical Physics* **91**, 3061 (1989).
- [248] Jens Braun, Marc Leonhardt, and Jan M. Pawłowski, *SciPost Phys.* **6**, 56 (2019).
- [249] Niklas Zorbach, Jonas Stoll, and Jens Braun, *Optimization and Stabilization of Functional Renormalization Group Flows*, 2024.
- [250] Michael Buballa and Stefano Carignano, *Progress in Particle and Nuclear Physics* **81**, 39 (2015).
- [251] D. Litim and N. Tetradis, *Approximate solutions of exact renormalization group equations*, 1995.
- [252] J. Iliopoulos, C. Itzykson, and A. Martin, *Rev. Mod. Phys.* **47**, 165 (1975).
- [253] N. Dupuis, L. Canet, A. Eichhorn, W. Metzner, J. M. Pawłowski, M. Tissier, and N. Wschebor, *Phys. Rept.* **910**, 1 (2021).
- [254] Jan M. Pawłowski, *Annals of Physics* **322**, 2831 (2007).
- [255] James D. Bjorken and Sidney D. Drell, *Relativistic Quantum Mechanics, International Series In Pure and Applied Physics* (McGraw-Hill, New York, 1965).
- [256] S. Pokorski, *GAUGE FIELD THEORIES* (Cambridge University Press, ADDRESS, 2005).
- [257] Edwige Godlewski and P. A. Raviart, *Applied Mathematical Sciences* (1996).
- [258] Begnaud Francis Hildebrand, *Introduction to Numerical Analysis: 2nd Edition* (Dover Publications, Inc., New York, NY, USA, 1987).
- [259] L. Brugnano and F. Iavernaro, *Advanced Numerical Methods in Applied Sciences* (MDPI AG, Switzerland, 2019).
- [260] Jonathan Goodman, Alexander Kurganov, and Philip Rosenau, *Nonlinearity* **12**, 247 (1999).
- [261] E. Bladé, M. Gómez-Valentín, J. Dolz, J.L. Aragón-Hernández, G. Corestein, and M. Sánchez-Juny, *Advances in Water Resources* **42**, 17 (2012).
- [262] K. O. Friedrichs, *Communications on Pure and Applied Mathematics* **7**, 345 (1954).

- [263] Peter D. Lax, *Communications on Pure and Applied Mathematics* **7**, 159 (1954).
- [264] Haim Nussli and Eitan Tadmor, *Journal of Computational Physics* **87**, 408 (1990).
- [265] Bram van Leer, *Journal of Computational Physics* **32**, 101 (1979).
- [266] Randall J. LeVeque, *Finite Volume Methods for Hyperbolic Problems, Cambridge Texts in Applied Mathematics* (Cambridge University Press, ADDRESS, 2002).
- [267] Bernd Einfeldt, *SIAM Journal on Numerical Analysis* **25**, 294 (1988).

## Notations and conventions

### A.1 Natural units

Throughout this work we used the natural-units convention:

$$\hbar = 1, \quad c = 1, \quad k_B = 1. \quad (\text{A.1})$$

If one wants to convert back the results to the SI units, one can use the relation

$$\hbar c \simeq 197.32698 \text{ MeV} \cdot \text{fm}, \quad (\text{A.2})$$

and the value of the Boltzmann constant

$$k_B = 1.380649 \times 10^{-23} \text{ m}^2 \cdot \text{kg} \cdot \text{s}^{-2} \cdot \text{K}^{-1}. \quad (\text{A.3})$$

### A.2 Euclidean and Minkowski metric

When performing FRG calculations, we used the Euclidean-metric convention

$$g_{\mu\nu} = \begin{pmatrix} 1 & 0 & 0 & 0 \\ 0 & 1 & 0 & 0 \\ 0 & 0 & 1 & 0 \\ 0 & 0 & 0 & 1 \end{pmatrix}, \quad (\text{A.4})$$

which is obtained from the standard (mostly minus) Minkowski metric

$$g_{\mu\nu} = \begin{pmatrix} 1 & 0 & 0 & 0 \\ 0 & -1 & 0 & 0 \\ 0 & 0 & -1 & 0 \\ 0 & 0 & 0 & -1 \end{pmatrix}, \quad (\text{A.5})$$

by performing a Wick rotation  $t \rightarrow -i\tau$ .

### A.3 Pauli matrices

The Pauli matrices are defined as follows:

$$\sigma_1 = \begin{pmatrix} 0 & 1 \\ 1 & 0 \end{pmatrix}, \quad \sigma_2 = \begin{pmatrix} 0 & -i \\ i & 0 \end{pmatrix}, \quad \sigma_3 = \begin{pmatrix} 1 & 0 \\ 0 & -1 \end{pmatrix}. \quad (\text{A.6})$$

They are Hermitian matrices and fulfill the commutation relations of the SU(2) algebra

$$\left[ \frac{\sigma_l}{2}, \frac{\sigma_m}{2} \right] = i \varepsilon_{lmn} \frac{\sigma_n}{2}. \quad (\text{A.7})$$

## A.4 Dirac matrices

The Euclidean  $\gamma$  matrices are defined as follows

$$\gamma_0 = \begin{pmatrix} 0 & \mathbb{I}_{2 \times 2} \\ \mathbb{I}_{2 \times 2} & 0 \end{pmatrix}, \quad \gamma_k = \begin{pmatrix} 0 & -i\sigma_k \\ i\sigma_k & 0 \end{pmatrix}, \quad k = 1, 2, 3. \quad (\text{A.8})$$

where we used the chiral representation. They fulfill the Clifford algebra

$$\{\gamma_\mu, \gamma_\nu\} = 2\delta_{\mu\nu} \mathbb{I}_{4 \times 4}, \quad (\text{A.9})$$

and are Hermitian

$$(\gamma_\mu)^\dagger = \gamma_\mu. \quad (\text{A.10})$$

Furthermore, we introduce the fifth Euclidean gamma matrix as follows

$$\gamma_5 = \gamma_0 \gamma_1 \gamma_2 \gamma_3 = \begin{pmatrix} -\mathbb{I}_{2 \times 2} & 0 \\ 0 & \mathbb{I}_{2 \times 2} \end{pmatrix}, \quad (\text{A.11})$$

which fulfils the following properties

$$(\gamma_5)^\dagger = \gamma_5, \quad \{\gamma_\mu, \gamma_5\} = 0. \quad (\text{A.12})$$

The corresponding  $\gamma$  matrices in Minkowski spacetime are given by

$$\gamma_0^M = \gamma_0^E, \quad \gamma_k^M = i\gamma_k^E, \quad k = 1, 2, 3, \quad (\text{A.13})$$

and

$$\gamma_5^M = i\gamma_0^M \gamma_1^M \gamma_2^M \gamma_3^M = \gamma_5^E. \quad (\text{A.14})$$

## A.5 Fourier transform

The momentum space representation for bosonic fields reads

$$\phi(x) = \int \frac{d^4 p}{(2\pi^4)} \phi(p) e^{ipx}. \quad (\text{A.15})$$

Analogously, the momentum space representation for fermionic fields reads

$$\Psi(x) = \int \frac{d^4 p}{(2\pi^4)} \Psi(p) e^{ipx}, \quad (\text{A.16})$$

$$\bar{\Psi}(x) = \int \frac{d^4 p}{(2\pi^4)} \bar{\Psi}(p) e^{-ipx}. \quad (\text{A.17})$$

Finally, the corresponding representations in position space are given by

$$\phi(p) = \int d^4 x \phi(x) e^{-ipx}, \quad (\text{A.18})$$

$$\Psi(p) = \int d^4 x \Psi(x) e^{-ipx}, \quad (\text{A.19})$$

$$\bar{\Psi}(p) = \int d^4 x \bar{\Psi}(p) e^{ipx}. \quad (\text{A.20})$$



## Introductory elements to functional approaches

As the name suggests, functional methods are based on the formulation of QFT which arises from functional integrals, which are performed over the fields themselves as functions of the space-time variables. For this section, one can also refer to [47, 69, 72, 80, 173, 252, 253, 254]. An analogous description can be used to formulate statistical field theories, thus we will specify the analogy when new quantities are introduced.

In both quantum and statistical field theory, the main goal is to compute the *generating functional*  $\mathcal{Z}[J]$ , or the *partition function* in the statistical field-theory language,

$$\mathcal{Z}[J] \equiv \mathcal{N} \int \mathcal{D}\varphi e^{-S[\varphi] + \int J\varphi}, \quad (\text{B.1})$$

where  $\varphi = \varphi(x)$  is a generic field,  $S[\varphi]$  is the classical action describing the theory,  $J = J(x)$  corresponds to a space-time dependent external source and  $\int_x J\varphi = \int d^Dx J(x)\varphi(x)$  represents the source term.  $\mathcal{N}$  is a normalization constant and it is usually chosen, in the QFT context, in order to satisfy the condition

$$\mathcal{Z}[J = 0] = 1. \quad (\text{B.2})$$

As the name suggests,  $\mathcal{Z}[J]$  is a functional of the source term  $J$  and it is defined via a functional integral over all the possible field configurations, assuming that a properly regularized definition of the measure (for instance, with the introduction of a cutoff) is given. The desired results of functional approaches are the computation of the correlation functions as well as the free energy of the system. That is why the generating functional plays a crucial role, since it is possible to extract all the  $n$ -point functions

$$\langle \varphi(x_1) \cdots \varphi(x_n) \rangle := \mathcal{N} \int \mathcal{D}\varphi \varphi(x_1) \cdots \varphi(x_n) e^{-S[\varphi]} \quad (\text{B.3})$$

by functional differentiation w.r.t. the source  $J$ :

$$\langle \varphi(x_1) \cdots \varphi(x_n) \rangle = \frac{1}{\mathcal{Z}[0]} \left( \frac{\delta^n \mathcal{Z}[J]}{\delta J(x_1) \cdots \delta J(x_n)} \right)_{J=0}. \quad (\text{B.4})$$

This means that, in principle, once the generating functional is computed, the theory is solved. This is the idea, in the FRG framework, behind the so-called Polchinski equation, which we will not cover in this work, but one may refer to [78].

Particularly interesting for us is the 2-point function, or the *propagator*

$$G(x_1, x_2) = \langle \varphi(x_1) \varphi(x_2) \rangle = \frac{1}{\mathcal{Z}[0]} \left( \frac{\delta^2 \mathcal{Z}[J]}{\delta J(x_1) \delta J(x_2)} \right)_{J=0}. \quad (\text{B.5})$$

The functional derivatives of  $\mathcal{Z}[J]$  give us the complete set of  $n$ -point Green functions, including both connected and disconnected diagrams. However, in general one focuses on the calculation of the connected diagrams, disregarding the disconnected contributions because of redundancy. These diagrams can be obtained moving the focus away from the partition function  $\mathcal{Z}[J]$  and introducing the *generating functional of connected correlators*  $W[J]$ , also called *Schwinger functional*:

$$W[J] \equiv \ln \mathcal{Z}[J] = \ln \int \mathcal{D}\varphi e^{-S[\varphi] + \int J\varphi}. \quad (\text{B.6})$$

As the name suggests, functional derivatives of  $W[J]$  lead to the connected  $n$ -point functions:

$$\langle \varphi(x_1) \cdots \varphi(x_n) \rangle_c = \left( \frac{\delta^n W[J]}{\delta J(x_1) \cdots \delta J(x_n)} \right)_{J=0}. \quad (\text{B.7})$$

In the language of statistical field theory, the analogue of the Schwinger functional is the *Helmoltz free energy*. The previous definition can be easily obtained considering that  $W[J]$  takes into account all the connected diagrams, thus the most generic connected and disconnected diagram (which is computed starting from  $\mathcal{Z}[J]$ ) can be obtained from

$$\mathcal{Z}[J] = \sum_{n=0}^{\infty} \frac{1}{n!} (W[J])^n \equiv e^{W[J]}, \quad (\text{B.8})$$

where the factor  $1/n!$  takes into account the equivalent permutations.

Analogously to Eq. (B.5), we can then introduce the *connected 2-point function* or *connected propagator*

$$G_c(x_1, x_2) = \langle \varphi(x_1) \varphi(x_2) \rangle_c = \left( \frac{\delta^2 W[J]}{\delta J(x_1) \delta J(x_2)} \right)_{J=0}. \quad (\text{B.9})$$

Going further in the calculation, one can clearly see that  $W[J]$  removes the redundant information on the disconnected diagrams:

$$\begin{aligned} G_c(x_1, x_2) &= \left( \frac{\delta^2 W[J]}{\delta J(x_1) \delta J(x_2)} \right)_{J=0} = \left[ \frac{\delta}{\delta J(x_1)} \left( \frac{\delta \ln \mathcal{Z}[J]}{\delta J(x_2)} \right) \right]_{J=0} = \\ &= \left[ \frac{\delta}{\delta J(x_1)} \left( \frac{1}{\mathcal{Z}[J]} \frac{\delta \mathcal{Z}[J]}{\delta J(x_2)} \right) \right]_{J=0} = -\frac{1}{\mathcal{Z}[0]^2} \left( \frac{\delta \mathcal{Z}[J]}{\delta J(x_1)} \right)_{J=0} \left( \frac{\delta \mathcal{Z}[J]}{\delta J(x_2)} \right)_{J=0} + \\ &= \frac{1}{\mathcal{Z}[0]} \left( \frac{\delta^2 \mathcal{Z}[J]}{\delta J(x_1) \delta J(x_2)} \right)_{J=0} = \langle \varphi(x_1) \varphi(x_2) \rangle - \langle \varphi(x_1) \rangle \langle \varphi(x_2) \rangle. \end{aligned} \quad (\text{B.10})$$

We can now make one step further and introduce the *effective action*  $\Gamma$ , or the *Gibbs free energy* of the system in the language of statistical mechanics, simply via a Legendre transform of  $W[J]$ :

$$\Gamma[\phi] = \sup_J \left( \int_x J\phi - W[J] \right). \quad (\text{B.11})$$

Especially for the sake of FRG, it is important to remark that, due to the properties of the Legendre transform, this definition automatically ensures that  $\Gamma$  is convex.

When introducing the effective action, the Legendre transform changes the dependence of the functional from the source  $J$  to its canonically conjugated variable  $\phi$ . This

means that  $J$  in Eq. (B.11) has to be considered as a functional of  $\phi$ , namely  $J_{\text{sup}}[\phi]$  for which the sup is reached.  $J_{\text{sup}}[\phi]$  can be obtained via the standard definitions used in a Legendre transform:

$$\frac{\delta}{\delta J(x)} \left( \int J\phi - W[J] \right) = 0. \quad (\text{B.12})$$

In particular, this allows us to identify the physical meaning of the new variable  $\phi$ . Simply computing the derivative in Eq. (B.12), one obtains

$$\phi = \frac{\delta W[J]}{\delta J} = \frac{1}{\mathcal{Z}[J]} \frac{\delta \mathcal{Z}[J]}{\delta J} = \langle \phi \rangle_J, \quad (\text{B.13})$$

where we used the definitions Eqs. (B.6) and (B.4). This then implies that  $\phi$  represents the expectation value of the field  $\phi$  in the presence of the source  $J$ . That is the reason why it is usually referred to as the *classical field*.

As far as the physical content of the functional is concerned, while  $W[J]$  is the generating functional of the connected diagrams,  $\Gamma[\phi]$  is the generating functional of the *one-particle irreducible (1PI) proper vertices*, which, once again, can be obtained via functional derivatives of  $\Gamma[\phi]$ :

$$\Gamma^{(n)}(x_1, \dots, x_n) = \frac{\delta^n \Gamma[\phi]}{\delta \phi(x_1) \dots \delta \phi(x_n)}. \quad (\text{B.14})$$

Thus, all the physical information about the theory is encoded in the vertex functions and once one calculates  $\Gamma$  the theory is solved.

We now want to justify the name effective action for  $\Gamma$ . If we consider the derivative of  $\Gamma[\phi]$  w.r.t.  $\phi$  at  $J = J_{\text{sup}}[\phi]$ , using Eqs. (B.11) and (B.13), we obtain

$$\frac{\delta \Gamma[\phi]}{\delta \phi(x)} = - \int_y \frac{\delta W[J]}{\delta J(y)} \frac{\delta J(y)}{\delta \phi(x)} + \int_y \frac{\delta J(y)}{\delta \phi(x)} \phi(y) + J(x) = J(x). \quad (\text{B.15})$$

Equation (B.15) is the so-called *quantum equation of motion*, in analogy with the classical equation of motion

$$\frac{\delta S[\phi]}{\delta \phi(x)} = 0, \quad (\text{B.16})$$

which is equivalent to (B.15) when replacing  $\Gamma$  with the classical action  $S$  and setting the source term  $J = 0$ . Thus, following the parallelism, the effective action  $\Gamma[\phi]$  contains the information on the evolution of the field expectation value, also taking into account all the quantum corrections.

As a final remark for this section, we show a useful identity which links the 2-point connected propagator and the 2-point vertex functions. To do so we will exploit the trivial relation

$$\delta(x_1 - x_2) = \frac{\delta J(x_1)}{\delta J(x_2)}. \quad (\text{B.17})$$

Using the quantum equation of motion Eq. (B.15), one can trivially verify that

$$\frac{\delta J(x_1)}{\delta \phi(x_2)} = \frac{\delta^2 \Gamma[\phi]}{\delta \phi(x_2) \delta \phi(x_1)} = \Gamma^{(2)}(x_1, x_2). \quad (\text{B.18})$$

Considering now the definition of the classical field Eq. (B.13) and taking a derivative w.r.t the source  $J$ , one obtains

$$\frac{\delta\phi(x_1)}{\delta J(x_2)} = \frac{\delta^2 W[J]}{\delta J(x_2)\delta J(x_1)} = G_c(x_1, x_2). \quad (\text{B.19})$$

Thus, the combination of Eqs. (B.17) to (B.19) results in

$$\delta(x_1 - x_2) = \frac{\delta J(x_1)}{\delta J(x_2)} = \int d^D x \frac{\delta J(x_1)}{\delta\phi(x)} \frac{\delta\phi(x)}{\delta J(x_2)} = \int d^D x \Gamma^2(x_1, x) G_c(x, x_2), \quad (\text{B.20})$$

which we can write in a more compact form:

$$\mathbb{I} = \Gamma^{(2)} G_c \quad (\text{B.21})$$

implying that, in terms of operators

$$\Gamma^{(2)} = (G_c)^{-1} \quad \Longleftrightarrow \quad G_c = (\Gamma^{(2)})^{-1}. \quad (\text{B.22})$$

From Eq. (B.22) one can derive other relations between the  $n$ -point vertex functions and the propagators. As an example we show the one involving  $\Gamma^3$ . In particular, one has just to take a field derivative of Eq. (B.22)

$$\frac{\delta G_c}{\delta\phi} = \frac{\delta(\Gamma^{(2)})^{-1}}{\delta\phi} = -(\Gamma^{(2)})^{-1} \frac{\delta\Gamma^{(2)}}{\delta\phi} (\Gamma^{(2)})^{-1} = -G_c \Gamma^3 G_c \quad (\text{B.23})$$

or, in a more extensive format:

$$\frac{\delta}{\delta\phi(x_3)} G_c(x_1, x_2) = - \int d^D x d^D y G_c(x_1, x) \Gamma^3(x, x_2, y) G_c(y, x_3). \quad (\text{B.24})$$

## Derivation of the Wetterich equation

In this appendix, we will show the simple but slightly tedious steps that one has to follow in order to derive the Wetterich flow equation. Our starting point will be the definition of the average effective action Eq. (3.10) and of the scale-dependent classical average field Eq. (3.12).

In particular, computing the functional derivative of Eq. (3.10) with respect to  $\phi$  and following analogous steps to the ones we followed in Eq. (B.15) we get:

$$\frac{\delta\Gamma_k[\phi]}{\delta\phi(x)} = J(x) - (R_k\phi)(x), \quad (\text{C.1})$$

which means that the quantum equation of motion receives a contribution from the regulator. Taking once again the functional derivative of Eq. (C.1) w.r.t.  $\phi$ , we get

$$\frac{\delta J(x)}{\delta\phi(y)} = \frac{\delta^2\Gamma_k[\phi]}{\delta\phi(x)\delta\phi(y)} + R_k(x, y). \quad (\text{C.2})$$

Now, we easily derive from Eq. (3.12) that:

$$\frac{\delta\phi(y)}{\delta J(x')} = \frac{\delta^2 W_k[J]}{\delta J(x')\delta J(y)} \equiv G_k(y, x'), \quad (\text{C.3})$$

where we have defined the *connected propagator*

$$G_k(x, y) = \frac{\delta^2 W_k[J]}{\delta J(y)\delta J(x)} = \langle\varphi(x)\varphi(y)\rangle - \langle\varphi(x)\rangle\langle\varphi(y)\rangle. \quad (\text{C.4})$$

Following then the steps described in Eq. (B.20), we obtain the identity

$$\delta(x_1 - x_2) = \int d^D x (\Gamma_k^{(2)}[\phi] + R_k)(x_1, x) G_k(x, x_2). \quad (\text{C.5})$$

One can express the previous relation in a compact operator form

$$\mathbb{I} = (\Gamma_k^{(2)} + R_k) G_k, \quad (\text{C.6})$$

where we have introduced the *scale-dependent IPI vertices*

$$\Gamma_k^{(n)}(x_1, \dots, x_n) = \frac{\delta^n \Gamma_k[\phi]}{\delta\phi(x_1) \dots \delta\phi(x_n)}. \quad (\text{C.7})$$

This implies that the exact scale-dependent propagator is not anymore the mere inverse of the two-point function, but receives an extra, scale-dependent mass-like contribution given by the regulator.

We now have all the ingredients to derive an equation for the  $t$ -evolution of  $\Gamma_k$ . Computing the  $t$  derivative of  $W_k$  we get:

$$\begin{aligned}
\partial_t W_k[J] &= -\frac{1}{2} \frac{1}{\mathcal{Z}_k[J]} \int \mathcal{D}\varphi \int \frac{d^D q}{(2\pi)^D} \varphi(-q) \partial_t R_k(q) \varphi(q) e^{-S - \Delta S_k + \int J\varphi} = \\
&= -\frac{1}{2} \int \frac{d^D q}{(2\pi)^D} \partial_t R_k(q) \frac{1}{\mathcal{Z}_k[J]} \int \mathcal{D}\varphi \varphi(-q) \varphi(q) e^{-S - \Delta S_k + \int J\varphi} = \\
&= -\frac{1}{2} \int \frac{d^D q}{(2\pi)^D} \partial_t R_k(q) \left[ \langle \varphi(-q) \varphi(q) \rangle - \langle \varphi(-q) \rangle \langle \varphi(q) \rangle + \langle \varphi(-q) \rangle \langle \varphi(q) \rangle \right] = \\
&= -\frac{1}{2} \int \frac{d^D q}{(2\pi)^D} \partial_t R_k(q) G_k(q) - \partial_t \Delta S_k[\phi]. \tag{C.8}
\end{aligned}$$

Finally, taking the  $t$ -derivative of  $\Gamma_k$  for fixed  $\phi$  and at  $J = J_{\text{sup}}$  we get:

$$\begin{aligned}
\partial_t \Gamma_k[\phi] &= -\partial_t W_k[J]|_{\phi} + \int (\partial_t J) \phi - \partial_t \Delta S_k[\phi] = -\partial_t W_k[J]|_J - \partial_t \Delta S_k[\phi] = \\
&= \frac{1}{2} \int \frac{d^D q}{(2\pi)^D} \partial_t R_k(q) G_k(q) = \\
&= \frac{1}{2} \text{Tr} \left[ \partial_t R_k(\Gamma_k^{(2)}[\phi] + R_k)^{-1} \right], \tag{C.9}
\end{aligned}$$

where the trace indicates an integral over momenta and a sum over all internal degrees of freedom (for example colors for a  $SU(N)$  gauge theory). Thus we obtained the *Wetterich equation*.

## Derivation of the flow equations for different models

In this appendix, we provide some details on the derivation of the different flow equations for the two different models we used throughout this work, namely the  $O(N)$  model and the QM model. In both cases we used the LPA as the ansatz for the effective average action, thus we derive the flow equations for the effective potential.

### D.1 $O(N)$ model

Our starting point is the LPA ansatz Eq. (4.3) for the effective average action, which we rewrite in the Fourier transform

$$\Gamma_k(\rho) = \int \frac{d^d p}{(2\pi)^d} \left\{ \frac{1}{2} \phi_a(p) \phi_a(-p) p^2 + V_k(\rho) \right\}. \quad (\text{D.1})$$

Once the ansatz for the effective action is fixed, we choose the regulator, specifically the regulator Eq. (4.4) and the Litim shape function Eq. (4.5). We can now proceed calculating the regularized propagator, or equivalently the two-point vertex function. To do so, one usually chooses a simple background field

$$\vec{\phi} = (0, \dots, 0, \sqrt{2\rho}), \quad (\text{D.2})$$

or equivalently

$$\phi_a = \sqrt{2\rho} \delta_{aN}. \quad (\text{D.3})$$

In this way, it is straightforward to obtain the Fourier transform of the two-point function

$$\Gamma_{k,ab}^{(2)}(q, p; \rho) \equiv \frac{\partial^2 \Gamma_k(\rho)}{\partial \phi_a(p) \partial \phi_b(q)} = (2\pi)^d \delta^{(d)}(q+p) \left\{ [q^2 + V'_k(\rho)] \delta_{ab} + 2\rho V''_k(\rho) \delta_{aN} \delta_{bN} \right\}, \quad (\text{D.4})$$

where we use the notation introduced in Eq. (4.7). The indices  $a, b, N$  refer to the  $O(N)$  field space, while  $p$  and  $q$  indicate the momentum dependence. The presence of  $\delta^{(d)}(q+p)$ ,  $\delta_{ab}$ ,  $\delta_{aN} \delta_{bN}$  denotes that  $\Gamma_{k,ab}^{(2)}$  is diagonal both in momentum and in field spaces. Furthermore,  $\delta_{aN} \delta_{bN}$  selects a contribution which will appear only for the radial mode when  $a = b = N$ .

The next step is then to add the regulator to the two-point function, which is trivial since also the regulator Eq. (4.4) is diagonal in both field and momentum spaces:



$$\begin{aligned} \Gamma_{k,ab}^{(2)}(q, p; \rho) + R_k(q, p) \delta_{ab} &= (2\pi)^d \delta^{(d)}(q + p) \times \\ &\times \left\{ [q^2 + V'_k(\rho) + R_k(p, q)] \delta_{ab} + 2\rho V''_k(\rho) \delta_{aN} \delta_{bN} \right\}. \end{aligned} \quad (\text{D.5})$$

We now insert the general definition of the regulator Eq.(4.4) into Eq.(D.5) and invert it, obtaining

$$\begin{aligned} [\Gamma_{k,ab}^{(2)}(q, p; \rho) + R_k(q, p) \delta_{ab}]^{-1} &= (2\pi)^d \delta^{(d)}(q + p) \times \\ &\times \begin{pmatrix} \frac{1}{q^2[1+r_k(q)]+V'_k(\rho)} & 0 & 0 & \cdots & 0 & 0 & 0 \\ 0 & \frac{1}{q^2[1+r_k(q)]+V'_k(\rho)} & 0 & \cdots & 0 & 0 & 0 \\ \vdots & 0 & \ddots & & \vdots & & \vdots \\ 0 & 0 & 0 & \cdots & 0 & \frac{1}{q^2[1+r_k(q)]+V'_k(\rho)} & 0 \\ 0 & 0 & 0 & \cdots & 0 & 0 & \frac{1}{q^2[1+r_k(q)]+V'_k(\rho)+2\rho V''_k(\rho)} \end{pmatrix}, \end{aligned} \quad (\text{D.6})$$

which is an  $N \times N$  diagonal square matrix. Now the computation of the trace in field space is trivial and inserting Eq. (D.6) into the flow equation Eq. (3.13) and carrying out the trace up to the momentum integral one obtains:

$$\partial_k V_k(\rho) = \frac{1}{2} \int_q \left[ \left( \frac{N-1}{q^2[1+r_k(q)]+V'_k(\rho)} + \frac{1}{q^2[1+r_k(q)]+V'_k(\rho)+2\rho V''_k(\rho)} \right) q^2 \partial_k r_k(q) \right], \quad (\text{D.7})$$

where

$$\int_q \equiv \int \frac{d^D q}{(2\pi)^D}. \quad (\text{D.8})$$

Considering the Litim shape function Eq. (4.5), we calculate

$$\partial_k r_k(q) = \partial_k \left[ \left( \frac{k^2}{q^2} - 1 \right) \Theta \left( \frac{k^2}{q^2} - 1 \right) \right] = \left( \frac{2k}{q^2} \right) \Theta \left( \frac{k^2}{q^2} - 1 \right), \quad (\text{D.9})$$

where we neglected the singular Dirac- $\delta$  contribution since its coefficient vanishes when the condition of the  $\delta$  is satisfied.

Finally, inserting Eq. (4.5) and Eq. (D.9) into Eq. (D.7), the momentum integration becomes trivial and we arrive at the flow equation for the effective potential in the LPA:

$$\partial_k V_k(\rho) = A_d k^{d+1} \left( \frac{N-1}{k^2 + V'_k(t, \rho)} + \frac{1}{k^2 + V'_k(t, \rho) + 2\rho V''_k(t, \rho)} \right), \quad (\text{D.10})$$

with the factor  $A_d$  defined in Eq. (4.8).

## D.2 Quark-Meson model

### D.2.1 Bosonic contribution

Due to the similarity of the bosonic sector of the QM model with the  $O(N)$  model, and since linear terms in the bosonic field do not contribute to the flow equation, we can actually adapt most of the calculations we performed in the previous section to the QM-model case. Nevertheless, we now have to derive the bosonic contribution to the flow equation at finite temperature and density. In particular, as we discussed in the main text, we used the flow equation in the  $(3 + 1)$ -dimensional case, where the imaginary temporal dimension has been compactified. This implies that we can use Eq. (D.7) as our starting point, but we have to replace the  $D$ -dimensional integral with a combination of a discrete Matsubara sum and a  $(D - 1)$ -dimensional momentum integral:

$$\int \frac{d^D q}{(2\pi)^D} \rightarrow T \sum_{n \in \mathbb{Z}} \int \frac{d^{D-1} \mathbf{q}}{(2\pi)^{D-1}}. \quad (\text{D.11})$$

We also have to specify the dimension,  $D = 4$ , such that we correctly capture the aforementioned  $(3 + 1)$ -dimensional case. This implies that, in order to explicitly perform the Matsubara summation, we can use a three-dimensional regulator which does not regulate the 0th component of the 4-momentum  $q$  involved in the integration. Thus, we use the regulator function defined in Eq. (5.88). Furthermore, we set the number of bosons,  $N = 4$ , such that the model correctly takes into account the contributions of the 3 pions and the radial sigma meson. Finally, in order to be consistent with the notation used throughout this work, we switch to the RG-time notation  $t$  instead of the RG-momentum scale  $k$ , and use  $U_t$  instead of  $V_k$  to indicate the effective potential. With these specifications, we can adjust Eq. (D.7) to the finite-temperature QM-model bosonic contribution and obtain:

$$\begin{aligned} \partial_t U_t(\rho) \Big|_{\text{Bosons}} = & \frac{1}{2} T \sum_{n \in \mathbb{Z}} \int \frac{d^3 \mathbf{q}}{(2\pi)^3} \left[ \left( \frac{3}{q_0^2 + \mathbf{q}^2 [1 + r_t^B(\mathbf{q})] + U_t'(\rho)} + \right. \right. \\ & \left. \left. + \frac{1}{q_0^2 + \mathbf{q}^2 [1 + r_t^B(\mathbf{q})] + U_t(\rho) + 2\rho U_t''(\rho)} \right) \mathbf{q}^2 \partial_k r_t(\mathbf{q}) \right]. \end{aligned} \quad (\text{D.12})$$

As a final preliminary step, we switch from the notation involving the theory invariant  $\rho$  to the  $\sigma$ -field notation, and we use the definitions of the particle energies given by Eqs. (5.90) and (5.91), thus obtaining:

$$\partial_t U_t(\sigma) \Big|_{\text{Bosons}} = \frac{1}{2} T \sum_{n \in \mathbb{Z}} \int \frac{d^3 \mathbf{q}}{(2\pi)^3} \left[ \left( \frac{3}{q_0^2 + E_{k,\pi}^2(\mathbf{q})} + \frac{1}{q_0^2 + E_{k,\sigma}^2(\mathbf{q})} \right) \mathbf{q}^2 \partial_k r_t(\mathbf{q}) \right], \quad (\text{D.13})$$

where

$$q_0 = \omega_n^B \quad (\text{D.14})$$

and  $\omega_n^B = 2\pi n T$  are the discrete bosonic Matsubara frequencies.

The next step is to perform the Matsubara sum. In this case, it is possible to do so analytically, due to the simple dependence of Eq. (D.13) on the Matsubara frequencies  $\omega_n^B$ . In particular, we can exploit the textbook result

$$T \sum_{n \in \mathbb{Z}} \left( \frac{1}{(\omega_n^B)^2 + E^2} \right) = \frac{1}{2E} \left[ 1 + 2n_B \left( \frac{E}{T} \right) \right] = \frac{1}{2E} \coth \left( \frac{E}{2T} \right), \quad (\text{D.15})$$

where

$$n_B(x) = \frac{1}{e^x - 1} \quad (\text{D.16})$$

is the Bose-Einstein distribution and we used the identity

$$n_B(x) = \frac{1}{2} \left[ \coth \left( \frac{x}{2} \right) - 1 \right]. \quad (\text{D.17})$$

Finally, using the result in Eq. (D.15), we obtain the bosonic contribution to the flow equation of the QM model in the LPA

$$\partial_t U_t(\sigma) \Big|_{\text{Bosons}} = \frac{1}{8\pi^2} \int_0^\infty dq q^4 \partial_t r_t(q) \left\{ \frac{3}{E_{k,\pi}(q)} \coth \left( \frac{E_{k,\pi}(q)}{2T} \right) + \frac{1}{E_{k,\sigma}(q)} \coth \left( \frac{E_{k,\sigma}(q)}{2T} \right) \right\}, \quad (\text{D.18})$$

where  $q = |\mathbf{q}|$ .

We point out that, at this stage, no further calculations can be performed unless the regulator shape function is specified. If we then choose the Litim shape function Eq. (5.110), the momentum integral in Eq. (D.18) can be easily performed analytically and leads to

$$\partial_t U_t(\sigma) \Big|_{\text{Bosons}}^{\text{Litim}} = -\frac{k^5}{12\pi^2} \left[ \frac{3}{E_{k,\pi}} \coth \left( \frac{E_{k,\pi}}{2T} \right) + \frac{1}{E_{k,\sigma}} \coth \left( \frac{E_{k,\sigma}}{2T} \right) \right]. \quad (\text{D.19})$$

where the energies for the pions and for the sigma meson are defined in Eq. (5.115).

## D.2.2 Fermionic contribution

As for the previous sections, we start by considering the 4-dimensional 0-temperature equivalent of the LPA ansatz Eq. (5.87) for the effective average action

$$\begin{aligned} \Gamma_t[\bar{\Psi}, \Psi, \phi] = \int d^4x \left\{ \bar{\psi}(\gamma_\mu \partial^\mu + h(\sigma + i\gamma^5 \vec{\tau} \cdot \vec{\pi}) - \mu\gamma_0)\psi \right. \\ \left. + \frac{1}{2}(\partial_\mu \sigma)^2 + \frac{1}{2}(\partial_\mu \vec{\pi})^2 + U_t(\sigma^2 + \vec{\pi}^2) - c\sigma \right\}. \end{aligned} \quad (\text{D.20})$$

We now focus on the fermionic sector of the effective average action  $\Gamma_t^F$  and we rewrite it into the Fourier transform

$$\Gamma_t^F[\bar{\Psi}, \Psi, \phi] = \int \frac{d^4q}{(2\pi)^4} \left\{ \bar{\psi}(-p)(i\gamma_\mu p^\mu + h(\sigma + i\gamma^5 \vec{\tau} \cdot \vec{\pi}) - \mu\gamma_0)\psi(p) \right\}. \quad (\text{D.21})$$

The next step is the calculation of the two-point function:

$$\Gamma_t^{(2)}(q, p; \bar{\Psi}, \Psi, \phi) \equiv \frac{\partial^2 \Gamma_t^F(\bar{\Psi}, \Psi, \phi)}{\partial \Psi(p) \partial \bar{\Psi}(q)} = (2\pi)^4 \delta^{(4)}(q+p) \left[ i\gamma_\mu p^\mu + h(\sigma + i\gamma^5 \vec{\tau} \cdot \vec{\pi}) - \mu\gamma_0 \right], \quad (\text{D.22})$$

which is diagonal both in the fermionic field space and in momentum space. We can also point out that the fermionic two-point function is independent of the effective potential. This has as a consequence the fact that the whole fermionic contribution is independent of the effective potential, as we pointed out in the main text.

We now can set the bosonic fields to their expectation value:

$$\langle \sigma \rangle = \sigma \neq 0, \quad \langle \vec{\pi} \rangle = 0. \quad (\text{D.23})$$

Inserting Eq.(D.23) into the two-point function Eq.(D.22) we obtain:

$$\Gamma_t^{(2)}(q, p; \bar{\Psi}, \Psi, \phi) = (2\pi)^4 \delta^{(4)}(q + p) [i\gamma_\mu p^\mu + h\sigma - \mu\gamma_0]. \quad (\text{D.24})$$

Adding the regulator function Eq.(5.93) to Eq.(D.24) the inversion is trivial and it leads to

$$\partial_t U_t(\sigma) \Big|_{\text{Fermions}} = -12N_c \int \frac{d^4 q}{(2\pi)^4} \frac{\mathbf{q}^2 [1 + r_t^F(q)] \partial_t r_t^F(\mathbf{q})}{(q_0 + i\mu)^2 + E_{k,\Psi}^2(\mathbf{q})}, \quad (\text{D.25})$$

where we also performed the trace in Dirac, color and flavor space, and the definition of  $E_{k,\Psi}$  is given in Eq.(5.97).

We now introduce the finite-temperature equation via the standard Matsubara formalism for fermions:

$$\int \frac{d^4 q}{(2\pi)^4} \rightarrow T \sum_{n \in \mathbb{Z}} \int \frac{d^3 \mathbf{q}}{(2\pi)^3}. \quad (\text{D.26})$$

The fermionic fields now satisfy the anti-periodic boundary conditions Eqs.(5.47) and (5.48) in the compactified Euclidean direction and the fermionic Matsubara frequencies are

$$q_0 = \omega_n^F = (2n + 1)\pi T. \quad (\text{D.27})$$

Once again, we can use standard procedures to evaluate the Matsubara sum analytically. In particular, we use the known result

$$T \sum_{n \in \mathbb{Z}} \left( \frac{1}{(\omega_n^f + i\mu)^2 + E^2} \right) = \frac{1}{2E} \left[ 1 - n_F \left( \frac{E - \mu}{T} \right) - n_F \left( \frac{E + \mu}{T} \right) \right] = \quad (\text{D.28})$$

$$= \frac{1}{4E} \left[ \tanh \left( \frac{E - \mu}{2T} \right) + \tanh \left( \frac{E + \mu}{2T} \right) \right], \quad (\text{D.29})$$

where  $n_F(x)$  is the Fermi-Dirac distribution defined in Eq.(5.96) and we used the identity

$$n_F(x) = \frac{1}{2} \left[ 1 - \tanh \left( \frac{x}{2} \right) \right] \quad (\text{D.30})$$

Finally, combining Eq.(D.25) with the finite-temperature definition Eq.(D.26) and performing the Matsubara sum according to Eq.(D.28), we obtain the fermionic contribution to the flow equation of the QM in the LPA:

$$\begin{aligned} \partial_t U_t(\sigma) \Big|_{\text{Fermions}} &= -\frac{N_c}{4\pi^2} \int_0^\infty dq q^4 \left\{ \left( 1 + r_t^F(q) \right) \partial_t r_t^F(q) \frac{1}{E_{k,\Psi}(q)} \times \right. \\ &\quad \left. \times \left[ 1 - n_F \left( \frac{E_{k,\Psi}(q) + \mu}{T} \right) - n_F \left( \frac{E_{k,\Psi}(q) - \mu}{T} \right) \right] \right\}, \quad (\text{D.31}) \end{aligned}$$

where  $q = |\mathbf{q}|$ .

If we now specify the shape function for the regulator and use the Litim one defined in Eq. (5.111), the momentum integration becomes trivial and we obtain

$$\partial_t U_t(\sigma) \Big|_{\text{Fermions}}^{\text{Litim}} = N_c \frac{k^5}{3\pi^2} \frac{1}{E_{k,\Psi}} \left[ \tanh\left(\frac{E_{k,\Psi} - \mu}{2T}\right) + \tanh\left(\frac{E_{k,\Psi} + \mu}{2T}\right) \right], \quad (\text{D.32})$$

where we used Eq. (D.29) and the energy of the fermions is defined in Eq. (5.117).

### D.2.3 Fermi-surface regulator

In this section we consider the flow equation which arises from a different class of regulators for the fermions, i.e., the Fermi surface or quasi-particle regulator, discussed in Ref. [87]. In the following discussion we will focus on the chiral limit case, neglecting the finite current quark mass. For the moment we also neglect the Yukawa coupling with the mesons, which we discussed leads to the dynamically generated quark mass via SSB, and we will reintroduce it later after some considerations.

First of all, we introduce the following projectors

$$P_{\pm} = \frac{1}{2i} \left( i\gamma_0 \mp \frac{\vec{\not{p}}}{|\vec{p}|} \right) \gamma_0, \quad (\text{D.33})$$

which project onto positive and negative energy solutions of the Dirac equation, thus onto particle and antiparticle states [255, 256]. The projectors, by construction, fulfill the following useful identities:

1.

$$P_{\pm}(-\vec{p}) = P_{\mp}(\vec{p}), \quad (\text{D.34})$$

in agreement with the particle/antiparticle state projection;

2.

$$P_+ P_+ = P_+ \quad P_- P_- = P_-, \quad (\text{D.35})$$

which implies that, once a projection has been performed, the application of another projection of the same sign results in the identity;

3.

$$P_+ P_- = P_- P_+ = 0, \quad (\text{D.36})$$

signaling that, once a projection onto a particle (anti-particle) state has been performed, a projection onto an antiparticle (particle) state is vanishing;

4.

$$P_+ + P_- = \mathbb{I} \quad (\text{D.37})$$

since particle and anti-particle states give a complete solution to the Dirac equation;

5.

$$\text{Tr} P_{\pm} = 2 \quad (\text{D.38})$$

which is a consequence of the fact that free Dirac equation has two solutions with positive energy and two solutions with negative energy;

6. other useful properties are:

$$P_{\pm}\gamma_0 = \gamma_0 P_{\mp} \quad (\text{D.39})$$

and

$$\{P_{\pm}, \gamma_0\} = \gamma_0. \quad (\text{D.40})$$

Once the projectors have been introduced, we consider the kinetic operator of the fermionic action in momentum space, which can be read from Eq. (D.21):

$$T = i\gamma_0 p_0 + i\vec{\not{p}} - \mu\gamma_0. \quad (\text{D.41})$$

Using the projectors we defined, we can now rewrite the kinetic operator as

$$T = C_- P_- \gamma_0 + C_+ P_+ \gamma_0, \quad (\text{D.42})$$

where we defined

$$C_{\pm} = ip_0 + (-\mu \pm |\vec{p}|). \quad (\text{D.43})$$

In order to understand the physical meaning of  $C_{\pm}$ , we now want to invert the kinetic operator  $T$ . This is straightforward using the properties Eqs. (D.34)-(D.40):

$$T^{-1} = C_-^{-1} P_- \gamma_0 + C_+^{-1} P_+ \gamma_0, \quad (\text{D.44})$$

This quantity is the one that appears in the propagator and thus in the computation of loop diagrams. In this way we can clearly see the physical meaning of  $C_{\pm}$ , since the Euclidean inverse propagator  $T^{-1}$  exhibits poles at  $p_0 = iE_{\pm}$  where

$$E_{\pm} = \pm |\vec{p}| - \mu, \quad (\text{D.45})$$

which in Minkowski spacetime, become poles at  $p_0 = E_{\pm}$ . The poles of the inverse propagator give the dispersion relations of the particles and anti particles. Due to the presence the chemical potential then,  $C_{\pm}$  contain information about the energy of the particles and anti-particles involved, with respect to the Fermi surface, given by  $|\vec{p}| = \mu$ .

Coming back to the free Euclidean fermionic action in Fourier space

$$S_{\bar{\Psi}\Psi} = \int \frac{d^4 p}{(2\pi)^4} \bar{\Psi}(-p) T \Psi(p) \quad (\text{D.46})$$

and using the decomposition Eq. (D.42), we can observe that the action splits into two contributions

$$\int \frac{d^4 p}{(2\pi)^4} \bar{\Psi}(-p) C_- P_- \gamma_0 \Psi(p), \quad \int \frac{d^4 p}{(2\pi)^4} \bar{\Psi}(-p) C_+ P_+ \gamma_0 \Psi(p). \quad (\text{D.47})$$

One can observe that these two pieces are not independently invariant under the operation of charge conjugation

$$\Psi \rightarrow \Psi^c = \mathcal{C} \bar{\Psi}^T, \quad (\text{D.48})$$

$$\bar{\Psi} \rightarrow \bar{\Psi}^c = \Psi^T, \quad (\text{D.49})$$

where  $\mathcal{C} = \gamma_2 \gamma_0$  is the charge conjugation operator and the superscript  $T$  denotes the transpose of the Dirac spinors. However, in the case of vanishing chemical potential

$\mu = 0$ ,  $S_{\bar{\psi}\psi}$  is invariant under charge conjugation, since the two terms in Eq. (D.47) transform into each other under this transformation. This clearly derives from the fact that by constructions  $P_{\pm}$  project onto the particle and antiparticle contributions respectively. Obviously, the charge conjugation symmetry is then explicitly broken by the presence of a finite chemical potential.

On the other hand both terms are independently invariant under chiral transformation, as expected.

As far as the inversion of  $T$  is considered, one has to notice that the term involving  $C_-$  is always invertible, since  $C_- \neq 0$  for any finite  $\mu$ , while this does not hold for the  $C_+$  one, since it vanishes at the Fermi surface, i.e., for  $p_0 = 0$  and  $|\vec{p}| = \mu$ . This point corresponds to a singular one which, in the case of vanishing chemical potential, is located at vanishing four-momentum and usually can be regulated via the insertion of a mass-like regulator. If the chemical potential is non-vanishing, this divergence is cured, but the one associated to the Fermi surface is still present. That is why we now want to construct of a class of regulators which can handle this singularity dealing properly with the dispersion relations of the fermions.

As a first step, we can consider the decomposition Eq. (D.42), which, by construction, distinguishes between the positive and negative energy contributions to the kinetic operator  $T$ , relatively to the Fermi surface. We can now utilize this decomposition in order to regularize the particle and anti-particle modes separately. A possible class of regulators which can be used for this purpose can be expressed as follows:

$$R_{k,F}(p, \mu) = (-\mu - |\vec{p}|)r_- P_- \gamma_0 + (-\mu + |\vec{p}|)r_+ P_+ \gamma_0, \quad (\text{D.50})$$

where

$$r_{\pm} = r(x_{\pm}) \quad (\text{D.51})$$

are generic dimensionless regulator shape functions which depend on the dimensionless variables

$$x_{\pm} k^2 = (-\mu \pm |\vec{p}|)^2, \quad (\text{D.52})$$

which represent the dimensionless squared energies relative to the Fermi surface for particles and anti-particles.

We observe that we constructed this regulators class using the same functional form for  $r_{\pm}$ , in such a way that the two regularizations for particles and anti-particles coincide when considering a vanishing chemical potential, in order not to explicitly break the charge conjugation symmetry in this case. As a final constrain we also imposed that the regulator does not break chiral symmetry. On the other hand, the regulator class we defined breaks the Silver-Blaze symmetry by construction. However, this symmetry breaking is necessary in a derivative expansion of the effective action in order to properly deal with the presence of Fermi-surface divergences and the related BCS scaling (see Ref. [87] for more details). Analogously to the constraints we defined in Eq. (3.8),  $r_{\pm}$  should fulfill the following requirements:

$$\lim_{x_{\pm} \rightarrow 0} \sqrt{x_{\pm}} r_{\pm} > 0, \quad (\text{D.53})$$

which implements the regularization of fluctuations around the Fermi surface, as we will see in more detail soon, and



$$\lim_{x_{\pm} \rightarrow \infty} r_{\pm} = 0, \quad (\text{D.54})$$

which implies that the full effective action is recovered when  $k \rightarrow 0$ .

We also require that

$$1 + r_{\pm} \geq 0 \quad \forall x_{\pm} \quad (\text{D.55})$$

in order not to introduce unphysical divergences in the calculations of loop diagrams.

We can now understand how the regulator acts by introducing the regularized kinetic operator

$$T + R_{k,F} = \bar{C}_- P_- \gamma_0 + \bar{C}_+ P_+ \gamma_0, \quad (\text{D.56})$$

where we defined

$$\bar{C}_{\pm} = ip_0 + (-\mu \pm |\vec{p}|) (1 + r_{\pm}), \quad (\text{D.57})$$

which are nothing but the regularized quasi-particle dispersion relations. As for Eq. (D.44), the inversion of Eq. (D.56) is straightforward using the properties of the projectors  $P_{\pm}$ , and results in

$$(T + R_{k,F})^{-1} = \bar{C}_-^{-1} P_- \gamma_0 + \bar{C}_+^{-1} P_+ \gamma_0. \quad (\text{D.58})$$

We now consider the implications of Eq. (D.53), and in particular from it we deduce that

$$r(x_+) = \frac{k}{|\mu - |\vec{p}||} + \mathcal{O}(|\mu - |\vec{p}||). \quad (\text{D.59})$$

We can notice that, after the introduction of the regulator, the Fermi surface  $|\vec{p}| = \mu$  does not represent a singular point for the inverse propagator anymore. In fact, if we consider the particle modes, whose dispersion relation can be read from

$$\mathcal{R}(\bar{C}_+) = (|\vec{p}| - \mu) (1 + r_{\pm}), \quad (\text{D.60})$$

we can deduce from Eq. (D.59) that, close to the Fermi surface,

$$\mathcal{R}(\bar{C}_+) = k \operatorname{sgn}(|\vec{p}| - \mu) + \dots. \quad (\text{D.61})$$

This implies that the regulator effectively introduces a gap of order  $k$  for these modes and that, by construction, this gap vanishes in the limit  $k \rightarrow 0$ , implying that fluctuations are integrated out around the Fermi surface. Furthermore,  $\mathcal{R}(C_+)$  is not positive definite but changes sign at the Fermi surface, implying that is discontinuous at  $|\vec{p}| = \mu$ . This can be seen in Fig. D.1, where we show  $\mathcal{R}(C_+)$  as a function of  $p/\mu$ , where  $p = |\vec{p}|$ , for various values of  $k/\mu$  as obtained using the Litim shape function Eq. (5.111) (solid lines) and the polynomial shape function

$$r(x_{\pm}) = -1 + \frac{1}{\sqrt{1 - \left(\sum_{n=0}^N \frac{1}{n!} x_{\pm}^n\right)^{-1}}} \quad (N > 2) \quad (\text{D.62})$$

for  $N = 4$  (dashed lines).

We note that the negative-energy modes associated with  $\bar{C}_-$  are regularized by the presence of the chemical potential, such that

$$\mathcal{R}(\bar{C}_-) < 0 \quad (\text{D.63})$$

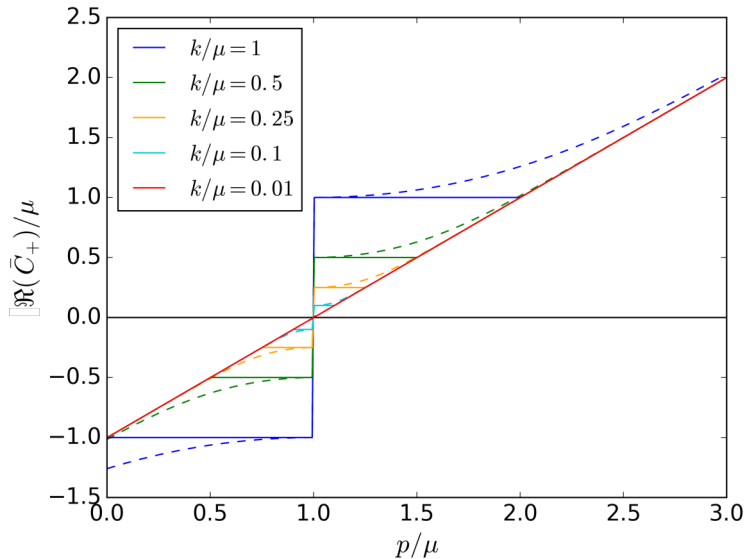


Figure D.1:  $\Re(\bar{C}_+)$  as a function of  $p/\mu$  for various values of  $k/\mu$  as obtained from employing the litim shape function Eq. (5.111) (solid lines) and the polynomial shape function Eq. (D.62) for  $N = 4$  (dashed lines). Plot taken from [87].

even in the limit  $k \rightarrow 0$ .

As emphasized at the beginning of this section, up to this point we discussed the case of massless fermions. However, in the Quark-Meson model, fermions do have a mass,  $h\sigma$ , which is dynamically generated by the Yukawa coupling with the  $\sigma$  field and its non-vanishing expectation value. Indeed the kinetic operator  $T$  includes also the mass term

$$T = i\gamma_0 p_0 + i\vec{\gamma} \cdot \vec{p} - \mu\gamma_0 + h\sigma. \quad (\text{D.64})$$

This implies that the Fermi surface gets deformed by the presence of the mass, namely it is now located at

$$\mu = \pm \varepsilon, \quad (\text{D.65})$$

with

$$\varepsilon = \sqrt{\vec{p}^2 + (h\sigma)^2}. \quad (\text{D.66})$$

In Ref. [87] a generalization to the massive fermions case of the approach we described so far is presented. However, following similar steps to the previous ones, one has to introduce a regulator which explicitly depends on the mass term, since the Fermi surface divergence to regularized has been shifted. This approach works then perfectly fine in the context of a bare current-quark mass, but the issue has to be treated more carefully in presence of SSB. This is such since if we naively consider as a mass term  $h\sigma$  and insert it into the regulator, this would then result in a field dependent regulator. This certainly imply a non-trivial modification of the Wetterich equation and thus it is still object of an ongoing research.

In order to avoid this issue, we decided to use the previously described chiral regulator, which does not contain the mass term. As previously emphasized, this regulator does not regularize the true Fermi surface, but since the Quark meson model does not involve Fermi surface dynamics (such as, for example, the formation of Cooper pairs) we can still use the chiral quasi-particle regulator as another possibility to investigate the model via the FRG.

As for Eq. (D.42), we use the projectors  $P_{\pm}$  to rewrite the kinetic operator Eq. (D.64) as

$$T = C_- P_- \gamma_0 + C_+ P_+ \gamma_0 + h\sigma, \quad (\text{D.67})$$

where  $C_{\pm}$  are the massless dispersion relations defined in Eq. (D.43).

We now proceed to the regularization of the kinetic operator by adding the regulator defined in Eq. (D.50) to it:

$$T + R_{k,F} = \bar{C}_- P_- \gamma_0 + \bar{C}_+ P_+ \gamma_0 + h\sigma, \quad (\text{D.68})$$

where  $\bar{C}_{\pm}$  are the regularized dispersion relations introduced in Eq. (D.57). The inversion of Eq. (D.68) is once again pretty straightforward using the properties of the projectors  $P_{\pm}$ , and it leads to:

$$(T + R_{k,F})^{-1} = \frac{\bar{C}_- P_- \gamma_0 + \bar{C}_+ P_+ \gamma_0 - h\sigma}{\bar{C}_+ \bar{C}_- - (h\sigma)^2} \quad (\text{D.69})$$

Since  $T = \Gamma_{\bar{\Psi}\Psi}^2$ , the final ingredient we need for the computation of the FRG flow equation is  $\partial_t R_{k,F}$ , which trivially results in

$$\partial_t R_{k,F}(p, \mu) = (-\mu - |\vec{p}|)(\partial_t r_-) P_- \gamma_0 + (-\mu + |\vec{p}|)(\partial_t r_+) P_+ \gamma_0. \quad (\text{D.70})$$

Thus, we now have to evaluate the quantity

$$-\text{Tr}[(\partial_t R_{k,F})(T + R_{k,F})^{-1}], \quad (\text{D.71})$$

where the trace has to be intended in momentum (and Matsubara) space and in Dirac, color and flavor spaces. It is convenient to evaluate the Dirac trace first, since some terms will drop out. In particular we can use the properties Eqs. (D.34)-(D.40), together with

$$\text{Tr}(P_{\pm} \gamma_0) = 0, \quad (\text{D.72})$$

to obtain the following flow equation in the mean-field approximation

$$\partial_t U_k(\sigma) = -2TN_c N_f \int \frac{d^3 \vec{p}}{(2\pi)^3} \sum_{n=-\infty}^{\infty} \frac{(-\mu - |\vec{p}|)(\partial_t r_+) \bar{C}_- + (-\mu + |\vec{p}|)(\partial_t r_-) \bar{C}_+}{\bar{C}_- \bar{C}_+ - (h\sigma)^2}, \quad (\text{D.73})$$

where the sum over  $n$  has to be intended as over the fermionic Matsubara frequencies  $p_0 = \nu_n = (2n + 1)\pi T$ . Eq. (D.73) can be easily rewritten as

$$\partial_t U_k(\sigma) = -2TN_c N_f \int \frac{d^3 \vec{p}}{(2\pi)^3} \sum_{n=-\infty}^{\infty} \partial_t \ln \left( \bar{C}_- \bar{C}_+ - (h\sigma)^2 \right). \quad (\text{D.74})$$

In order to perform the Matsubara sum analytically, since we are interested in the RG flow of  $u_t(\sigma) = \partial_{\sigma} U_k(\sigma)$ , we take the  $\sigma$ -derivative of both sides of Eq. (D.74), thus obtaining

$$\partial_t u_t(\sigma) = 4TN_c N_f (h^2 \sigma) \int \frac{d^3 \vec{p}}{(2\pi)^3} \sum_{n=-\infty}^{\infty} \partial_t \left[ \frac{1}{\bar{C}_- \bar{C}_+ - (h\sigma)^2} \right]. \quad (\text{D.75})$$

We now introduce the following quantities:

$$\omega_{\pm} = (\mu \mp |\vec{p}|)(1 + r_{\pm}). \quad (\text{D.76})$$

In this way we can rewrite

$$\begin{aligned}
\bar{C}_- \bar{C}_+ - (h\sigma)^2 &= (iv_n - \omega_+)(iv_n - \omega_-) - (h\sigma)^2 = \\
&= -v^2 - iv(\omega_+ + \omega_-) + \omega_+ \omega_- - (h\sigma)^2 = \\
&= - \left[ \left( v + i \frac{\omega_+ + \omega_-}{2} \right)^2 + \left( \frac{\omega_+ - \omega_-}{2} \right)^2 + (h\sigma)^2 \right] \\
&= - \left[ (v + i\tilde{\mu})^2 + \tilde{E}^2 \right], \tag{D.77}
\end{aligned}$$

where we defined

$$\tilde{E} = \sqrt{\left( \frac{\omega_+ - \omega_-}{2} \right)^2 + h^2 \sigma^2}, \quad \tilde{\mu} = \frac{\omega_+ + \omega_-}{2}. \tag{D.78}$$

These two quantities play the role of an effective regulated quasi-particle energy and chemical potential, respectively. In fact, when  $r_{\pm} = 0$ ,  $\tilde{E} = |\vec{p}|$ , which is the energy of a massless particle, and  $\tilde{\mu} = \mu$ .

Substituting Eq. (D.77) into Eq. (D.75), we obtain

$$\partial_t u_t(\sigma) = -4N_c N_f (h^2 \sigma) \partial_t \left( \int \frac{d^3 \vec{p}}{(2\pi)^3} T \sum_{n=-\infty}^{\infty} \frac{1}{(v + i\tilde{\mu})^2 + \tilde{E}^2} \right). \tag{D.79}$$

In this way, we can use Eq. (D.28) to perform the sum over the Matsubara frequencies analytically, thus obtaining

$$\partial_t u_t(\sigma) = -\partial_t \left( 4N_c N_f (h^2 \sigma) \int \frac{d^3 p}{(2\pi)^3} \frac{1}{2\tilde{E}} \left[ 1 - n_f \left( \frac{\tilde{E} - \tilde{\mu}}{T} \right) - n_f \left( \frac{\tilde{E} + \tilde{\mu}}{T} \right) \right] \right), \tag{D.80}$$

which is the flow equation we obtain when choosing the quasi-particle regulator class. The final flow equation depends then on the choice of the specific regulator shape functions  $r_{\pm}$ , which are contained in the definitions of  $\tilde{E}$  and  $\tilde{\mu}$ .

## Finite-Volume schemes and conservation laws

### E.1 Conservation laws and advection-diffusion equations

Conservation laws and advection-diffusion equations are of great practical importance since they govern a variety of physical phenomena that appear in fluid mechanics, astrophysics, groundwater flow, meteorology, semiconductors, traffic flow, financial modeling, and several other areas [169, 257, 258, 259, 260, 261]. Due to their wide range of applications, the construction of approximate solutions for nonlinear conservation laws and the related advection-diffusion equations is a very relevant task.

Let us now try to understand the physical meaning of this kind of equations. In particular, let us consider a generic conserved quantity  $Q$  enclosed in a volume  $\Omega \subseteq \mathbb{R}^n$ . We define the *density*  $u(x, t)$  of the conserved quantity as

$$u(x, t) = \frac{\text{conserved quantity}}{\text{unit volume}}, \quad (\text{E.1})$$

where, in general,  $u$  depends on time  $t$  and on the position  $x \in \Omega \subseteq \mathbb{R}^n$ . This means that the total amount of the conserved quantity inside the volume  $\Omega$  is given by

$$Q = \int_{\Omega} u(x, t) dV. \quad (\text{E.2})$$

The easiest conservation law possible is given by

$$\frac{d}{dt} \int_{\Omega} u(x, t) dV = 0, \quad (\text{E.3})$$

which represents the *static limit*, according to which inside the volume  $\Omega$  there is no modification in time of  $Q$ , which is thus trivially conserved.

Let us now consider a more realistic scenario, the one in which there is a vector *flux*  $f[u(x, t), x, t]$  of the conserved quantity through the boundary of the domain  $\partial\Omega$ . In this case the conservation law is given by

$$\frac{d}{dt} \int_{\Omega} u(x, t) dV = - \int_{\partial\Omega} f[u(x, t), x, t] \cdot \hat{n} d\sigma, \quad (\text{E.4})$$

where  $\hat{n}$  is the normal vector to the boundary of the domain, which is directed towards the outside of the domain. This explains why we put the minus sign on the r.h.s., since if we have an outflow ( $f \cdot \hat{n} > 0$ ) the value of  $Q$  inside  $\Omega$  decreases and vice versa.

Eq. (E.4) reduces to the trivial conservation law Eq. (E.3) assuming that the volume  $\Omega$  extends to all the  $\mathbb{R}^n$  space, and that the flux  $f$  vanishes at  $\partial\mathbb{R}^n$ .

The form in which we wrote Eq. (E.4) is the so-called *integral or global form* of the conservation law.

Now we want to introduce also the *differential or local form*. To do so, we just use Gauss's theorem on the flux integral:

$$\int_{\partial\Omega} f[u(x,t), x, t] \cdot \hat{n} \, d\sigma = \int_{\Omega} \nabla \cdot f[u(x,t), x, t] \, dV. \quad (\text{E.5})$$

Exploiting now the Reynolds transport theorem we can write

$$\int_{\Omega} \left( \frac{\partial u(x,t)}{\partial t} + \nabla \cdot f[u(x,t), x, t] \right) dV = 0 \quad (\text{E.6})$$

and if this holds  $\forall\Omega$  we can choose in the fluid, then we can write Eq. (E.4) in the local form:

$$\frac{\partial}{\partial t} u(x,t) + \nabla \cdot f[u(x,t), x, t] = 0. \quad (\text{E.7})$$

This will be the starting point of all our further investigations.

A straightforward generalization of Eq. (E.4) and Eq. (E.7) may include a dissipation term, leading to the so-called *advection-diffusion equations*, which, in the global form, are represented by

$$\frac{d}{dt} \int_{\Omega} u(x,t) \, dV = \int_{\partial\Omega} \left( q[u(x,t), \nabla u(x,t), x, t] - f[u(x,t), x, t] \right) \cdot \hat{n} \, d\sigma \quad (\text{E.8})$$

or equivalently in the local form

$$\frac{\partial}{\partial t} u(x,t) + \nabla \cdot f[u(x,t), x, t] = \nabla \cdot q[u(x,t), \nabla u(x,t), x, t], \quad (\text{E.9})$$

where  $q[u(x,t), \nabla u(x,t), x, t]$  is a *dissipation or diffusion flux*.

For the sake of simplicity, we will now specify our further studies in one spatial dimension, such that  $\Omega$  reduces to an interval and  $\partial\Omega$  is just given by the endpoints of the interval. Then we will deal with the 1D version of the conservation law and the advection-diffusion equation:

$$\frac{\partial}{\partial t} u(x,t) + \frac{\partial}{\partial x} f[u(x,t), x, t] = 0, \quad (\text{E.10})$$

$$\frac{\partial}{\partial t} u(x,t) + \frac{\partial}{\partial x} f[u(x,t), x, t] = \frac{\partial}{\partial x} q[u(x,t), u_x(x,t), x, t]. \quad (\text{E.11})$$

However, higher-dimensional generalizations are straightforward. The formulation Eq. (E.11) is also-called *conservative form* of the conservation law. If one explicitly calculates the  $x$ -derivatives, one obtains the so-called *primitive form* of the PDE

$$\frac{\partial}{\partial t} u(x,t) + \frac{\partial}{\partial x} f[u(x,t), x, t] + \frac{\partial}{\partial u} f[u(x,t), x, t] \frac{\partial u(x,t)}{\partial x} = \frac{\partial}{\partial x} q[u(x,t), u_x(x,t), x, t] + \quad (\text{E.12})$$

$$+ \frac{\partial}{\partial u} q[u(x,t), u_x(x,t), x, t] \frac{\partial u(x,t)}{\partial x} + \frac{\partial}{\partial u_x} q[u(x,t), u_x(x,t), x, t] \frac{\partial u_x(x,t)}{\partial x}, \quad (\text{E.13})$$

which, if the flux  $f$  does not depend explicitly on  $x$  and  $q$  does not depend explicitly on  $x$  and on  $u$ , takes a much more familiar form

$$\frac{\partial}{\partial t} u(x,t) + \frac{\partial}{\partial u} f[u(x,t), t] \frac{\partial u(x,t)}{\partial x} = \frac{\partial}{\partial u_x} q[u_x(x,t), t] \frac{\partial u_x(x,t)}{\partial x}. \quad (\text{E.14})$$

## E.2 Finite-Volume (FV) schemes

Finite-Volume Methods (FVM) represent one of the possible tools available to numerically solve partial differential equations and in particular conservation laws. As the name suggests, this class of methods transform a PDE into a system of algebraic equations by the use of the average of the solution inside some portions of the computational domain. One of its main advantages is to be well suited to deal with functions which present discontinuities, since in this case the derivative of the solution simply does not exist and finite-difference (FD) methods produce an infinite truncation error. Let us try to outline the key steps to build a FV scheme.

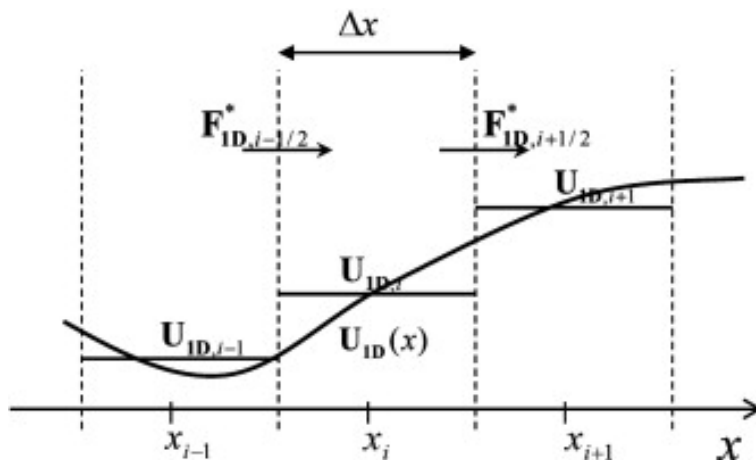


Figure E.1: Visual description of FV schemes [261].

The main feature of all numerical FV methods is the use of the so-called *control volumes* (in space and time), which are the elements in which the computational domain is discretized, such that all the domain is covered by the control volumes. In order to keep the discussion as simple as possible but retaining the general idea, we will focus on the 2D case (1 spatial + 1 temporal dimension), but the generalization to the higher-dimensional case is straightforward. In order to fix the notation, we call  $V$  the total 2D volume, divided into the total spatial volume  $I$  (which in our case is simply an interval) and the time domain  $T = [t_{initial}, t_{final}]$ , such that  $V = I \times T$ . Then  $V$  is discretized in the control volumes  $I_x \times [t^n, t^n + \Delta t]$ , where  $|I_x| = |I|/N_x$  is the spatial control volume of width  $\Delta x$  centered around the point  $x$  obtained sampling  $I$  with  $N_x$  grid points, and  $t^n$  is the  $n$ -th point in which  $T$  is discretized.

The next step to build a FVM is to consider the average  $\bar{u}$  of the solution  $u$  in the interval  $I_x$ :

$$\bar{u}(x, t) = \frac{1}{|I_x|} \int_{I_x} u(\xi, t) d\xi, \quad I_x = \left\{ \xi : |\xi - x| \leq \frac{\Delta x}{2} \right\}. \quad (\text{E.15})$$

Once we defined the averages, we discretize the partial differential equations, transforming them into algebraic equations by integrating them over each discrete element. Thus, we integrate (E.7) over the control volume  $I_x \times [t^n, t^n + \Delta t]$  and we get the exact equation:

$$\begin{aligned} \bar{u}(x, t^n + \Delta t) = \bar{u}(x, t^n) - \frac{1}{\Delta x} \left[ \int_{t^n}^{t^n + \Delta t} f \left( u \left( x + \frac{\Delta x}{2}, \tau \right) \right) d\tau \right. \\ \left. - \int_{t^n}^{t^n + \Delta t} f \left( u \left( x - \frac{\Delta x}{2}, \tau \right) \right) d\tau \right]. \end{aligned} \quad (\text{E.16})$$

Computing Eq. (E.16) at each grid point  $x = x_j$ , at each time step  $t^n$  we obtain the algebraic system for the unknown quantities  $\bar{u}_j^{n+1} = \bar{u}(x_j, t^n + \Delta t)$ , assuming that we already know the solution at the previous time step  $\bar{u}_j^n = \bar{u}(x_j, t^n)$ .





$$u(x, t^n) \approx \hat{u}(x, t^n) = \sum_j [\bar{u}_j^n + (u_x)_j^n (x - x_j)] \mathbb{I}_{[x_{j-1/2}, x_{j+1/2}]}, \quad (\text{E.18})$$

where

$$\mathbb{I}_{[x_{j-1/2}, x_{j+1/2}]} = \begin{cases} 1 & \text{if } x_{j-1/2} \leq x \leq x_{j+1/2} \\ 0 & \text{elsewhere} \end{cases}$$

and  $(u_x)_j^n$  are approximations to the exact derivatives,  $u_x(x_j, t^n)$ . These approximate derivatives are reconstructed from the computed cell averages, and this can be done in several ways, leading to different central schemes.

The easiest possible central scheme was introduced by Lax and Friedrichs ([262], [263]) in 1954, the celebrated Lax–Friedrichs (LxF) scheme.

This scheme simply derives from the choice of a piecewise-constant reconstruction

$$u(x, t^n) \approx \hat{u}(x, t^n) = \sum_j \bar{u}_j^n \mathbb{I}_{[x_{j-1/2}, x_{j+1/2}]}, \quad (\text{E.19})$$

which corresponds to set  $(u_x)_j^n = 0$  in Eq. (E.18). In this way, we can easily evaluate the staggered cell averages

$$\bar{u}_{j+1/2}^n = \bar{u}(x_{j+1/2}, t^n) = \frac{1}{\Delta x} \int_{x_j}^{x_{j+1}} u(\xi, t) d\xi = \frac{\bar{u}_{j+1}^n + \bar{u}_j^n}{2}. \quad (\text{E.20})$$

Now the flux integrals are trivial and thus we obtain the LxF scheme:

$$\bar{u}_{j+1/2}^{n+1} = \frac{\bar{u}_{j+1}^n + \bar{u}_j^n}{2} - \frac{\lambda}{2} [f(\bar{u}_{j+1}^n) - f(\bar{u}_j^n)], \quad (\text{E.21})$$

where  $\lambda = \Delta t / \Delta x$  is the fixed mesh ratio.

Despite its simplicity, the LxF scheme is hampered by a significantly large numerical dissipation, which of course prevents the correct detection of discontinuities and non-analyticities.

We highlighted that in the LxF scheme we used a piecewise-constant reconstruction. Thus, the most immediate generalization would involve a piecewise-linear approximation. This result in the so-called Nessyahu–Tadmor (NT) scheme [264].

Moving along the previously described steps, we start again from Eq. (E.17) and we assume the knowledge of the approximate solution at time  $t = t^n$  as piecewise-linear approximation  $\hat{u}(x, t^n)$ , the so-called MUSCL reconstruction [265], of the form

$$u(x, t^n) \approx \hat{u}(x, t^n) = \sum_j [\bar{u}_j^n + (u_x)_j^n (x - x_j)] \mathbb{I}_{[x_{j-1/2}, x_{j+1/2}]}. \quad (\text{E.22})$$

In this case, we do not have access to the derivatives of the function  $(u_x)_j^n$ , thus they need to be reconstructed using as an input the already known cell averages. This reconstruction process involves the use of the so-called TVD (Total Variation Diminishing) limiter functions, which, as the word says, have the task of limiting the reconstructed slopes to avoid unphysical oscillations of the solution close to the cell interfaces. However, we will not further comment on such a topic and the interested reader can refer to [266]. As an example, we present the limiter used in this work, the so-called *minmod limiter*

$$(u_x)_j^n = \text{minmod} \left( \frac{\bar{u}_j^n - \bar{u}_{j-1}^n}{\Delta x}, \frac{\bar{u}_{j+1}^n - \bar{u}_j^n}{\Delta x} \right), \quad (\text{E.23})$$

with

$$\text{minmod}(a, b) = \frac{1}{2} [\text{sgn}(a) + \text{sgn}(b)] \cdot \min(|a|, |b|). \quad (\text{E.24})$$

We then proceed to solve Eq. (E.16) subject to the piecewise-linear initial data (E.22). In this case the cell averages will trivially result in

$$\bar{u}_{j+1/2}^n = \bar{u}(x_{j+1/2}, t^n) = \frac{1}{\Delta x} \int_{x_j}^{x_{j+1}} u(\xi, t) d\xi = \frac{\bar{u}_{j+1}^n + \bar{u}_j^n}{2} + \frac{\Delta x}{8} \left( (u_x)_j^n - (u_x)_{j+1}^n \right). \quad (\text{E.25})$$

The next step is to approximate the flux integrals by the midpoint rule:

$$\int_{t^n}^{t^n + \Delta t} f(u(x_{j+1}, \tau)) d\tau \approx \Delta t \cdot f(u(x_{j+1}, \tau = t^n + \Delta t/2)) = \Delta t \cdot f(u_j^{n+1/2}). \quad (\text{E.26})$$

Here, the midpoint values,  $u_j^{n+1/2}$  are given by Taylor expansion

$$u_j^{n+1/2} = u(x_j, t^n + \Delta t/2) = \bar{u}_j^n + \frac{\Delta t}{2} \partial_t u(x_j, t^n) = \bar{u}_j^n - \frac{\Delta t}{2} (f_x)_j^n. \quad (\text{E.27})$$

Putting together what we got so far we obtain the discrete formulation of the NT scheme

$$\bar{u}_{j+1/2}^{n+1} = \frac{\bar{u}_j^n + \bar{u}_{j+1}^n}{2} + \frac{\Delta x}{8} \left( (u_x)_j^n - (u_x)_{j+1}^n \right) - \lambda [f(u_{j+1}^{n+1/2}) - f(u_j^{n+1/2})]. \quad (\text{E.28})$$

Thus, this scheme allows us to compute the numerical solution  $\bar{u}_{j+1/2}^{n+1}$  at the next time step  $t = t^{n+1}$  using as an input the staggered cell averages  $u_j, u_{j+1}$ .

The great improvement w.r.t. the LxF scheme is that, thanks to the use of higher-order reconstructions, the resulting numerical dissipation is significantly lower, allowing to achieve a higher resolution of shocks, rarefactions, and discontinuities in general. Another significant advantage of this scheme, as the whole central schemes class, is that they do not require the solution of the Riemann problem, which is usually required in other types of schemes, usually via an approximate Riemann solver (see for example [267]). One can easily notice that, if the reconstructed derivatives are set to zero,  $(u_x)_j^n = 0$ , the NT scheme simply results, as expected from the previous discussion, into a staggered version of the LxF scheme.

One of the main issues with the NT scheme is that it does not admit a semi-discrete formulation (see [142]), which means that it is not allowed to take the limit  $\Delta t \rightarrow 0$ . This could result in problems when a very small time step is needed, for example when the equation becomes particularly stiff, as in the case of FRG flow equation.

That is why we now finally move to the Kurganov and Tadmor scheme, which while retaining all the positive aspects of the NT scheme, allows indeed for a semi-discrete formulation.

In order to simplify the notation, due to the fact that most of the considered quantities are cell averages of the solution, when there is no possibility of ambiguity, we will omit the bar notation from now on.

## E.4 Kurganov and Tadmor fully discrete scheme

In this section we follow closely [142], the paper in which the KT scheme was firstly introduced. In particular, we sketch how to derive the discrete formulation of the KT scheme. In the previous section we deliberately provided several details on how the schemes are built such that the reader can understand the steps even omitting some of the tedious explicit calculations.

In the NT scheme we performed an average over the nonsmooth Riemann fans using spatial cells of the fixed width,  $\Delta x$ . The key forward step made in the Kurganov and Tadmor central scheme is to extrapolate more precise information about the local speed of wave propagation, and use it to average the nonsmooth parts of the computed solution over smaller cells of variable size. As previously, we start from the piecewise-linear reconstruction, which we assume is a solution at time level  $t^n$  based on the cell averages  $u_j^n$ , and we approximate derivatives  $(u_x)_j^n$  in (E.22) using a limiter. We now estimate the local speed of propagation at the cell interfaces,  $x_{j+1/2}$ : the upper bound is denoted by  $a_{j+1/2}^n$  and given by

$$a_{j+1/2}^n = \max \left\{ \rho \left( \frac{\partial f}{\partial u}(u_{j+1/2}^-) \right), \rho \left( \frac{\partial f}{\partial u}(u_{j+1/2}^+) \right) \right\}, \quad (\text{E.29})$$

where  $\rho$  denotes the spectral radius of the flux Jacobian,  $u_{j+1/2}^- = u_{j+1}^n - \frac{\Delta x}{2}(u_x)_{j+1}^n$  and  $u_{j+1/2}^+ = u_j^n + \frac{\Delta x}{2}(u_x)_j^n$  are the correspondent left and right intermediate values of  $\hat{u}(x, t)$  at  $x_{j+1/2}$ .

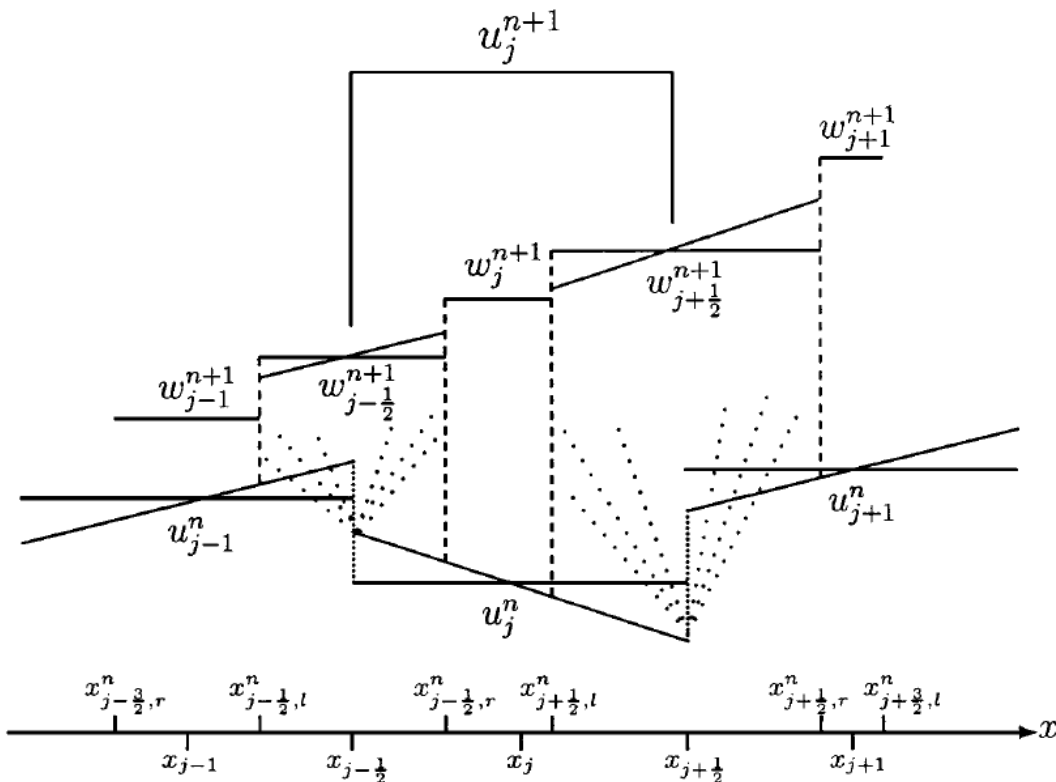


Figure E.3: Kurganov and Tadmor central approach. [142]

The Kurganov and Tadmor scheme is then constructed in two steps. First, we proceed along the lines of the NT scheme. The NT scheme is based on averaging over the staggered control volumes  $[x_j, x_{j+1}] \times [t^n, t^{n+1}]$  of fixed spatial width  $\Delta x$ . Instead, we now use narrower control volumes, where at each time step we integrate over the intervals  $[x_{j+1/2,l}^n, x_{j+1/2,r}^n] \times [t^n, t^{n+1}]$  where:

$$x_{j+1/2,r}^n = x_{j+1/2} + a_{j+1/2}^n \Delta t, \quad x_{j+1/2,l}^n = x_{j+1/2} - a_{j+1/2}^n \Delta t. \quad (\text{E.30})$$

We proceed with the exact evaluation of the new cell averages  $w_{j+1/2}^{n+1}$  and  $w_j^{n+1}$  at  $t^{n+1}$ . Let

$$\Delta x_{j+1/2} = x_{j+1/2,r}^n - x_{j+1/2,l}^n = 2a_{j+1/2}^n \Delta t \quad (\text{E.31})$$

denote the width of the Riemann fan which originates at  $x_{j+1/2}$ . Due to the finite speed of propagation, the points  $x_{j+1/2,l}^n$  and  $x_{j+1/2,r}^n$  separate between smooth and nonsmooth regions, and hence the nonsmooth parts of the solution are contained inside these narrower control volumes of spatial width  $2a_{j+1/2}^n \Delta t$ . Exact computation of the spatial integrals, combined to midpoint rule to approximate the flux integrals yields to

$$\begin{aligned} w_{j+1/2}^{n+1} &= \frac{1}{\Delta x_{j+1/2}} \int_{x_{j+1/2,l}^n}^{x_{j+1/2,r}^n} u(\xi, t^{n+1}) = \frac{1}{\Delta x_{j+1/2}} \int_{x_{j+1/2,l}^n}^{x_{j+1/2,r}^n} u(\xi, t^n) \\ &\quad - \frac{1}{\Delta x_{j+1/2}} \left[ \int_t^{t+\Delta t} f(u_{j+1/2,r}, \tau) d\tau - \int_t^{t+\Delta t} f(u_{j+1/2,l}, \tau) d\tau \right] = \\ &= \frac{u_j^n + u_{j+1}^n}{2} + \frac{\Delta x - a_{j+1/2}^n \Delta t}{4} ((u_x)_j^n - (u_x)_{j+1}^n) \\ &\quad - \frac{1}{2a_{j+1/2}^n} [f(u_{j+1/2,r}^{n+1/2}) - f(u_{j+1/2,l}^{n+1/2})], \end{aligned} \quad (\text{E.32})$$

where the midpoint values are obtained through Taylor expansions for the time integrals, and via the linear-piecewise reconstruction for the spatial midpoints:

$$u_{j+1/2,l}^{n+1/2} = u_{j+1/2,l}^n - \frac{\Delta t}{2} f(u_{j+1/2,l}^n)_x, \quad u_{j+1/2,l}^n = u_j^n + \Delta x (u_x)_j^n \left( \frac{1}{2} - \lambda a_{j+1/2}^n \right), \quad (\text{E.33})$$

$$u_{j+1/2,r}^{n+1/2} = u_{j+1/2,r}^n - \frac{\Delta t}{2} f(u_{j+1/2,r}^n)_x, \quad u_{j+1/2,r}^n = u_{j+1}^n - \Delta x (u_x)_{j+1}^n \left( \frac{1}{2} - \lambda a_{j+1/2}^n \right). \quad (\text{E.34})$$

Analogously, let

$$\Delta x_j = x_{j+1/2,l}^n - x_{j-1/2,r}^n = \Delta x - \Delta t (a_{j-1/2}^n + a_{j+1/2}^n) \quad (\text{E.35})$$

denote the width of strip around  $x_j$  which is free of the neighboring Riemann fans. Then as previously we obtain

$$\begin{aligned} w_j^{n+1} &= \frac{1}{\Delta x_j} \int_{x_{j-1/2,r}^n}^{x_{j+1/2,l}^n} u(\xi, t^{n+1}) = \frac{1}{\Delta x_j} \int_{x_{j-1/2,r}^n}^{x_{j+1/2,l}^n} u(\xi, t^n) \\ &\quad - \frac{1}{\Delta x_j} \left[ \int_t^{t+\Delta t} f(u_{j+1/2,l}, \tau) d\tau - \int_t^{t+\Delta t} f(u_{j-1/2,r}, \tau) d\tau \right] = \\ &= u_j^n + \frac{\Delta t}{2} (a_{j-1/2}^n - a_{j+1/2}^n) (u_x)_j^n \\ &\quad - \frac{\lambda}{1 - \lambda (a_{j-1/2}^n + a_{j+1/2}^n)} [f(u_{j+1/2,r}^{n+1/2}) - f(u_{j+1/2,l}^{n+1/2})]. \end{aligned} \quad (\text{E.36})$$

So we computed the solution at time level  $t = t^{n+1}$  in terms of the approximate cell averages,  $w_{j+1/2}^{n+1}$ ,  $w_j^{n+1}$ . These averages spread over a nonuniform grid which is oversampled by twice the number of the original cells at  $t = t^n$ . So the second and final step of the construction of Kurganov and Tadmor scheme is to convert these nonuniform averages back into the original grid we started with at  $t = t^n$ .

To obtain the cell averages over the original grid of the uniform, nonstaggered cells  $[x_{j-1/2}, x_{j+1/2}]$ , we consider the piecewise-linear reconstruction over the nonuniform cells at  $t = t^{n+1}$ , and we project its averages back onto the original uniform grid. Note that we do not need to reconstruct the average of the smooth portion of the solution,  $w_j^{n+1}$ , as it will be averaged out. Hence the required piecewise-linear approximation takes the form:

$$\begin{aligned} \hat{w}(x, t^{n+1}) = \sum_j \{ & [w_{j+1/2}^{n+1} + (u_x)_{j+1/2}^{n+1}(x - x_{j+1/2})] \mathbb{I}_{[x_{j+1/2,l}^n, x_{j+1/2,r}^n]} \\ & + w_j^{n+1} \mathbb{I}_{[x_{j-1/2,r}^n, x_{j+1/2,l}^n]} \}, \end{aligned} \quad (\text{E.37})$$

where the spatial derivatives  $u_x(x_{j+1/2}, t^{n+1})$  are approximated by

$$(u_x)_{j+1/2}^{n+1} = \frac{2}{\Delta x} \cdot \text{minmod} \left( \frac{w_{j+1}^{n+1} - w_{j+1/2}^{n+1}}{1 + \lambda(a_{j+1/2}^n - a_{j+3/2}^n)}, \frac{w_{j+1/2}^{n+1} - w_j^{n+1}}{1 + \lambda(a_{j+1/2}^n - a_{j-1/2}^n)} \right). \quad (\text{E.38})$$

Finally, the desired cell averages,  $u_j^{n+1}$  are obtained by averaging the approximate solution in (E.37). Kurganov and Tadmor fully discrete second-order central scheme then takes the form

$$\begin{aligned} u_j^{n+1} = \frac{1}{\Delta x} \int_{x_{j-1/2}}^{x_{j+1/2}} \hat{w}(\xi, t^{n+1}) d\xi = & \lambda a_{j-1/2}^n w_{j-1/2}^{n+1} + [1 - \lambda(a_{j-1/2}^n + a_{j+1/2}^n)] w_j^{n+1} \\ & + \lambda a_{j+1/2}^n w_{j+1/2}^{n+1} + \frac{\Delta x}{2} [(\lambda a_{j-1/2}^n)^2 (u_x)_{j-1/2}^{n+1} - (\lambda a_{j+1/2}^n)^2 (u_x)_{j+1/2}^{n+1}]. \end{aligned} \quad (\text{E.39})$$

## E.5 Semi-discrete formulation

### E.5.1 One-dimensional hyperbolic conservation laws

Let us consider the previously derived fully discrete second-order central scheme. To perform the semi-discrete reduction it is sufficient to send  $\Delta t \rightarrow 0$ , which also means  $\lambda \rightarrow 0$ . Rearranging the divided differences and separating the vanishing terms proportional to  $\lambda$  we find the semi-discrete formulation of the Kurganov and Tadmor scheme:

$$\begin{aligned} \frac{d}{dt} u_j(t) = - \frac{(f(u_{j+1/2}^+(t)) + f(u_{j+1/2}^-(t))) - (f(u_{j-1/2}^+(t)) + f(u_{j-1/2}^-(t)))}{2\Delta x} \\ + \frac{1}{2\Delta x} \{ a_{j+1/2} [u_{j+1/2}^+(t) - u_{j+1/2}^-(t)] - a_{j-1/2} [u_{j-1/2}^+(t) - u_{j-1/2}^-(t)] \}, \end{aligned} \quad (\text{E.40})$$

where we used

$$\lim_{\Delta t \rightarrow 0} \frac{u_j^{n+1} - u_j^n}{\Delta t} = \frac{d}{dt} u_j(t), \quad (\text{E.41})$$

$$u_{j+1/2}^+(t) = \lim_{\Delta t \rightarrow 0} u_{j+1/2,r}^{n+1/2} = u_{j+1}(t) - \frac{\Delta x}{2} (u_x)_{j+1}(t), \quad (\text{E.42})$$

$$u_{j+1/2}^-(t) = \lim_{\Delta t \rightarrow 0} u_{j+1/2,l}^{n+1/2} = u_j(t) + \frac{\Delta x}{2} (u_x)_j(t). \quad (\text{E.43})$$

In this reduction the maximal local speed  $a_{j+1/2}(t)$  takes the form

$$a_{j+1/2}^n(t) = \max \left\{ \rho \left( \frac{\partial f}{\partial u}(u_{j+1/2}^-(t)) \right), \rho \left( \frac{\partial f}{\partial u}(u_{j+1/2}^+(t)) \right) \right\}. \quad (\text{E.44})$$

This semi-discrete scheme admits a conservative form

$$\frac{d}{dt}u_j(t) = -\frac{H_{j+1/2}(t) - H_{j-1/2}(t)}{\Delta x}, \quad (\text{E.45})$$

with the numerical flux

$$H_{j+1/2}(t) = \frac{f(u_{j+1/2}^+(t)) + f(u_{j+1/2}^-(t))}{2} - \frac{a_{j+1/2}(t)}{2}[u_{j+1/2}^+(t) - u_{j+1/2}^-(t)]. \quad (\text{E.46})$$

One verifies that  $H_{j+1/2}(t) \equiv H(u_{j-1}(t), u_j(t), u_{j+1}(t), u_{j+2}(t))$  is a numerical flux consistent with Eq. (E.7), i.e.,  $H(v, v, v, v) = f(v)$ .

We again would like to emphasize the simplicity of the second-order semi-discrete central scheme, so that it does not require any information about the eigenstructure of the underlying problem beyond the CFL-related speeds,  $a_{j+1/2}(t)$ . The computation of the numerical derivatives,  $(u_x)_j(t)$  is carried out componentwise; no specific knowledge of characteristic decomposition based on (approximate) Riemann solvers is required.

## E.5.2 One-dimensional advection–diffusion equations

Let us consider the advection–diffusion equation (E.11). The Kurganov and Tadmor second-order semi-discrete scheme can be applied to this kind of equations in a straightforward manner, since we can treat the advection flux  $f$  and the diffusion flux  $q$  simultaneously. This results in the following scheme:

$$\frac{d}{dt}u_j(t) = -\frac{H_{j+1/2}(t) - H_{j-1/2}(t)}{\Delta x} + \frac{P_{j+1/2}(t) - P_{j-1/2}(t)}{\Delta x}. \quad (\text{E.47})$$

Here,  $H_{j+1/2}(t)$  is our numerical advection flux, and  $P_{j+1/2}(t)$  is a reasonable approximation to the diffusion flux, e.g., the simplest central-difference approximation

$$P_{j+1/2}(t) = \frac{1}{2} \left[ q \left( u_j(t), \frac{u_{j+1}(t) - u_j(t)}{\Delta x} \right) + q \left( u_{j+1}(t), \frac{u_{j+1}(t) - u_j(t)}{\Delta x} \right) \right]. \quad (\text{E.48})$$

Higher-dimensional generalizations are immediate and follow the same line of reasoning without significant differences.

In conclusion, the one-dimensional semi-discrete central scheme leads to a system of coupled nonlinear ODEs. Of course, if one wants to solve it numerically one has to introduce a time discretization, with the definition of a time step,  $\Delta t$ , stepping forward from time level  $t^n$  to  $t^{n+1} = t^n + \Delta t$ . In particular it is convenient to exploit high-precision built-in steppers provided by ODE solvers libraries. For example most of the result showed in this thesis are obtained using GNU Scientific Library (GSL) or SUNDIALS CVODE for stiff problems.





Publiziert unter der Creative Commons-Lizenz Namensnennung (CC BY) 4.0 International.  
Published under a Creative Commons Attribution (CC BY) 4.0 International License.  
<https://creativecommons.org/licenses/by/4.0/>